TECHNISCHE
UNIVERSITÄT
DARMSTADT

Fachbereich Physik
Institut für Kernphysik
Theoriezentrum

ELECTROMAGNETIC PROPERTIES OF LIGHT NUCLEI WITH CHIRAL EFFECTIVE FIELD THEORY CURRENTS

Vom Fachbereich Physik
der Technischen Universität Darmstadt

zur Erlangung des Grades
Doctor rerum naturalium (Dr. rer. nat.)

genehmigte Dissertation von
M.Sc. Rodric Bernard Johan Stéphane Seutin
aus Leuven, Belgien

Referent: Prof. Ph.D. Achim Schwenk
Korreferent: Privatdozent Dr. habil. Kai Hebeler

Tag der Einreichung: 09.10.2020
Tag der Prüfung: 18.11.2020

Darmstadt 2020
D17

Electromagnetic Properties of Light Nuclei with Chiral Effective Field Theory Currents

Elektromagnetische Eigenschaften leichter Kerne mit Strömen basierend auf
chiraler effektiver Feldtheorie

Genehmigte Dissertation von M.Sc. Rodric Bernard Johan Stéphane Seutin
aus Leuven, Belgien

Referent: Prof. Ph.D. Achim Schwenk

Korreferent: Privatdozent Dr. habil. Kai Hebeler

Tag der Einreichung: 09.10.2020

Tag der Prüfung: 18.11.2020

Darmstadt 2020 - D17

Bitte zitieren Sie dieses Dokument als:

URN: urn:nbn:de:tuda-tuprints-146498

URL: https://tuprints.ulb.tu-darmstadt.de/id/eprint/14649

ABSTRACT

The ability to describe electromagnetic properties of nuclei is fundamental to our understanding of nuclear structure and dynamics. Experimental methods that measure these properties enable a clean way to isolate the nuclear physics content, because the relatively weak and well understood electromagnetic interaction is perturbative in nature and thus appropriately described.

In this thesis we study electromagnetic properties of light nuclei within the framework of chiral effective field theory (EFT). The modern approach to low-energy nuclear physics is formulated by chiral EFT which describes the nucleus in terms of nucleon and pion degrees of freedom based on the symmetries of the underlying fundamental theory of quantum chromodynamics. It provides a systematically improvable calculation scheme and permits a unified description of the strong-interaction dynamics between nucleons and the interaction with an external probe. The nuclear component of such an interaction is described by nuclear currents. Both nuclear interactions and currents are consistently derived within chiral EFT and exhibit a naturally emerging many-body operator structure. Recent progress on the development of nuclear interactions and nuclear currents have set the stage for high-precision calculations complemented with systematic truncation uncertainty estimates.

We study the deuteron, the triton, and the helion electromagnetic form factors with two- and three-nucleon chiral interactions developed in an order-by-order manner which allows us to compute the associated truncation uncertainty estimates. We find good agreement at low momentum transfers for the charge form factors and a consistent description of the experimental first minimum once the uncertainty estimates are incorporated. For the trinucleon magnetic form factors we find that leading two-body currents (2BCs), which arise from the exchange of a pion between a pair of nucleons, lead to better agreement with data over the entire momentum-transfer region. To obtain insights into the effect of various chiral interactions with and without three-nucleon forces and to quantify the impact of 2BCs on the zero-momentum-transfer region, we analyze the magnetic moments and the electromagnetic radii of these light nuclei. We observe that three-nucleon forces reduce the radii slightly and have a negligible effect on the magnetic moment, while 2BCs significantly modify both the magnetic radius and magnetic moment indicating that the exchange dynamics between the nucleons are essential for magnetic observables.

As a first step towards a consistent study of other light nuclei, we examine the magnetic moment and a magnetic transition of ^{6}Li which is the next light nucleus after the three-nucleon nuclei with nonvanishing magnetic ground-state properties. To achieve this, we include contributions to the magnetic dipole operator beyond leading order which arise from the leading 2BCs and we employ similarity renormalization group evolved chiral interactions to enhance the many-body convergence. Our results are in remarkable agreement with a new precision experiment after consistently evolving and including 2BCs to the magnetic dipole operator, thus advancing our understanding of nuclear interactions and electromagnetic currents in many-nucleon systems.

ZUSAMMENFASSUNG

Die Fähigkeit, elektromagnetische Eigenschaften zu beschreiben, ist grundlegend für unser Verständnis von Kernstruktur und Kerndynamik. Experimentelle Methoden zum Messen dieser Eigenschaften ermöglichen es, den kernphysikalischen Inhalt zu isolieren, da die relativ schwache und gut verstandene stattfindende elektromagnetische Wechselwirkung perturbativer Natur ist und daher angemessen beschrieben wird.

In der vorliegenden Dissertation untersuchen wir die elektromagnetischen Eigenschaften leichter Kerne im Rahmen der chiralen effektiven Feldtheorie (EFT). Der moderne Ansatz der Niederenergie-Kernphysik wird durch die chirale EFT formuliert, die den Kern in Form von Nukleonen und Pionen als Freiheitsgrade beschreibt, basierend auf den Symmetrien der zugrunde liegenden fundamentalen Theorie der Quantenchromodynamik. Sie ermöglicht ein systematisch verbesserbares Berechnungsschema und erlaubt eine einheitliche Beschreibung der Dynamik der starken Wechselwirkung zwischen Nukleonen und der Ankopplung externer Felder. Die Kernkomponente einer solchen Wechselwirkung wird durch Kernströme beschrieben. Sowohl die Kernkräfte als auch Ströme werden konsistent in der chiralen EFT hergeleitet und weisen eine natürlich entstehende Vielteilchenoperatorstruktur auf. Jüngste Fortschritte bei der Entwicklung von Kernkräften und Kernströmen haben die Voraussetzungen für hochpräzise Berechnungen geschaffen, welche durch systematische Abschätzungen der Trunkierungsunsicherheit ergänzt werden.

Wir untersuchen die elektromagnetischen Formfaktoren des Deuterons, Tritons und des Helions mit Zweinukleonen und Dreinukleonen chiralen Wechselwirkungen. Die systematische Entwicklung dieser Kräfte erlaubt es uns, die zugehörigen Trunkierungsunsicherheitsabschätzungen zu berechnen. Wir finden gute Übereinstimmung der Ladungsformfaktoren bei niedrigen Impulsüberträgen und eine konsistente Beschreibung des experimentellen ersten Minimums, sobald die Unsicherheitsabschätzungen miteinbezogen sind. Für die magnetischen Trinukleonformfaktoren finden wir, dass führende Zweikörperströme (2BCs), die aus dem Austausch eines Pions zwischen einem Nukleonenpaar entstehen, für eine bessere Übereinstimmung mit den Daten über den gesamten Bereich des Impulsübertrags notwendig sind. Um Einblicke in die Wirkung verschiedener chiraler Wechselwirkungen mit und ohne Dreinukleonenkräfte zu erhalten und den Einfluss der 2BCs auf die Region mit null Impulstransfer zu quantifizieren, analysieren wir die magnetischen Momente und die elektromagnetischen Radien dieser leichten Kerne. Wir beobachten, dass Dreinukleonenkräfte die Radien geringfügig reduzieren und einen vernachlässigbaren Einfluss auf das magnetische Moment haben, während 2BCs sowohl den magnetischen Radius als auch das magnetische Moment signifikant modifizieren, was darauf hinweist, dass die Austauschdynamik zwischen den Nukleonen einen wesentlichen Beitrag für magnetische Eigenschaften darstellt.

Als ersten Schritt zu einer konsistenten Untersuchung anderer leichter Kerne untersuchen wir das magnetische Moment und einen magnetischen Übergang von ^{6}Li, welcher der nächste leichte Kern mit nicht verschwindenden magnetischen Grundzustandseigenschaften ist. Um dies zu erreichen, beziehen wir Beiträge zum magnetischen Dipoloperator jenseits der führenden Ordnung mit ein, die sich aus den führenden 2BCs ergeben, und verwenden Similarity Renormalization Group (SRG) transformierte chirale Wechselwirkungen, um die Vielteilchenkonvergenz zu verbessern. Unsere Ergebnisse stimmen in bemerkenswerter Weise mit einem neuen Präzisionsexperiment überein, nachdem wir die 2BCs konsistent SRG transformiert und in den magnetischen Dipoloperator einbezogen haben und fördern somit unser Verständnis der nuklearen Wechselwirkungen und der elektromagnetischen Ströme in Vielteilchensystemen.

CONTENTS

1 INTRODUCTION 1
- 1.1 Advances in low-energy nuclear theory . . . 1
- 1.2 Electromagnetic probes of nuclei . . . 7
- 1.3 Focus of this thesis . . . 11
- 1.4 Outline . . . 12

2 NUCLEAR FORCES AND CURRENTS FROM CHIRAL EFFECTIVE FIELD THEORY 15
- 2.1 Quantum chromodynamics . . . 16
- 2.2 Chiral effective field theory . . . 19
- 2.3 Nuclear forces from chiral EFT . . . 20
- 2.4 Nuclear currents from chiral EFT . . . 23
  - 2.4.1 External sources in QCD . . . 23
  - 2.4.2 Unitary transformation and time-ordered perturbation theory . . . 24
  - 2.4.3 Power counting and electromagnetic nuclear currents . . . 26
  - 2.4.4 Consistent description of nuclear forces and currents . . . 28
- 2.5 Effective field theory uncertainty quantification . . . 29

3 FEW-BODY FORMALISM 33
- 3.1 Two-body system . . . 33
  - 3.1.1 Definition of coordinates and two-body momentum basis . . . 33
  - 3.1.2 Momentum-space partial-wave basis . . . 34
  - 3.1.3 General current operator expansion . . . 36
  - 3.1.4 Deuteron wave function and electromagnetic observables . . . 37
- 3.2 Three-body system . . . 39
  - 3.2.1 Jacobi momenta and three-body momentum basis . . . 39
  - 3.2.2 Momentum-basis representation of a general current operator . . . 41
  - 3.2.3 Partial-wave expansion of a general current operator . . . 41
  - 3.2.4 Faddeev equations for three-nucleon bound states . . . 44

4 FEW-NUCLEON ELECTROMAGNETIC FORM FACTORS 47
- 4.1 Elastic electron scattering . . . 48
  - 4.1.1 Current experimental and theoretical status . . . 48
  - 4.1.2 Classical electron scattering . . . 50
  - 4.1.3 Born approximation . . . 51
- 4.2 Nucleon form factors . . . 53
- 4.3 Deuteron form factors . . . 56
  - 4.3.1 From matrix elements to form factors . . . 57

4.3.2 Two-body partial-wave matrix elements 59
4.3.3 Numerical evaluation and computational methods 62
4.3.4 Charge and quadrupole form factors 63
4.3.5 Magnetic form factor 67
4.4 Trinucleon form factors 68
4.4.1 Electromagnetic form factors with leading-order currents 69
4.4.2 Magnetic form factor with next-to-leading-order currents 78
4.5 Charge and magnetic radius determination 82
4.5.1 Deuteron electromagnetic radii 82
4.5.2 Trinucleon electromagnetic radii 84

5 MAGNETIC PROPERTIES OF LIGHT NUCLEI 87
5.1 Current theoretical status 88
5.2 Electromagnetic interaction 88
5.2.1 Multipole expansion 89
5.2.2 Long-wavelength limit 91
5.3 Magnetic moment from form factor 93
5.3.1 Spin-1/2 nucleus 93
5.3.2 Spin-1 nucleus 94
5.4 Magnetic moment operator 95
5.4.1 NLO magnetic moment operator from current operator 95
5.4.2 Two-body current Fourier transform 96
5.4.3 Intrinsic and Sachs operators 97
5.5 Deuteron and trinucleon magnetic moments 99
5.6 Current matrix elements in harmonic-oscillator basis 101
5.6.1 Two-body harmonic-oscillator transformation 102
5.6.2 Three-body Jacobi harmonic-oscillator states 105
5.6.3 Magnetic moment operator benchmark 106
5.7 Magnetic properties of ^{6}Li 107
5.7.1 Magnetic transition probabilities 108
5.7.2 Importance-truncated no-core shell model 109
5.7.3 ^{6}Li magnetic dipole strength and magnetic moment 112
5.8 Comparison against new S-DALINAC experiment 114

6 CONCLUSIONS AND OUTLOOK 117

A DEUTERON, TRITON, AND HELION PARTIAL-WAVE CONFIGURATIONS 121

B PARTIAL-WAVE EXPANDED FORM FACTORS 123
B.1 Deuteron form factors 123
B.1.1 One-body charge and quadrupole form factor 123
B.1.2 One-body magnetic form factor 125
B.2 Trinucleon form factors 128
B.2.1 One-body charge and magnetic form factor 129
B.2.2 Two-body magnetic form factor 133

C NLO MAGNETIC MOMENT OPERATOR 137

C.1 Fourier transform of NLO current operator 137
C.2 Intrinsic magnetic moment operator 139

D THREE-BODY TALMI-MOSHINSKY TRANSFORMATION 143

E EXPERIMENTAL QUANTITIES OF A =2, 3, AND 6 NUCLEI 149
E.1 Deuteron experimental results 149
E.2 Triton and helion experimental results 152
E.3 ^{6}Li experimental results 152

BIBLIOGRAPHY 157

1

INTRODUCTION

1.1 Advances in low-energy nuclear theory

Our understanding of atomic nuclei is essential for a broad and diverse scope of physical phenomena, ranging from fundamental symmetries to astronomical processes. For example, neutrinoless double beta decay investigations attempt to elucidate the nature of neutrinos, while precise knowledge about nuclear reactions is important for, e.g., nucleosynthesis and stellar evolution. *Nuclear structure theory's* goal is to develop a framework that describes and makes predictions about the properties of atomic nuclei, nuclear reactions and decays, and nuclear matter, which is a hypothetical system composed of an infinite number of nucleons in an infinite volume. One of the major hurdles yet to clear is the construction of a consistent theory beginning with a formulation in terms of the fundamental microscopic degrees of freedom. During the last decades, substantial efforts have been made in this direction leading to new insights that broadened our basic understanding of the dynamics between the building blocks of atomic nuclei, protons and neutrons, which in turn are composite structures consisting of elementary quarks. In particular, an important observation is that one can restrict to study nuclear phenomena at the relevant energy scale, such that a hierarchy of models appears which could all be connected to each other. There are approximately 3000 known nuclei, among which only 288 stable ones [1]. These, as well as hypothesized nuclei are classified in the nuclear chart according to their number of neutrons and protons, see Fig. 1.1. In the emerging nuclear landscape, stable nuclei establish the so-called valley of stability and the limits of nuclear existence are indicated by the drip lines. These drip lines are defined as the boundary beyond which nuclei decay by emitting protons or neutrons. Atomic nuclei are subject to all known fundamental interactions: the electromagnetic, the weak, the strong, and the gravitational interaction. They are shaped by the strong interaction, binding together protons and neutrons, and their structure can be precisely studied through electroweak probes, as the interaction has a weaker strength and well-understood properties. Low-energy nuclear structure theory has experienced a lot of advances in recent years, especially starting to connect to the fundamental strong interaction.

The strong interaction between quarks is described by *quantum chromodynamics* (QCD). Quarks are spin-$1/2$ particles that carry fractional elementary electromagnetic charge and the so-called color charge as an additional degree of freedom. The color charge comes in three different values, red, green, and blue and has similar properties to the electromagnetic charge. Interactions between quarks are mediated by so-called gluons, which have color charge themselves. Bound states of three quarks and quark-antiquark pairs are labeled as baryons and mesons, respectively. Together they make up a class of subatomic particles called hadrons.

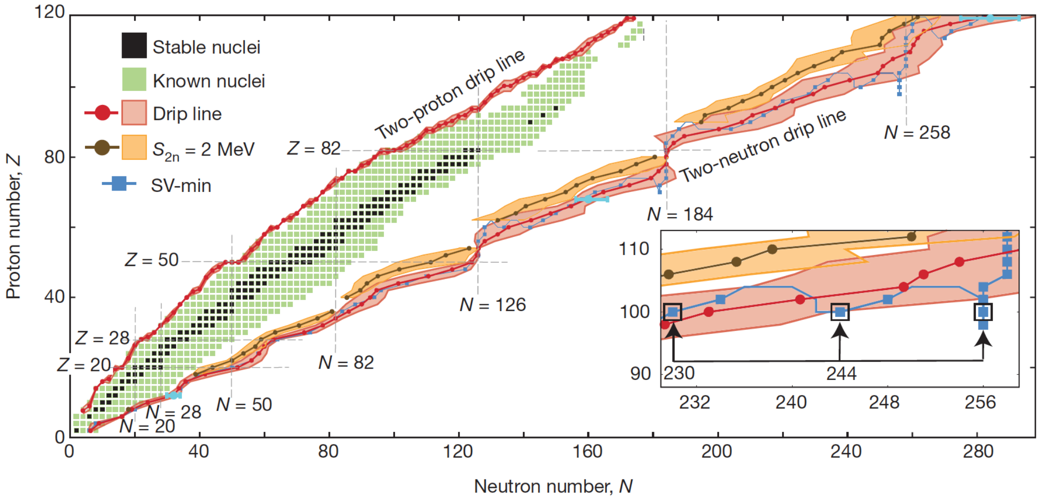

Figure 1.1: The nuclear chart of even-even nuclei as a function of proton number (Z) and neutron number (N), status of 2012. Known stable nuclei are shown as black squares, while known unstable nuclei as green squares. Red lines and red shaded areas represent calculated two-nucleon drip lines, i.e., emission of two nucleons, and their uncertainties. The line where the two-neutron separation energy equals 2 MeV is shown in brown. The blue line shows the results for a specific model and the inset focuses on the region near $Z = 100$. Figure taken from [1].

Examples of baryons are neutrons and protons, while pions are examples of mesons. Matter that is governed by QCD is usually referred to as *strong-interaction matter*. Two closely related and important properties of QCD are *color confinement* and *asymptotic freedom*. The former expresses that quarks are confined to color-singlet bound states at low-energies, i.e., they are trapped inside hadrons, while the latter describes the decreasing interaction strength with increasing momentum transfer. As a result, at low energies QCD is highly nonperturbative in terms of its fundamental degrees of freedom, and baryons and mesons emerge as new effective degrees of freedom. In fact, this low-energy regime is where atomic nuclei and nuclear matter exist. The nuclear interaction between nucleons can be understood as a residual interaction of the fundamental interaction between quarks inside the nucleons. Due to its nonperturbative nature a direct analytical or computational calculation of the nuclear interaction from QCD is extremely challenging or even impossible. Nevertheless, nonperturbative methods like *lattice QCD* [2, 3] tackle the challenge by performing calculations on a grid of discretized points in spacetime. Still, these calculations require enormous computational resources so that accurate and realistic calculations of few-nucleon systems remain out of reach, at least for the time being [4–7].

Clearly, in order to obtain a better understanding of the complex nuclear dynamics and to make valuable predictions about atomic nuclei as well as nuclear matter, alternative approaches have to be considered. While nuclear phenomenological models have experienced great successes [8], they possess inherent limitations, e.g., no (trivial) connection to the underlying theory of QCD, no systematic way of obtaining consistent many-body forces and currents, or no reliable method to estimate the theoretical uncertainty. This is why, during the last three decades, a paradigm shift from phenomenological models to *effective field theories* (EFTs) occurred. The conceptual foundations of EFTs are traced back to the work of Weinberg in the beginning of the 1960's, with modern formulations dating back to the late 1960's [9, 10] and the 1970's [11–13]. In general, they are based on the principle of *separation*

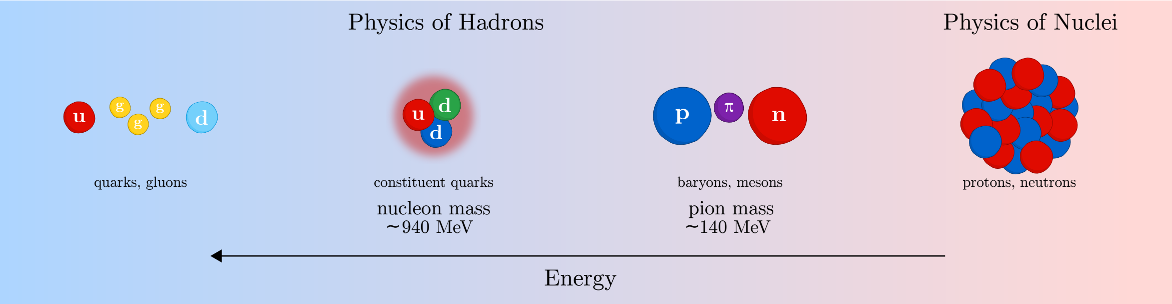

Figure 1.2: Hierarchy of energy scales and degrees of freedom of hadronic and nuclear physics. Figure adapted from [17].

of scales. This principle dictates that a specific physical phenomenon is associated with a certain energy scale, which in turn can be isolated and studied on its own. Constructing an EFT involves three main components: determining the *degrees of freedom* relevant to the process of interest, identifying the *symmetries* which constrain the process, and introducing an *expansion parameter*, e.g., a ratio of momenta p/Λ, where p represents the typical energy of the process and Λ is the energy scale of the omitted physics. A *power-counting* scheme for the expansion parameter is used to establish an importance hierarchy regarding the potentially infinite number of terms satisfying the symmetries. The unresolved high-energy physics gives rise to so-called *low-energy constants* (LECs). These constants could in principle be obtained from calculations of the higher-energy (effective) field theory, but are typically determined from fits to experimental data. This formulation then allows the computation of observables by means of a perturbative expansion in these small parameters. The main advantages of EFTs are that they simplify the calculation while keeping a connection to the underlying theory, they provide results to a given accuracy by truncating the perturbative expansion at some order while simultaneously giving an estimation of the theoretical uncertainty, and they predict their own breakdown as the perturbative approach becomes unreliable when the expansion parameter reaches $\mathcal{O}(1)$. If the fundamental theory is not known or when exact or even approximate predictions from the fundamental theory are difficult to obtain, then EFTs are necessary in order to make progress. Their conceptual simplicity and practical feasibility explains the onmipresence of EFTs nowadays, not only in nuclear physics but also in various other fields, e.g., beyond Standard Model physics [14], gravitational dynamics and cosmological large-scale structures [15], as well as superconductor physics [16].

The most widely employed EFT in nuclear physics today is *chiral EFT*, which was introduced in the seminal works of Weinberg in the beginning of the 1990's [18–20]. It is based on two main components: the separation of the nucleon and pion mass, and the symmetries of QCD, most importantly, the approximate chiral symmetry. These components allow one to construct an effective Lagrangian with nucleon and pion fields as the degrees of freedom, which contains all possible terms consistent with the symmetries of QCD, and omit the fundamental degrees of freedom. The associated expansion parameter consists of the ratio of the pion mass m_π to approximately the mass of the ρ-mesons $\Lambda_\mathrm{b}\sim$ 500 MeV $< m_\rho$, with Λ_b the breakdown scale. Figure 1.2 displays the hierarchy of energy scales exploited by chiral EFT: at high energies, strong-interaction matter is best described in terms of quarks and gluons, whereas lowering the energy to scales relevant for nuclear physics reveals that protons, neutrons, and pions are the ideal degrees of freedom to describe nuclei. The ideas presented by Weinberg

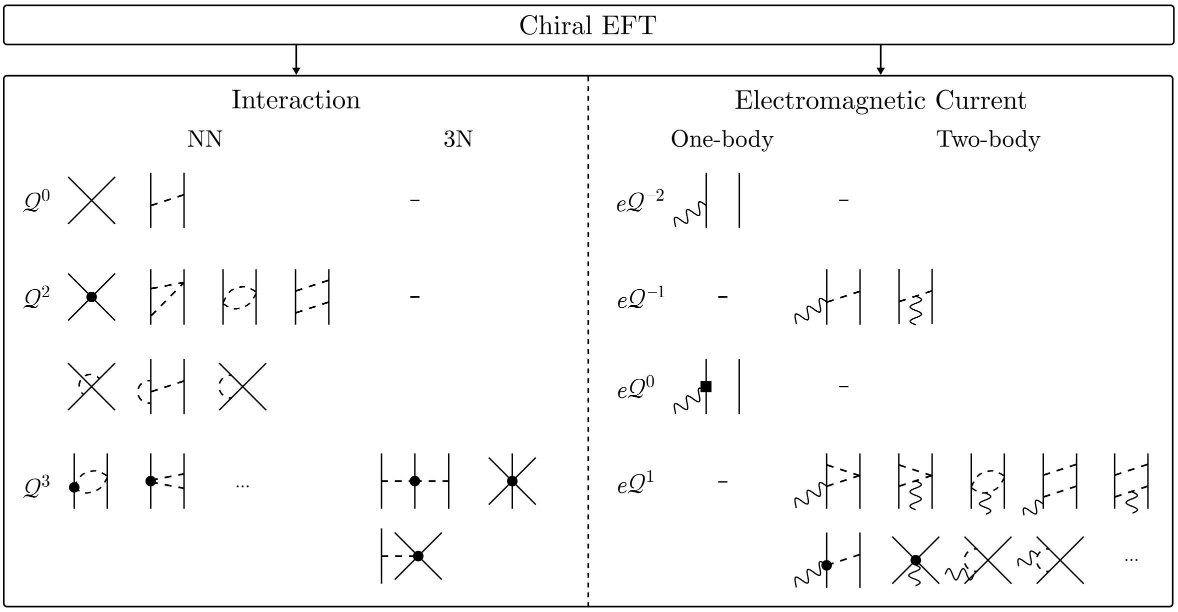

Figure 1.3: Diagrammatic representation of NN and 3N interactions up to third order (Q^3) and electromagnetic one- and two-body current operators up to fourth order (Q^1) relative to the first order (Q^{-2}). Nucleons, pions, and photons are displayed by solid, dashed, and wiggly lines, respectively. Chiral EFT provides a framework that allows for a consistent derivation of nuclear interactions and nuclear current operators.

established a new era in nuclear physics research by unlocking a systematic approach to derive nuclear interactions directly based on the symmetries of the underlying fundamental strong interaction. Chiral EFT describes the interaction between nucleons in terms of contact interactions that parametrize short-distance physics and one-or multiple-pion-exchange terms that account for intermediate- and long-range physics. This gives rise to *nucleon-nucleon* (NN), *three-nucleon* (3N), and many-nucleon interactions ordered according to their importance based on the Weinberg power-counting scheme, see the left section of Fig. 1.3. In fact, the resulting hierarchy of many-nucleon forces provides a natural explanation for the dominance of the NN interaction. Chiral EFT thus allows to show that nuclear phenomenological models constitute the correct first step in an approximation scheme to nuclear forces [21]. At present, chiral EFT is believed to provide the best answer to a practical and microscopic theory to describe nucleon interactions at low energies.

The last two decades have seen tremendous progress in the development of chiral EFT resulting in high-precision chiral NN potentials [22, 23]. Recently, for the first time, they matched and even outperformed the most accurate phenomenological potentials, albeit with fewer adjustable parameters [24]. For example, the left four panels of Fig. 1.4 illustrate the excellent agreement between neutron-proton scattering phase shifts and chiral NN potentials at fifth order. Even though the NN sector seems to be under control, 3N interactions are still less understood, both on a conceptual and quantitative level. Three-nucleon as well as higher-body interactions arise naturally due to the composite structure of nucleons and are well-known to have a substantial impact on nuclear systems [25, 26]. Chiral EFT explains their importance relative to the NN counterparts and provides a framework to systematically include and study their contributions in calculations, note the left part of Fig. 1.3. During the last decade, NN and 3N chiral potentials have been successfully applied in the few- and many-

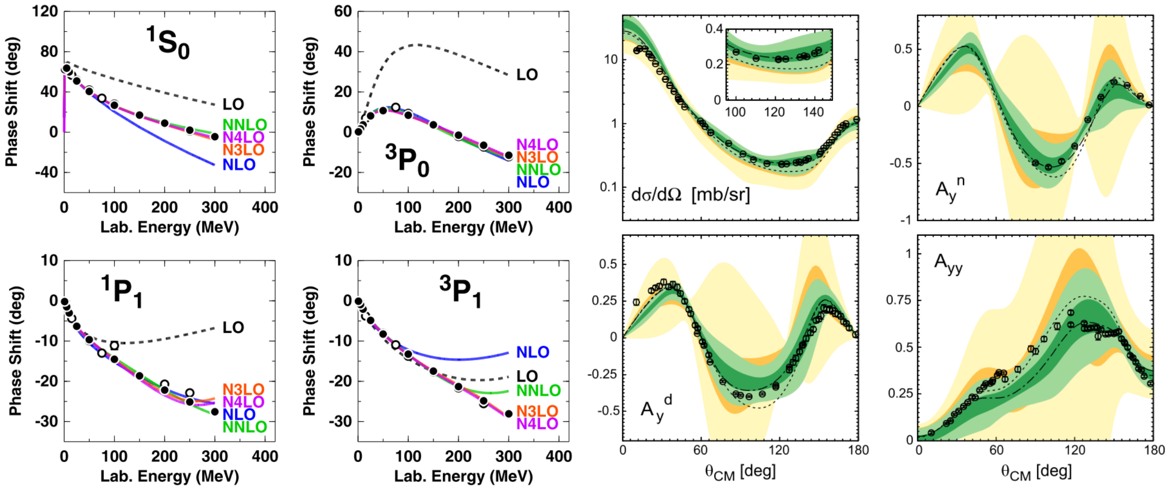

Figure 1.4: Left: Neutron-proton scattering phase shifts (in degrees) as a function of laboratory energy (in MeV) for S and P waves obtained from chiral NN interactions. Results are shown for five orders of the chiral expansion as denoted. Open and filled circles represent results from the Nijmegen analysis [36] and the George-Washington-University analysis [37]. Figure taken from Ref. [23]. Right: Differential cross section $\mathrm{d}\sigma/\mathrm{d}\Omega$ (in mb/sr), nucleon and deuteron analyzing powers A_y^{n} and A_y^{d}, and deuteron tensor analyzing power A_{yy} as a function of center-of-mass angle (in degrees) for elastic nucleon-deuteron scattering at a laboratory energy of $E_{\mathrm{lab}} = 135$ MeV. Results from calculations with consistent NN and 3N chiral interactions at second (yellow) and third (green) order are shown together with their truncation uncertainty estimation. Dotted and dashed lines show result based on phenomenological interactions and open circles are proton-deuteron data. Figure taken from Ref. [34].

nucleon sector [27–30] as well as in calculations of infinite nuclear matter [31, 32]. Nevertheless, ongoing efforts seek to improve the conceptual development and practical implementation of 3N interactions, currently making it a very active field of research [33–35]. For example, the four panels on the right half of Fig. 1.4 present recent results of elastic nucleon-deuteron scattering observables obtained with consistent NN and 3N interactions up to third order in the chiral expansion. The agreement with data is worse compared to the NN scattering observables which implies the possibility for improvements by, e.g., consistently including higher-order 3N interactions.

In the last few years, considerable attention has been devoted to the issue of quantifying uncertainties in theoretical calculations [38, 39]. The systematic expansion of the chiral Lagrangian, and successively the chiral interaction in principle permits to systematically quantify the *truncation uncertainty*, i.e., the uncertainty caused by truncating a calculation at finite order. This uncertainty is often the dominant error in EFT calculations. If the power counting is implemented correctly and systematically, uncertainties of observables should decrease for increasing order of the calculations. This property is exploited by *Bayesian methods* for EFTs to quantify the systematic uncertainties arising from truncating the expansion, and consequently to provide a statistically solid interpretation of truncation uncertainties [40–43]. An example of these truncation uncertainties obtained with a Bayesian model can be observed in the four panels on the right half of Fig. 1.4, where dark and light shades provide a 68% and 95% degree of belief interval, respectively. Note the decrease in the width of the confidence intervals in going from second to third order results. Efforts to quantify uncertainties are important, not only, to carry out meaningful comparisons to experimental and other theoretical results, but also to provide reliable predictive capabilities and extrapolations to unknown territories of the nuclear chart. In addition, they shed light on more fundamental questions about the EFT, e.g., the nature of the convergence pattern, the validity of the breakdown scale, and the naturalness assumption [41, 42]. Bayesian methods have already been applied in various studies [34, 44, 45], while current efforts attempt to quantify all EFT related uncertainties [46–48].

Another advantage of the chiral EFT framework is the possibility to consistently include external sources. These sources describe nucleus-probe interactions and are incorporated by extending the chiral Lagrangian with, e.g., vector and axial-vector terms which are associated with electromagnetic and weak interactions, respectively. The resulting *nuclear current operator*, generally denoted by J^μ, is then used to calculate the nuclear current by evaluating its expectation value with respect to initial $|i\rangle$ and final $|f\rangle$ wave functions of the nucleus of interest, i.e., $\langle f|\, J^\mu \,|i\rangle$. This prediction of the current serves as a test for nuclear models, in particular, for chiral EFT. Nuclear currents and interactions are tightly connected by the gauge invariance of the framework. In fact, similar to nuclear interactions, a systematic expansion arises for nuclear currents, see the right half of Fig. 1.3. They can also be organized based on their importance according to a power-counting scheme. Many-body currents are naturally generated in the expansion. The one-body current is the dominant part of the nuclear current operator: at lowest order, the interaction with the nucleus is well described by summing up the contribution of the interaction with each nucleon inside the nucleus. At the simplest level, many-body currents manifest themselves as *two-body currents* (2BCs) arising from the exchange of a pion between two nucleons. These 2BCs are small, however necessary for precision calculations, where they often provide the missing part to bring theory in better agreement with experiment. Although their necessity was confirmed more than 40 years ago [49], only now, with the arrival of chiral EFT, they are embedded in a consistent framework such that they can be consistently computed and implemented in calculations. In addition, the power-counting scheme provides a natural explanation for the importance and hierarchy of two- and many-body currents. The connection between current operators and interactions becomes more apparent by observing the LECs: the same LEC appears in a leading contribution to the 3N interaction and in the so-called contact 2BC. It was then realized that this relation allows to study and constrain this LEC not only by bound-state observables, but also by electroweak observables [50]. Remarkably, chiral EFT allows to study these strong interaction dynamics and electroweak processes in the low-energy regime of nuclear physics in a single theoretical framework. All these aspects suggest that nuclear current operators offer a unique tool to test chiral EFT and vice versa. Despite great efforts, much is still to be understood about the conceptual development of 2BCs, e.g., consistently regularized interactions and currents [35], and their effect on electroweak observables. Therefore, one of the frontiers in nuclear theory is to include and study these two- and higher-body currents in calculations of few- and many-nucleon systems.

In nuclear theory, few-nucleon systems are well suited to study nuclear models. As they consist of only a few interacting particles, solutions can be obtained with high accuracy at a relatively moderate computational cost. In comparison, approaches attempting to solve many-nucleon systems have to resort to approximations in order to reduce the complexity of the problem. Therefore, the computations might suffer from systematic effects that do not reflect genuine physical differences of the system under investigation. In addition, few-nucleon systems provide the advantage to study two- and three-body effects in isolation without

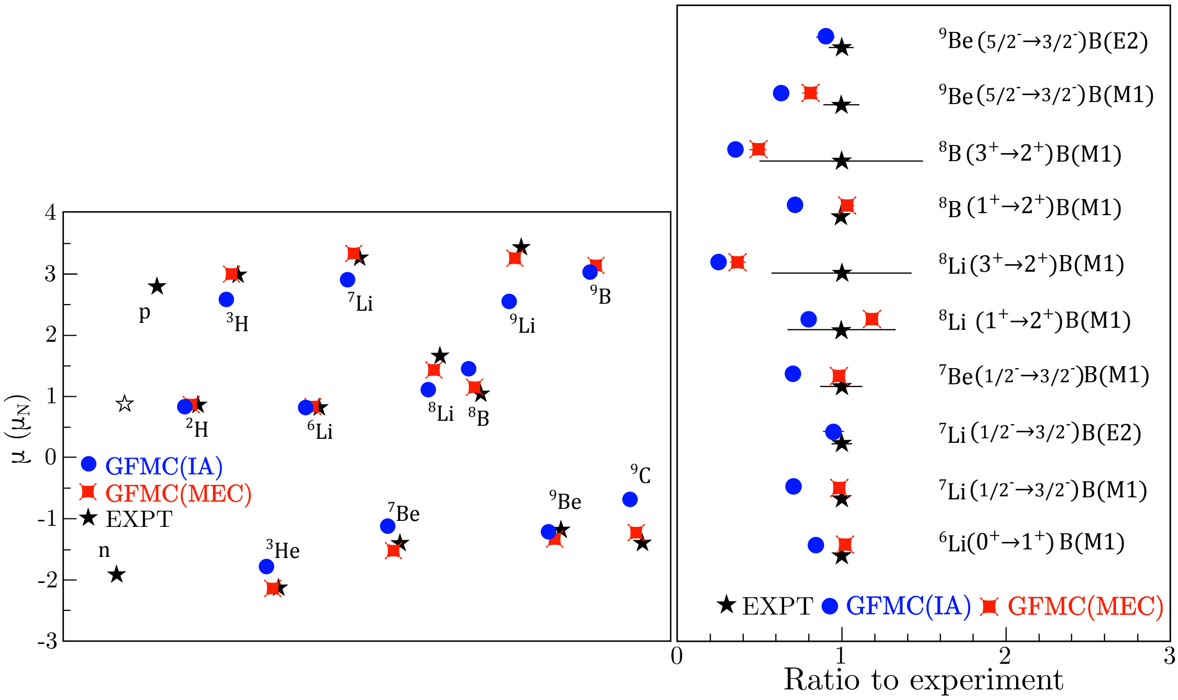

Figure 1.5: Left panel: Magnetic moments of light nuclei with $A \leqslant 9$ obtained with the Green's function Monte Carlo (GFMC) many-body method. Black stars, blue dots, and red diamonds represent experimental values, one-body operator (IA) calculations, and two-body operator (MEC) results, respectively. The two-body operator results include current operators up to fourth order in the chiral expansion. Right panel: Electromagnetic transition widths for light nuclei up to ^{9}Be shown as the ratio to experiment. Figures taken from Ref. [51].

contamination of higher-body interactions or currents. In that sense, a clear connection to the microscopic physics is preserved. A first exploratory step towards other nuclei is achieved by calculating observables of light nuclei, i.e., $A \sim 10$, with A the number of nucleons. Their relatively low number of nucleons implies that many-body approximations can be kept under control. A variety of methods exist to solve the nuclear many-body problem, such that possible cross checks of results can be made. Taking all these aspects into account, few-nucleon and light nuclei make ideal testing grounds to assess our understanding of nuclei. The possibility to obtain accurate results for light nuclei and the advances made in deriving nuclear current operators have resulted in high-precision calculations of electromagnetic observables in light nuclei. For example, Fig. 1.5 shows magnetic moments and electromagnetic transitions including chiral 2BC operators. The important impact of 2BCs demonstrates the importance of including consistent electromagnetic operators in calculations of light nuclei.

1.2 Electromagnetic probes of nuclei

Electron-scattering experiments provide the best known evidence of the internal structure of nuclei and nucleons. The detection of high-energy electrons scattered off nuclei or nucleons provides information on the target, e.g., its shape, much in the same way as the detection of light scattered off and object in a microscope. Similarly, experiments where only the final state of the electron is observed, obtain information about the size and shape of the nucleus in terms of its static charge and current density. In other words, they provide knowledge on the charge and current spatial distributions inside the nucleus. Electron scattering is an intensely studied field with a long and rich history of experimental and theoretical work, and exciting new developments at every frontier.

In the beginning of the 1950's, electron scattering experiments were performed to test the current understanding of the electromagnetic interaction with nuclei and nucleons. The first experiments on, e.g., copper and gold, observed a finite nuclear size and were performed by Lyman *et al.* [52]. At the *High Energy Physics Laboratory* at Stanford university, Hofstadter and his team performed systematic measurements with high-energy electron beams up to $E_\mathrm{e} \sim 550$ MeV on a range of nuclei, uncovering their charge distributions [53]. During the same period, they also performed experiments on nucleons for the first time, resulting in the first determination of the proton charge radius which was determined to have a nonzero size of 0.77(10) fm [54]. For this discovery and his pioneering work on electron-nucleus scattering, Hofstadter received the Nobel prize in 1961 [55]. In general, electron scattering played a dominant role in the progress of theories describing strong-interaction matter. For example, the influential experiments carried out at the *Stanford Linear Accelerator Center* at much higher electron energies and momentum transfers revealed that electrons scatter off approximately free pointlike particles, showing that nucleons have a substructure as well [56, 57]. This observation, in turn, led to the search for asymptotically free theories [58]. For nuclear structure theory, on the other hand, an important achievement attributed to electron-nucleus scattering is the demonstration of the existence of exchange currents [58, 59]. These additional currents can be described as arising from the exchange of charged mesons between nucleons. They are essential to explain the observed charge and current distributions of nuclei and other electromagnetic processes, e.g., the thermal neutron radiative capture on the proton. Still today, efforts on both the experimental and theoretical side continue to contribute to our understanding of the internal structure of nuclei and nucleons.

In the last decade, the study of the electromagnetic structure of nucleons, especially of the proton, with elastic electron scattering has been in the focus of great attention. The proton radius extracted from *atomic hydrogen* experiments and from *muonic hydrogen* experiments revealed a statistically significant discrepancy.[1] The former type of experiments found a value of 0.8751(61) fm [60], according to the *Committee on Data* (CODATA) 2014 update, while the latter a value of 0.84087(39) fm [61]. This discrepancy is better known as the so-called *proton-radius puzzle* and led to intense investigations. However, recent electron-proton (e-p) scattering measurements at momentum transfers one order of magnitude lower than previous measurements [62], and two spectroscopy measurements in atomic hydrogen [63, 64], found radii in agreement with values from muonic hydrogen experiments. Therefore, the recommended proton radius in the updated CODATA-2018 release is changed to 0.8414(19) fm [65]. Nonetheless, the new data is unable to explain the difference observed in the pre-2010 data, still leaving the proton-radius puzzle not fully solved. The near future will point out if the proton-radius puzzle is completely resolved or needs further investigation.

The proton-radius puzzle triggered searches for similar discrepancies in light nuclei, mainly to help clarify the puzzle. For example, a similar observation of the deuteron radius resulted in a *deuteron-radius puzzle*. This puzzle indicates the disagreement between radius measurements from *muonic deuterium* spectroscopy and *atomic deuterium* experiments, i.e., atomic

---

[1] Atomic hydrogen data includes results from two different types of experiments. The first type is e-p scattering from which the radius can be extracted by calculating the slope at zero momentum transfer, while the second type measures energy-level shifts of transitions in hydrogen atoms with spectroscopy. These shifts in the energy levels are related to finite nuclear size effects, such that the radius can be inferred from them.

spectroscopy or electron-deuteron (e-d) scattering. Despite taking into account the corrected proton radius, the recommended CODATA-2018 deuteron radius is 2.12799(74) fm [65], which is 1.9σ larger than the muonic experiment result [66] and still 2.9σ smaller than the value from atomic deuterium spectroscopy [67]. These observations set off a renewed interest to perform e-d scattering experiments at low momentum transfers for which results are expected in the near future [68, 69]. Because the radius is sensitive to the zero-momentum-transfer region, precise data at low momentum transfers ensures that fewer assumptions have to be made in extrapolating experimental results to zero momentum transfer. For now, nuclear structure calculations of the deuteron radius are not precise enough [70–72] to offer any help in resolving the deuteron-radius puzzle, as the experimental uncertainty is still one order of magnitude smaller. Experimental results from atomic and muonic spectroscopy of three-nucleon systems are expected in the near future [73, 74] and will greatly advance nuclear structure theory. Electromagnetic radii extracted from scattering experiments have a low precision of the order of $\sim 5\%$ [75], which is too large to study nuclear structure effects arising from 3N interactions and isospin effects which show variations of $\leqslant 1\%$. Even though these experimental efforts are mainly undertaken to help clarify the proton-radius puzzle, they will provide valuable results for advanced nuclear structure calculations in the future.

To interpret experimental data, a theoretical description of the scattering event and the target itself is required. Because an electron probe is used, only an electromagnetic interaction occurs between the incident electron and the target under investigation. The electromagnetic interaction is simple, well understood, and described by *quantum electrodynamics* (QED). This theory prescribes how to compute the elastic differential cross section in the so-called *Born approximation*. This approximation provides a perturbative description of the scattering event which, to lowest order, is given by the exchange of a single photon between the scatterer and the target. The resulting differential cross section takes into account the finite target size by means of a so-called *form factor*. This function is related to specific current operator matrix elements of the target and represents the nuclear structure input to the calculation. The prediction of form factors by using specific nuclear models can be well assessed in experimental studies.

In the lowest order Born approximation, a single virtual photon is exchanged between the electron and the target, transferring energy ω and momentum $\mathbf{q}$. This process is well understood, as the interaction strictly happens with the charge and current density of the target. The electromagnetic interaction is weak compared to the strong interaction as the fine-structure constant α, which characterizes the interaction strength between charged particles, is considerably smaller than the strong coupling constant, i.e., $\alpha \approx 1/137 \ll \alpha_{\mathrm{s}}$. This provides two main advantages: first, the structure of the target stays undisturbed during the scattering process. Second, it allows a perturbative description of the event, in form of a simple one-photon exchange. This results in accessible expressions for the scattering cross section from which the nuclear structure contribution can be straightforwardly isolated. The scattering cross section is proportional to Fourier transforms of the electromagnetic densities of the target. These functions depend on the momentum transfer and are related to specific matrix elements. In experiments, the momentum transfer to the target can be varied while the energy loss of the electron is kept fixed. The only required constraint is that the four-momentum transfer has to stay spacelike, i.e., $q^2 = q_\mu q^\mu = \omega^2 - \mathbf{q}^2 < 0$. This allows to access the Fourier transforms of the charge and current densities, gaining access to the internal electromagnetic structure of the nucleus. These Fourier transforms are exactly the form factors introduced

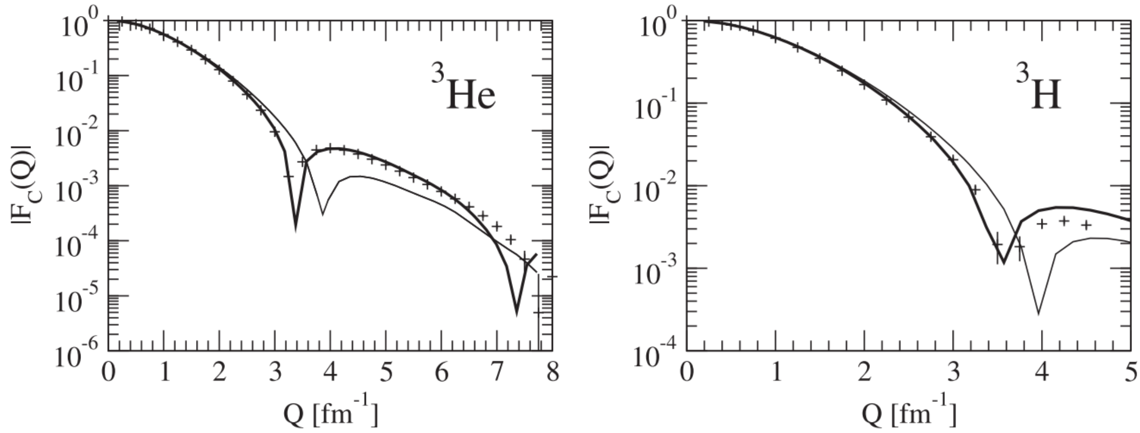

Figure 1.6: Charge form factor of ^{3}He (left) and ^{3}H (right) as a function of momentum transfer Q (in fm^{-1}) obtained from calculations using the SNPA. Thin and thick solid lines correspond to results with one- and many-body operators, respectively. Crosses represent experimental data. Figure taken from [76].

above, see Fig. 1.6 for an example of a charge form factor. They are the quantities providing information about the internal electromagnetic structure of the target and they depend the magnitude of the momentum transfer $q = |\mathbf{q}|$. Events that do not transfer energy to the nucleus, i.e., $\omega = 0$, are classified as *elastic electron scattering*.

The resolution of the electron probe is inversely proportional to the momentum transfered, i.e., $\propto 1/|\mathbf{q}|$. Typical nuclear scales of interest range from 0.1 fm to 10 fm, such that electron beams must have relativistic energies ranging from around 12 MeV to 1250 MeV. Low momentum transfers probe long-range dynamics of the target, e.g., nuclear radii and moments, while high momentum transfers explore short-distance details within the nucleus. Going to even higher energies, i.e., $E_\mathrm{e} > 1250$ MeV, and hence to higher momentum transfers, the substructure of nucleons themselves is resolved. The exploration of these much shorter distances belongs to the realm of particle physics. However, accounting for the substructure of nucleons in nuclear form factor calculations provides an important correction and is achieved by including the nucleon form factor. Often, these nucleon form factors are given in terms of a parametrization of experimental data.

There exists a rich history of theoretical work that describes elastic electron scattering and nuclear electromagnetic structure in great detail [76–81]. Until recently, what is often referred to in the literature as the *standard nuclear physics approach* (SNPA), was the dominant method to study the nucleus and electromagnetic reactions with it. The SNPA provides a theoretical description of few-nucleon electromagnetic structure and corresponding dynamics by regarding the nucleus as pointlike nucleons interacting through two-body potentials. These potentials are then fit to two-body scattering and bound-state data. The resulting potentials from this approach are called *realistic*. Electromagnetic charge and current operators are then constructed from a nonrelativistic expansion of the covariant single-nucleon current [81].[2] These single-nucleon charge and current operators constitute the well-known nonrelativistic *Impulse Approximation* (IA) and provide the dominant contribution to the nuclear current. Improving upon this description is done by considering effects of NN (and even 3N) interactions

---

[2] One can also employ a fully relativistic treatment of the nuclear dynamics as described in the covariant spectator theory [76]. We will, however, leave out the relativistic treatment from our discussion.

through the application of the continuity equation, which is derived from the gauge invariance of the theory. This results in the construction of many-body currents, establishing the so-called *meson-exchange currents* (MECs). Currents constructed from the continuity equation are called *model independent* as they are completely constrained by the gauge invariance of the theory. On the other hand, the continuity equation does not constrain components of the current orthogonal to the virtual photon momentum, leaving the possibility to construct *model dependent* currents. Most realistic potentials include a one-pion exchange (OPE) process to describe the long-range behavior of the nuclear interaction. In turn, this generates a two-body OPE current which describes the interaction of the virtual photon with a nucleon pair that interacts through the exchange of a virtual pion. Meson-exchange currents are often the missing contribution that bring observables in agreement with experimental observations, as was first suggested by Villars [82] and Miyazawa [83], and quantitatively demonstrated by Riska and Brown [49]. Because MECs contribute essential corrections to observables their effect has been studied very carefully, especially in the case of light nuclei [80]. As an example, Fig. 1.6 displays charge form factors of $A = 3$ nuclei which are obtained with the SNPA and include MECs.

1.3 Focus of this thesis

Electron scattering promises to be a great instrument to study nuclear models: given that the electromagnetic interaction is well known, the nuclear structure component is readily isolated from the external structureless probe content. The nuclear structure information then provides an excellent way to test the nuclear models, as both nuclear forces and nuclear current operators required to compute the observables are derived from the model. Even though the SNPA approach has led to many successes, it is unsatisfactory to understand electromagnetic properties of nuclei from a microscopic perspective. As previously mentioned, chiral EFT describes the interaction among nucleons themselves and with external probes in terms of hadronic degrees of freedom, while making a direct connection with QCD and providing a systematic improvable calculation scheme. Indeed, leading electromagnetic current operators and their corrections are naturally derived within the framework of chiral EFT, in line with nuclear forces. This way, chiral EFT provides a practical calculation scheme for nuclear interactions and nuclear currents to consistently study nuclear electromagnetic processes in terms of relevant degrees of freedom. In addition, the promise of a systematic expansion allows one to devise methods that reliably quantify the neglected terms in a statistically sound fashion. Doing so, provides a way to test the applicability and predictive power of the electromagnetic observables and to make meaningful comparisons to experimental data. We remark that literature results which combine currents derived within chiral EFT with wave functions obtained from realistic potentials are called *hybrid calculations*. Such calculations are inherently inconsistent as there is no connection between the currents and the interaction, and therefore can lead to results with an unclear interpretation.

This thesis contributes to the understanding of the nucleus by calculating electromagnetic observables of few-nucleon systems in light of the new developments in chiral EFT we introduced above. We mainly focus on calculating electromagnetic form factors of the *deuteron*, the *triton*, and the *helion*. Commonly, the two $A = 3$ systems are denoted by *trinucleons*. The central theme in our investigation is the inclusion of the leading 2BCs in calculations, as these operators constitute the dominant correction to electromagnetic observables. By nature, the leading 2BCs have an isovector operator structure, which implies that they do not contribute to the isoscalar deuteron. Accordingly, their effect has to be studied by analyzing the trinucleon electromagnetic properties. A calculation of the electromagnetic form factor allows one to extract two more observables: the static moments of the nucleus correspond to the normalization of the form factors, i.e., its value at $q = 0$, while the radius is given by the slope of the form factor at $q = 0$. The various existing form factors, static moments or radius results either adopt a hybrid approach or make use of "first generation" chiral interactions, which are not available at every order, have a low precision, and moreover display a mismatch between the order of the NN and 3N interaction. Considering the exciting new developments in the field of chiral EFT, these results are in need of an update.

The ability to estimate the truncation uncertainty has several benefits. Recall that the form factor is a function of the momentum transfer between the electron probe and the target nucleus. The high momentum transfer region is particularly sensitive to the wave function, and thus the interaction. Indeed, one always aims to reproduce the experimental first minimum of the form factor exactly. However, the region of the first minimum coincides with the kinematic domain where the predictive power of chiral EFT starts to decrease due to a large expansion parameter, leading to poor convergence of the chiral expansion. At the same time, the truncation uncertainty increases in this region given that it depends on the momentum scale at which the process happens. This implies that the uncertainty is large in the region of the first minimum, suggesting that the expectation to reproduce it exactly might be too strict. Another benefit is the ability to make meaningful comparisons to experimental data and to quantify the possible disagreement.

A possibility to further study the effect of leading 2BCs, is to extend the analysis to other light nuclei. As a first step in this direction we examine their effect on the magnetic properties of ^{6}Li. Magnetic observables are particularly sensitive to the dynamics between the nucleons, making them suitable candidates to study 2BCs. Specifically, we analyze the magnetic moment and an isovector magnetic transition between an excited state and the ground state of ^{6}Li. Such electromagnetic transitions are calculated with the same tools as we used for the form factors and the static moments, and thus are also sensitive to the 2BC corrections of the operator. However, because the solution of the system is more involved, it is beneficial to simplify the operator expression. This simplification is realized by considering the long-wavelength limit of the current operator, i.e., the operator in the limit of $q \to 0$, which is connected to the well-known magnetic moment operator. Even though this only provides long-range physics observables, the full dependence on the 2BCs is still included in the results.

Figure 1.7 summarizes the focus points of this thesis and shows the connections between the different topics. Each element of the figure shows what we consider in each chapter. The starting point of our discussion is chiral EFT, which allows us to construct matrix elements and calculate observables. In the next section, we give an outline and provide details about the contents of each chapter.

1.4 Outline

This thesis is constructed as follows: in Chapter 2 we outline the foundational framework of this thesis, chiral EFT. We begin in Section 2.1 by discussing the QCD Lagrangian and show how chiral symmetry naturally emerges in the limit of vanishing quark masses. Then, we

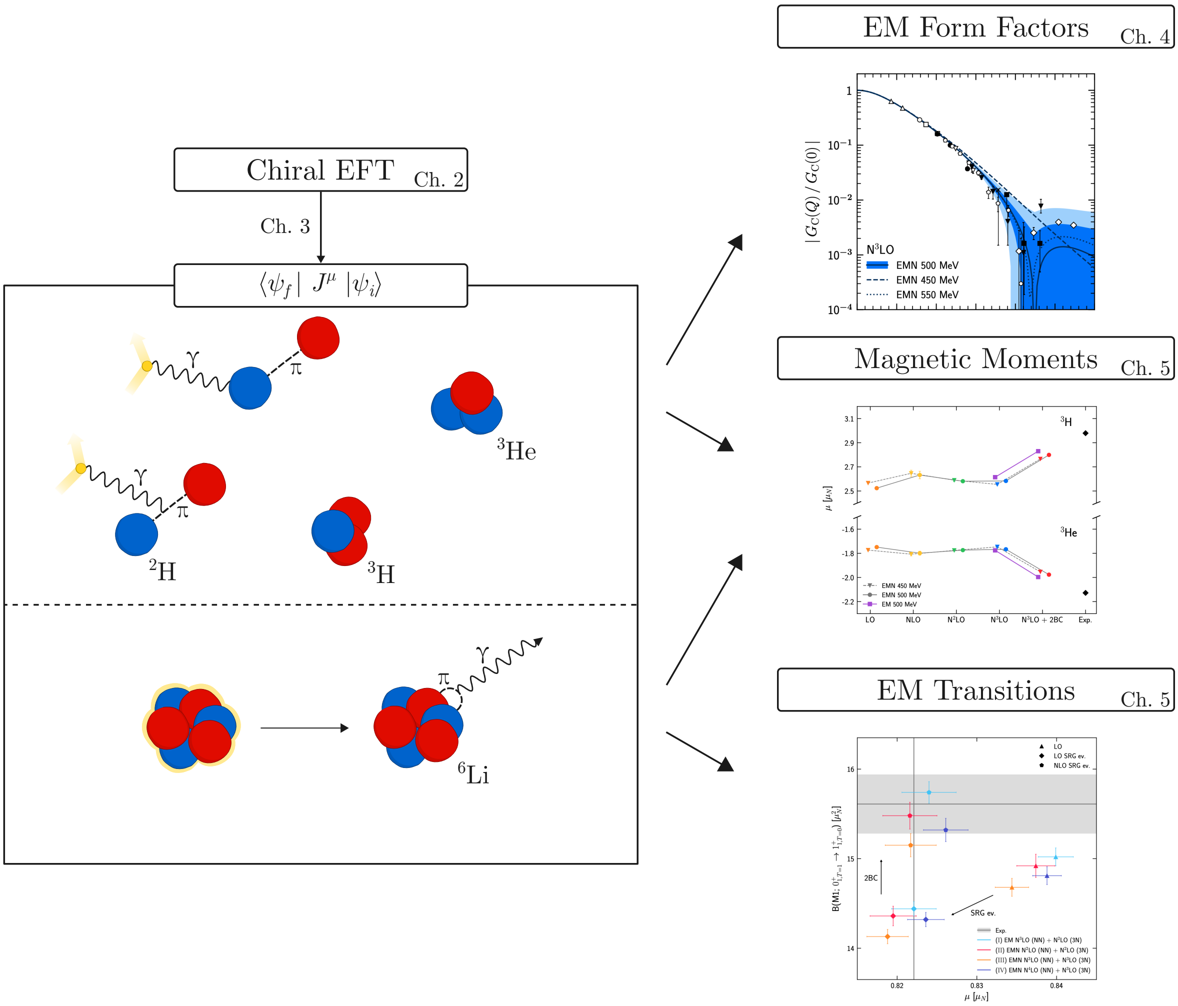

Figure 1.7: Illustration of the topics considered in this thesis. Chiral EFT forms the basis of our discussion. From this framework, we are able to construct matrix elements that we can connect to observables. The illustrations inside the box represent the nuclei we examine: the deuteron, the triton, the helion, and ^{6}Li. The deuteron sketches display scattering events which take into account the two leading 2BCs and the ^{6}Li graphic represents an electromagnetic (EM) transition which also includes 2BCs. From the general matrix element we can extract EM form factors, magnetic moments, and EM transitions.

focus on the low-energy regime of QCD, where nucleons are the relevant degrees of freedom, and introduce the chiral Lagrangian in Section 2.2. Because the derivation of nuclear forces and nuclear currents from the chiral Lagrangian is nontrivial we highlight the important ideas in Sections 2.3 and 2.4, with a more elaborate discussion for the latter. Finally in Section 2.5, we end the chapter by presenting Bayesian methods for the uncertainty estimation of EFTs and specify the model that we use to estimate the errors of electromagnetic observables.

In Chapter 3 we present the few-nucleon formalisms we employ for two- and three-body systems. We show the two-body partial-wave basis, expand the general current operator with respect to this basis, and illustrate how to obtain the deuteron wave functions in Section 3.1. Then, in Section 3.2 we start by representing a three-body system in momentum space with Jacobi momenta. Afterwards, we demonstrate the three-body partial-wave basis, we again expand the general current operator with respect to this basis, and outline the Faddeev formalism, which is the few-nucleon method that provides the triton and the helion wave functions.

Chapter 4 is devoted to the study of elastic electron scattering of two- and three-nucleon systems. We start by giving a historical overview of the most important experimental and theoretical developments to date and recapitulate the Born approximation for electron scattering in Section 4.1. Then, in Section 4.2 we discuss nucleon form factors as they are an important input in calculations. We present several nucleon form factor parametrizations and justify our particular choice that we use in calculations. Sections 4.3 and 4.4 are dedicated to present one of the main results of this thesis: deuteron and trinucleon electromagnetic form factors with truncation uncertainty estimates. We start each section by presenting the expansion of the form factor expressions with respect to the previously defined two- and three-body basis, followed by results. For the deuteron we present the charge, quadrupole, and magnetic deuteron form factors obtained with the one-body charge and current operators. For the trinucleons, we provide the charge and magnetic form factors, where the magnetic form factor includes 2BC corrections. We finish the chapter in Section 4.5 by extracting the deuteron and trinucleon radii, and by investigating the effect of different interactions on the radius. In the case of the trinucleons, we additionally analyze the impact of 3N interactions on the radius.

We proceed in Chapter 5 with our investigation of magnetic properties of light nuclei, particularly, the magnetic moments of $A = 2$, 3, and 6 nuclei and a magnetic transition strength of ^{6}Li. In Section 5.1 we give a brief overview of existing calculations for both observables which, remarkably, only consist of hybrid calculations. To understand the connection between the magnetic observables and the formalism from Chapter 4, we present the electromagnetic interaction Hamiltonian in Section 5.2 and provide the long-wavelength-limit derivation of the current operator. In Section 5.3, we show that the normalization of the electromagnetic form factors coincides with their static moments. This fact will be used to our advantage to benchmark results later on. Afterwards in Section 5.4, we continue by specifying the magnetic moment operator, which is defined in terms of the current operator. This relation implies that the magnetic moment operator possesses a similar many-body expansion as the current operator. Consequently, we derive the leading correction to the magnetic moment operator which originates from the leading 2BCs. In Section 5.5 we present results for the deuteron and trinucleon magnetic moments obtained from the normalization of the form factor calculations from the previous chapter. The last three sections are devoted to extending the formalism to calculations of light nuclei. To achieve this, a first step consists of making a basis transformation, which we show in Section 5.6. In order to validate the transformation, we benchmark the results from the basis transformation to the magnetic moments from the form factor normalization we obtained before. Then, in Section 5.7 we briefly describe the many-body method of choice to solve ^{6}Li and show results of the first-ever calculation with nuclear currents, including the leading corrections, and forces from chiral EFT for the magnetic moment and magnetic transition of ^{6}Li. To close the chapter, we compare the calculations to a recent precision experiment in Section 5.8.

Finally in Chapter 6 we give a conclusion and an outlook. Aspects of the few-body bases, detailed derivations, and experimental values and measurement techniques are presented in the Appendix.

2

NUCLEAR FORCES AND CURRENTS FROM CHIRAL EFFECTIVE FIELD THEORY

The derivation of nuclear interactions, governing the dynamics between nucleons, is one of the central objectives in nuclear theory research. We know that QCD is the underlying theory of the strong interaction from which nuclear forces emerge. However, due to the nonperturbative nature of the strong interaction in the low-momentum regime of nuclear physics, a direct construction of nuclear interactions from QCD is extremely hard. In a modern approach to derive nuclear interactions, additional requirements apart from a connection with the underlying theory are to be satisfied: there needs to be a physics-driven systematical improvable scheme which allows for a consistent description of interactions with external probes and provides access to uncertainty estimation.

Chiral EFT meets these requirements by taking into account only those degrees of freedom relevant to the scale of interest, i.e., nucleons and pions, and by subsequently constructing the most general Lagrangian consistent with symmetries from QCD, in particular chiral symmetry. The resulting infinite amount of terms are systematically organized according to the Weinberg power-counting scheme, which was introduced by Steven Weinberg in his pioneering papers [18–20], in terms of powers of $\mathcal{Q} = p/\Lambda_\mathrm{b}$,[1] where p is the typical momentum inside the nucleus and Λ_b the chiral breakdown scale. The power-counting scheme creates a hierarchy of importance depending on the order, where many-body forces naturally appear at higher orders in the expansion, and each order only has a finite number of terms. The unresolved high-momentum physics is contained in the expansion parameters denoted by LECs. Although these LECs could be obtained directly from QCD, in practice they are fit to nucleon-nucleon scattering data and properties of two- and three-body systems.

The coupling of nucleons and pions to external fields is described by currents, which can be derived consistently with respect to the interaction from the chiral Lagrangian. Given that the chiral Lagrangian satisfies gauge invariance, electroweak fields can be coupled to nuclear currents acquired from the continuity equation with chiral potentials. A first investigation of chiral EFT currents was performed in Refs. [84, 85] by using covariant perturbation theory. More recently, two separate derivations were published: the first one employed standard *time-ordered perturbation theory* (TOPT), first used in chiral EFT in Refs. [86, 87], combined with a transfer-matrix inversion and was carried out by the JLab-Pisa group [70, 88–90], while

---

[1] We use the symbol $\mathcal{Q}$ to denote the expansion parameter instead of the typically used Q, to avoid confusion with the symbol for the momentum transfer in later chapters.

the second approach, by the Bochum-Bonn group [91, 92], used the *unitary transformation* (UT) [93, 94] which was first introduced for chiral EFT in Ref. [95].

In order to make quantitative comparisons against experiment, reliable predictions, and extrapolations, it is essential to estimate the inherent model uncertainties. Several different sources of uncertainty in nuclear Hamiltonians from chiral EFT exist. These include, for example, uncertainties emerging from experimental data used to fit the LECs, uncertainties connected to fitting strategies, and systematic uncertainties as a result of truncating the chiral Lagrangian. During the last few years, great progress has been made to quantify these uncertainties. These efforts were in part initiated by the "Information and Statistics in Nuclear Experiment and Theory" (ISNET) workshops [38, 47], which led to two focus issues dedicated to the subject of uncertainty quantification in theoretical and experimental nuclear physics [39, 46]. Furthermore, an inspection of a recent special issue on nuclear interactions confirms the importance of uncertainty quantification and the ongoing endeavors in this direction, see, e.g., Refs. [35, 48]. Even though there are multiple sources of errors in nuclear Hamiltonians from chiral EFT, it is assumed that truncation errors are often the dominant ones [40]. Attempts to estimate these uncertainties are made by variation of the cutoff parameter of the regulator function. However, this method only measures the effect of higher-order contact terms, i.e., short-distance physics, and cannot be interpreted as rigorous statistical errors [96]. In fact, the EFT framework inherently provides uncertainty-quantification possibilities, based on the prescription for calculations from the power-counting scheme. Specifically, the expansion of the Lagrangian is expected to be directly inherited by calculations of observables whose truncation uncertainties decrease if higher orders of the expansion are included. As a rigorous approach to address the quantification of truncation uncertainties in chiral EFT, Bayesian procedures were introduced in Refs. [40, 41]. These methods provide well-founded statistical error bars for theoretical results such that meaningful comparisons with other theoretical calculations and experimental data can be made and they are even capable of addressing other sources of uncertainties arising from, e.g., fitting strategies or experimental data used to fit the LECs, which we mentioned above.

We start this chapter by discussing the fundamentals of QCD important for the understanding of chiral EFT in Section 2.1. Afterwards, in Sections 2.2 and 2.3 we demonstrate how chiral EFT emerges as a low-energy theory of QCD and, respectively, how nuclear forces are obtained from the chiral Lagrangian. These three sections follow Refs. [97, 98] which we refer to for a more detailed introduction to the topic. In Section 2.4 we examine the derivation of nuclear currents from the chiral Lagrangian, which now includes external sources. Finally, we finish the chapter by presenting the truncation uncertainty quantification method in Section 2.5.

2.1 Quantum chromodynamics

The quantum field theory of the strong interaction is QCD. It is a non-Abelian gauge theory which describes the interaction between its fundamental degrees of freedom: these are spin-1/2 fermions, called quarks, and the gauge bosons of the theory, gluons, which mediate the interaction between the quarks. As a consequence of the non-Abelian character, gluons also interact among themselves. At present, there are six different flavors of quarks ($N_f = 6$), up, down, strange, charm, bottom, and top, see Table 2.1 for their electric charge and mass. Each quark carries an additional degree of freedom of color charge. Three different color charges

Table 2.1: Electric charge, in units of the elementary charge, and approximate masses [103] of the six quark flavors.

Flavor	up	down	strange	charm	bottom	top
Charge	$+2/3$	$-1/3$	$-1/3$	$+2/3$	$-1/3$	$+2/3$
Mass	2.2 MeV	4.7 MeV	95 MeV	1275 MeV	4.18 GeV	173 GeV

($N_c = 3$) exist, red (r), green (g), and blue (b), which create the underlying $SU(N_c)$ color gauge group. Accordingly, antiquarks carry anticolor. At low temperatures and densities, quarks are confined in color-neutral hadrons, preventing the observation of individual quarks under these conditions. Such a color neutral hadron can be composed of a quark-antiquark pair, called mesons, three quarks each having a unique color, called baryons, combinations of four quarks and an antiquark bound together which are the so-called pentaquarks [99, 100], and there are indications for four-quark bound states called tetraquarks [101, 102]. Low-energy nuclear physics is determined by the three lightest quarks only: up, down, and strange. Therefore, we leave the remaining quarks out of the discussion below.

The QCD Lagrangian for the lowest mass quarks up, down, and strange, is given by

$$\mathcal{L}_{\text{QCD}} = \sum_{f=u,d,s} \bar{q}_f (i\not{D} - m_f) q_f - \frac{1}{2}\mathcal{G}^a_{\mu\nu}\mathcal{G}^{a\mu\nu}, \tag{2.1}$$

where q_f represents the quark fields with mass m_f. We used the *Feynman slash notation* for the covariant derivative $\not{D} \equiv \gamma^\mu D_\mu = \gamma^\mu(\partial_\mu + ig_s\mathcal{A}_\mu)$, with strong coupling constant g_s, gamma matrices γ^μ, and gluon field $\mathcal{A}_\mu$. The gluon-field-strength tensor is defined by

$$\mathcal{G}^a_{\mu\nu} = \partial_\mu\mathcal{A}_{a\nu} - \partial_\nu\mathcal{A}_{a\mu} - g_s f_{abc}\mathcal{A}_{b\mu}\mathcal{A}_{c\nu}, \tag{2.2}$$

with f_{abc} representing the $SU(N_c)$ structure constants and $a, b, c = 1, 2, ..., 8$ the color indices, which are implicitly summed over.

We proceed by examining Eq. (2.1) in the limit of vanishing quark masses, i.e., $m_f \to 0$, such that it becomes

$$\mathcal{L}^0_{\text{QCD}} = \sum_{f=u,d,s} \bar{q}_f \, i\not{D} \, q_f - \frac{1}{2}\mathcal{G}^a_{\mu\nu}\mathcal{G}^{a\mu\nu}. \tag{2.3}$$

By introducing left- and right-handed projection operators

$$P_R = \frac{1}{2}(1+\gamma_5) \quad \to \quad P_R q = q_R, \tag{2.4a}$$

$$P_L = \frac{1}{2}(1-\gamma_5) \quad \to \quad P_L q = q_L, \tag{2.4b}$$

we can write the previous equation in terms of left- and right-handed quark fields:

$$\mathcal{L}^0_{\text{QCD}} = \sum_{f=u,d,s} (\bar{q}_{R,f} \, i\not{D} \, q_{R,f} + \bar{q}_{L,f} \, i\not{D} \, q_{L,f}) - \frac{1}{2}\mathcal{G}^a_{\mu\nu}\mathcal{G}^{a\mu\nu}. \tag{2.5}$$

Note that there are no terms mixing left- and right-handed quark fields, which results from $m_f \to 0$. This Lagrangian is invariant under global $U(3)_L \times U(3)_R$ transformations in flavor space, in other words, the Lagrangian is invariant under separate rotations of the left- and right-handed quark fields by unitary matrices. More generally, the transformation can be written as $U(1)_A \times U(1)_V \times SU(3)_L \times SU(3)_R$, where $U(1)_V$ is connected to baryon number conservation and $U(1)_A$ is not a symmetry of the quantum theory as a result of the axial anomaly. The remaining $SU(3)_L \times SU(3)_R$ is known as *chiral symmetry* and leaves the left- and right-handed quark fields of the Lagrangian in Eq. (2.5) invariant under rotations by $SU(3)$ matrices. An exact chiral symmetry would appear in nature through parity doublets in the hadron spectrum: two particles with the same quantum numbers and mass, but with opposite parity. Given that observed masses of parity partners are very different, e.g., the nucleon $\mathrm{N}(J^\pi = \frac{1}{2}^+)$ with $m_\mathrm{N} \approx 940$ MeV and its chiral opposite $\mathrm{N}^*(J^\pi = \frac{1}{2}^-)$ with $m_{\mathrm{N}^*} \approx 1535$ MeV, chiral symmetry must be *spontaneously broken.* To each spontaneously broken symmetry belongs a massless excitation of the vacuum, called a *Goldstone boson* [104]. In addition, as quark masses are nonzero, chiral symmetry is *explicitly broken* because the mass term couples left- and right-handed quark fields,

$$\sum_f m_f \, \bar{q}_f \, q_f = \sum_f \bar{q}_{R,f} \, m_f \, q_{L,f} + \text{h.c.}. \tag{2.6}$$

As a result of the explicit symmetry breaking, Goldstone bosons acquire mass and are therefore called *pseudo-Goldstone bosons.* In QCD they are the pions, kaons, and the η-meson. The kaons and the η have a nonzero strange-quark content. Given the stronger symmetry breaking in the strange sector due to the larger strange-quark mass compared to the up and down masses, kaons and the η are much heavier compared to pions.

A distinctive property of QCD is its dependence of the coupling constant on the momentum scale Q [105, 106],

$$\alpha_s(Q) = \frac{g_s}{4\pi} = \frac{4\pi}{b_0} \log^{-1}\left[\frac{Q}{\Lambda_\mathrm{QCD}}\right], \tag{2.7}$$

where $b_0 = (33 - 2N_f)/(12\pi)$ and where the characteristic scale of QCD is $\Lambda_\mathrm{QCD} \approx 200 - 400$ MeV. At high energies the strong coupling constant becomes small, i.e., $\alpha_s \ll 1$, causing quarks to become free and allowing perturbative QCD calculations. This phenomenon is called asymptotic freedom and is a typical feature of non-Abelian gauge theories. On the other hand, at low energies $Q \lesssim 1$ GeV the coupling strength becomes large, i.e., $\alpha_s \gg 1$, making QCD calculations nonperturbative in this energy regime. Therefore, calculations at low energies are extremely hard, essentially prohibiting direct determination of nuclear observables from QCD.

One method that attempts to obtain observables in the low-energy regime is *lattice QCD.* For introductory texts on the subject we refer to, e.g., Refs. [107, 108], and for its application to nuclear physics to Ref. [4]. In this approach, space-time is discretized into a four-dimensional Euclidean lattice with quarks on the lattice points connected by links where gluons are located. Additionally, space and time are constrained to finite sizes to reduce computational costs so that results obtained with different parameters have to be extrapolated to the continuum limit. As the computational cost increases for decreasing quark mass, calculations are carried out at large values for the quark masses leading to nonphysical results.[2] Despite these

---

[2] There are two main reasons for this effect. The first originates from the fact that lattice QCD calculations compute the inverse of the Dirac operator. Given that the difficulty of inverting an operator depends on the smallest eigenvalue, it becomes harder to calculate the inverse of the Dirac operator for decreasing quark mass. The second reason arises from the signal-to-noise ratio for A-nucleon correlation functions, given by $\exp[-A(m_N - 3m_\pi/2)t]$, which becomes unfavorable at large time scales t for low m_π and large A [4].

challenges, lattice QCD shows a lot of progress: predicted masses of the lightest hadrons were calculated [3], and nuclear and hypernuclear[3] properties of light nuclei at a nonphysical pion mass of $m_\pi \approx 800$ MeV were calculated as well [5, 109]. For example, isovector magnetic moments of nuclei up to $A = 4$ were obtained in Refs. [110, 111].

2.2 Chiral effective field theory

The main principle of any EFT is the existence of a separation of scales in the physical system of interest. One can then choose relevant degrees of freedom below a breakdown scale Λ_b and construct the most general Lagrangian consistent with symmetry properties of the physical system. The Lagrangian is ordered in terms of powers of an expansion parameter p/Λ_b, which consists of a typical low-momentum scale p to a breakdown scale Λ_b. An illustration of such a general Lagrangian is given by

$$\mathcal{L} = \sum_\nu \left(\frac{p}{\Lambda_\mathrm{b}}\right)^\nu \mathcal{F}_\nu(q, g_i), \tag{2.8}$$

where $\mathcal{F}_\nu$ is a function of order one and g_i represent the unknown LECs, which contain the high-energy physics that is integrated out. To ensure a correct convergence pattern of the EFT, LECs are assumed to be *natural*, i.e., of $\mathcal{O}(1)$, such that individual terms in the expansion are not enhanced. The power-counting scheme orders the expansion according to decreasing importance in terms of powers ν of the expansion parameter, so that $\nu = 0$ or leading order (LO) terms include the dominant contributions, while $\nu = 1$ or next-to-leading order (NLO) terms, $\nu = 2$ or next-to-next-to-leading order (N^{2}LO), and etc. add smaller and smaller corrections. This ordering provides a prescription to systematically improve order-by-order EFT calculations such that a given accuracy is achieved by including a finite number of terms.

Several EFTs of QCD exist to tackle the low-energy regime of nuclear physics. At very low energies, the relevant energy scale is provided by neutron-proton S-wave scattering lengths which are unnaturally large in comparison to the pion Compton wavelength $\lambda_\pi = 1/m_\pi \approx 1.4$ fm. As a result, one can formulate the so-called *pionless EFT* [112–114] with a breakdown scale of the order of the pion mass to describe processes at these low energies. This EFT only consists of contact interactions to describe the forces between nucleons. Increasing the typical momentum scale beyond the pion mass implies that pions have to be explicitly included in the EFT. As mentioned before, chiral EFT includes pions to account for the intermediate- and long-range part of the nuclear interaction by one-or multiple-pion exchanges between nucleons. Additionally, pions set the low-momentum scale of the theory. The breakdown scale is roughly determined by the mass of heavier mesons without strange-quark content that are not included in the EFT, i.e., $\Lambda_\mathrm{b} \approx 500$ MeV which is somewhat smaller than the mass of the ρ meson, $m_\rho = 775$ MeV. Based on a comparison between the breakdown scale of chiral EFT and the excitation spectrum of hadrons, inclusion of the delta isobar $\Delta(1232)$ as an explicit degree of freedom might be important to improve convergence properties, given that it only differs about 300 MeV in mass with the nucleon. An EFT which explicitly includes the delta isobar is called *Δ-full chiral EFT* [86, 87] and is currently being further developed [115, 116]. Still other EFTs describe more exotic systems: one example is *halo/cluster EFT* [117–

---

[3] A hypernucleus is a nucleus with nonzero strange-quark content.

119] which describes weakly bound nuclei with a core surrounded by one or more valence nucleons or nuclei with a cluster structure. Typical examples of such nuclei are found at the limits of stability close to the *driplines*. Other examples of exotic EFTs are found in extensions of pionless, chiral, and halo/cluster EFTs which accommodate the description of hypernuclei [120–122]. Developing EFTs for low-energy nuclear physics is a very active field of research which is well documented in the literature. Because we exclusively use chiral EFT in this thesis we give a more detailed overview below and refer the reader to Ref. [123] for a modern and comprehensive review on nuclear EFTs.

As mentioned above, organizing the terms of the Lagrangian is achieved according to the power of the expansion parameter $\mathcal{Q}$. The order of each term in the chiral Lagrangian is given by

$$\Delta_i = d_i + \frac{1}{2}n_i - 2, \tag{2.9}$$

with d_i the number of derivatives or pion masses and n_i the number of nucleon fields in vertex i. To lowest orders of the chiral expansion, $\Delta_i = 0, 1$, the effective Lagrangian is given by [124]

$$\begin{aligned}\mathcal{L}^{(0)} =& \frac{1}{2}\partial_\mu \boldsymbol{\pi}\cdot\partial^\mu\boldsymbol{\pi} - \frac{1}{2}m_\pi^2\boldsymbol{\pi}^2 + N^\dagger\Big[i\partial_0 + \frac{g_A}{2F_\pi}\boldsymbol{\tau}\boldsymbol{\sigma}\cdot\boldsymbol{\nabla}\boldsymbol{\pi} - \frac{1}{4F_\pi^2}\boldsymbol{\tau}\cdot(\boldsymbol{\pi}\times\dot{\boldsymbol{\pi}})\Big]N \\ &- \frac{C_S}{2}(N^\dagger N)(N^\dagger N) - \frac{C_T}{2}(N^\dagger\boldsymbol{\sigma}N)(N^\dagger\boldsymbol{\sigma}N) + ..., \qquad (2.10)\\ \mathcal{L}^{(1)} =& N^\dagger\Big[4c_1 m_\pi^2 - \frac{2c_1}{F_\pi^2}m_\pi^2\boldsymbol{\pi}^2 + \frac{c_2}{F_\pi^2}\dot{\boldsymbol{\pi}}^2 + \frac{c_3}{F_\pi^2}(\partial_\mu\boldsymbol{\pi}\cdot\partial^\mu\boldsymbol{\pi}) - \frac{c_4}{2F_\pi^2}\epsilon_{ijk}\epsilon_{abc}\,\sigma_i\tau_a(\nabla_j\pi_b)(\nabla_k\pi_c)\Big]N \\ &- \frac{D}{4F_\pi}(N^\dagger N)(N^\dagger\boldsymbol{\sigma\tau}N)\cdot\boldsymbol{\nabla}\boldsymbol{\pi} - \frac{1}{2}\,E\,(N^\dagger N)(N^\dagger\boldsymbol{\tau}N)\cdot(N^\dagger\boldsymbol{\tau}N) + ..., \qquad (2.11)\end{aligned}$$

where $\boldsymbol{\pi}$ represents pion fields, $\boldsymbol{\sigma}$ and $\boldsymbol{\tau}$ the spin and isospin Pauli matrices, m_π the pion mass, N the nucleon fields, g_A the axial coupling, and F_π the pion-decay constant. The superscripts denote the vertex dimension Δ_i, dots over the symbols represent derivatives, LECs are given by c_i, C_S, C_T, D, and E, and ellipsis indicate terms with more pion fields and derivatives.

2.3 NUCLEAR FORCES FROM CHIRAL EFT

Nuclear forces are obtained from the chiral Lagrangian by using a diagrammatic representation. Such diagrams do not correspond to Feynman diagrams originating from the scattering amplitude, but are best understood to be a schematic visualization of their irreducible components. The power counting then assigns an order ν to each diagram and determines its importance. Weinberg power counting [18, 19] is based on a naive dimensional analysis and gives the order ν as [125, 126]

$$\nu = -4 + 2N + 2L + \sum_i V_i\Delta_i, \tag{2.12}$$

where N is the number of nucleons, L the number of pion loops, V_i the number of vertices of type i, and Δ_i as specified in Eq. (2.9). Figure 2.1 displays the hierarchy of nuclear forces arising from the power-counting scheme introduced above up to next-to-next-to-next-to-leading order (N^{3}LO). At LO ($\nu = 0$) and NLO ($\nu = 2$) only two-nucleon forces appear, while 3N and four-nucleon (4N) forces first emerge at N^{2}LO ($\nu = 3$) and N^{3}LO ($\nu = 4$), respectively. This natural appearance of many-body forces is inherent to chiral EFT and

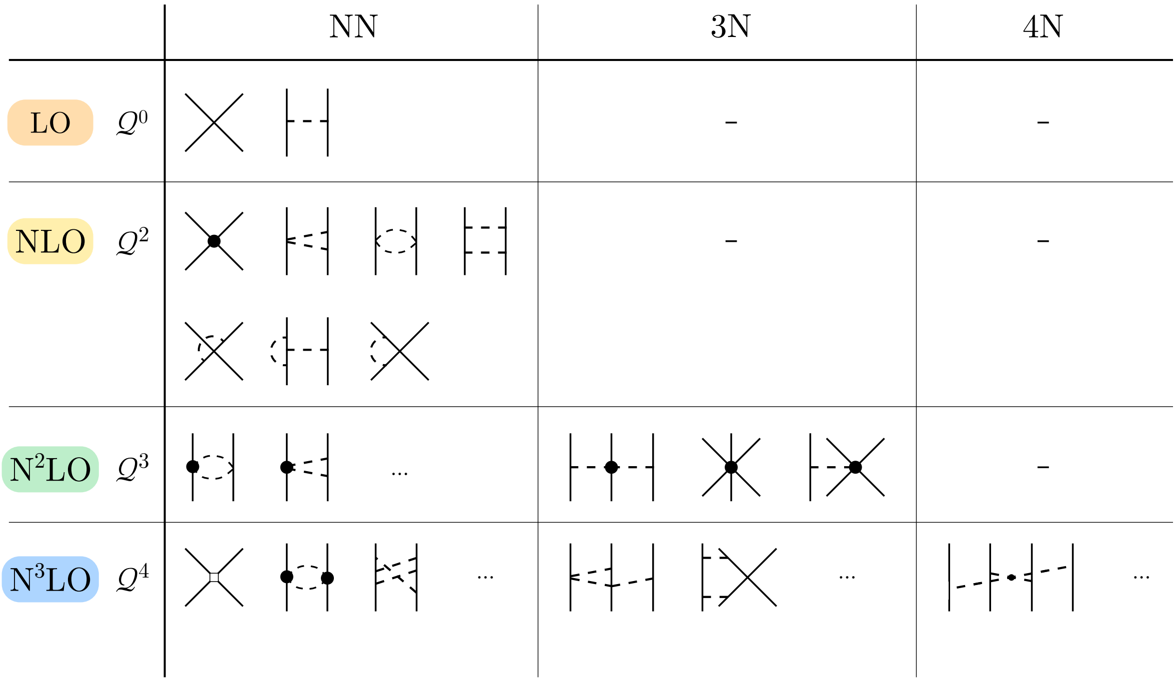

Figure 2.1: Hierarchy of NN, 3N, and 4N chiral nuclear forces up to N^{3}LO. Solid and dashed lines in the diagrams represent nucleons and pions, respectively, while different vertex symbols denote the vertex order: small dots, large solid dots, solid squares, and empty squares correspond to $\Delta_i = 0, 1, 2,$ and 4, respectively.

is one of its main benefits compared to other methods to obtain nuclear interactions. Note that there is no contribution for $\nu = 1$, as this order is forbidden due to parity and time-reversal invariance [19]. In general, there are two types of diagrams: contact diagrams that parametrize the short-distance physics through LECs which are fit to NN scattering data, and pion-exchange diagrams that account for the intermediate- and long-range parts of the interaction with LECs obtained from pion-nucleon scattering data. At LO there is only a one-pion-exchange contribution to these intermediate- and long-range parts, however, at higher-orders two- and multiple-pion exchange diagrams appear. Another benefit of chiral EFT is its systematic improvable calculation scheme that is provided by the power counting: including the next order in calculations systematically increases the accuracy of the result.

The dominant contribution to the NN interaction is given by the LO forces. Their momentum-space expression, which consists of two contact interactions and a one-pion-exchange term, is given by

$$V_{\mathrm{LO}}(\mathbf{q}) = V^{(0)}_{\mathrm{cont}} + V^{(0)}_{\mathrm{OPE}} = C_S + C_T\, \boldsymbol{\sigma}_1 \cdot \boldsymbol{\sigma}_2 - \frac{g_A^2}{4F_\pi^2} \frac{(\boldsymbol{\sigma}_1 \cdot \mathbf{q})(\boldsymbol{\sigma}_2 \cdot \mathbf{q})}{q^2 + m_\pi^2} \boldsymbol{\tau}_1 \cdot \boldsymbol{\tau}_2, \tag{2.13}$$

where $\mathbf{q} = \mathbf{p}' - \mathbf{p}$ is the momentum transfer with $\mathbf{p}$ and $\mathbf{p}'$ the initial and final relative momenta of the two nucleons. The two contact interactions describe the allowed S-wave channels $^3\mathrm{S}_1$ and $^1\mathrm{S}_0$ of the two nucleons, and C_S and C_T are correspondingly obtained from a fit to the phase shift. On the other hand, the one-pion-exchange term is completely determined by the pion-decay constant F_π and the axial coupling g_A. Higher orders of the NN interaction introduce many new diagrams including more contact interactions, pion-loop diagrams, and two- or more-pion exchanges. Two-nucleon interactions have been derived up to next-to-next-to-next-to-next-to-leading order (N^4LO) [22–24], with first explorations for NN scattering at sixth order [127, 128].

The leading 3N interactions appear at N^2LO and are accompanied by five LECs, three of which are predicted from the NN sector such that only two new LECs are introduced. These new LECs are connected to the one-pion-exchange contact and the three-nucleon-contact term, whose expressions are given by

$$V^{(3)}_{1\pi,\mathrm{cont}} = -\frac{g_A}{8F_\pi^2} D \sum_{i\neq j\neq k} \frac{\boldsymbol{\sigma}_j \cdot \mathbf{q}_j}{q_j^2 + m_\pi^2} (\boldsymbol{\tau}_i \cdot \boldsymbol{\tau}_j)(\boldsymbol{\sigma}_i \cdot \mathbf{q}_j), \qquad V^{(3)}_{\mathrm{cont}} = \frac{E}{2} \sum_{j\neq k} \boldsymbol{\tau}_j \cdot \boldsymbol{\tau}_k. \tag{2.14}$$

Here, the LECs D and E are the ones from the chiral Lagrangian at order $\Delta_i = 1$. More commonly, they are given in terms of the constants c_D and c_E, which are related by

$$D = \frac{c_D}{F_\pi^2 \Lambda_\chi}, \qquad E = \frac{c_E}{F_\pi^4 \Lambda_\chi}, \tag{2.15}$$

with $\Lambda_\chi = 700$ MeV. These two new LECs are determined by a fit to uncorrelated few-nucleon properties. Different strategies exist to perform this fit, to name a few: by using the binding energies of $A = 3$ nuclei [129], the binding energy of ^{3}H and the charge radius of ^{4}He [31], the binding energy of ^{3}H and nuclear matter saturation properties [32], or the binding energies of $A = 3$ nuclei and the triton β-decay half-life as an extra constraint [50]. This last approach is possible because c_D and c_E appear in the the contact two-nucleon weak current at N^2LO, see the next section for a discussion about power counting for currents, which adds a higher-order correction to the Gamow-Teller matrix element in triton β-decay. Subleading 3N interactions at N^3LO have also been derived, see Refs. [130–132], and only depend on NN contact couplings C_S and C_T. Efficiently including interactions at this order in calculations is done by a specialized partial-wave decomposition [133]. Furthermore, the derivation of 3N forces at N^4LO is also in progress [134, 135], but it is currently not used in nuclear observable calculations.

An inherent property of chiral EFT are ultraviolet (UV) divergences which arise from the nonperturbative summations of the interactions in the *Lippmann-Schwinger* (LS) equation [96]. To circumvent this issue, a finite UV cutoff Λ of the order of the breakdown scale is introduced to the integrals in the form of regulating functions f^Λ_{NN}. These functions are multiplied to potential expressions and have the effect to suppress the high-momentum parts of the interactions:

$$V(\mathbf{p}, \mathbf{p}') \to f^\Lambda_{\mathrm{NN}}(p) V(\mathbf{p}, \mathbf{p}') f^\Lambda_{\mathrm{NN}}(p') = V_{\mathrm{reg}}(\mathbf{p}, \mathbf{p}'). \tag{2.16}$$

Given that different few- and many-body methods require different formulations of the interactions, three different classes of regulator functions exist: local, semilocal, and nonlocal, where each class has its specific properties. In a momentum-space formulation, local regulator functions only depend on differences between momenta, i.e., $f^\Lambda_{\mathrm{local}} = f^\Lambda(\mathbf{p}' - \mathbf{p})$, while nonlocal regulator functions typically depend on combinations of $\mathbf{p}'$ and $\mathbf{p}$. Semilocal regularization schemes combine both local and nonlocal regulator functions: short-range parts of the interaction are nonlocally regularized, whereas the long-range pion exchanges are regularized with local regulator functions. The interactions used in this thesis are all nonlocal. In that case, the regulator function for NN interactions is generically given by

$$f_{\mathrm{NN}}^{\Lambda}(p) = \exp\left[- \left(\frac{p}{\Lambda} \right)^{2n} \right], \tag{2.17}$$

with n an integer and $p = |\mathbf{p}|$. The generalization to a three-body nonlocal regulator function is introduced by

$$f_{\mathrm{3N}}^{\Lambda_{\mathrm{3N}}}(p,q) = \exp\left[- \left(\frac{p^2 + \frac{3}{4}q^2}{\Lambda_{\mathrm{3N}}} \right)^{n} \right], \tag{2.18}$$

where $p = \mathbf{p}$ and $q = \mathbf{q}$ now represent the more general Jacobi momenta (see Section 3.2.1) and Λ_{3N} is the 3N cutoff parameter. As a side effect of regulating the interactions, finite-cutoff effects are induced which appear as a dependence of observables on the cutoff parameter Λ. If the convergence of the chiral expansion works as expected, then this cutoff dependence should reduce with increasing order.

2.4 Nuclear currents from chiral EFT

Nuclear currents are, similar to nuclear forces, derived from a chiral Lagrangian except now with external sources. Once again, we begin with the QCD Lagrangian and demonstrate the addition of external sources before we consider two methods to obtain nuclear currents and discuss their properties. This section is largely based on a recent review provided in Ref. [136], which we refer to for an in-depth discussion about the topic of nuclear currents from chiral EFT.

2.4.1 External sources in QCD

External sources form the basis to derive nuclear current operators. Let us start by observing the interaction of quarks with external probes in QCD. We introduce vector, axial-vector, scalar, and pseudoscalar sources by extending Eq. (2.3) to

$$\mathcal{L}_{\mathrm{QCD}}^{\mathrm{ext}} = \mathcal{L}_{\mathrm{QCD}}^{0} + \sum_{f} \left[\bar{q}_f \gamma^{\mu} (v_{\mu} + \gamma_5 a_{\mu}) q_f - \bar{q}_f (s - i\gamma_5 p) q_f \right], \tag{2.19}$$

where $v_{\mu}(x)$, $a_{\mu}(x)$, $s(x)$, and $p(x)$ represent the external vector, axial-vector, scalar, and pseudoscalar fields, which are hermitian and color-neutral matrices in flavor space. In addition, the scalar field includes the quark mass matrix. The QCD Lagrangian is invariant under local chiral transformations if the external fields transform as

$$v'_{\mu} + a'_{\mu} = P_R (v_{\mu} + a_{\mu}) P_R^{\dagger} + i P_R \, \partial_{\mu} \, P_R^{\dagger}, \tag{2.20a}$$

$$v'_{\mu} - a'_{\mu} = P_L (v_{\mu} - a_{\mu}) P_L^{\dagger} + i P_L \, \partial_{\mu} \, P_L^{\dagger}, \tag{2.20b}$$

$$s' + ip' = P_R (s + ip) P_L^{\dagger}, \tag{2.20c}$$

where the projection operators were introduced in Eqs. (2.4a) and (2.4b). By accounting for all possible external sources, the interaction with different probes can be studied.

2.4.2 Unitary transformation and time-ordered perturbation theory

It is possible to construct an effective Lagrangian with nucleons, pions, and external fields that is invariant under local chiral transformations given in (2.20a)-(2.20c). From the effective Lagrangian one can derive an effective Hamiltonian, which then also depends on the external fields s, p, a, and v, see Refs. [91, 137, 138] for explicit expressions. We denote this Hamiltonian by

$$H_{\text{eff}}[s, p, a, v]. \tag{2.21}$$

There are two different methods to find the nuclear current from this Hamiltonian: the first one uses the UT [93–95] and the second one uses TOPT [86, 87] with a transfer-matrix inversion. The former is the method of choice employed by the Bochum-Bonn group [91, 92], while the latter technique is employed by the JLab-Pisa group [70, 88–90]. Below, we highlight the important conceptual steps of both methods.

In the UT approach, to ensure renormalizability, the effective Hamiltonian is transformed by a time-dependent unitary transformation that explicitly depends on the external sources [136]:

$$H'_{\text{eff}}[s, p, a, v] = U(t)^{\dagger} H_{\text{eff}}[s, p, a, v] U(t) + \left(i \frac{\partial}{\partial t} U(t)^{\dagger} \right) U(t), \tag{2.22}$$

with $U(t)$ the time-dependent unitary transformation. Then, the current operator is obtained by taking a functional derivative of the time-dependent unitary transformed effective Hamiltonian with respect to one of the external sources:

$$J_X = \frac{\delta}{\delta X} H'_{\text{eff}}[s, p, a, v] \bigg|_{s=m_q, p=a=v=0}, \tag{2.23}$$

where H'_{eff} denotes the time-dependent unitary transformed effective Hamiltonian, X represents s, p, a, or v, depending on the nuclear current of interest, and where the scalar source is set to the quark-mass matrix. We refer to Refs. [136, 138] for an in-depth introduction to the UT method for chiral nuclear currents.

The TOPT method starts from the transition amplitude, i.e., T-matrix, given by [88, 90]

$$\langle f | T | i \rangle = \langle f | H_1 \sum_{n=1}^{\infty} \left(\frac{1}{E_i - H_0 + i\eta} H_1 \right)^{n-1} | i \rangle \,, \tag{2.24}$$

where $|i\rangle$ ($|f\rangle$) is the initial (final) state with eigenvalue E_i and the total Hamiltonian $H_{\text{eff}} = H_0 + H_1$ is split into a free part H_0 and an interaction part H_1. In the following, we only assume an electromagnetic interaction, however, the same general arguments hold for any other type of interaction. The T-matrix can be expanded in chiral orders using first-order perturbation theory as follows

$$T_{\gamma} = T_{\gamma}^{(-3)} + T_{\gamma}^{(-2)} + T_{\gamma}^{(-1)} + \ldots, \tag{2.25}$$

where $T_{\gamma}^{(n)}$ is of chiral order $e\mathcal{Q}^n$, with e the elementary charge, and the ellipsis denote higher orders in the expansion. Based on the power counting for nuclear currents the LO charge operator is given by $\nu = -3$, while the LO current operator has order $\nu = -2$. Higher-order operators are classified relative to the LO contributions. In Section 2.4.3 we will explain the power-counting scheme in more detail. Nuclear currents are found by inverting the LS equation and matching each T-matrix component, order by order, to each LS equation component. We introduce $v_\gamma = A_\mu \cdot j^\mu$, with A_μ the electromagnetic field vector and j^μ the nuclear current, and we iteratively derive the current order by order [90]:

$$v_\gamma^{(-3)} = T_\gamma^{(-3)}, \tag{2.26}$$

$$v_\gamma^{(-2)} = T_\gamma^{(-2)} - \left[v_\gamma^{(-3)} G_0 v_\gamma^{(0)} + v_\gamma^{(0)} G_0 v_\gamma^{(-3)} \right], \tag{2.27}$$

$$\ldots, \tag{2.28}$$

where $G_0 = (E_i - E_I + i\eta)^{-1}$, with E_I the intermediate energy which also includes the photon energy, and where the ellipsis denotes higher orders. A comprehensive introduction to the TOPT method is given in Refs. [88, 90].

Nuclear vector currents derived from both methods agree up to order $\mathcal{Q}^0$, with differences occurring at order $\mathcal{Q}$. One apparent difference comes from the fact that the JLab-Pisa group have unrenormalized expressions, while the Bochum-Bonn group provides renormalized results. Furthermore, the Bochum-Bonn group claims that they are unable to renormalize the JLab-Pisa results [136]. In addition, there are differences in the one-pion and two-pion exchange contributions to the current and charge operators. Differences in the one-pion exchange contributions to the current operator imply a difference in the resulting magnetic moment operator (in Section 5.4 we show the connection between the current operator and the magnetic moment operator). The calculation of two-pion exchange contributions in both approaches leads to differences in the charge operator, which are claimed to be unitarily equivalent according to the JLab-Pisa group. However, in Ref. [136] it is shown that the argument of unitary equivalence is based on wrong assumptions, making the claim invalid. We refer the reader to Refs. [90–92, 136] for extensive discussions about these differences.

Up until now the analysis was kept general and any possible probe-nucleus interaction was allowed. In this thesis however, we exclusively consider electromagnetic interactions which correspond to vector sources. Therefore, we only mention the relevance of the other sources briefly. Axial-vector currents are used to describe weak processes like β-decay. There are two primary motivations to develop these currents. First, the lowest-order two-nucleon axial-vector current depends on LECs which also contribute to the leading 3N force [139] and other processes like radiative capture reactions in two-nucleon systems [140]. Hence, chiral EFT offers a framework to study these distinct phenomena in a unified approach. Second, there is an interest from the neutrino-scattering and astrophysics community for more reliable and accurate predictions of low-energy nuclear reactions involving neutrinos. A first set of chiral EFT expressions up to fourth order was provided in Ref. [84, 141] by Park *et al.* using covariant perturbation theory. These derivations, however, were not complete as pion-pole terms and contributions from reducible-like diagrams were omitted. Nevertheless, these expressions have been used in several nuclear structure calculations see, e.g., Refs. [50, 141–143]. More recently, axial-vector currents have been developed in the TOPT framework [137] and the UT framework [138]. These currents have been used in calculations of tritium β-decay [144–146], QMC studies of weak decays in $A \leqslant 10$ [147], and β-decay studies of medium-mass nuclei up to ^{100}Sn where the inclusion of 2BCs suggested a solution to the well-known quenching of the axial coupling constant [148].

Scalar currents are important in beyond-standard-model physics searches, because they arise in a variety of dark matter models. For example, weakly-interacting massive particles (WIMPs) are a prominent class of hypothetical particles that could be searched for by direct-detection experiments, where the recoil energy of a WIMP-nucleus scattering event is measured. To interpret future signals and to derive constraints from experiments on the parameter space of these hypothetical particles, it is important to systematically incorporate knowledge about the nuclear system. Pioneering derivations of nuclear scalar currents from chiral EFT were provided in Refs. [149, 150]. Several applications using these scalar currents have appeared in recent years, see, e.g., Refs. [151–153]. Recently, nuclear scalar currents including leading one-loop corrections to the two-nucleon scalar current were derived within chiral EFT using the UT method [154].

Vector and axial-vector currents have to satisfy certain relations that are rooted in their symmetry properties. Therefore, verifications of these relations amount to important and convenient checks of the obtained expressions. For example, given that currents are four-vectors, they have to behave correctly under boost transformations. That is, a general (axial-)vector current J_μ has to meet the following requirement [136]:

$$e^{-i\mathbf{e}\cdot\mathbf{K}\theta}\, J_\mu(x)\, e^{i\mathbf{e}\cdot\mathbf{K}\theta} = \Lambda(\theta)_\mu^\nu J_\mu(\Lambda(\theta)^{-1}x), \tag{2.29}$$

with $\mathbf{K}$ the boost generator, $\mathbf{e}$ the boost direction, θ the boost angle, and $\Lambda(\theta)$ a 4×4 boost matrix. This relation can be generalized by applying a time-dependent unitary transformation to the (axial-)vector current operator. Considering the more general transformation property of the vector operator provides a prescription to derive the charge operator from the current operator [136]. Hence, calculating boost transformation properties not only assure a successful derivation of the (axial-)vector current, but also, in the case of a vector current operator, provides a relation between the charge and current operators. More importantly, (axial-)vector currents have to satisfy the continuity equation, which emerges from the gauge invariance of chiral EFT. Because we exclusively work with vector currents in this thesis, we only present the continuity equation with respect to vector currents and refer to Ref. [136] for an expression of the continuity equation for the axial-vector current. The continuity equation connects the current operator with the nuclear potential and is given by

$$\mathbf{q}\cdot\mathbf{j} = [H_{\text{eff}}, \rho], \tag{2.30}$$

where $[...,...]$ denotes a commutator. Here, the charge and current operator correspond to the temporal and spatial component, respectively, of the vector current operator, i.e., $J_\mu = (\rho, \mathbf{j})$. Equation (2.30) has to be satisfied at each order of the chiral expansion in order for the currents to be correct.

2.4.3 Power counting and electromagnetic nuclear currents

Nuclear currents from chiral EFT are, similar to nuclear forces, arranged in hierarchical classes of importance based on a power counting. Again, following Weinberg's analysis [18, 19], we adjust the power counting introduced in Eq. (2.12) to account for external fields [136]:

$$\nu = -3 + \sum_i V_i(d_i + \frac{3}{2}n_i + p_i + s_i - 4), \tag{2.31}$$

Table 2.2: Power counting of the charge, ρ, and current operator, $\mathbf{j}$, up to $\nu = 1$, for which the LO is given by $\nu = -3$ and $\nu = -2$, respectively. Note that there is no contribution at NLO for the charge operator. Fourth order current operator expressions have been recently derived in Ref. [156].

Operator	LO	NLO	N^{2}LO	N^{3}LO	N^{4}LO
ρ	-3	-2	-1	0	1
$\mathbf{j}$	-2	-1	0	1	2

with p_i the number of pion fields and s_i the number of external sources, which can only be 0 or 1 for current operators, in the vertex i. For the leading charge and current operator this results in an order $\mathcal{Q}^{-3}$ and $\mathcal{Q}^{-2}$, respectively. The scaling in $\mathcal{Q}^{\nu}$ of both operators up to $\nu = 1$ is given in Table 2.2 which also shows the corresponding order. Although this power counting is generally accepted, a study of the power counting of 2BCs showed that short-range contributions to the current operator are in fact enhanced and should appear at a lower order compared to counting presented here [155]. Further studies along these lines as well as more quantitative investigations have not been published until now.

In this thesis, we will only consider vector operators up to NLO to calculate electromagnetic observables. As there is no NLO contribution for the charge operator, we only consider its LO contribution. On the other hand, for the current operator both contributions are nonvanishing, where the NLO contribution introduces the leading 2BC.

The momentum-space LO one-body charge operator is given by [70]

$$\rho^{(-3)} = e\, e_{N,1}(Q^2)\, \delta(\mathbf{k}_2' - \mathbf{k}_2) + 1 \leftrightharpoons 2, \tag{2.32}$$

where e represents the elementary charge, $\mathbf{k}_i$ ($\mathbf{k}_i'$) the initial (final) momentum of nucleon i, and $e_{N,1}(Q^2)$ is given by,

$$e_{N,i} = \frac{G_{\mathrm{E}}^{S}(Q^2) + G_{\mathrm{E}}^{V}(Q^2)\tau_{i,z}}{2}, \tag{2.33}$$

with Q the momentum transfer, $G_{\mathrm{E}}^{S/V}$ the isoscalar (S) or isovector (V) nucleon electric form factor, normalized to $G_{\mathrm{E}}^{S}(0) = G_{\mathrm{E}}^{V}(0) = 1$ [157]. Note that, in the limit of $Q \to 0$, Eq. (2.33) becomes the proton-projection operator. At N^{2}LO there is a relativistic correction to the one-body charge operator and the leading two-body charge operator first appears at N^{3}LO.

The momentum-space LO one-body current operator is specified by [70]

$$\mathbf{j}^{(-2)} = \frac{e}{2m_N}\left(2\, e_{N,1}(Q^2)\mathbf{K}_1 + i\, \mu_{N,1}(Q^2)\boldsymbol{\sigma}_1 \times \mathbf{q}\right) \delta(\mathbf{k}_2' - \mathbf{k}_2) + 1 \leftrightharpoons 2, \tag{2.34}$$

where m_N expresses the nucleon mass, $\mathbf{K}_1$ is given by $\mathbf{K}_i = (\mathbf{k}_i' + \mathbf{k}_i)/2$, $\boldsymbol{\sigma}_i$ the Pauli spin matrix operating on nucleon i, and

$$\mu_{N,i} = \frac{G_{\mathrm{M}}^{S}(Q^2) + G_{\mathrm{M}}^{V}(Q^2)\tau_{i,z}}{2}, \tag{2.35}$$

with $G_{\mathrm{M}}^{S/V}$ the isoscalar (S) or isovector (V) nucleon magnetic form factor, normalized to $G_{\mathrm{M}}^{S}(0) = 0.880\ \mu_N$ and $G_{\mathrm{M}}^{V}(0) = 4.706\ \mu_N$ [157].

At NLO, the leading 2BC operators appear. They are connected to the one-pion exchange

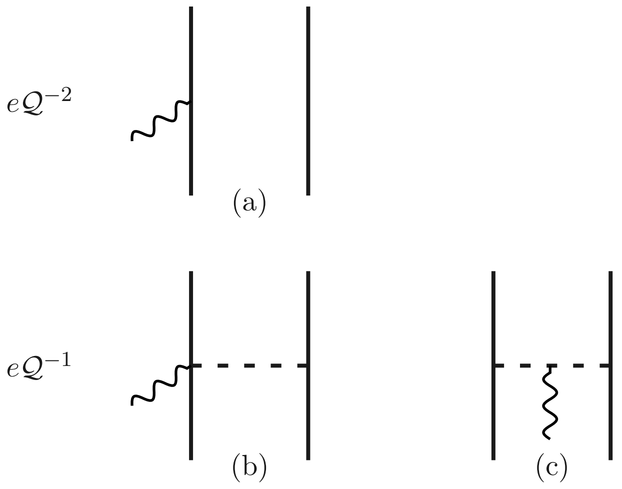

Figure 2.2: Diagrams for the LO (top row) and NLO (bottom row) contributions to the current operator, indicated by their scaling according to $e\mathcal{Q}^{\nu}$. Solid lines represent nucleons, while dashed and wiggly lines represent pions and virtual photons. Diagram (a) is the one-body current, while diagrams (b) and (c) are the leading 2BCs and depict the seagull and pion-in-flight contribution, respectively. Note that the one-body charge operator can be represented by diagram (a) as well, but then with order $e\mathcal{Q}^{-3}$. Figure taken from [81].

potential, see Eq. (2.13), and their momentum-space expressions are given by [70]

$$\mathbf{j}^{(-1)} = -i\, e \frac{g_A^2}{4F_\pi^2} G_{\mathrm{E}}^{V}(Q^2)(\boldsymbol{\tau}_1 \times \boldsymbol{\tau}_2)_z \left(\boldsymbol{\sigma}_1 - \mathbf{q}_1 \frac{\boldsymbol{\sigma}_1 \cdot \mathbf{q}_1}{q_1^2 + m_\pi^2} \right) \frac{\boldsymbol{\sigma}_2 \cdot \mathbf{q}_2}{q_2^2 + m_\pi^2} + 1 \rightleftharpoons 2, \qquad (2.36)$$

with $\mathbf{q}_i = \mathbf{k}_i' - \mathbf{k}_i$. Figure 2.2 shows the LO and NLO diagrams for the current operator. The first and second term between brackets in Eq. (2.36) corresponds to diagram (b) and to diagram (c) which are the so-called *seagull* and *pion-in-flight* term, respectively. Equations (2.32), (2.34), and (2.36) are the main operators used to calculate electromagnetic observables in this thesis. For a complete set of expressions of the electromagnetic charge and current operators up to N^{3}LO we refer to Refs. [70, 136, 156].

2.4.4 Consistent description of nuclear forces and currents

Expectation values of currents at fourth order in the chiral expansion no longer preserve chiral symmetry as a result of the different regularization schemes used to obtain nuclear currents and nuclear forces [136]. In a specific example, the cutoff regularization used for the forces introduces a linear cutoff singularity which could only be canceled by the current if it were derived using cutoff regularization instead of dimensional regularization. A naive approach to circumvent this issue by simply multiplying the current operator with a cutoff regulator function does not mitigate the problem. To resolve this issue, both currents and nuclear forces have to be derived using the same cutoff regulator. In addition, this regulator has to respect chiral symmetry itself. Examples of preliminary studies with first steps in that direction were performed in Ref. [158] and more recently in Ref. [72]. In the latter study, the authors calculated the deuteron charge form factor up to N^{4}LO in the chiral expansion. The deuteron was specifically chosen because its isoscalar nature ensures that complicated isovector contributions vanish. Only a relativistic correction to the leading one-pion-exchange charge operator remains for the deuteron, which can be straightforwardly regularized [136].

2.5 Effective field theory uncertainty quantification

Any EFT promises a systematic expansion and, therefore intrinsically allows to estimate theoretical uncertainties arising from truncating the expansion. In particular, information about the EFT convergence pattern for any given observable can be used to determine the size of neglected higher-order terms. Let $X(p)$ be an observable of interest which depends on a given momentum scale p, then we represent its chiral expansion in orders of ν as

$$X(p) = X^{(0)} + \Delta X^{(2)} + \Delta X^{(3)} + \ldots, \tag{2.37}$$

where the corrections are defined by $\Delta X^{(2)} \equiv X^{(2)} - X^{(0)}$ and $\Delta X^{(n)} \equiv X^{(n)} - X^{(n-1)}$ for $n > 2$, with $X^{(n)}$ a prediction at order $\mathcal{Q}^n$. These corrections are expected to be of the order of $\mathcal{O}(\mathcal{Q}^\nu X^{(0)})$, where the expansion parameter is given by $\mathcal{Q} = \max(m_\pi/\Lambda_\mathrm{b}, p/\Lambda_\mathrm{b})$, with m_π the pion mass, Λ_b the breakdown scale, and p a given momentum scale. In other words, the correction for each successive order is smaller by a factor of $\mathcal{Q}$ compared to the previous order. If corrections for the observable are known explicitly up to order $n = k$, then the goal is to estimate the size of

$$\delta X^{(k)} \equiv \sum_{n=k+1}^{\infty} \Delta X^{(n)}. \tag{2.38}$$

In recent years, there have been two approaches to estimate the size of $\delta X^{(k)}$: the first approach by Epelbaum, Krebs, and Meißner (EKM) [96] provides a simple and straightforward implementation, while the second one by Furnstahl *et al.* [40, 41] introduces a general Bayesian framework that permits a well-defined statistical interpretation of the estimated uncertainties.

The EKM algorithm assumes that the dominant error comes from the first omitted term $\Delta X^{(k+1)}$. The prescription to find the truncation uncertainty at orders $\mathcal{Q}^i$ for $0 \leqslant i \leqslant k$, is given by [35]

$$\begin{aligned} \delta X^{(0)} &= \mathcal{Q}^2 |X^{(0)}|, \\ \delta X^{(i)} &= \max_{2 \leqslant j \leqslant i} \left(\mathcal{Q}^{i+1} |X^{(0)}|, \mathcal{Q}^{i+1-j} |\Delta X^{(j)}|\right) \text{ for } i \geqslant 2. \end{aligned} \tag{2.39}$$

To ensure that estimated uncertainties are larger than known higher-order contributions, an extra constraint is imposed:

$$\delta X^{(i)} = \max_{j,m=i,\ldots,k} \left(|X^{(j)} - X^{(m)}|\right). \tag{2.40}$$

Calculating the truncation uncertainties according to this scheme, guarantees overlapping uncertainties at different orders. The clear disadvantage of the EKM method is that estimated uncertainties do not have a meaningful statistical interpretation. Nevertheless, its convenient implementation and improvement upon standard cutoff variation have made it a valuable tool that is implemented in single-baryon low-energy reactions, e.g., Refs. [159, 160], as well as calculations of few- and many-nucleon systems, e.g., Refs. [22, 161, 162]. A discussion about the robustness of this method is given in Ref. [163].

A Bayesian model, on the other hand, provides a more general and complete method to quantify truncation uncertainties by calculating *probability distribution functions* (pdfs) for the truncation uncertainties. Furnstahl *et al.* [40] introduced such a framework for EFTs by adapting a Bayesian model developed for perturbative expansions in QCD, with further refinements made in Ref. [42]. In Chapter 4 we will use a modification of a particular model presented in Ref. [42], which we outline below.

Instead of examining the observable in terms of its corrections, as in Eq. (2.37), the observable can be expanded in terms of the dimensionless EFT expansion parameter $\mathcal{Q}$:

$$X = X_{\text{ref}}(c_0 + c_2\mathcal{Q}^2 + c_3\mathcal{Q}^3 + \ldots) = X_{\text{ref}} \sum_{n=0}^{\infty} c_n \mathcal{Q}^n, \tag{2.41}$$

where X_{ref} is a reference scale for the observable and c_n are dimensionless expansion coefficients assumed to be roughly of the same size. Particularly, we make the choice $X_{\text{ref}} = |X^{(0)}|$. However, other alternatives are possible, for example, a reference scale which does not only depend on the LO contribution but also on higher-order corrections has been shown to be more robust for observables that depend on continuous parameters [34]. To achieve the naturalness assumption, the coefficients are considered as random variables distributed according to a common pdf with an upper bound $\bar{c}$. Such a pdf for the coefficients is called a *prior distribtuion.*

If we truncate Eq. (2.41) at order k, then the error is given by $X_{\text{ref}}\Delta_k$ where

$$\Delta_k \equiv \sum_{n=k+1}^{\infty} c_n \mathcal{Q}^n, \tag{2.42}$$

is the dimensionless residual that determines the truncation error. For practical estimations of the error, however, only the first h higher-order terms in the expansion are considered which is denoted by $\Delta_k \approx \Delta_k^{(h)} \equiv \sum_{n=k+1}^{k+h} c_n \mathcal{Q}^n$. The objective is then to find a *posterior distribution* $\text{pr}_h(\Delta_k^{(h)}|\{c_{n\leqslant k}\})$,[4] that is, a probability distribution for the residual $\Delta_k^{(h)}$ given specific values for the first k coefficients, based on the assumption that only the first h higher-order terms significantly contribute to the error. The resulting posterior pdf for the residual which equals $\Delta_k^{(h)} = \Delta$ is given by [42]

$$\text{pr}_h(\Delta|\{c_{i\leqslant k}\}) = \frac{\int_0^\infty \mathrm{d}\bar{c}\,\text{pr}_h(\Delta|\bar{c})\,\text{pr}(\bar{c})\,\prod_{n=2}^{k}\text{pr}(c_n|\bar{c})}{\int_0^\infty \mathrm{d}\bar{c}\,\text{pr}(\bar{c})\,\prod_{n=2}^{k}\text{pr}(c_n|\bar{c})}, \tag{2.43}$$

with

$$\text{pr}_h(\Delta|\bar{c}) = \left[\prod_{i=k+1}^{k+h}\int_{-\infty}^{\infty}\mathrm{d}c_i\,\text{pr}(c_i|\bar{c})\right]\delta\Big(\Delta - \Delta_k^{(h)}\Big). \tag{2.44}$$

The result in Eq. (2.43) is assumed to include all the information about the dimensionless residual.

In order to obtain quantitative results for the posterior, specific choices for the prior distributions $\text{pr}(c_n|\bar{c})$ and $\text{pr}(\bar{c})$ have to be made. Furnstahl *et al.* [40] introduced three different sets denoted by “Set A”, “Set B”, and “Set C”, where each set has a different combination of priors.[5] In particular, set C consists of a log-uniform prior for $\bar{c}$ and a

---

[4] In this thesis we denote a conditional probability distribution by $\text{pr}(x|A)$, which means the probability distribution of x given information A.

[5] See Table I in Ref. [40].

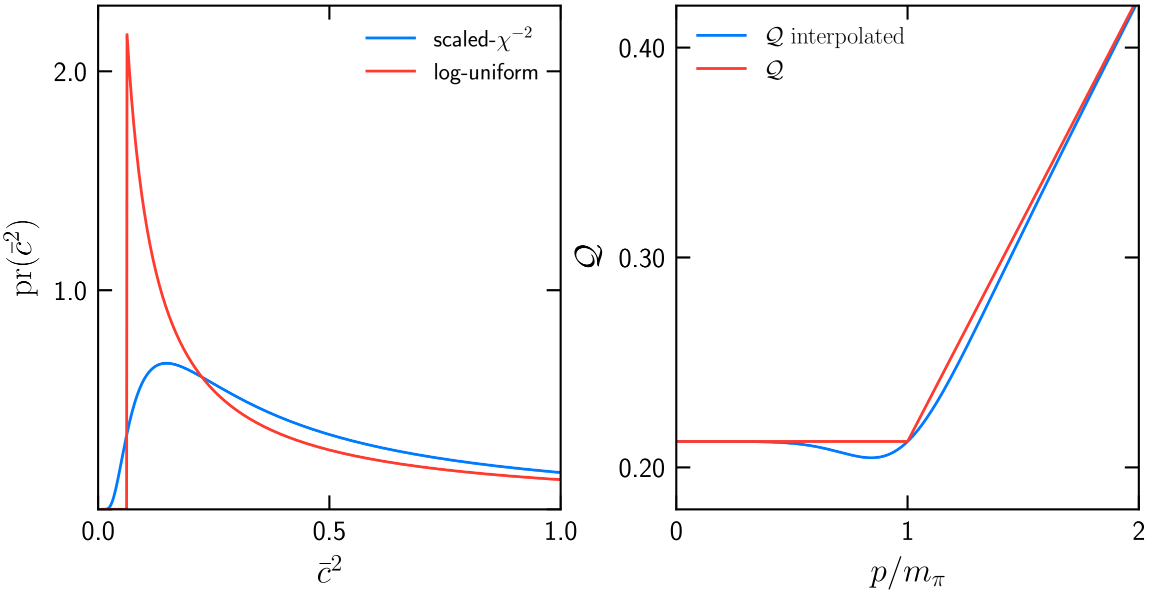

Figure 2.3: Left panel: Prior distribution for $\bar{c}^2$ as a function of $\bar{c}^2$. The red line corresponds to the log-uniform distribution with $\bar{c}_< = 0.25$ and $\bar{c}_> = 10$, while the blue line corresponds to the scaled inverse chi-squared distribution whose parameters are given by $\nu = 0.6$ and $\tau = 0.8$. Right panel: Expansion parameter as a function of the momentum scale p normalized by m_π. The red and the blue line represent the conventional and the interpolated expansion parameter, respectively, with $\Lambda_b = 650$ MeV.

Gaussian prior for $\mathrm{pr}(c_n|\bar{c})$, which are given by

$$\mathrm{pr}(c_n|\bar{c}) = \frac{1}{\sqrt{2\pi}\bar{c}} e^{-c_n^2/(2\bar{c}^2)}, \tag{2.45}$$

$$\mathrm{pr}(\bar{c}) = \frac{1}{\ln(\bar{c}_>/\bar{c}_<)}\,\frac{1}{\bar{c}}\,\theta(\bar{c}-\bar{c}_<)\,\theta(\bar{c}_>-\bar{c}). \tag{2.46}$$

To denote this specific set we use the notation $\mathrm{C}^{\Lambda_\mathrm{b}}_{\bar{c}_<-\bar{c}_>}$. However, here and in what follows, we will employ a slightly modified prior for $\bar{c}$, namely a *scaled inverse chi-squared distribution*:

$$\text{Scale-inv-}\chi^2(\bar{c};\nu,\tau^2) = \frac{(\tau^2\nu/2)^{\nu/2}}{\Gamma(\nu/2)}\,\bar{c}^{-\nu/2-1}\exp\left[\frac{-\nu\tau^2}{2\,\bar{c}}\right], \tag{2.47}$$

where ν represents the degree of freedom of the distribution and τ^2 the scaling parameter. Figure 2.3 displays the log-uniform distribution with values $\bar{c}_< = 0.25$ and $\bar{c}_> = 10$ and the scaled inverse chi-squared distribution with hyperparameters $\nu = 0.6$ and $\tau = 0.8$.[6] These hyperparameter values were chosen given that a scaled inverse chi-squared distribution with these parameters reproduces the results presented in Ref. [42]. Furthermore, we use an interpolation for the expansion parameter $\mathcal{Q}$ to smooth out the transition at $p = m_\pi$, given by

$$\mathcal{Q} = \frac{m_\pi^n + p^n}{m_\pi^{n-1} + p^{n-1}}\Lambda_\mathrm{b}^{-1} \tag{2.48}$$

---

[6] These specific lower and upper bounds for the parameter $\bar{c}$ were shown in Refs. [35, 42] to give robust results for the truncation uncertainty.

with $n = 8$. We choose a rather high breakdown scale of $\Lambda_\mathrm{b} = 650$ Mev, which was also employed in a recent study of the deuteron charge form factor, see Ref. [72]. Values of $\Lambda_\mathrm{b} \sim 650 - 700$ MeV were found to be statistically consistent upon empirical analysis in Refs. [42] for potentials from Refs. [96]. Still, a similar analysis for other potentials has not yet been performed. The momentum scale p depends on the system under investigation such that we will specify its form later on when we discuss the particular system. The right panel of Fig. 2.3 illustrates the smooth function of $\mathcal{Q}$ and compares it to the conventional form. To express set C with the adapted prior distribution we use the following notation: $\mathrm{C}^{\Lambda_\mathrm{b}}_{\chi^{-2},\bar{c}_<-\bar{c}_>}$, where the subscript is understood as the scaled inverse chi-squared distribution that best approximates the log-uniform distribution with $\bar{c}_<$ and $\bar{c}_>$. For our particular choice of parameters this becomes $\mathrm{C}^{650}_{\chi^{-2},0.25-10}$.

The information about the residual Δ_k is contained in degree-of-belief (DoB) intervals. Having obtained the posterior pdf in Eq. (2.43), the DoBs are calculated by inverting the following integral for $d_k^{(p)}$

$$p = \int_{-d_k^{(p)}}^{d_k^{(p)}} \mathrm{d}\Delta \, \mathrm{pr}_h(\Delta | \{c_{n \leqslant k}\}). \tag{2.49}$$

Typically, 68% and 95% DoBs are given for the observable by $\pm X_\mathrm{ref} d_k^{(p)}$ for $p = 0.68 \times 100\%$ and $p = 0.95 \times 100\%$, respectively.

As part of the "Bayesian Uncertainty Quantification: Errors in Your EFT" (BUQEYE) program [40, 164], whose goal is to quantify all uncertainties for EFT applications by developing statistical tools, the software package `gsum` [43, 165] was made public to analyze the convergence pattern of EFTs and quantify truncation uncertainties. Throughout this work we use this tool to calculate truncation uncertainties for our results with the model specified above.

3

FEW-BODY FORMALISM

As we introduced in Chapter 1, low-energy nuclear structure calculations of few-body systems are perfect to test our understanding of microscopic interactions. Few-body systems can be solved exactly with relatively low computational effort. For example, basic properties about the NN interaction can be inferred from the deuteron and the importance of including 3N interactions becomes clear in 3N systems. To evaluate interactions and operators an appropriate basis is necessary, which represents the particular system including its internal degrees of freedom. This evaluation is carried out within few-body frameworks which, in this work, are formulated in a momentum-space partial-wave basis representation. Therefore, in this chapter we discuss the details of such a basis and give a short description of the few-body frameworks.

Below, we specify for both two- and three-body systems their respective basis representations by starting to represent them in terms of relative and center-of-mass coordinates in momentum space. These momenta are subsequently projected onto partial waves, resulting in a separation of radial and angular dependence. We then examine the expansion of general current operators with respect to the obtained two- and three-body bases.

In particular, in Section 3.1 we discuss the well known partial-wave basis for a two-body system, expand the current operator and obtain the wave functions before we continue in Section 3.2 with describing the three-body basis and, again, expanding the current operator. We end this chapter with a short description of the Faddeev framework, which solves the three-body problem exactly.

3.1 Two-body system

3.1.1 Definition of coordinates and two-body momentum basis

To describe a two-body system in coordinate or momentum space in terms of its center-of-mass and relative coordinates we transform the lab frame coordinates. The spatial coordinates $\mathbf{x}_1$ and $\mathbf{x}_2$ describe the position of two particles with mass m_1 and m_2, respectively. We construct the center-of-mass frame coordinates in terms of lab coordinates by

$$\mathbf{r} = \mathbf{x}_1 - \mathbf{x}_2, \qquad \mathbf{R}_{\mathrm{NN}} = \frac{m_1 \mathbf{x}_1 + m_2 \mathbf{x}_2}{m_1 + m_2}. \tag{3.1}$$

Here, $\mathbf{r}$ represents the relative position of the two particles and $\mathbf{R}_{\mathrm{NN}}$ the center-of-mass coordinate. In momentum space the individual momenta $\mathbf{k}_1$ and $\mathbf{k}_2$ characterize the two-body system, which in the center-of-mass frame become

$$\mathbf{p} = \frac{m_2\mathbf{k}_1 - m_1\mathbf{k}_2}{m_1 + m_2}, \qquad \mathbf{P}_{\mathrm{NN}} = \mathbf{k}_1 + \mathbf{k}_2, \tag{3.2}$$

where $\mathbf{p}$ describes the relative momentum between the two particles and $\mathbf{P}_{\mathrm{NN}}$ the center-of-mass momentum. We note that the subscript NN indicates we consider a two-nucleon system.

This approach separates the motion and simplifies the description of the system because the interaction between nucleons only depends on the relative coordinate of the particles. As a result the Hamiltonian separates into two parts, the relative and the center-of-mass part.

As we discussed in the previous chapter, current operators as well as nuclear interactions admit straightforward momentum-space implementations. Accordingly, evaluating these operators and interactions requires a suitable momentum-space basis. A convenient choice for a momentum-space basis representing two noninteracting particles consists of a plane-wave basis, i.e., $\{|\mathbf{k}_1\,\mathbf{k}_2\rangle\}$, with $|\mathbf{k}_1\,\mathbf{k}_2\rangle = |\mathbf{k}_1\rangle\,|\mathbf{k}_2\rangle$. Such a plane-wave basis is normalized and complete:

$$\langle\mathbf{k}_1'\,\mathbf{k}_2'|\mathbf{k}_1\,\mathbf{k}_2\rangle = (2\pi)^6\delta(\mathbf{k}_1 - \mathbf{k}_1')\,\delta(\mathbf{k}_2 - \mathbf{k}_2'), \qquad \int\frac{\mathrm{d}\mathbf{k}_1}{(2\pi)^3}\int\frac{\mathrm{d}\mathbf{k}_2}{(2\pi)^3}\,|\mathbf{k}_1\,\mathbf{k}_2\rangle\,\langle\mathbf{k}_1\,\mathbf{k}_2| = 1, \tag{3.3}$$

providing a full description of two particles in momentum space in terms of the individual momenta.

The final result of an observable is independent of the basis choice. Accordingly, we transform Eq. (3.3) to center-of-mass momentum states. Again, we choose a plane-wave basis to represent the center-of-mass momentum-space states, i.e., $\{|\mathbf{p}\,\mathbf{P}_{\mathrm{NN}}\rangle\}$. For two particles with equal mass, i.e., $m_1 = m_2$, the overlap

$$\langle\mathbf{k}_1\,\mathbf{k}_2|\mathbf{p}\,\mathbf{P}_{\mathrm{NN}}\rangle = (2\pi)^6\,\delta(\mathbf{p} - \frac{1}{2}[\mathbf{k}_1 - \mathbf{k}_2])\,\delta(\mathbf{P}_{\mathrm{NN}} - \mathbf{k}_1 - \mathbf{k}_2), \tag{3.4}$$

connects the states with the single-particle momentum basis. The center-of-mass momentum-space states are normalized and complete

$$\langle\mathbf{p}'\,\mathbf{P}_{\mathrm{NN}}'|\mathbf{p}\,\mathbf{P}_{\mathrm{NN}}\rangle = (2\pi)^6\,\delta(\mathbf{p} - \mathbf{p}')\,\delta(\mathbf{P}_{\mathrm{NN}} - \mathbf{P}_{\mathrm{NN}}'), \qquad \int\frac{\mathrm{d}\mathbf{p}}{(2\pi)^3}\frac{\mathrm{d}\mathbf{P}_{\mathrm{NN}}}{(2\pi)^3}\,|\mathbf{p}\mathbf{P}_{\mathrm{NN}}\rangle\,\langle\mathbf{p}\mathbf{P}_{\mathrm{NN}}| = 1. \tag{3.5}$$

These momentum states establish the starting point to construct appropriate basis states to evaluate current operators and to express the deuteron wave function.

3.1.2 Momentum-space partial-wave basis

In addition to the momentum dependence, current operators and nuclear forces also depend on internal degrees of freedom like spin S and isospin T.[1] Hence, the basis states need to incorporate these internal degrees of freedom as well. We construct such a basis by expanding the momentum states in partial waves and, subsequently, making linear combinations with spin and isospin states. A partial-wave expansion expresses plane waves in terms of linear combinations of spherical waves. These are characterized by $|p\,\ell\,m\rangle$, with p the relative

---

[1] Throughout this work, we denote two-body quantum numbers with a capital, e.g., the two-body spin is given by $S = s_1 + s_2$, where s_1 and s_2 are single-particle spin quantum numbers.

momentum, ℓ the orbital angular momentum, and m its projection. They form a complete set of states:

$$\langle p'\ell'm'|p\ell m\rangle = \frac{\delta(p-p')}{p\,p'}\delta_{\ell\ell'}\delta_{mm'}, \qquad \sum_{\ell m}\int \mathrm{d}p\,p^2\;|p\ell m\rangle\,\langle p\ell m| = 1. \tag{3.6}$$

Consequently, we define the partial-wave state for a two-body system with orbital angular momentum L by

$$\langle \mathbf{p}'|p\,LM_L\rangle \equiv \sqrt{(2\pi)^3}\frac{\delta(p-p')}{p\,p'}Y_{LM_L}(\hat{\mathbf{p}}')\,, \tag{3.7}$$

where $p' = |\mathbf{p}'|$ represents the magnitude of the relative momentum, $\hat{\mathbf{p}}'$ the azimuthal angle $\theta_{p'}$ and polar angle $\phi_{p'}$ of $\mathbf{p}'$, and $Y_{LM_L}(\hat{\mathbf{p}}')$ the spherical harmonic, which is defined by

$$Y_{\ell m}(\hat{\mathbf{a}}) \equiv \langle \hat{\mathbf{a}}|\ell m\rangle\,. \tag{3.8}$$

Note that the factor $\sqrt{(2\pi)^3}$ in Eq. (3.7) sets a normalization for the two-body partial-wave state. Adopting this factor results in clean calculations with partial waves later on. Particularly, it minimizes the number of π factors in partial-wave expanded matrix elements. Additionally, it allows one to generalize relations for matrix elements with respect to a three-body basis. Besides the partial-wave states, we express the total spin state $|SM_S\rangle$ in terms of its single-nucleon spins through

$$|SM_S\rangle = \sum_{m_1m_2}\mathcal{C}^{SM_S}_{s_1m_1s_2m_2}\;|s_1m_1\,s_2m_2\rangle\,, \tag{3.9}$$

where $\mathcal{C}^{SM_S}_{s_1m_1s_2m_2} \equiv \langle s_1m_1s_2m_2|SM_S\rangle$ defines the standard *Clebsch-Gordan coefficient* [166] coupling s_1 and s_2 to S. The same holds for the total isospin state $|TM_T\rangle$. Coupling total spin and orbital angular momentum to the total angular momentum $J = S + L$ and adding isospin degrees of freedom yields the complete two-body state:

$$|p\,(LS)JM_J\,TM_T\rangle \equiv \sum_{M_LM_S}\mathcal{C}^{JM_J}_{LM_LSM_S}\;|p\,LM_L\,SM_S\,TM_T\rangle\,. \tag{3.10}$$

The normalization and completeness of these states is given by

$$\langle p'\,(L'S')J'M_J'\,T'M_T'|p\,(LS)JM_J\,TM_T\rangle = \frac{\delta(p-p')}{p\,p'}\,\delta_{LL'}\,\delta_{SS'}\,\delta_{JJ'}\,\delta_{M_JM_J'}\,\delta_{TT'}\,\delta_{M_TM_T'}, \tag{3.11a}$$

$$\sum_{LS}\sum_{\substack{JM_J\\TM_T}}\int \mathrm{d}p\,p^2\,|p\,(LS)JM_J\,TM_T\rangle\,\langle p(LS)JM_J\,TM_T| = 1. \tag{3.11b}$$

Note that the total angular momentum restricts the values for L and S by $|L-S| \leqslant J \leqslant L+S$. We denote the states defined in Eqs. (3.11a) and (3.11b) by two-body partial-wave basis states. They describe the system in momentum space, including all relevant degrees of freedom.

3.1.3 General current operator expansion

In the following, we examine the expansion of a general current operator with respect to a partial-wave basis. For this purpose we need to develop the partial-wave expansion of a general current operator, where a general current operator in our case consists of a one- or two-body current for either the scalar or vector component of the four-current J^μ. In line with our previous development, we treat the matrix elements in momentum space.

These two-body matrix elements serve mostly as a toy problem, since the analytical and the computational evaluations turn out to be instructive. In fact, they provide a valuable sketch for numerical calculations as well as some first insights to better approach the extension to three particles later on in Section 3.2.2.

We obtain an analytic expression for the matrix element with respect to a specific configuration, i.e., a set of quantum numbers, by evaluating the operator between an initial and a final state of the form given in Eq. (3.11a). Such a configuration specifies the relative momentum, isospin, and orbital angular momentum and spin coupled to a total angular momentum. First, we evaluate the current operator between center-of-mass momentum states [167]:

$$\langle \mathbf{p}'\, \mathbf{P}'_{\mathrm{NN}} | J^\mu | \mathbf{p}\, \mathbf{P}_{\mathrm{NN}} \rangle = \langle \mathbf{p}' | J^\mu(\mathbf{Q}) | \mathbf{p} \rangle \,, \tag{3.12}$$

with $\mathbf{Q} = \mathbf{P}'_{\mathrm{NN}} - \mathbf{P}_{\mathrm{NN}}$ the momentum transfer. The partial-wave-expanded matrix element is then given by substituting the complete two-body state, Eq. (3.10), and using the definition of the partial wave, Eq. (3.7):

$$\begin{aligned} &\langle p'\, (L'S')J'M'_J\, T'M'_T | J^\mu(\mathbf{Q})\, | p\, (LS)JM_J\, TM_T \rangle \\ &\qquad = \frac{1}{(2\pi)^3} \int \mathrm{d}\mathbf{p}_1 \int \mathrm{d}\mathbf{p}'_1 \sum_{M'_L M'_S} \sum_{M_L M_S} \mathcal{C}^{J'M'_J}_{L'M'_L S'M'_S}\, \mathcal{C}^{JM_J}_{LM_L SM_S} \\ &\qquad\quad \times \frac{\delta(p'_1 - p')}{p'_1\, p'}\, Y^*_{L'M'_L}(\hat{\mathbf{p}}'_1)\, \langle \mathbf{p}'_1\, S'M'_S\, T'M'_T | J^\mu(\mathbf{Q}) | \mathbf{p}_1\, SM_S\, TM_T \rangle \\ &\qquad\quad \times \frac{\delta(p - p_1)}{p\, p_1}\, Y_{LM_L}(\hat{\mathbf{p}}_1) \,. \end{aligned} \tag{3.13}$$

Note that without further information about the operator, obtaining the matrix element amounts to calculating a six-dimensional integral while summing over several projection quantum numbers. Two general implications follow for the matrix element evaluation based on our knowledge about the general current operator structure. First, the current operator introduces a preferred direction in the system defined by the momentum transfer $\mathbf{Q}$. This prohibits the use of spherical harmonic properties to resolve one of the angular integrals. As a result, the angular integrals are typically solved numerically by discretizing the integral and introducing an appropriate angular mesh. Second, the current operator acts on isospin, spin, and orbital angular momentum variables. The resulting isospin matrix elements are always diagonal. Spin and orbital angular momentum matrix elements, on the other hand, are most of the time off-diagonal because of the operator action.

In summary, the detailed structure of the partial-wave expanded matrix element in Eq. (3.13) depends on specific properties of the current operators. In Chapter 4, we will investigate matrix elements of the current operators defined in Chapter 2 and we will obtain their detailed structure. These matrix elements then allow one to calculate electromagnetic observables of the deuteron.

In the next section, we state some experimental results for the deuteron from which we infer the deuteron wave function in terms of partial waves and we present basic expressions for electromagnetic properties based upon these wave functions.

3.1.4 Deuteron wave function and electromagnetic observables

To express the deuteron wave function, we employ partial-wave basis states previously defined in Eqs. (3.11a) and (3.11b). These states are practical because they include S and J as good quantum numbers, which are conserved by nuclear interactions. Only few partial-wave states contribute to the deuteron wave function and the ones that contribute can be determined from experimental observations.

We know that the deuteron is a weakly bound system without excited states. Therefore, we expect the system to be in an S-state because higher orbital angular momentum states are at higher energy. Experiments show that the deuteron has an integer total angular momentum of $J = 1$ with positive parity, a magnetic moment $\mu_\mathrm{d} = 0.857438\mu_N$ [60], and an electric quadrupole moment $Q_\mathrm{d} = 0.2859(3)\ \mathrm{fm}^2$ [168, 169].[2] These results imply a triplet state for the total spin, i.e., $S = 1$, along with a non-S-wave component, i.e., $L \neq 0$, causing the quadrupole deformation. Given that $P = (-1)^L$, the positive parity of the nucleus only allows states with even orbital angular momentum, resulting in an $L = 2$ or D-wave component in addition to the S-wave component. This mixing of S- and D-wave components reveals the noncentral character of the nuclear force which emerges from the tensor part of the interaction. Additionally, the wave function has to be antisymmetric, i.e., $(-1)^{L+S+T}$ has to equal -1 such that with $L = 0, 2$ and $S = 1$ it follows that $T = 0$. Combining these facts to describe the deuteron wave function in terms of partial-waves yields:

$$\begin{aligned}\phi_\mathrm{d}(\mathbf{p}) &= \sum_{L=0,2} \langle \mathbf{p}|\phi_\mathrm{d}\,(LS)JM_J\rangle \\ &= \sum_{L=0,2}\sum_{M_L M_S} \mathcal{C}^{JM_J}_{LM_LSM_S}\,\tilde{u}_L(p)Y_{LM_L}(\hat{\mathbf{p}})\ |SM_S\rangle\,. \end{aligned} \tag{3.14}$$

The wave function is a linear combination of spatial and spin wave functions, where $\tilde{u}_L(p)$ represents the radial part of the wave function. Note that we left out the trivial isospin dependence and that the spherical harmonics completely encode the angular information. This wave function illustrates an example how partial-waves describe a nuclear system and how experimental facts determine which configurations to include.

So far, the radial part of the wave function $\tilde{u}_L(p)$ remains unspecified. Conventionally, the radial functions are denoted by

$$\tilde{u}(p) \equiv \tilde{u}_0(p) \text{ and } \tilde{w}(p) \equiv \tilde{u}_2(p), \tag{3.15}$$

representing the S- and D-wave components, respectively. The momentum-space wave functions relate to the coordinate-space radial wave functions through a spherical Bessel transformation:

$$\tilde{u}_L(p) = i^L 4\pi \int \mathrm{d}r j_L(pr)\, r\, u_L(r), \tag{3.16}$$

with $j_L(pr)$ the L-th spherical Bessel function. Furthermore, they define probability densities,

---

[2] A list with experimental results for deuteron observables can be found in Appendix E. Together with these results, a short comment explains how each quantity was obtained.

i.e., $\rho_{\mathrm{S}} \equiv \tilde{u}(p)^2$ and $\rho_{\mathrm{D}} \equiv \tilde{w}(p)^2$, and corresponding S- and D-state probabilities:

$$P_{\mathrm{S}} = \int \mathrm{d}r\, \rho_{\mathrm{S}}(r), \qquad P_{\mathrm{D}} = \int \mathrm{d}r\, \rho_{\mathrm{D}}(r), \tag{3.17}$$

which fulfill the normalization

$$P_{\mathrm{S}} + P_{\mathrm{D}} = 1. \tag{3.18}$$

The radial wave functions are obtained by solving the time-independent Schrödinger equation in momentum space. In particular, this corresponds to solving[3]

$$\frac{p^2}{2\mu}\, \tilde{u}_L(p) + \int \mathrm{d}p'\, p'^2 \sum_{L'} V_{LL'}(p,p')\, \tilde{u}_{L'}(p') = E_{\mathrm{d}}\, \tilde{u}_L(p), \tag{3.19}$$

where μ represents the reduced mass, $V_{LL'}(p,p') \equiv \langle p'\, L'|\hat{V}|p\, L\rangle$ the partial-wave expanded potential matrix element of the noncentral and nonlocal two-body nuclear interaction, and E_{d} the deuteron binding energy. A solution can be found by recasting the expression into a matrix equation and diagonalizing the resulting Hamiltonian. Remember, the interaction mixes states with different orbital angular momentum generating off-diagonal potential matrix elements. Therefore, to construct the Hamiltonian we require partial-wave expanded two-body potential matrix elements. In particular, they consist of $V_{00}(p,p')$, $V_{22}(p,p')$, $V_{02}(p,p')$, and $V_{20}(p,p')$, where $V_{20}(p,p')$ is provided by transposing $V_{02}(p,p')$ because the hermiticity of the Hamiltonian. These partial-wave expanded matrix elements depend on which potential is used.[4] After constructing the Hamiltonian we solve Eq. (3.19) by diagonalization which provides the eigenstates $\tilde{u}(p)$ and $\tilde{w}(p)$ defined in Eq. (3.15) corresponding to the lowest eigenvalue.

Using radial wave functions we can calculate the deuteron magnetic and quadrupole moment to a first approximation. As a first example, we present the magnetic moment which can be defined in terms of the D-wave probability [170]

$$\mu_{\mathrm{d}} = \mu_{\mathrm{s}} - \frac{3}{2}\left(\mu_{\mathrm{s}} - \frac{1}{2}\right) P_{\mathrm{D}}, \tag{3.20}$$

with $\mu_{\mathrm{s}} = \mu_{\mathrm{n}} + \mu_{\mathrm{p}}$ the sum of the neutron and proton magnetic moment. Because the neutron and proton magnetic moments are known, a measurement of the deuteron magnetic moment suggests one can determine P_{D}. However, we remark that the D-wave probability is not an observable, demonstrating that two-body current effects in Eq. (3.20) are neglected. The second example is the deuteron quadrupole moment in terms of the radial wave functions in momentum space and their derivatives [171]:

$$Q_{\mathrm{d}} = -\frac{1}{20} \int \mathrm{d}p \left\{ \sqrt{8} \left[p^2\, \frac{\mathrm{d}\tilde{u}(p)}{\mathrm{d}p} \frac{\mathrm{d}\tilde{w}(p)}{\mathrm{d}p} + 3\, p\, \tilde{w}(p)\, \frac{\mathrm{d}\tilde{u}(p)}{\mathrm{d}p} \right] + p^2 \left(\frac{\mathrm{d}\tilde{w}(p)}{\mathrm{d}p} \right)^2 + 6\, \tilde{w}(p)^2 \right\}. \tag{3.21}$$

Equations (3.20) and (3.21) provide informative examples for the magnetic and quadrupole moment, however, they are only approximations. As a result, calculations fail to agree with measured electromagnetic quantities.

---

[3] Throughout this thesis we work in natural units, i.e., $\hbar = c = 1$ and $e^2/(4\pi) = \alpha = 1/137$, such that length and energy are related through 1 fm $\approx 1/200$ MeV^{-1}.

[4] In the next chapter, we will specify different NN interactions used in this work to obtain the wave functions.

To summarize, the deuteron constitutes a fundamental system for nuclear physics. It provides a perfect example to test our understanding of the NN interaction. Describing the deuteron in terms of partial-wave states, defined in Eq. (3.10), guarantees a practical description of observed properties. This is because the representation offers particularly efficient calculations since they only need to include two relevant states. The details of the radial wave functions $\tilde{u}_L(p)$, solutions of Eq. (3.19), are determined by the NN interaction $V_{LL'}(p, p')$. As stated above, simplified calculations of the magnetic, Eq. (3.20), and quadrupole moment, Eq. (3.21), neglect important contributions. However, by using current operators we can extend the evaluation of Eq. (3.20) and Eq. (3.21) beyond these approximations and study the effects of two-body currents on electromagnetic observables.

3.2 THREE-BODY SYSTEM

In this section we present the three-body partial-wave basis, the expansion of a general current operator in this basis and an exact method to obtain three-body wave functions for bound systems. Again, it is useful to start by specifying the momentum coordinates before we continue to develop the basis.

3.2.1 Jacobi momenta and three-body momentum basis

A three-particle system with individual masses m_1, m_2 and m_3 can be represented by their positions in coordinate space, $\mathbf{x}_1$, $\mathbf{x}_2$ and $\mathbf{x}_3$, respectively, or their individual momenta $\mathbf{k}_1$, $\mathbf{k}_2$ and $\mathbf{k}_3$ in momentum space. If we examine the relative and center-of-mass momenta of the three particles, we can introduce three equivalent sets of *Jacobi momenta*. One such set is defined by [172]:

$$\mathbf{p}_{\{12\}} = \frac{m_2\mathbf{k}_1 - m_1\mathbf{k}_2}{m_1 + m_2}, \tag{3.22a}$$

$$\mathbf{q}_{\{12\}} = \frac{1}{M}\Big[(m_1 + m_2)\mathbf{k}_3 - m_3(\mathbf{k}_1 + \mathbf{k}_2)\Big], \tag{3.22b}$$

$$\mathbf{P}_{3\mathrm{N}} = \mathbf{k}_1 + \mathbf{k}_2 + \mathbf{k}_3, \tag{3.22c}$$

where $M = m_1 + m_2 + m_3$ is the total mass. We observe that $\mathbf{p}_{\{12\}}$ is the relative momentum between particle 1 and 2, defining the subsystem and the subscript naming convention. The second relative momentum, i.e., $\mathbf{q}_{\{12\}}$, is given by the momentum of the third particle relative to the center-of-mass momentum of the two-body subsystem. We will denote this third particle as *spectator particle* in what follows. Finally, $\mathbf{P}_{3\mathrm{N}}$ defines the three-body center-of-mass momentum. We obtain the two other sets by constructing pairs from the leftover combinations, i.e., $\{12\} \to \{23\}, \{31\}$. Figure 3.1 shows the three equivalent sets of Jacobi momenta for particles with equal masses $m_1 = m_2 = m_3$, and depicts very well that the center-of-mass momentum is the same for all sets.

The separation of $\mathbf{P}_{3\mathrm{N}}$ is possible due to expressing the system in terms of its relative momenta and is very useful for three-body systems exhibiting translational invariance. A complete description of such systems only needs the relative momenta without the center-of-mass momentum, reducing the complexity for practical calculations.

Each set of Jacobi momenta $\{12\}$, $\{23\}$, and $\{31\}$ describes the relative motion completely and, thus, forms a complete basis. Therefore, linear combinations of one set give a description

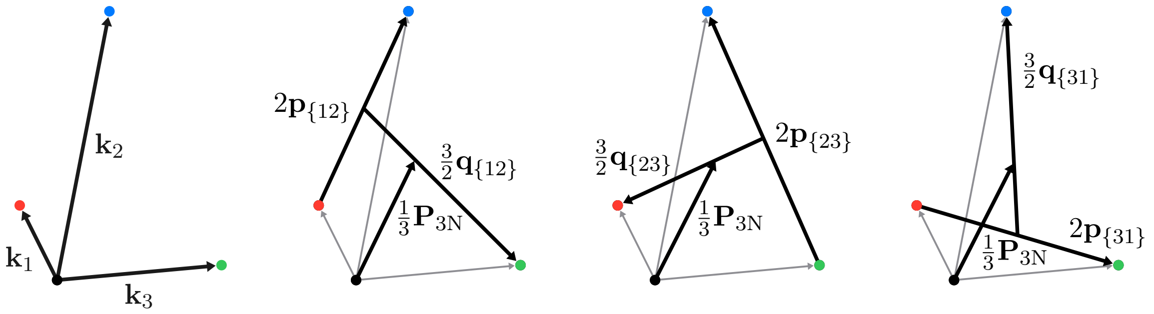

Figure 3.1: Transformation of the individual momenta to the Jacobi momenta. The individual momenta $\mathbf{k}_1$, $\mathbf{k}_2$ and $\mathbf{k}_3$ are shown on the left. The Jacobi momenta $\mathbf{p}_{\{\mathrm{ab}\}}$ and $\mathbf{q}_{\{\mathrm{ab}\}}$ for equal mass are shown for the three equivalent sets $\{\mathrm{ab}\} = \{12\}$, $\{23\}$ and $\{31\}$ as well as a fraction of the center-of-mass momentum, i.e., $1/3\mathbf{P}_{3\mathrm{N}}$, from left to right. Figure adapted from [33].

of the other two, e.g., $\mathbf{p}_{\{23\}} = -1/2\,\mathbf{p}_{\{12\}} - 3/4\,\mathbf{q}_{\{12\}}$ and $\mathbf{q}_{\{23\}} = \mathbf{p}_{\{12\}} - 1/2\,\mathbf{q}_{\{12\}}$. This is equivalent to performing a cyclic permutation of the single-particle momenta

$$\mathbf{k}_1 \to \mathbf{k}_2, \qquad \mathbf{k}_2 \to \mathbf{k}_3, \qquad \mathbf{k}_3 \to \mathbf{k}_1, \tag{3.23}$$

which transforms representation $\{12\}$ into $\{23\}$. For more details on the transformation properties of Jacobi momenta see, e.g., Refs. [33, 172].

The momentum-space representation of a three-particle system can be realized in terms of its single-particle momenta in a plane-wave basis $\{|\mathbf{k}_1\,\mathbf{k}_2\,\mathbf{k}_3\rangle\}$ which forms a complete set of states and extends Eq. (3.3) to three nucleons. Alternatively, we can choose to represent the system in terms of its relative momenta and its center-of-mass momentum, i.e., $|\mathbf{p}\,\mathbf{q}\,\mathbf{P}_{3\mathrm{N}}\rangle$, such that (3.22a)-(3.22c) define the overlap

$$\begin{aligned}\langle \mathbf{k}_1\,\mathbf{k}_2\,\mathbf{k}_3|\mathbf{p}\,\mathbf{q}\,\mathbf{P}_{3\mathrm{N}}\rangle_{\{12\}} =& (2\pi)^9\delta(\mathbf{p}_{\{12\}} - \frac{1}{2}[\mathbf{k}_1 - \mathbf{k}_2])\,\delta(\mathbf{q}_{\{12\}} - \frac{2}{3}[\mathbf{k}_3 - \frac{1}{2}(\mathbf{k}_1 + \mathbf{k}_2)])\\ &\times \delta(\mathbf{P}_{3\mathrm{N}} - \mathbf{k}_1 - \mathbf{k}_2 - \mathbf{k}_3),\end{aligned} \tag{3.24}$$

where it is assumed that particles have equal masses, i.e., $m_1 = m_2 = m_3$. Note that we establish a normalization convention. The current operators under investigation are independent of the center-of-mass momentum, hence we will leave out the notation of $\mathbf{P}_{3\mathrm{N}}$ in the states. From the definition of the overlap we can verify that the Jacobi momenta basis states are orthogonal and complete

$${}_{\{12\}}\langle \mathbf{p}'\,\mathbf{q}'|\mathbf{p}\,\mathbf{q}\rangle_{\{12\}} = (2\pi)^6\delta(\mathbf{p} - \mathbf{p}')\,\delta(\mathbf{q} - \mathbf{q}'), \qquad \int\frac{\mathrm{d}\mathbf{p}}{(2\pi)^3}\int\frac{\mathrm{d}\mathbf{q}}{(2\pi)^3}\,|\mathbf{p}\,\mathbf{q}\rangle_{\{12\}}\,{}_{\{12\}}\langle \mathbf{p}\,\mathbf{q}| = 1, \tag{3.25}$$

where the normalization factors follow from Eq. (3.24). The current operator acts on the spectator particle or on the two-body subsystem, depending on its one- or two-body structure. We choose that the one-body current always acts on the third spectator particle and the two-body current on subsystem $\{12\}$. This freedom arises because the wave function is antisymmetrized. Therefore we suppress the subscript, $\{12\}$, from now on. In fact, if necessary, the specific Jacobi set can always be transformed into another one by making linear combinations of the Jacobi momenta as mentioned before.

Now that we have established the Jacobi momenta and their basis states, we want to examine how to express the current matrix elements. The next section introduces how the evaluation of a general current operator matrix element benefits from the transformation from a single-particle basis to a Jacobi momentum basis, before we explore the actual basis states used in numerical calculations.

3.2.2 Momentum-basis representation of a general current operator

In general, current operators depend explicitly on the single-particle momenta. Thus, naively we would determine the matrix elements in a single-particle basis representation. Without taking into account internal degrees of freedom, the expectation value between single-particle momentum states is described by

$$\langle \mathbf{k}_1' \, \mathbf{k}_2' \, \mathbf{k}_3' | J^\mu | \mathbf{k}_1 \, \mathbf{k}_2 \, \mathbf{k}_3 \rangle \, . \tag{3.26}$$

Here, J^μ represents a general current operator. This matrix element depends on six vector variables, which makes the numerical evaluation extremely difficult. As stated before, the electromagnetic current operators presented in Section 2.4.3 shift the center-of-mass momentum $\mathbf{P}_{3\mathrm{N}}$ and depend on the difference between the final and initial momentum. Therefore, making a transformation to momentum states represented in a Jacobi basis, which describes the three-particle center-of-mass momentum, simplifies the matrix element determination. Evaluating the current operator between Jacobi basis states, we find

$$\langle \mathbf{p}' \, \mathbf{q}' \, \mathbf{P}_{3\mathrm{N}}' | J^\mu | \mathbf{p} \, \mathbf{q} \, \mathbf{P}_{3\mathrm{N}} \rangle = \langle \mathbf{p}' \, \mathbf{q}' | J^\mu(\mathbf{Q}) | \mathbf{p} \, \mathbf{q} \rangle \, , \tag{3.27}$$

where $\mathbf{Q} = \mathbf{P}_{3\mathrm{N}}' - \mathbf{P}_{3\mathrm{N}}$. Only four vector variables are left after separating out the center-of-mass momentum such that calculations of the matrix elements become more feasible. In the next chapter, we will analytically evaluate one- and two-body current operators. There we will observe a further simplification of matrix elements because one-body currents leave the two-body subsystem invariant while two-body currents do not act on the spectator particle.

Numerical calculations of the matrix elements are more naturally evaluated in a partial-wave representation, meaning that the angular dependence of the Jacobi momenta is represented in terms of spherical harmonics. In turn, this representation allows one to separate the radial and angular integrals.

In what follows, we specify the partial-wave expansion of the Jacobi states. On top of this expansion spin and isospin internal degrees of freedom will be included to allow for a complete description of the system and the action of the operator.

3.2.3 Partial-wave expansion of a general current operator

Before we present the partial-wave expansion of a general current operator, we define the partial-wave representation of the momentum states and introduce how to add the spin and isospin degrees of freedom. As a first step, we define the partial-wave states

$$\langle \mathbf{p}' \, \mathbf{q}' | p \, q \, (L\ell) \mathcal{L} \mathcal{M}_\mathcal{L} \rangle \equiv (2\pi)^3 \frac{\delta(p-p')}{p \, p'} \frac{\delta(q-q')}{q \, q'} \mathcal{Y}_{L\ell}^{\mathcal{L}\mathcal{M}_\mathcal{L}}(\hat{\mathbf{p}}', \hat{\mathbf{q}}'). \tag{3.28}$$

Here L describes the orbital angular momentum of the two-body subsystem, ℓ that of the spectator particle, and $\mathcal{L}$ represents the total orbital angular momentum of the system. The *coupled spherical harmonic* is defined by

$$\mathcal{Y}^{\ell m}_{\ell_a \ell_b}(\hat{\mathbf{a}}, \hat{\mathbf{b}}) \equiv \sum_{m_a\, m_b} \mathcal{C}^{\ell m}_{\ell_a m_a \ell_b m_b}\, Y_{\ell_a m_a}(\hat{\mathbf{a}})\, Y_{\ell_b m_b}(\hat{\mathbf{b}})\,. \tag{3.29}$$

Note that the normalization for the three-body partial waves naturally extends the one for the two-body states defined in Eq. (3.7). Remember, we chose this normalization to minimize factors of π in partial-wave expanded matrix elements and to easily generalize expressions including two-body states to three-body states. The expansion in terms of spherical harmonics sets the angular dependence of the Jacobi momenta $\mathbf{p}$ and $\mathbf{q}$. Determining the normalization of the partial-wave states is accomplished by adopting the conventions from Eqs. (3.25) and (3.28):

$$\langle p'\, q'\, (L'\ell')\mathcal{L}'\mathcal{M}'_{\mathcal{L}} | p\, q\, (L\ell)\mathcal{L}\mathcal{M}_{\mathcal{L}}\rangle = \frac{\delta(p-p')}{p\,p'} \frac{\delta(q-q')}{q\,q'}\, \delta_{LL'}\, \delta_{\ell\ell'}\, \delta_{\mathcal{L}\mathcal{L}'}\, \delta_{\mathcal{M}_{\mathcal{L}}\mathcal{M}'_{\mathcal{L}}}\,. \tag{3.30}$$

Given that current operators act on spin as well as isospin quantum numbers, it is necessary to include these degrees of freedom into the basis states. An extension of the partial-wave basis defined in Eqs. (3.28) and (3.30), which incorporates spin and isospin, is given by a Jj-coupled basis [172]:

$$|p\, q\, \alpha\rangle \equiv |p\, q\, [(LS)J\, (\ell s)j]\mathcal{J}\mathcal{M}_{\mathcal{J}}\, (Tt)\mathcal{T}\mathcal{M}_{\mathcal{T}}\rangle\,. \tag{3.31}$$

Here S represents the two-body spin associated with particles in the subsystem and s the spin of the spectator particle, and the isospin quantum numbers T and t are analogous. The total three-body isospin is represented by $\mathcal{T}$ and the total three-body angular momentum $\mathcal{J}$ is obtained by coupling the two-body angular momentum J with the spectator angular momentum j, hence the label Jj-coupled basis.[5] An explicit decoupling of the total three-body state into two- and one-body (spectator particle) quantum numbers is given by

$$\begin{aligned} |p\, q\, \alpha\rangle = & \sum_{\substack{M_L M_S M_J \\ m_\ell m_s m_j}} \mathcal{C}^{\mathcal{J}\mathcal{M}_{\mathcal{J}}}_{JM_J jm_j}\, \mathcal{C}^{JM_J}_{LM_L SM_S}\, \mathcal{C}^{jm_j}_{\ell m_\ell s m_s}\, |p\, q\, LM_L\, SM_S\, \ell m_\ell\, sm_s\rangle \\ & \times \sum_{M_T m_t} \mathcal{C}^{\mathcal{T}\mathcal{M}_{\mathcal{T}}}_{TM_T tm_t}\, |TM_T tm_t\rangle\,. \end{aligned} \tag{3.32}$$

This decoupling prescription will be useful later on when we evaluate the partial-wave expansion of a general current operator.

---

[5] The reader might be more familiar with the $\mathcal{LS}$-coupled basis for a three-body system, defined by [172]:

$$|p\, q\, \beta\rangle \equiv |p\, q\, [(L\ell)\mathcal{L}\, (Ss)\mathcal{S}]\mathcal{J}\mathcal{M}_{\mathcal{J}}\, (Tt)\mathcal{T}\mathcal{M}_{\mathcal{T}}\rangle\,,$$

where $\mathcal{S}$ represents the total three-body spin. Although these basis states describe the system completely, they are not practical for evaluating current matrix elements because the current operator acts on quantum numbers of the spectator particle or of the two-body subsystem. As a result, the total orbital angular momentum and the total spin have to be decoupled, adding undesirable sums over Clebsch-Gordan coefficients. A better approach consists of grouping the quantum numbers according to the subsystems involved, as done in the Jj-coupled basis. The two bases are coupled to each other through a standard recoupling relation [166]:

$$|p\, q\, \alpha\rangle = \sum_{\mathcal{LS}} \sqrt{\hat{\mathcal{L}}\, \hat{\mathcal{S}}\, \hat{J}\, \hat{j}} \begin{Bmatrix} L & S & J \\ \ell & s & j \\ \mathcal{L} & \mathcal{S} & \mathcal{J} \end{Bmatrix} |p\, q\, \beta\rangle\,,$$

where we introduced the abbreviation $\hat{a} \equiv 2a+1$ and the $9j$-symbol $\{...\}$ [166].

The normalization and completeness of the Jj-coupled basis are given by

$$\langle p'\,q'\,\alpha'|p\,q\,\alpha\rangle = \frac{\delta(p-p')}{p\,p'}\frac{\delta(q-q')}{q\,q'}\,\delta_{\alpha\alpha'}, \qquad \sum_{\alpha}\int \mathrm{d}p\,p^2 \int \mathrm{d}q\,q^2\,|p\,q\,\alpha\rangle\,\langle p\,q\,\alpha| = 1, \tag{3.33}$$

where $\delta_{\alpha\alpha'}$ imposes all quantum numbers to be diagonal and the sum runs over the allowed values for the quantum numbers.

The discrete quantum numbers in the Jj-coupled basis are collected by the index $\alpha = \{L, S, J, T, \ell, j\}$, leaving out the trivial quantum numbers $s = t = \frac{1}{2}$ which represent the spin and isospin of the spectator proton or neutron. We call a specific set of values for the quantum numbers in α a *configuration* or a *channel*. Such a set is given for the three-body partial wave described by $\{\mathcal{J}, \mathcal{T}, \mathcal{P}\}$, with the three-body parity $\mathcal{P} = (-1)^{L+\ell}$. To build the configurations that make up the basis some requirements have to be met. First of all, the two-body subsystem has to be antisymmetric, in other words, it has to fulfill $(-1)^{L+S+T} = -1$. Furthermore, as we only study the triton and the helion, we have $\mathcal{J} = \mathcal{T} = \frac{1}{2}$, positive parity $\mathcal{P} = +1$, and an isospin projection $\mathcal{M}_{\mathcal{T}} = -\frac{1}{2}$ and $+\frac{1}{2}$ for the triton and helion, respectively. A complete list of all configurations of the partial-wave basis states up to a maximum two-body angular momentum of $J_{\max} = 8$ can be found in Appendix A. Truncating the channels with respect to $J_{\max}$ proves to be sufficient to reach converged results for observables of finite nuclei and infinite matter including NN and 3N matrix elements [33, 173].

We started out by specifying the relative momenta and their corresponding basis states in Eqs. (3.22a), (3.22b), and (3.25) to arrive at a suitable partial-wave expanded basis established in Eqs. (3.31) and (3.33) including the relevant internal degrees of freedom. We are now in a position to address the partial-wave expansion of a general current operator using this basis. Combining Eqs. (3.28), (3.31), and (3.33) we obtain the expression for a matrix element of a general current operator in partial-wave basis states:

$$\begin{aligned}\langle p'\,q'\,\alpha'|\,J^{\mu}\,|p\,q\,\alpha\rangle = &\sum_{\substack{M_J M'_J\\ m_j m'_j}} \mathcal{C}^{\mathcal{J}'\mathcal{M}'_{\mathcal{J}}}_{J'M'_J j' m'_j}\,\mathcal{C}^{\mathcal{J}\mathcal{M}_{\mathcal{J}}}_{JM_J j m_j} \sum_{\substack{M_T M'_T\\ m_t m'_t}} \mathcal{C}^{\mathcal{T}'\mathcal{M}'_{\mathcal{T}}}_{T'M'_T t' m'_t}\,\mathcal{C}^{\mathcal{T}\mathcal{M}_{\mathcal{T}}}_{TM_T t m_t}\\ &\times \mathcal{P}^{M'_J M'_T M_J M_T}_{(L'S')J'T'\,(LS)JT}(p,p')\,\mathcal{Q}^{m'_j m'_t m_j m_t}_{(\ell' s')j't'\,(\ell s)jt}(q,q'),\end{aligned} \tag{3.34}$$

where we will specify the functions $\mathcal{P}$ and $\mathcal{Q}$ below. Note that we grouped the quantum numbers and the relative momentum of the two-body subsystem as well as the quantum numbers and momentum of the spectator particle. Depending on the one- or two-body character of the operator, it only acts on the spectator particle or the two-body subsystem. Accordingly, we parametrize the parts of the partial-wave matrix elements into two suitable functions:

$$\begin{aligned}\mathcal{P}^{M'_J M'_T M_J M_T}_{(L'S')J'T'\,(LS)JT}(p,p') \equiv &\frac{1}{(2\pi)^3}\int \mathrm{d}\mathbf{p}_1 \int \mathrm{d}\mathbf{p}'_1\,\frac{\delta(p'_1-p')}{p'_1\,p'}\mathcal{Y}^{*J'M'_J}_{L'S'}(\hat{\mathbf{p}}'_1)\\ &\times \langle \mathbf{p}'_1\,T'M'_T|J^{\mu}|\mathbf{p}_1\,TM_T\rangle\,\frac{\delta(p-p_1)}{p\,p_1}\mathcal{Y}^{JM_J}_{LS}(\hat{\mathbf{p}}_1)\,,\end{aligned} \tag{3.35}$$

$$\begin{aligned}\mathcal{Q}^{m'_j m'_t m_j m_t}_{(\ell' s')j't'\,(\ell s)jt}(q,q') \equiv &\frac{1}{(2\pi)^3}\int \mathrm{d}\mathbf{q}_1 \int \mathrm{d}\mathbf{q}'_1\,\frac{\delta(q'_1-q')}{q'_1\,q'}\mathcal{Y}^{*j'm'_j}_{\ell' s'}(\hat{\mathbf{q}}'_1)\\ &\times \langle \mathbf{q}'_1\,t'm'_t|J^{\mu}|\mathbf{q}_1\,tm_t\rangle\,\frac{\delta(q-q_1)}{q\,q_1}\mathcal{Y}^{jm_j}_{\ell s}(\hat{\mathbf{q}}_1).\end{aligned} \tag{3.36}$$

These two parametrizations are the starting point to evaluate the current operator matrix elements for general spin and isospin. In the next chapter, we will obtain detailed partial-wave expanded expressions for the operators defined in Section 2.4.3. Note that, without further information about the operator structure, we have to evaluate a twelve-dimensional integral. Unfortunately, current operators introduce a preferred direction in the system defined by the momentum transfer, breaking rotational invariance and prohibiting the simplification of angular integrals.

The matrix elements specified in Eq. (3.34) are the ingredients for subsequent calculations. First of all, they are used to calculate observables of three-body systems for which we evaluate the expectation value of the current operator with wave functions and current operator matrix elements given in a partial-wave basis. This is done explicitly in Chapter 4. Secondly, the calculation of observables in light- and medium-mass nuclei using basis-expansion methods like, e.g., Hartree-Fock (HF) theory, Coupled Cluster (CC) theory or the In-Medium Similarity Renormalization Group (IMSRG), is conveniently performed using operator representations with respect to a single-particle basis used for computations. In the past a variety of different formulations have been employed, e.g., harmonic oscillator (HO) basis, natural orbitals or HF basis, each of which having specific advantages. Therefore, we have to perform a transformation of the partial-wave expanded matrix elements. Fortunately, partial-wave basis states as introduced in Eq. (3.31) can be directly transformed to a three-body HO basis, with an equivalent two-body subsystem and spectator particle structure. In turn, these can then be transformed to a single-particle HO basis. Other single-particle bases are conveniently obtained by a single-particle transformation starting from the initial HO basis. We will carry out this basis transformation of the matrix elements later (see Section 5.6).

Before we continue with calculating observables, we present a method that solves the three-body problem exactly. The next section clarifies, without going into too much detail, how we obtain these three-body solutions from the *Faddeev equations*.

3.2.4 Faddeev equations for three-nucleon bound states

In general, observables are obtained by calculating the expectation value of an operator:

$$\langle \Phi | \hat{O} | \Phi \rangle \, . \tag{3.37}$$

This requires one to have an expression for the operator and a wave function describing the system under investigation. Obtaining an expression for the current and representing it in a specific basis has been discussed in Section 3.2.3. For 3N systems, the Faddeev equations solve the quantum-mechanical three-body problem exactly in a nonperturbative way for scattering and bound states by iteration. This exactness implies that a numerical solution can be obtained with any desired accuracy, where the uncertainties originate from using a finite basis size.

We start by stating the Schrödinger equation for a bound state of a 3N system including a three-body force

$$|\Phi\rangle = \frac{1}{E - H_0} \left(\sum_{i=1}^{3} V_{\mathrm{NN}}^{i} + V_{3\mathrm{N}} \right) |\Phi\rangle \, , \tag{3.38}$$

with $|\Phi\rangle$ the total 3N state, $V_{\mathrm{NN}}^{i} \equiv V_{\mathrm{NN}}^{\{jk\}}$ the NN potential where we use the same notation as in Eqs. (3.22a) and (3.22b) to denote the two-body subsystem, and $V_{3\mathrm{N}}$ the three-body interaction which is required to be totally symmetric. Here, the kinetic energy, H_0, is given in terms of the Jacobi momenta

$$H_0 = \sum_{i=1}^{3} \frac{\mathbf{k}_i^2}{2m_i} = \frac{\mathbf{P}_{3\text{N}}^2}{2M} + \frac{\mathbf{p}_{\{12\}}^2}{2\mu_1} + \frac{\mathbf{q}_{\{12\}}^2}{2\mu_2}, \tag{3.39}$$

where the reduced masses μ_1 and μ_2 are specified by $\mu_1^{-1} = m_1^{-1} + m_2^{-1}$ and $\mu_2^{-1} = (m_1 + m_2)^{-1} + m_3^{-1}$.

The three-body interaction in Eq. (3.38) decomposes into three parts

$$V_{3\text{N}} = \sum_{i=1}^{3} V_{3\text{N}}^{(i)}, \tag{3.40}$$

such that each individual part $V_{3\text{N}}^{(i)}$ is symmetric under the exchange of j and k. Cyclic permutations of $V_{3\text{N}}^{(i)}$ then result in $V_{3\text{N}}^{(j)}$ and $V_{3\text{N}}^{(k)}$. In fact, this shows that $V_{3\text{N}}^{(i)}$ is not uniquely defined and one just has to make a particular choice to determine Eq. (3.40). The decomposition of the three-body interaction suggests to group V_{NN}^{i} and $V_{3\text{N}}^{(i)}$ together, since both behave symmetric under the exchange of j and k. This leads us to decompose the 3N wave function and to define the *Faddeev components* [172]

$$|\phi_i\rangle = G_0 \left(V_{\text{NN}}^{i} + V_{3\text{N}}^{(i)} \right) |\Phi\rangle \,. \tag{3.41}$$

Note that we defined the resolvent operator $G_0 \equiv (E - H_0)^{-1}$. Obviously, the single Faddeev components sum up to the total 3N wave function $|\Phi\rangle = \sum_{i=1}^{3} |\phi_i\rangle$.

Considering that the particles are identical and that the 3N state has to be totally antisymmetric, the Faddeev components have to fulfill the following permutations

$$|\phi_2\rangle = P_{12}P_{23}\,|\phi_1\rangle\,, \qquad |\phi_3\rangle = P_{13}P_{23}\,|\phi_1\rangle\,, \tag{3.42}$$

with P_{ij} the two-body permutation operator which exchanges the labels of particles i and j, e.g., $P_{12}\,|a\,b\,c\rangle = |b\,a\,c\rangle$. As a result, the three-body wave function is obtained by permutations of a single Faddeev component

$$|\Phi\rangle = (1 + P_{12}P_{23} + P_{13}P_{23})\,|\phi_1\rangle = (1 + P)\,|\phi_1\rangle\,, \tag{3.43}$$

with $P \equiv P_{12}P_{23} + P_{13}P_{23}$. Substituting this result in Eq. (3.41) yields

$$|\phi_i\rangle = G_0 \left(V_{\text{NN}}^{i} + V_{3\text{N}}^{(i)} \right) (1 + P)\,|\phi_i\rangle\,. \tag{3.44}$$

We rewrite this equation to

$$|\phi_i\rangle = \left[1 - G_0 V_{\text{NN}}^{i}\right]^{-1} G_0 \left[V_{\text{NN}}^{i} P + V_{3\text{N}}^{(i)}(1 + P)\right] |\phi_i\rangle\,. \tag{3.45}$$

We recognize the factor $\left[1 - G_0 V_{\text{NN}}^{i}\right]^{-1} G_0$ to be the Green's function of channel i, i.e., $G_i = (E - H_0 - V_{\text{NN}}^{i})^{-1}$, which can also be written as $G_i = G_0 + G_0 T_i G_0$. Here, T_i is the two-body transition matrix which is given by the LS equation

$$T_i = V^i_{\mathrm{NN}} + V^i_{\mathrm{NN}} G_0 T_i. \tag{3.46}$$

Substituting the definition of the Green's function and using the relation $G_i V_i = G_0 T_i$ eliminates the two-body potential from Eq. (3.45) such that we find [174]:

$$|\phi_i\rangle = G_0 \big[T_i P + (1 + T_i G_0) V^{(i)}_{3\mathrm{N}} (1 + P) \big] |\phi_i\rangle\,. \tag{3.47}$$

This result provides a set of three iterative equations including three-body forces determining the Faddeev components $|\phi_i\rangle$. As we have stated, they transform into each other by cyclic permutations, thus, it is sufficient to calculate one component and subsequently perform permutations to find the total three-body wave function $|\Phi\rangle$.

Practical implementations of these Faddeev equations need to represent them in a specific basis. A widely-used implementation of the equations is to express them in a momentum-space partial-wave basis, i.e., the same basis as specified in the previous section. For more information on solving the Faddeev equations in a practical way including three-body interactions see, e.g., Refs. [174–176].

After obtaining a solution, the momentum-space representation of the wave function in a partial-wave basis is given by

$$\langle p\, q\, \alpha | \Phi \rangle \equiv \Phi_\alpha(p, q). \tag{3.48}$$

Here also, α indicates the quantum numbers of the partial-wave state for which possible configurations are listed in Appendix A. Note that the angular momentum quantum numbers in α account for the angular dependence, while p and q provide the dependence on the magnitude. These wave functions can now be used in order to calculate observables.

4

FEW-NUCLEON ELECTROMAGNETIC FORM FACTORS

Using high-energy electrons to investigate nuclei offers a clean method to reveal the internal structure of nuclei and the dynamics between nucleons. The relatively weak and well-understood electromagnetic interaction that happens between the electron and the nucleus is perturbative in nature, ensuring the nuclear structure content to be cleanly isolated. This nuclear structure information is contained in the measured cross sections and is given by the so-called form factors. A calculation of these form factors involves both strong-interaction dynamics and electromagnetic nuclear currents, such that a comparison against experimental data provide a good test of our nuclear models. In that sense, electromagnetic reactions are fundamental to our understanding and progress of nuclear models.

This chapter presents a brief theoretical description of the electron-scattering process and a more in-depth analysis of the calculation of two- and three-nucleon form factors. Performed within the framework of chiral EFT. We show the relation between matrix elements and form factors before analyzing the form factors for different NN and 3N interactions. We further extract results for the charge and magnetic radii. Finally, we compare the obtained information on the electromagnetic structure of two- and three-nucleon nuclei to experimental results.

In Section 4.1 we provide a review about elastic electron scattering. First we present a short overview of the experimental and theoretical status of the different few-nucleon form factors. We then continue with a comprehensible classical example of electron scattering from a uniform charge distribution before introducing the Born approximation.

In Section 4.2 we show different nucleon form factor parametrizations and explain the particular choice we make. We employ parametrizations for the proton and the neutron electric and magnetic form factors, which are fit to world electron-nucleon scattering data [177–179]. Chiral expansions of the nucleon form factors exist as well. However, they have been shown to lead to deviations from experiment, even at low momentum transfers, as a result of their slow convergence [180, 181].

Afterwards we discuss the deuteron in detail in Section 4.3, where we begin by stating the the deuteron form factors, characterizing its electromagnetic structure. Then, we relate deuteron matrix elements to these form factors by calculating the relativistic deuteron current. This then leaves us in a position to express the form factors in terms of two-body partial-wave states, defined in Section 3.1.2, and deuteron wave functions. We end the section by showing and discussing results for the form factors.

Three-nucleon systems and their form factors are discussed in Section 4.4, which has the same structure as the deuteron section. The results for the triton and helion include an important addition: they take into account the NLO 2BC. This addition is crucial to achieve a better agreement with experiment for magnetic observables.

We finish the chapter with extracting the radius by calculating the slope of the form factor at zero momentum transfers and present results for the deuteron, the triton, and the helion in Section 4.5.

4.1 Elastic electron scattering

Elastic-electron scattering is a field with a rich history that shaped much of our understanding about the electromagnetic structure of nuclei. It provides us information about long-range physics from low momentum transfer reactions, e.g., the electromagnetic radii and moments, while short-distance parts are investigated by high momentum transfer reactions. Advances in both experiment and theory are necessary to progress our understanding of nuclear structure.

4.1.1 Current experimental and theoretical status

In the introduction, we mentioned the current efforts to measure the proton, the deuteron, and the trinucleon form factors at low momentum transfers to extract precise electromagnetic radii, and hence to gain insights into the proton- and deuteron-radius puzzles. One immediate consequence of an updated proton radius is the influcence on the nucleon form factor paramtetrization, which is an important input in form factor calculations. Such a parametrization should be able to support the updated proton radius. In Section 4.2 we discuss different parametrizations typically employed in nuclear calculations and argue for our particular choice based on these new developments.

Charge and magnetic radii provide information about the zero-momentum-transfer region only, while experimental observations capturing the form factor structure at finite momentum transfers provide additional information on the electromagnetic structure for the deuteron and trinucleons. The majority of experimental work on scattering off few-nucleon nuclei consists of rather old data as there have been almost no new cross section measurements in the last two decades. Despite this scarcity of new data, the quality of the existing data is sufficient to check against theoretical calculations.

There exists an extensive amount of e-d scattering data covering a large range of momentum transfers. The information on e-d scattering is extensive because it is also used to extract neutron form factors, as free neutron targets are nonexistent. Data points at low and intermediate momentum transfers are most accurate and reach an accuracy of the order of 1% [76]. The charge and quadrupole form factor are determined up to a momentum transfer of ~ 7 fm^{-1} [76], extending the data beyond the first minimum of the charge form factor.[1] On the other hand, the magnetic form factor is known to a much larger momentum transfer of ~ 9 fm^{-1} [182]. We will compare our results against deuteron form factor data up to a momentum transfer of 6 fm^{-1}.

As the triton is radioactive, data for it is fairly limited because safety regulations complicate experiments. Therefore, only a small range of data up to a momentum transfer of

---

[1] A form factor is displayed as a function of the momentum transfer in terms of its absolute value on a logarithmic scale. The minimum is the region where the form factor approaches zero and eventually flips sign. This results in a characteristic 'dip' or minimium.

~ 5.7 fm^{-1} [59] is available for the charge and magnetic form factor. Nonetheless, the first minimum is covered in both cases. Experiments on ^{3}He are less challenging, resulting in data points reaching higher momentum transfers. The charge form factor is known up to ~ 10 fm^{-1} and the magnetic form factor up to ~ 6 fm^{-1} [59], again extending beyond the first minimum for both. To present the available scattering data and compare to theory results, we will use a parametrization for the three-nucleon form factors given by Ref. [75]. The authors perform a global fit to the world data and emphasize that the fit contains the full experimental information for the three-body system. One exception to the parametrization is a new measurement for the helion form factors at high momentum transfers of 5 fm^{-1} $\leq q \leq$ 7.8 fm^{-1} [183]. For a detailed review on elastic electron scattering on light nuclei and an analysis of the world data see, e.g., Refs. [59, 76].

As we mentioned in the introduction, the SNPA has been very successful in describing electromagnetic form factors and properties, but fails to provide a satisfacotry microscopic understanding. Therefore, we will only focus on developments from chiral EFT. An extensive overview of conventianl applications to examine the electromagnetic structure of light nuclei, and specifically the electromagnetic form factors, is given in Ref. [80].

The tremendous progress of chiral EFT over the last two decades resulted in several consistent electromagnetic form factor calculations for few-nucleon nuclei. Pioneering investigations of charge and current operators to calculate electromagnetic form factors of the deuteron up to N^{2}LO were introduced Phillips and Cohen [167] , Walzl and Meißner [184], and Phillips [185, 186]. They used a chiral description for the single-nucleon form factors which limited the agreement with experiment to a momentum transfer up to ~ 2 fm^{-1}. This limited range of agreement could be circumvented by examining form factor ratios, effectively factoring out the single-nucleon dependence. Instead of accounting for single-nucleon form factors by means of a chiral description, a parametrization which is fit to electron-nucleon scattering data can be used [71]. Employing such a parametrization shows good agreement with experiment for deuteron form factors up to a momentum transfer of ~ 3 fm^{-1} [70, 181, 187, 188]. For example, the most recent precision calculation of the deuteron charge form factor performs a calculation at fifth order in the chiral expansion including state-of-the-art nucleon form factors, to subsequently extract a value of the neutron charge radius [72]. This example shows again the interdependence of the nucleon and nuclear electromagnetic structure. Most 2BC operators up to N^{3}LO are mainly of isovector type, i.e., they only have a nonvanishing contribution for nuclei with nonzero isospin $T \neq 0$. As a result, they do not provide corrections to deuteron electromagnetic observables, given that the deuteron is isoscalar, i.e., $T = 0$. Therefore, to study their impact in more detail it is necessary to investigate nuclei with three or more nucleons. In this regard, Piarulli *et al.* [70] provide a comprehensive set of results for the electromagnetic form factors of three-nucleon nuclei with charge and current operator at the N^{3}LO level, and with NN [126, 189] interactions at N^{3}LO and 3N interactions [129] at N^{2}LO. Their results show a satisfactory description of the form factors at low momentum transfers with crucial contributions from 2BCs. Recent new results for the magnetic form factor of two- and three-nucleon systems can be found in [190], where the authors explicitly include Δ intermediate states in the interaction and at the OPE level for the current operators, pushing the development of chiral EFT further. This short overview sums up most of the present work in the new and active field of electromagnetic structure investigations within the chiral EFT framework. We refer the reader to the reviews [71] and [81] which focusses only on few-nucleon nuclei and light nuclei, respectively.

4.1.2 Classical electron scattering

To obtain a first elementary description of electron scattering we make an analogy with light scattered off an object. Optics determines the amplitude of light scattered off a solid cylindrically or spherically shaped object by calculating the interference of the outgoing waves. The resulting interference pattern, far away from the scattering event, contains information about the shape of the object. Similarly, electrons detected far away from the scattering event carry information about the magnetic and electric charge distribution of the target.

According to the particle-wave duality postulated by de Broglie, every particle has a wave-like structure with wavelength [191]

$$\lambda = \frac{h}{p}, \tag{4.1}$$

where h is the Planck constant and $p = |\mathbf{p}|$ the particles momentum. Hence, an electron could be described by a plane wave with momentum p. As a crude simplification, we consider the nucleus as a solid sphere with a spherical charge distribution. An electron scattered off a nucleus then has an analog interpretation as light scattered off a spherical object. The outgoing electron plane waves interfere and determine the resulting net outgoing wave. This outgoing wave consists of adding the contributions from each infinitesimal element of the sphere weighted by an exponential factor. The scattering amplitude will, therefore, be proportional to the total charge present. We determine the amplitude of the detected electron wave, far away from the scattering event, by summing each element of the sphere weighted with a factor $\exp(i\mathbf{q}\cdot\mathbf{x})$,

$$\mathcal{A}_{\text{el}} = \int_{\text{nucleus}} \mathrm{d}\mathbf{x}\, \rho_{\text{ch}}(x)\, e^{i\mathbf{q}\cdot\mathbf{x}}, \tag{4.2}$$

where $\mathbf{q} = \mathbf{p}_1 - \mathbf{p}_2$ represents the momentum transfer with $\mathbf{p}_1$ and $\mathbf{p}_2$ the incoming and outgoing particle momentum, respectively. The expression for the amplitude demonstrates that measured electrons provide the Fourier transform of the target charge distribution, denoted by $\rho_{\text{ch}}(x)$. The left panel of Fig. 4.1 sketches elastic electron scattering from a spherical charge distribution in the classical Coulomb picture.

We can make some basic observations about the Fourier transform of the target charge distribution from this simple model of the nucleus. Let a be the radius of the sphere, the solution of Eq. (4.2) is then given by

$$\begin{aligned}\mathcal{A}_{\text{el}} &= \int_0^a \mathrm{d}r\, r^2 \int \mathrm{d}\hat{\mathbf{r}}\, e^{iqr\cos\theta_r} \\ &= \frac{4\pi a^3}{3}\left[\frac{3j_1(qa)}{qa}\right],\end{aligned} \tag{4.3}$$

where $j_n(x)$ is the spherical Bessel function. The factor between brackets is the so-called form factor, it represents the Fourier transform of the target's charge distribution. From the result we see that the first zero of the Bessel function, occuring around 1.22π, is related to the radius of the uniform sphere, i.e., $qa \sim 1.22\pi$. Therefore, one can extract an estimate for the radius from scattering experiments by adopting this simple model of the nucleus. A quantum mechanical analysis consists of replacing the charge density in Eq. (4.2) with the appropriate expectation value of the charge operator or transition density of the target. The right panel of Fig. 4.1 shows a sketch of the absolute form factor squared for two different

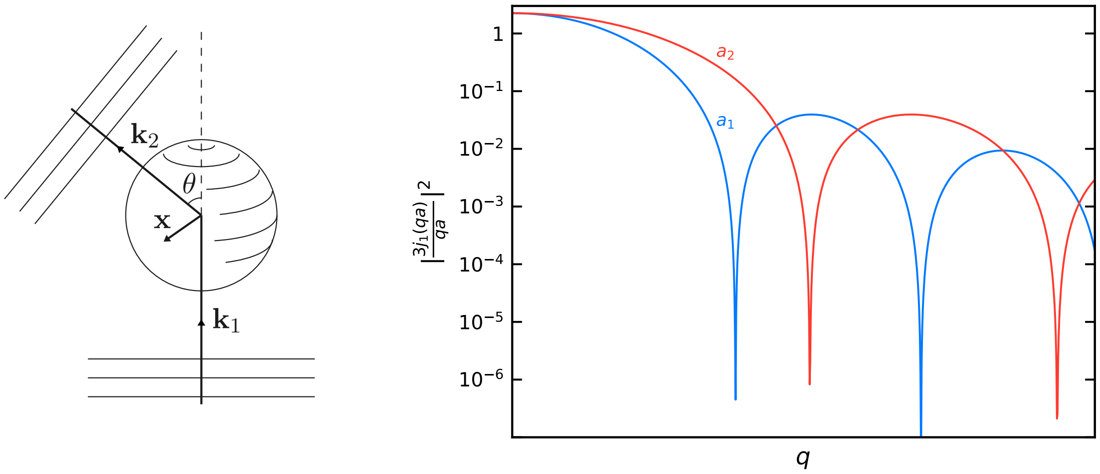

Figure 4.1: Left panel: Sketch of elastic electron scattering off a uniform spherical charge distribution in the classical Coulomb picture. Electrons are denoted by plane waves, where $\mathbf{k}_1$ represents the incoming wave, $\mathbf{k}_2$ the outgoing wave, and θ the angle between them. An arbitrary element on the sphere is shown by $\mathbf{x}$. Right panel: The absolute value squared of the form factor as a function of the magnitude of the momentum transfer. The blue and red lines correspond to form factors with different values for the radius a, in this case $a_1 > a_2$. Note the characteristic minima of the form factor as well as the orders-of-magnitude over which it runs.

radii. Even though we only consider a simple model, the result displays important qualitative features, like the minima, that are also found for more complex systems like nuclei.

From Eq. (4.1) follows that high-energy electrons are needed to obtain a small enough wavelength to probe nuclei. To resolve charge densities of the order of the typical nuclear dimension, i.e.,

$$1 \text{ fm} \lesssim \lambda \lesssim 10 \text{ fm}, \tag{4.4}$$

relativistic electrons are needed,

$$125 \text{ MeV} \lesssim E_\mathrm{e} \lesssim 1240 \text{ MeV}, \tag{4.5}$$

where the electron energy is given by $E_\mathrm{e} = p$.

In the next section, we formalize the scattering event and present a quantum field description, relating form factors to nuclear matrix elements, which we can subsequently calculate and compare to experiment.

4.1.3 Born approximation

Describing the scattering of an electron off a nucleus to lowest order, in a perturbative description of scattering, is done by the so-called *Born* or *one-photon-exchange approximation*. Because of the small magnitude of the electromagnetic coupling constant, we expect this to be a good approximation of the scattering event. Figure 4.2 illustrates the general electron scattering process in the one-photon-exchange picture. The incoming and scattered electron have four-momentum $k_\mu = (\epsilon, \mathbf{k})$ and $k'_\mu = (\epsilon', \mathbf{k}')$, respectively, where ϵ is the energy and $\mathbf{k}$ the momentum. Both incoming and outgoing electrons are accurately described by plane waves, this assumption is valid for the outgoing wave because the proton number, Z, in two-

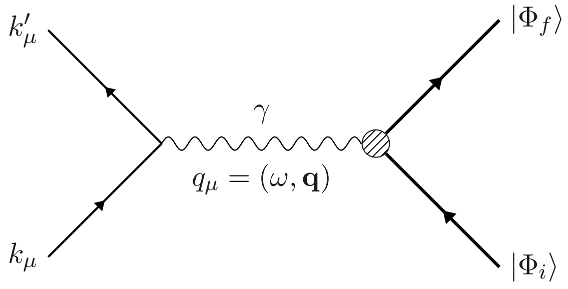

Figure 4.2: Electron scattering diagram of the Born or one-photon-exchange approximation. An incident electron (*thin solid line*) with initial four-momentum $k_\mu = (\epsilon, \mathbf{k})$ is scattered to four-momentum $k'_\mu = (\epsilon', \mathbf{k}')$. In the process a single virtual photon γ (*oscillating line*) with four-momentum $q_\mu = (\omega, \mathbf{q})$ is exchanged with the nucleus (*thick solid line*) represented by $|\Phi_i\rangle$ and $|\Phi_f\rangle$ for the initial and final state, respectively. The hatched circle represents the nuclear current.

and three-nucleon systems is small such that $Z\alpha \ll 1$.[2] Therefore, this approximation is also called the plane-wave Born approximation (PWBA). The exchange of the virtual photon transfers a four-momentum $q_\mu = (\omega, \mathbf{q})$ to the nucleus, changing its initial state $|\Phi_i\rangle$ with momentum $p_\mu = (E, \mathbf{p})$ to a final state $|\Phi_f\rangle$ with $p'_\mu = (E', \mathbf{p}')$. The virtual photon couples with charge and current densities of the target particle. The scattering amplitude of this process is given by multiplying the electron and nuclear current:

$$\mathcal{M} = \frac{ie^2}{q_\mu^2} \left[\bar{u}(k', \tau')\gamma^\mu u(k, \tau)\right] \langle \Phi_f(p'_\mu)|J_\mu|\Phi_i(p_\mu)\rangle \,, \tag{4.6}$$

where $u(k, \tau)$ ($\bar{u}(k', \tau')$) represents the state of the incoming (outgoing) electron with momentum k (k') and helicity τ (τ'), $|\Phi_i\rangle$ ($|\Phi_f\rangle$) the initial (final) state of the nucleus with four-momentum p_μ (p'_μ), and γ^ν Dirac matrices.

According to momentum conservation we have $q_\mu = k_\mu - k'_\mu = p_\mu - p'_\mu$, resulting in an energy transfer $\omega = \epsilon - \epsilon'$ and a three-momentum transfer $\mathbf{q}$, with its magnitude given by $|\mathbf{q}| = \sqrt{k^2 + k'^2 - 2kk' \cos\theta_\mathrm{e}}$, where θ_e is the angle between the initial and final electron. Because of the high electron-beam energies, the electrons are relativistic such that the four-momentum transfer squared is given by $q_\mu q^\mu = q_\mu^2 = 4\epsilon\epsilon' \sin^2\theta_\mathrm{e}/2$, i.e., the electron mass becomes negligible. The only restriction on the transfer momentum is that it has to be space-like, i.e., $q_\mu^2 = \omega^2 - \mathbf{q}^2 < 0$. This has the advantage that both the energy transfer ω and the momentum transfer $\mathbf{q}$ of the virtual photon can be varied independently, mapping out the entire electromagnetic response of the target. Experiments with real photons, on the other hand, only allow a single momentum transfer since the mass of the real photon is zero, leading to $q_\mu q^\mu = q_\mu^2 = \omega^2 - \mathbf{q}^2 = 0$. In elastic scattering there is no energy transferred during the process, i.e., $\omega = \epsilon - \epsilon' = 0$, which implies that the nuclear state remains unexcited. In this thesis we only study elastic processes, such that we can leave out the ω dependence in the following.

The differential cross section for the process (e, e') in the one-photon-exchange approximation for an unpolarized and unobserved target in the lab frame is obtained by squaring

---

[2] Nuclei with higher proton numbers have a large effect on the scattered particle. Taking into account this influence is done by the distorted-wave Born approximation (DWBA).

Eq. (4.6), averaging over initial spins and summing over final spins [77, 78]:

$$\frac{\mathrm{d}\sigma}{\mathrm{d}\Omega_\mathrm{e}} = 4\pi\sigma_\mathrm{M} f_\mathrm{rec}^{-1}\left[\frac{Q_\mu^4}{q^4}F_\mathrm{L}^2(Q) + \left(\frac{Q_\mu^2}{2q^2} + \tan^2\frac{\theta_\mathrm{e}}{2}\right)F_\mathrm{T}^2(Q)\right], \tag{4.7}$$

where $q = |\mathbf{q}|$ and we defined the negative of the momentum transfer as $Q_\mu^2 = -q_\mu^2$ for convenient notation. The Mott cross section σ_M and the recoil term f_rec are given by

$$\sigma_\mathrm{M} = \left[\frac{\alpha\cos\theta_\mathrm{e}/2}{2\epsilon\sin^2\theta_\mathrm{e}/2}\right]^2, \tag{4.8}$$

and

$$f_\mathrm{rec} = 1 + \frac{2\epsilon}{M_A}\sin^2\theta_\mathrm{e}/2, \tag{4.9}$$

respectively. Here, M_A is the mass of the target nucleus with mass number A. Note that the cross section presented this way is general, i.e., it does not yet depend on internal degrees of freedom of the target nucleus.

The functions $F_\mathrm{L}^2(Q)$ and $F_\mathrm{T}^2(Q)$ are the longitudinal and transverse form factors, sometimes called structure functions, and contain all the information on the distribution of the nuclear electromagnetic current density. As they only depend on the transfer momentum and not on the angle of the scattering event, they can be extracted by plotting the cross section as a function of $\tan^2\frac{\theta_\mathrm{e}}{2}$ for a fixed value of Q. This method of obtaining the form factors is called the *Rosenbluth separation*, and has been the standard method to extract the form factor. However, as mentioned, modern evaluations of cross sections use a parametrization to extract form factors from scattering data.

4.2 Nucleon form factors

As discussed before, performing calculations without any nucleon substructure, hence regarding the proton and neutron as pointlike, would require to factor out the nucleon structure from experimental results before any meaningful comparison can be made. Therefore, including nucleon form factors in the charge and current operator provides important corrections to the operator.

To express the amplitude of electron-nucleon scattering, we replace the nuclear current in Eq. (4.6) by the nucleonic current:

$$\langle\Phi_f|J^\mu|\Phi_i\rangle \to ie\,\bar{v}(p', s')\Gamma^\mu v(p, s), \tag{4.10}$$

with v ($\bar{v}$) a Dirac spinor representing the initial (final) nucleon, p (p') the initial (final) momentum, and s (s') the initial (final) spin four-vector. The vertex function, Γ^μ, in its most general form for particles with spin 1/2, satisfying Lorentz invariance and current conservation is given by

$$\Gamma^\mu = \gamma^\mu F_1(Q^2) + \kappa_j\frac{i\sigma^{\mu\nu}q_\nu}{2m_N}F_2(Q^2), \tag{4.11}$$

where m_N represents the nucleon mass, κ_j, with $j =$ proton, neutron,[3] the anomalous magnetic moment, γ^μ and $\sigma^{\mu\nu} = i/2[\gamma^\mu, \gamma^\nu]$ the Dirac matrices. The Dirac and Pauli form factors

---

[3] From now on we denote the proton and neutron with a subscript p and n, respectively. For example, the anomalous magnetic moment for the proton then becomes κ_p.

F_1 and F_2, respectively, parametrize the electromagnetic nucleon structure information in invariant functions which depend on the momentum transfer and are linear combinations of the longitudinal and transverse form factors given in Eq. (4.7). In the limit of zero momentum transfer these form factors equal $F_{1\mathrm{p}} = 1$, $F_{2\mathrm{p}} = \kappa_p$ and $F_{1\mathrm{n}} = 0$, $F_{2\mathrm{n}} = \kappa_n$ and coincide with the total charge an anomalous magnetic moment of the nucleons (where we have used the notation $\kappa_j F_2 \equiv F_{2j}$).

In e-p or electron-neutron (e-n) scattering it is conventional to then express the differential cross section for an unpolarized and unobserved target in terms of the Dirac and Pauli form factors:

$$\frac{\mathrm{d}\sigma}{\mathrm{d}\Omega_\mathrm{e}} = \sigma_\mathrm{M} f_\mathrm{rec}^{-1} \left[F_1^2(Q^2) + \tau \left(F_2^2(Q^2) + 2[F_1(Q^2) + F_2(Q^2)]^2 \tan^2 \frac{\theta_\mathrm{e}}{2} \right) \right]. \tag{4.12}$$

Note that this expression represents a specific case of Eq. (4.7). More commonly the nucleon structure is given in terms of the electric (E) and magnetic (M) Sachs form factors G, which are linear combinations of F_1 and F_2:

$$G_{\mathrm{E(p,n)}}(Q^2) = F_{1\mathrm{(p,n)}}(Q^2) - \tau F_{2\mathrm{(p,n)}}(Q^2), \tag{4.13a}$$

$$G_{\mathrm{M(p,n)}}(Q^2) = F_{1\mathrm{(p,n)}}(Q^2) + F_{2\mathrm{(p,n)}}(Q^2), \tag{4.13b}$$

with $\tau = \frac{Q^2}{4m_N^2}$. They are normalized such that $G_{\mathrm{Ep}}(0) = Z$, $G_{\mathrm{En}}(0) = 0$, and $G_{\mathrm{M(p,n)}}(0) = \mu_{\mathrm{(p,n)}}$, in units of μ_N. The Sachs form factors are used because they simplify the scattering cross section expression such that it is more straightforward to analyze experimental data as it cancels the interference term in Eq. (4.12):

$$\frac{\mathrm{d}\sigma}{\mathrm{d}\Omega_e} = \sigma_\mathrm{M}\, f_\mathrm{rec}^{-1} \frac{1}{1+\tau} \left[G_\mathrm{E}^2(Q^2) + \frac{\tau}{\epsilon} G_\mathrm{M}^2(Q^2) \right], \tag{4.14}$$

with the polarization of the virtual photon defined as $\epsilon = \left[1 + 2(1+\tau)\tan^2(\theta_\mathrm{e}/2)\right]^{-1}$. These form factors are then extracted from electron scattering data with the Rosenbluth separation.

Another combination of nucleon form factors often used in this work are the isoscalar and isovector, electric and magnetic Sachs form factors. They consist of the sum and difference of the proton and neutron form factors, and are given by

$$G_{\mathrm{E/M}}^S = G_{\mathrm{E/Mp}} + G_{\mathrm{E/Mn}}, \tag{4.15a}$$

$$G_{\mathrm{E/M}}^V = G_{\mathrm{E/Mp}} - G_{\mathrm{E/Mn}}, \tag{4.15b}$$

where the Q^2 dependence is left out for readability. Their normalization follows from the form factors in Eq. (4.13a), i.e., $G_\mathrm{E}^S(0) = G_\mathrm{E}^V(0) = 1$, $G_\mathrm{M}^S(0) = 0.880\mu_N$, and $G_\mathrm{M}^V(0) = 4.706\mu_N$ in units of the nuclear magneton μ_N.

Many experiments have been performed to measure nucleon cross sections and deduce from them the internal structure of the neutron and the proton in terms of Sachs form factors, for a review see Ref.[192]. The measurement of the proton form factors can be performed on free protons. For neutrons, however, experiments with light nuclei have to be carried out, e.g., ^{2}H or ^{3}He, to extract electromagnetic form factors. Experiments with deuteron targets require theoretical knowledge about the deuteron wave function, leading to sizable uncertainties in the neutron form factor [192]. Besides, neutron form factors are almost zero and much smaller

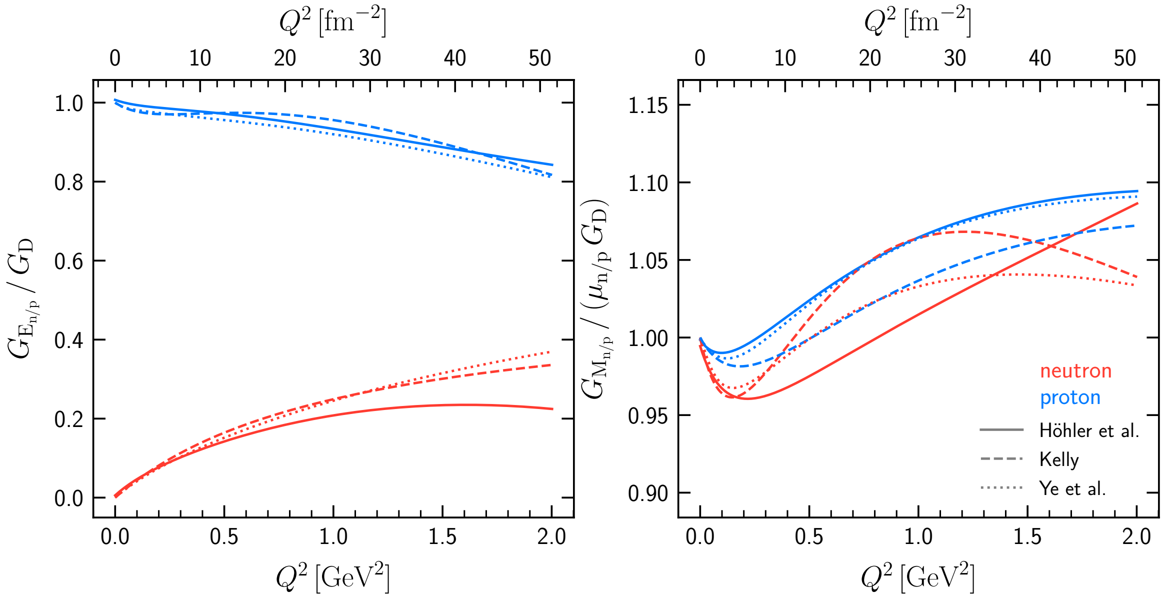

Figure 4.3: Parametrizations of the Sachs nucleon form factors normalized by the dipole form factor as a function of Q in GeV^2 (bottom x-axis) and fm^{-2} (top x-axis). Red always represents the neutron form factor (n), while blue shows the proton form factor (p). Left panel: The neutron and proton electric Sachs form factor $\mathrm{G}_{\mathrm{E}_{\mathrm{n/p}}}(Q^2)$. Right panel: The neutron and proton magnetic Sachs form factor $\mathrm{G}_{\mathrm{M}_{\mathrm{n/p}}}(Q^2)$. The three parametrizations are given by Höhler *et al.* [177] (*solid line*), Kelly [178] (*dashed line*), and Ye *et al.* [179] (*dotted line*).

than the proton contribution to the cross section, such that they are more difficult to obtain. However, the low Q region, relevant for chiral EFT, is known with sufficient accuracy for all form factors to be used in calculations.

By constructing parametrizations of the Sachs form factors, all scattering information is incorporated into practical objects. Commonly, nuclear theory analysis use two well-known nucleon form factor parametrizations, one from Höhler *et al.* [177] from 1976 which uses a dispersion theory analysis, and the second one from Kelly [178] from 2004 which uses a fraction with a polynomial in Q^2 in both numerator and denominator. Since the publication of these parametrizations, there has been much experimental as well as theoretical progress over the last two decades. For example, recently experiments with double-polarization are realized where beam or target or both can be polarized to make precise measurements [192]. This allows to skip the traditional Rosenbluth separation to extract the independent form factors, making the analysis less prone to errors and improving the precision. In addition, theoretical investigations understood the importance of the two-photon exchange process to have a significant impact [179, 192].

These new developments are not yet taken into account in the two analysis mentioned above. As the nucleon form factors represent important corrections to the charge and current operator, we would like to include these improvements. In order to have an up-to-date result with a recent analysis of electron-nucleon scattering data we include the recent parametrization performed by Ye *et al.* [179] in the nuclear form-factor calculations.[4] The authors in that work include two-photon exchange corrections as well as new high-precision measurements in their bounded polynomial z-expansion fit of the global data. Furthermore, they constrain

---

[4] This parametrization does not yet include the elastic electron scattering results from Ref. [62]

the fit to reproduce universally accepted nucleon radii, as such allowing to insert the newly recommended proton radius, and they provide reliable uncertainty estimates. The nucleon radii values they adopt are specified by: $(r_{\mathrm{E}}^{n})^2 = -0.1161(22)$ fm^2 [193], $r_{\mathrm{E}}^{p} = 0.879$ fm [60], $r_{\mathrm{M}}^{n} = 0.864$ fm [193], $r_{\mathrm{M}}^{p} = 0.851$ fm [193]. As an additional benefit, the fitting parameters and the uncertainty parametrization are made available in the additional information to their publication [179].

A comparison of the three-nucleon form-factor parametrizations we discussed, can be seen in Fig. 4.3. In order to amplify the differences between them, they are normalized by the dipole form factor:

$$G_{\mathrm{D}}(Q^2) = (1 + Q^2/\Lambda)^{-2}, \tag{4.16}$$

with $\Lambda = 0.71$ GeV^2. The solid line represents the Höhler *et al.* parametrization [177], while the dashed and dotted lines show the Kelly [178] and Ye *et al.* [179] parametrization, respectively. The left panel shows G_{Ex} for the neutron (red), $\mathrm{x} = \mathrm{n}$, and the proton (blue), $\mathrm{x} = \mathrm{p}$, and the right panel shows G_{Mx} for both. In the region of interest to this work, $0 \leqslant Q^2 \leqslant 36$ fm^{-2}, the different parametrizations for electric Sachs form factors show similar behavior, except for the neutron form factor Höhler *et al.* parametrization. For G_{Mx}, the three form factors show more variation, where the Höhler *et al.* parametrization for the neutron form factor (red solid line) deviates most compared to the other.

4.3 DEUTERON FORM FACTORS

We now address the calculation of nuclear form factors and discuss them in detail. The electromagnetic structure functions of the deuteron, that enter the cross-section expression, are parametrized into three form factors. The charge, quadrupole and magnetic form factors and are related to the two-body partial-wave expansion of the charge and current operator matrix elements, presented in Chapter 3. We show this relation in Section 4.3.1, by expressing the current in terms of a spherical basis and by considering a relativistic treatment of the deuteron current. In Section 4.3.2 we present the final form factor expressions used in numerical calculations, and in Section 4.3.3 we briefly outline the computational methods. We end this section by showing and discussing results for the deuteron form factors in Sections 4.3.4 and 4.3.5.

The Born approximation provides a general expression for the cross section of an unpolarized and unobserved target, as defined in Eq. (4.7). Since the deuteron has $S = 1$, it is more convenient to rewrite the general scattering cross section as:

$$\frac{\mathrm{d}\sigma}{\mathrm{d}\Omega_{\mathrm{e}}} = 4\pi\sigma_{\mathrm{M}} f_{\mathrm{rec}}^{-1}\left[A(Q) + B(Q)\,\tan^2\frac{\theta_{\mathrm{e}}}{2}\right], \tag{4.17}$$

where $A(Q)$ and $B(Q)$ define the so-called deuteron structure functions. Because of the integral spin there are three independent form factors which completely describe the electromagnetic structure. The deuteron structure functions can be expressed as linear combinations of a charge (G_{C}), a magnetic (G_{M}) and a quadrupole (G_{Q}) form factor:

$$A(Q) = G_{\mathrm{C}}^2(Q) + \frac{2}{3}\eta_{\mathrm{d}} G_{\mathrm{M}}^2(Q) + \frac{8}{9}\eta_{\mathrm{d}}^2 G_{\mathrm{Q}}^2(Q) \tag{4.18}$$

and

$$B(Q) = \frac{4}{3}\eta_\mathrm{d}(1+\eta_\mathrm{d})G_\mathrm{M}^2(Q), \tag{4.19}$$

with $\eta_\mathrm{d} = Q^2/(4M_\mathrm{d}^2)$, where M_d represents the deuteron mass. These three form factors offer a more physical choice than the structure functions. The charge and quadrupole form factors contain information about the distribution of charge and its shape, while the magnetic form factor provides information on the magnetization density. As explained before, experimental determination of the structure functions $A(Q)$ and $B(Q)$ uses the Rosenbluth technique to separate them. Because $A(Q)$ consists of three form factors, it is very difficult to separate charge and quadrupole contributions from each other. Such a separation can be done if one performs polarization experiments where the incoming electron beam, the deuteron target, or both are polarized. On the other hand, theoretical calculations can easily obtain the linear combination defined in Eq. (4.18) and compare these results to experiment, as done in, e.g., Ref. [70]. However, we only consider $G_\mathrm{C}(Q)$ and $G_\mathrm{Q}(Q)$ separately.

4.3.1 From matrix elements to form factors

In this section we connect the form factors, which appear in the expression of the cross section, to matrix elements of the charge and current operator. Conventionally, this is done by making a multipole expansion of the operators to then obtain reduced matrix elements by applying the *Wigner-Eckart theorem*, see, e.g., Refs. [77, 78, 81]. This approach is mainly carried out to exploit nuclear angular momentum and parity selection rules. However, we proceed without calculating the multipole expansion of the charge and current operator and directly evaluate the current operators between deuteron wave functions. Of course, multipole expanded reduced matrix elements can be related back to common matrix elements of current operators [77, 80].

To express the charge, quadrupole, and magnetic form factors as matrix elements of the current operator J^μ, we start by expressing the current in a spherical basis:

$$J_{\lambda_\gamma} = J_\mu \epsilon^\mu_{\lambda_\gamma}, \tag{4.20}$$

with the spherical four-vector states given by

$$\epsilon^\mu_{\lambda_\gamma} = \begin{cases} (0,\pm1,-i,0)/\sqrt{2} & \lambda_\gamma = \pm 1 \\ (0,0,0,1) & \lambda_\gamma = 0 \end{cases}. \tag{4.21}$$

Calculations are carried out in the Breit frame,[5] where the initial and final deuteron momentum are given by

$$P = (P_0, -\frac{1}{2}\mathbf{Q}), \qquad P' = (P_0, \frac{1}{2}\mathbf{Q}), \qquad P_0 = \sqrt{M_\mathrm{d}^2 + \frac{1}{4}Q^2}, \tag{4.22}$$

with $\mathbf{Q}$ the momentum transfer. In addition, we choose $\mathbf{Q}$ along the positive z-direction.

We define the matrix elements of the current operator in the spherical basis as

$$G^{\lambda_\gamma}_{\lambda'\lambda}(P', P) \equiv g_{\mu\nu} G^\mu_{\lambda'\lambda}(P', P)\epsilon^\nu_{\lambda_\gamma} = \langle P'\lambda' | J_{\lambda_\gamma} | P\lambda \rangle \,, \tag{4.23}$$

---

[5] For elastic reactions, $A + B \to A + B$, there is an inertial frame in which A recoils with its momentum reversed, i.e., $p_A = -p'_A$. This frame is called the Breit frame. Often, the scattering process kinematics are best understood in this reference frame.

where $|P\lambda\rangle$ and $|P'\lambda'\rangle$ are the initial and final deuteron states with helicities λ and λ', respectively. The helicities are understood to be the projection of the particle spin on the direction of the particles momentum. Because there are three form factors, there are only three independent matrix elements. We choose these matrix elements, which we denote by $g_{\pm 1,0}$, to be

$$g_{-1} \equiv \frac{1}{2M_\mathrm{d}} \langle P'\lambda' = -1|\rho|P\lambda = -1\rangle = \frac{1}{2M_\mathrm{d}} G^0_{-1-1}(P', P), \tag{4.24a}$$

$$g_0 \equiv \frac{1}{2M_\mathrm{d}} \langle P'\lambda' = 0|\rho|P\lambda = 0\rangle = \frac{1}{2M_\mathrm{d}} G^0_{00}(P', P), \tag{4.24b}$$

$$g_{+1} \equiv \frac{1}{2M_\mathrm{d}} \langle P'\lambda' = 1|j_{+1}|P\lambda = 0\rangle = \frac{1}{2M_\mathrm{d}} G^{+1}_{10}(P', P). \tag{4.24c}$$

A relativistic treatment of the deuteron current, taking into account Lorentz-invariance, current conservation, parity and time-reversal invariance, demonstrate that the electromagnetic deuteron current matrix elements, $G^\mu_{\lambda'\lambda}(P', P)$, are also equal to [194, 195]:

$$\begin{aligned} G^\mu_{\lambda'\lambda}(P', P) = &- \left[G_1(Q)\xi^*_{\lambda'} \cdot \xi_\lambda - G_3(Q) \frac{\xi^*_{\lambda'} \cdot q \xi_\lambda \cdot q}{2M_\mathrm{d}^2} \right] (P^{\mu\prime} + P^\mu) \\ &- G_2(Q)(\xi^\mu_\lambda \xi^*_\lambda \cdot q - \xi^{\mu*}_\lambda \xi_\lambda \cdot q), \end{aligned} \tag{4.25}$$

where ξ_λ and $\xi_{\lambda'}$ are the incoming and outgoing deuteron polarization four-vectors, q the magnitude of the four-momentum transfer as defined before, and $G_i(Q)$, with $i = 1, 2$, and 3, are form factors which are functions of Q only. The deuteron polarization four-vectors in the Breit frame are defined by

$$\xi_\lambda = \begin{cases} (0, \pm 1, -i, 0)/\sqrt{2} & \lambda = \pm 1 \\ (-Q/2, 0, 0, P_0)/M_\mathrm{d} & \lambda = 0 \end{cases}, \tag{4.26}$$

$$\xi'_{\lambda'} = \begin{cases} (0, \mp 1, -i, 0)/\sqrt{2} & \lambda' = \pm 1 \\ (Q/2, 0, 0, P'_0)/M_\mathrm{d} & \lambda' = 0 \end{cases}. \tag{4.27}$$

The scalar functions $G_i(Q^2)$ in Eq. (4.25), with $i = 1, 3$, can be related to the more physical charge and quadrupole form factors by the following linear combinations:

$$G_\mathrm{C}(Q) = G_1(Q) + \frac{2}{3}\eta_\mathrm{d} G_Q, \tag{4.28}$$

$$G_\mathrm{M}(Q) = G_2(Q), \tag{4.29}$$

$$G_\mathrm{Q}(Q) = G_1(Q) - G_2(Q) + (1 + \eta_\mathrm{d})G_3(Q). \tag{4.30}$$

The result in Eq. (4.25) allows us to match the invariant scalar functions to the deuteron matrix elements defined in Eq. (4.24), such that we find:

$$g_{-1} = \sqrt{1 + \eta_\mathrm{d}}\, G_1(Q), \tag{4.31a}$$

$$g_0 = \sqrt{1 + \eta_\mathrm{d}}\, \left[(1 + 2\eta_\mathrm{d})\, G_1(Q) - 2\,\eta_\mathrm{d}\, G_\mathrm{M}(Q) + 2\,\eta_\mathrm{d}\,(1 + \eta_\mathrm{d})\, G_3(Q) \right], \tag{4.31b}$$

$$g_{+1} = \sqrt{\eta_\mathrm{d}(1 + \eta_\mathrm{d})}\, G_\mathrm{M}(Q). \tag{4.31c}$$

Inverting these relations and using the linear combinations from (4.28)-(4.30) yields expressions for the electromagnetic form factors in terms of the independent deuteron matrix elements:

$$G_{\mathrm{C}}(Q) = \frac{1}{3\sqrt{1+\eta_{\mathrm{d}}}}(g_0 + 2g_{-1}), \tag{4.32}$$

$$G_{\mathrm{Q}}(Q) = \frac{1}{2\eta_{\mathrm{d}}\sqrt{1+\eta_{\mathrm{d}}}}(g_0 - g_{-1}), \tag{4.33}$$

$$G_{\mathrm{M}}(Q) = \frac{1}{\sqrt{\eta_{\mathrm{d}}(1+\eta_{\mathrm{d}})}} g_{+1}. \tag{4.34}$$

The electromagnetic form factors defined in this way are normalized by the charge, magnetic and quadrupole moment of the deuteron

$$G_{\mathrm{C}}(0) = 1, \qquad G_{\mathrm{Q}}(0) = M_{\mathrm{d}}^2 Q_{\mathrm{d}}, \qquad G_{\mathrm{M}}(0) = \frac{M_{\mathrm{d}}}{m_N}\mu_{\mathrm{d}}. \tag{4.35}$$

In this chapter, we focus on the analysis of electromagnetic form factors, while the next chapter is devoted to study static moments.

To summarize, we discussed the electromagnetic form factors of the deuteron, that make up the structure functions, Eqs. (4.18) and (4.19), to specific linear combinations of deuteron matrix elements. We achieved this by expressing the current operator in terms of a spherical basis to then define three independent matrix elements, Eq. (4.24). A relativistic treatment of the deuteron current determines three invariant scalar functions $G_i(Q)$ which in turn could be related to the independent matrix elements in (4.31a)-(4.31c). This finally resulted in expressing $G_{\mathrm{C}}(Q)$, $G_{\mathrm{Q}}(Q)$ and $G_{\mathrm{M}}(Q)$ in terms of linear combinations of the independent matrix elements in (4.32)-(4.34). With these expression it is clear how to proceed to calculate the electromagnetic form factors, which we will present below.

4.3.2 Two-body partial-wave matrix elements

In previous chapters, we defined the two-body partial-wave basis in Section 3.1.2 as well as showed the expansion of a general current operator in this basis in Section 3.1.3. Now that we have the relation between the form factors and the matrix elements given in (4.32)-(4.34), we can use the general expansion as a starting point to find expressions for the form factors in terms of the partial-wave basis. In the following, we show the result for each form factor, starting with the charge form factor to then present the expression for the quadrupole form factor and finish with the magnetic form factor.

Charge form factor

The charge form factor provides information about the distribution of electric charge inside the nucleus. We present here the analytic result, obtained by using the one-body charge operator which we presented in Section 2.4.3. Substituting the two-body partial-wave state and the deuteron wave function into Eq. (4.32) yields

$$G_{\mathrm{C}}(Q) = \frac{G_{\mathrm{E}}^{S}(Q^2)}{\sqrt{1+\eta_{\mathrm{d}}}} \sum_{LM_L} \frac{1}{2L+1} \int_{\mathbf{p}} \phi_L^*(|\mathbf{p}_Q|)\, Y_{LM_L}^*(\hat{\mathbf{p}}_Q)\, Y_{LM_L}(\hat{\mathbf{p}})\, \phi_L(p). \tag{4.36}$$

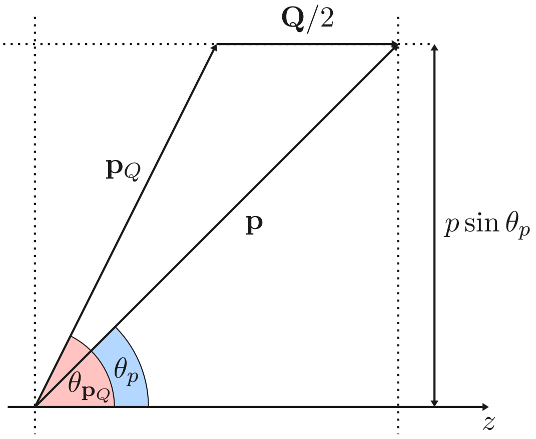

Figure 4.4: Illustration of the momentum shift to the relative momentum, $\mathbf{p}$, caused by the virtual photon. The shifted momentum is denoted by $\mathbf{p}_Q$ and its angle by $\theta_{\mathbf{p}_Q}$. We choose the momentum transfer along the positive z-direction.

Here ϕ_L represents the radial deuteron wave function ($\tilde{u}$ or $\tilde{w}$), $\mathbf{p}_Q$ defines the momentum shift in the deuteron state caused by the virtual photon, i.e., $\mathbf{p}_Q \equiv \mathbf{p} - \mathbf{Q}/2$, $\hat{\mathbf{p}}_Q$ represents the polar $\theta_{\mathbf{p}_Q}$ and the azimuthal $\varphi_{\mathbf{p}_Q}$ angle of $\mathbf{p}_Q$, and θ_p represents the angle between $\mathbf{p}$ and the z-axis. The magnitude of $\mathbf{p}_Q$ is given by

$$|\mathbf{p}_Q| = |\mathbf{p} - \mathbf{Q}/2| = \left(p^2 + \frac{Q^2}{4} - p\,Q\cos\theta_{\mathbf{p}_Q}\right)^{1/2}, \tag{4.37}$$

and the polar angle by

$$\theta_{\mathbf{p}_Q} = \arccos\frac{p_{Q,z}}{|\mathbf{p}_Q|}. \tag{4.38}$$

We introduced a shorthand notation for the integral:

$$\int \frac{\mathrm{d}\mathbf{p}}{(2\pi)^3} = \int_{\mathbf{p}}, \tag{4.39}$$

for better readability of the expressions. A detailed derivation of the result in Eq. (4.36) is given in Appendix B.1.

Since $\mathbf{Q}$ is chosen along the positive z-direction, $\mathbf{p}_Q$ has the same azimuthal angle as $\mathbf{p}$, while the polar angle is shifted. This shift in the polar angle together with $\mathbf{p}_Q$ is depicted in Fig. 4.4. The vectors and angles shown in the figure are the same in each deuteron form factor expression. Note that the charge form factor is diagonal in L and that the sum over S vanished as a result of the Clebsch-Gordan orthogonality.

Quadrupole form factor

The quadrupole form factor gives insights into the shape of the nuclear charge distribution and its normalization provides the deuteron quadrupole moment. Again, we present its final expression by evaluating the one-body charge operator. Starting from Eq. (4.33) we substitute the partial-wave expanded deuteron states to find

$$G_{\mathrm{Q}}(Q) = \frac{2\,M_{\mathrm{d}}^2\,G_{\mathrm{E}}^S(Q^2)}{Q^2\,\sqrt{1+\eta_{\mathrm{d}}}} \sum_{\substack{LM_L\\ SM_S}} \sum_{L'M_L'} \left(\mathcal{C}_{L'M_L'SM_S}^{10}\,\mathcal{C}_{LM_LSM_S}^{10} - \mathcal{C}_{L'M_L'SM_S}^{11}\,\mathcal{C}_{LM_LSM_S}^{11}\right)$$
$$\times \int_{\mathbf{p}} \phi_{L'}^*(|\mathbf{p}_Q|)\,Y_{L'M_L'}^*(\hat{\mathbf{p}}_Q)\,Y_{LM_L}(\hat{\mathbf{p}})\,\phi_L(p). \tag{4.40}$$

For a detailed derivation of this expression, we refer to Appendix B.1. We remark that different orbital angular momentum states are mixed and that the form factor is diagonal in the two-body spin.

Magnetic form factor

Compared to the charge and quadrupole form factors, we have to handle the spatial part of the current, i.e., $\mathbf{j}$, instead of the time-like component to calculate the magnetic form factor. The current operator has a spin-dependent term, mixing different spin states. Because the current consists of two terms, the evaluation naturally splits into two parts. For both terms, a detailed derivation is presented in Appendix B.1.

The first term includes a momentum operator without any spin dependence. Inserting the deuteron wave function decomposition into Eq. (4.34) yields

$$G_{\mathrm{M},1}(Q) = \frac{\sqrt{2}\,M_{\mathrm{d}}\,G_{\mathrm{E}}^S(Q^2)}{Q\,m_N\,\sqrt{1+\eta_{\mathrm{d}}}} \sum_{\substack{LM_L\\ SM_S}} \sum_{L'M_L'} \mathcal{C}_{L'M_L'S'M_S'}^{11}\,\mathcal{C}_{LM_LSM_S}^{10}$$
$$\times \int_{\mathbf{p}} \phi_{L'}^*(|\mathbf{p}_Q|)\,Y_{L'M_L'}^*(\hat{\mathbf{p}}_Q)\,(p_x + i\,p_y)\,Y_{LM_L}(\hat{\mathbf{p}})\,\phi_L(p). \tag{4.41}$$

The factor $(p_x + i\,p_y)$ acts as a ladder operator for the angular momentum L, changing its value. Hence, this term is nondiagonal in angular momentum L. The second term on the other hand involves a spin operator, which complicates the evaluation. The final expression is found to be

$$G_{\mathrm{M},2}(Q) = \frac{M_{\mathrm{d}}\,G_{\mathrm{M}}^S(Q^2)}{\sqrt{1+\eta_{\mathrm{d}}}} \sum_{\substack{LM_L\\ SM_S}} \sum_{\substack{L'M_L'\\ S'M_S'}} \mathcal{C}_{L'M_L'S'M_S'}^{11}\,\mathcal{C}_{LM_LSM_S}^{10}\,\mathcal{S}_{M_S'M_S}^{S'S}$$
$$\times \int_{\mathbf{p}} \phi_{L'}^*(|\mathbf{p}_Q|)\,Y_{L'M_L'}^*(\hat{\mathbf{p}}_Q)\,Y_{LM_L}(\hat{\mathbf{p}})\,\phi_L(p), \tag{4.42}$$

with the spin matrix element, $\mathcal{S}_{M_S'M_S}^{S'S}$, given by

$$\mathcal{S}_{M_S'M_S}^{S'S} = \sum_{\{m_i\}} \Bigg[\sqrt{\frac{3}{4} - m_1(m_1+1)}\,\mathcal{C}_{\frac{1}{2}\,m_1+1\,\frac{1}{2}\,m_2}^{S'M_S'}\,\mathcal{C}_{\frac{1}{2}\,m_1\,\frac{1}{2}\,m_2}^{SM_S}$$
$$+\sqrt{\frac{3}{4} - m_2(m_2+1)}\,\mathcal{C}_{\frac{1}{2}\,m_1\,\frac{1}{2}\,m_2+1}^{S'M_S'}\,\mathcal{C}_{\frac{1}{2}\,m_1\,\frac{1}{2}\,m_2}^{SM_S}\Bigg], \tag{4.43}$$

where $\sum_{\{m_i\}}$ indicates the sum over both indices m_1 and m_2. The total magnetic moment is then given by the sum of the two terms:

$$G_{\mathrm{M}}(Q) = G_{\mathrm{M},1}(Q) + G_{\mathrm{M},2}(Q). \tag{4.44}$$

4.3.3 Numerical evaluation and computational methods

To obtain the form factors defined in Eqs. (4.36) and (4.40) to (4.42), a three-dimensional integral has to be evaluated. The integral is computed numerically with the well-known *Gauss-Legendre* method which approximates the integral as a weighted sum of function values at specific mesh points inside the integration domain. Such an approximation holds for functions, $f(x)$, that are well described by a polynomial of degree $2n-1$ inside the interval $[-1,1]$. The n-point Gaussian quadrature rule is given by

$$\int_{-1}^{1} \mathrm{d}x\, f(x) \approx \sum_{i=1}^{n} w_i f(x_i), \tag{4.45}$$

where the weights w_i are specified by

$$w_i = \frac{2}{(1-x_i^2)[P_n'(x_i)]^2}, \tag{4.46}$$

with $P_n(x)$ the Legendre polynomials. The n points represent a suitable set for the nodes x_i and the weights w_i. If we apply this approximation to the spherical coordinates of a three-dimensional integral, we find:

$$\int \mathrm{d}\mathbf{p}\, f(\mathbf{p}) \approx \sum_{\{p_i\}} \sum_{\{\theta_i\}} \sum_{\{\varphi_i\}} w_{p_i} w_{\theta_i} w_{\varphi_i}\, f(p_i, \theta_i, \varphi_i), \tag{4.47}$$

where $\{p_i\}$, $\{\theta_i\}$ and $\{\varphi_i\}$ correspond to sets of suitable nodes for the momentum, the polar and the azimuthal angle, respectively. As the integration intervals of the spherical coordinates are not inside $[-1,1]$, we make an appropriate mapping of the integration interval for each variable.

The charge and current operator shift the evaluation of the wave function by $|\mathbf{Q}|/2$. This is in conflict with the choice of the Gaussian quadrature points $\{p_i\}$ for which the wave function is known. Therefore, we interpolate the wave function for each momentum transfer to solve the integral. To perform the interpolation, we use a global spline method developed in Ref. [196]. This methods is based on continuous spline functions, $S_i(p)$, for a given mesh, $\{p_i\}$. The value at an arbitrary point is then given by a sum over all mesh points

$$f^{\mathrm{interp}}(p) = \sum_{i=1}^{N_p} f(p_i) S_i(p), \tag{4.48}$$

where the spline functions are designed to let the interpolated function agree with the original function at the mesh points p_i. For a possible form of the spline functions and for more details, we refer to Ref. [196].

4.3.4 Charge and quadrupole form factors

In this section, we show and discuss results for the charge $G_{\mathrm{C}}(Q)$, quadrupole $G_{\mathrm{Q}}(Q)$ and magnetic form factor $G_{\mathrm{M}}(Q)$ obtained with the one-body charge operator. This is achieved by calculating the appropriate momentum space Breit frame matrix elements of the operators, as outlined in Sections 4.3.1 and 4.3.2.

To evaluate these matrix elements numerically, the integrals are approximated by the standard Gauss-Legendre method, as outlined above. The numerical stability has been ensured by choosing a sufficiently fine angular and momentum mesh, such that variations typically are $\leqslant 1\%$ over the entire momentum-transfer range. The wave functions are obtained by diagonalizing the Hamiltonian, as described in Section 3.1.4. We choose two-body matrix elements from the nonlocal NN interaction by Entem, Machleidt, and Nosyk (EMN) [23]. This rather new interaction reaches very high precision for nucleon-nucleon scattering data up to the pion-production threshold among all chiral NN interactions which exist to date. In addition, these interactions range from LO to N^{4}LO, spanning five orders of the chiral expansion. This order-by-order development allows to systematically determine the truncation error at each order, enabling for the construction of meaningful error bars for observables. We employ deuteron wave functions at each order, up to N^{3}LO, for cutoff values of 420, 450, 500, and 550 MeV. Consequently, we calculate truncation uncertainties at each order with a Bayesian analysis of the results, from methods developed in Refs. [42, 43], as outlined in Section 2.5.

We stress that calculations where the order of the operator and the Hamiltonian differ, are not consistent according to chiral EFT. However, using the one-body operator in combination with wave functions obtained by including higher orders of the interaction can be regarded as tests for wave functions themselves. Furthermore, the one-body operator is expected to provide good results since many higher-order operators are isovector, and thus, do not contribute to deuteron observables. For example, the first 2BC correction enters at NLO and has a factor $(\boldsymbol{\tau}_1 \times \boldsymbol{\tau}_2)_z$, while the first isoscalar two-body charge correction comes only at N^{3}LO, such that they are expected to produce small corrections.

We summarize the essential elements of the calculation:

- Static electromagnetic deuteron observables are, for the first time, calculated with recent nonlocal NN interactions from Ref. [23].
- The errors originating from truncating the Hamiltonian are estimated by Bayesian analysis, with the methods developed in Ref. [42, 43].
- The most recent and up-to-date parametrization for the nucleon form factors from Ref. [179] is employed to account for nucleon structure.

We begin by showing results for the truncation error of the normalized charge form factor at NLO, N^{2}LO and N^{3}LO in Fig. 4.5, for a momentum transfer up to $Q = 6.0\ \mathrm{fm}^{-1}$. The convergence of the uncertainty estimate has the same qualitative features for all deuteron form factors and for all cutoff values. Therefore, we select only this charge form factor example and describe the most important aspects here, such that we can, from here on, only show the N^{3}LO result.

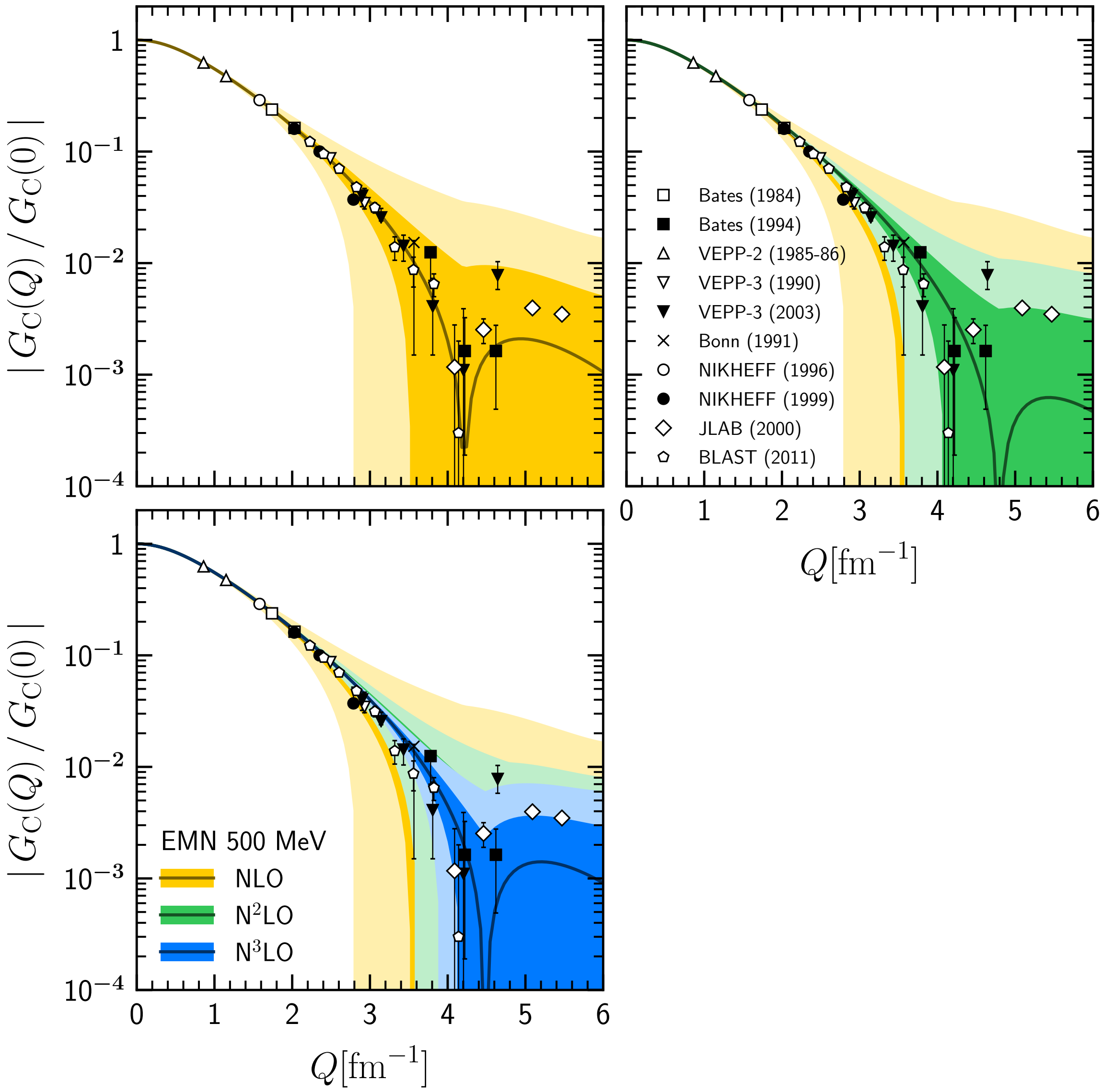

Figure 4.5: Normalized deuteron charge form factor at different chiral orders of the wave function as a function of the momentum transfer Q compared to experimental results. The three panels show the order-by-order convergence of the form factor truncation error estimate obtained by calculating the expectation value of the LO charge operator for order-by-order improved wave functions. Top left panel: The result for the NLO NN interaction with a cutoff of 500 MeV is given by the dark yellow solid line. The lightest shade shows the 95% DoB, while the slightly darker shade shows the 68% DoB interval. Top right panel: The dark green line shows the result for the calculation with an N^{2}LO interaction, and the colored bands are as before. Bottom left panel: The result for the N^{3}LO calculation is shown by the dark blue line, and the bands illustrate, again, the DoBs. Note that the bands for increasing orders lie inside each other. Experimental results for the charge form factor are given by [197] (*open squares*), [198] (*solid square*), [199, 200] (*open upward triangle*), [201] (*open downward triangle*), [202] (*solid downward triangle*), [203] (*solid cross*), [204] (*open circle*), [205] (*solid circle*), [206] (*open diamond*), and [207] (*open pentagon*).

Figure 4.5 shows results obtained with calculations including a cutoff of 500 MeV for wave functions at NLO (top left), $\mathrm{N^2LO}$ (top right) and $\mathrm{N^3LO}$ (bottom left). We make use of the Bayesian model $\mathrm{C}^{650}_{\chi^{-2},0.25-10}$, which means that a breakdown scale of $\Lambda_\mathrm{b} = 650$ MeV is chosen and that prior coefficients are drawn from a distribution with limits $\bar{c}_< = 0.25$ and $\bar{c}_> = 10$. Recall the discussion about truncation uncertainty estimation in chiral EFT presented in Section 2.5 for details about the Bayesian model. The 95% and 68% DoB intervals are shown by light and dark shaded bands, respectively. We observe that the errors of the next order always lie inside the error band of the previous order, showing explicitly the order-by-order convergence. Note that the band of the $\mathrm{N^3LO}$ result starts to strongly increase around 3.5 fm^{-1}. In this region, the truncation uncertainty is dominated by the momentum transfer as a result of $\mathcal{Q} = \min\left(\frac{m_\pi}{\Lambda_\mathrm{b}}, \frac{Q/2}{\Lambda_\mathrm{b}}\right)$, where $Q/2$ represents the characteristic momentum. The characteristic momentum scale for the deuteron is given by $Q/2$ at momentum transfers higher than m_π, because the wave function is probed at momentum scales only half the momentum transfer [71, 186]. This allows to extend the validity of calculations up to momentum transfers of ~ 6 fm^{-1}, as shown in the figure. Another important observation is that the onset of the DoB interval increase occurs consistently at higher momenta transfer for increasing orders. This suggests that including higher orders in the calculation could make the DoBs smaller at high Q. As a final remark, we point out that results at all orders perform well in the zero- and low-momentum region. In Section 4.5, we extract charge and magnetic radii to quantify this observation.

The top row of Fig. 4.6 depicts the results for calculations of the LO charge operator with wave functions at $\mathrm{N^3LO}$ for the charge (left) and quadrupole (right) form factor up to $Q = 6.0$ fm^{-1} together with experimental data. The two panels show results for cutoff values of 420, 450, 500, and 550 MeV with a dashed-dotted, dashed, solid, and dotted line, respectively. In addition, the 95% and 68% DoB for the $\mathrm{N^3LO}$ EMN 500 MeV results are shown by the light and dark shade, respectively. The results for the 500 and 550 MeV cutoffs show good agreement with data up to about 3 fm^{-1}, to then result in a minimum at too high momentum transfer compared to experiment. Corrections from higher-order charge operators have been shown to shift the minimum to lower Q values [70, 72]. This is traced back to the fact that the absolute value of $\mathrm{N^2LO}$ and $\mathrm{N^3LO}$ corrections are of the order of $10^{-2} - 10^{-3}$ over the entire momentum range [70], resulting in almost no effect at low Q and a big effect at high Q where the one-body charge operator result is of the same order. Taking into account this shift caused by higher-order operators suggests that the results in this work could agree with the experimental minimum. Note that at high momentum transfers, the theoretical error band overlaps most of the data and that the 550 MeV result completely lies inside the 500 MeV 68% DoB interval. This reduced cutoff dependence is expected at increasing order. However, not all residual cutoff dependence lies inside the truncation uncertainty band, as seen from the 420 and 450 MeV results. They start to deviate from the other two cutoff calculations already at ~ 2.5 fm^{-1} and completely fail to describe the higher momentum transfer regime, suggesting that the interactions are too soft to reliably account for the high momentum-transfer region. As two-body current corrections to the charge form factor are of order $\mathrm{N^3LO}$, they are rather small and have a limited impact.

The quadrupole form factor calculation shows results which are consistently lower than experimental data over the entire momentum transfer region. Calculations including $\mathrm{N^3LO}$ corrections to the charge operator have been shown to shift the result upwards [70]. On the other hand, the cutoff dependence is much less dramatic and the results for different cutoff

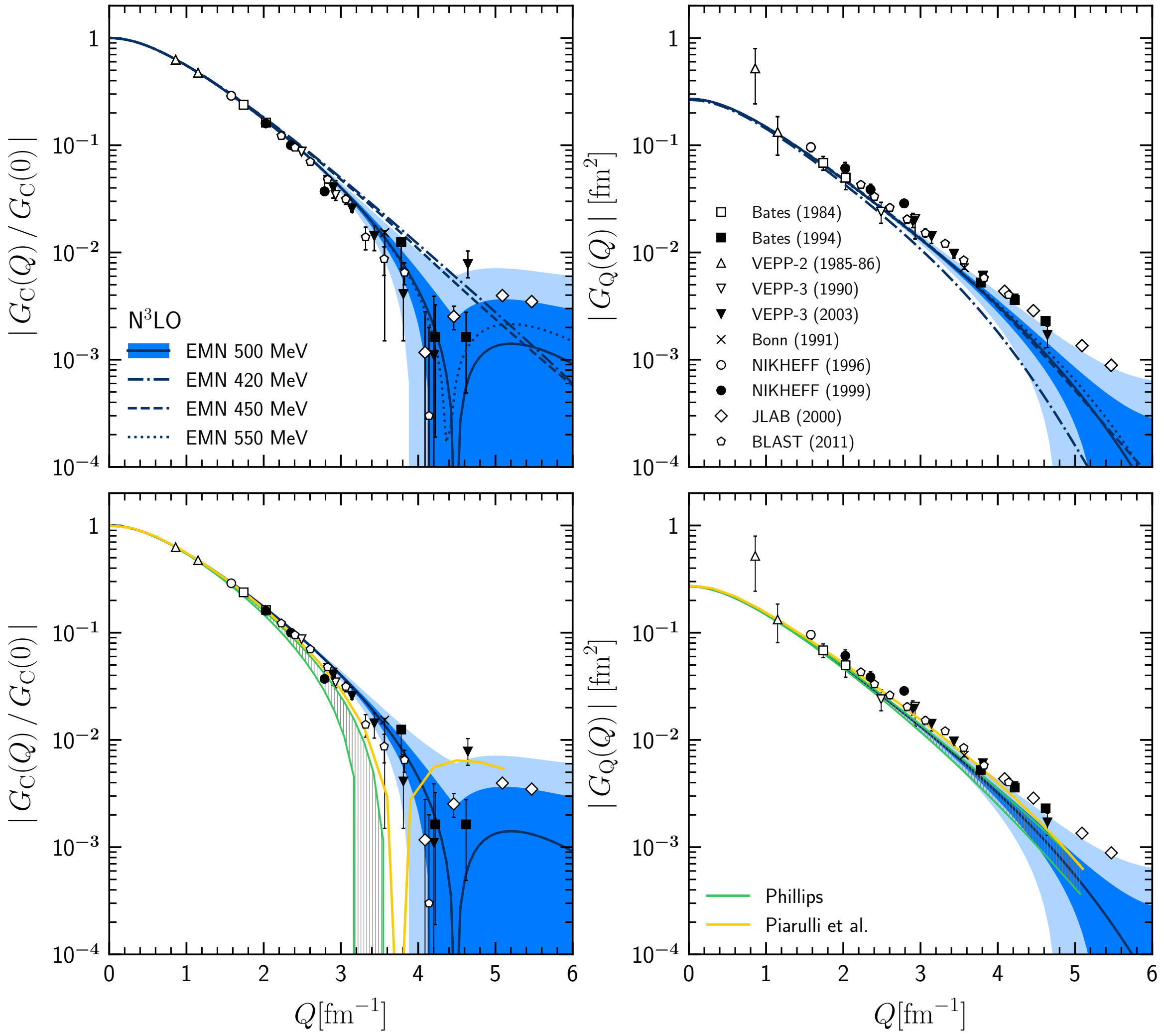

Figure 4.6: Deuteron charge and quadrupole form factor, in units of fm^2, as a function of Q, in units of fm^{-1}. Top row: Deuteron charge (left) and quadrupole form factor (right) at different cutoff values compared to experiment. The solid blue line represents the result for calculations with the EMN 500 MeV interaction at N^{3}LO. The dashed-dotted, dashed, and dotted lines show the outcome for the same interaction with a cutoff of 420, 450, and 550 MeV. The experimental data citation details are as in Fig. 4.5. Bottom row: Comparison to calculations from Phillips [186] (*green line, hatched band*) and from Piarulli *et al.* [70] (*yellow line*). Note that the charge form factor is much more sensitive to the details of the interactions, and thus to the wave function, than the quadrupole form factor.

values all lie within the 68% DoB of the 500 MeV result, except for the 420 MeV result. We conclude that results for the deuteron charge and quadrupole form factors including the one-body operator give the most important contribution to results, and describe the low Q region but fail to reproduce the minimum.

The bottom row of Fig. 4.6 shows a comparison to other calculations. The green lines, and the hatched area between them, are results obtained by Phillips [186] using a NN interaction from Ref. [208] at N^{3}LO and a charge operator at N^{2}LO. The yellow line represents the result obtained by Piarulli *et al.* [70] using an NN interaction with a cutoff of 500 MeV at N^{3}LO from Ref. [189], the predecessor of the interaction used in this thesis, and the LO charge operator.

Note that the hatched band, bounded by the green lines from the results of [186], are not equal to an error estimate as our results indicate with the band, it rather shows the sensitivity of the theory on the cutoff scale. For the charge form factor G_{C}, both calculations start to deviate from results in this thesis at 2 fm^{-1} and predict the minimum at much lower Q of $\sim 3.1 - 3.8$ fm^{-1} compared to ~ 4.5 fm^{-1}. As both calculations are also obtained from consistent chiral EFT calculations, we can assume a similar behavior of the truncation uncertainty at high Q compared to results obtained in this thesis. Therefore, we could conclude that the predicted minima agree within the 68% DoB, as the truncation uncertainty is relatively large. The result from Phillips underpredicts the observable in the region $Q \geqslant 2.5$ fm^{-1}. This qualitative disagreement most likely arises from differences in the deuteron wave functions obtained from the different NN interactions [70]. A similar observation was made between results obtained with the SNPA and chiral EFT, where it is known that the deuteron wave functions are different [126]. The quadrupole form factor G_{Q}, again, shows little or no dependence on the interaction as all calculations are basically overlapping. This small variability has been noticed before and results from the second-order spherical Bessel function presence in the impulse approximation result for $G_{\mathrm{Q}}(Q)$ [186] (see discussion below Eq. (36)).

4.3.5 Magnetic form factor

Figure 4.7 shows the LO results for $G_{\mathrm{M}}(Q)$ for different cutoff values of the N^3LO interaction and compares these to experimental data and another calculation of Piarulli *et al.* [70]. The results for cutoff values 420, 450 and 550 MeV all lie inside the 68% DoB interval of the truncation error of the 500 MeV result. However, the 420 and 450 results have a minimum at much higher transfer momenta, while the other two nearly coincide. The minima for the 500 and 550 MeV results are too low compared to the experimental one, which occurs at ~ 6.5 fm^{-1}. It is a well-known fact that 2BCs have a big impact on magnetic observables, resulting in a shift of the minimum to higher momentum transfers. The calcuation gives a good description of data up to a momentum transfer of ~ 3 fm^{-1}, before it starts to deviate. As seen for the charge form factor, the 68% and 95% DoB intervals rapidly increase around 3.5 fm^{-1}. As a result, the 68% DoB interval is consistent with experimental data up to $Q = 6$ fm^{-1}, such that more conclusive statements about the minima can only be made if the truncation uncertainty is reduced by including higher-order corrections. The result from Piarulli *et al.* is obtained by a calculation with the LO current operator and wave functions from the EM NN interaction [189] with a cutoff of 500 MeV at N^3LO. The calculation starts to deviate from the central value of our result at 2 fm^{-1} and predicts a minimum, again, at a lower momentum transfer than our result, similar as in the charge form factor comparison. This disagreement can be traced back to the difference in the deuteron wave functions, as for the charge form factor. On the other hand, if we assume that the truncation uncertainty for the result from Piarulli *et al.* is similar to the uncertainty of our result, then we could conclude that the predicted minima agree within the 68% DoB. It has been shown by Piarulli *et al.* that including high-order operators shifts the minimum in $G_{\mathrm{M}}(Q)$ to higher Q. In their work, they are unable to reach the experimentally observed minimum, even after including high-order effects. This suggests that high-order corrections to results from this thesis could shift the minimum far enough.

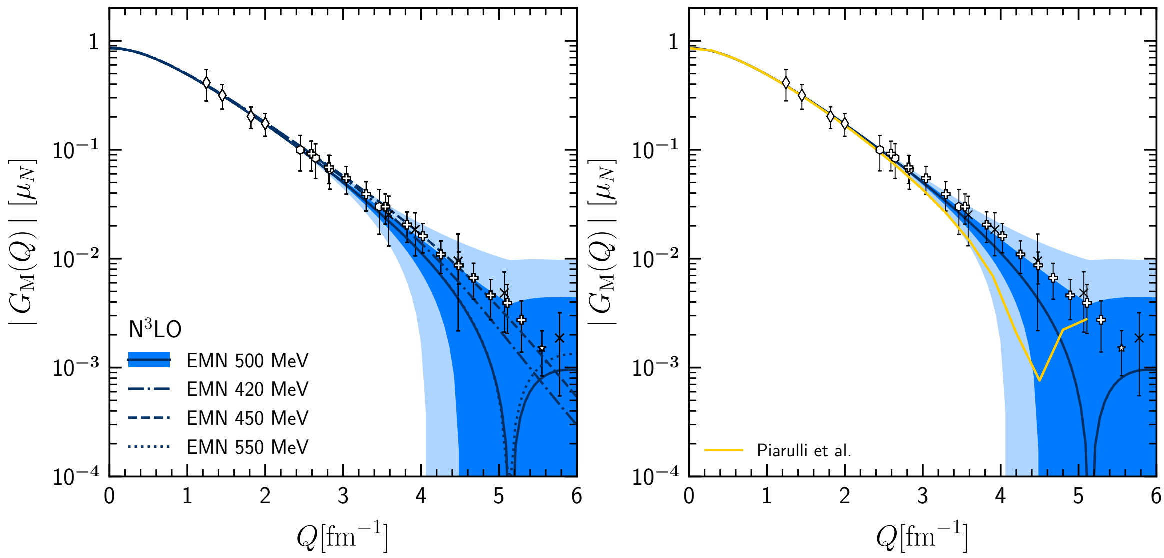

Figure 4.7: Deuteron magnetic form factor, in units of μ_N, from calculations with the LO order current operator and wave functions at $\mathrm{N^3LO}$ as a function of the transfer momentum Q. Left panel: The form factor is shown for three different cutoff values, where the dashed-dotted, dashed, solid, and dotted lines represent calculations with a cutoff of 420, 450, 500, and 550 MeV, respectively. The light and dark blue bands represent the 95% and 68% DoB of the truncation error of the 500 MeV result. Right panel: Deuteron form factor result in comparison to a similar calculation from Piarulli *et al.*[70], which is represented by the yellow line. Experimental results for the magnetic form factor are given by [209] (*open hexagon*), [210] (*open diamond*), [211] (*solid cross*), [212] (*open plus*), and [213] (*open star*).

4.4 TRINUCLEON FORM FACTORS

In this section we discuss the triton and the helion, hereafter also called trinucleons, electromagnetic form factors. We start by stating the electron-trinucleon scattering cross section in terms of the Dirac and Pauli form factors. They are related to the charge and magnetic form factor by a linear combination, and to Breit frame matrix elements of the triton and the helion. In Section 4.4.1, we show the three-body partial-wave expanded charge and magnetic form factors obtained with the one-body charge and current operator, respectively.

The trinucleons are not isoscalar like the deuteron. For this reason, the dominant isovector two-body correction to the current operator can be calculated and its effect studied in the magnetic form factor. We present the expression for this correction, entering at NLO, in Section 4.4.2. Three-nucleon interactions first appear at $\mathrm{N^2LO}$ in the chiral power counting, recall our discussion in Section 2.3, and they depend on two new LECs, i.e., c_D and c_E. It is well known that 3N interactions are important to obtain the correct binding energy of the triton and, in general, provide significant contributions in few-nucleon systems. Therefore, we present results with and without 3N interactions to investigate their impact on electromagnetic form factors. In addition, we also give results for interactions that are evolved to different SRG scales, without evolving the operator, to asses the influence on the high momentum transfer region. A consistent calculation must evolve the operator as well, which will be pursued in the next chapter.

The triton and the helion are both spin-1/2 particles, and therefore, have an elastic electron scattering cross section which is the same as the nucleons, see Eq. (4.12), except for a different target-mass dependence. We restate the cross section for a spin-1/2 particle, now with trinucleon-mass dependence:

$$\frac{\mathrm{d}\sigma}{\mathrm{d}\Omega_{\mathrm{e}}} = \sigma_{\mathrm{M}} f_{\mathrm{rec}}^{-1} \left[F_1^2(Q^2) + \tau_{\mathrm{T}} \left(F_2^2(Q^2) + 2[F_1(Q^2) + F_2(Q^2)]^2 \tan^2 \frac{\theta_{\mathrm{e}}}{2} \right) \right], \tag{4.49}$$

where $\tau_{\mathrm{T}} = Q^2/(4M_{\mathrm{T}}^2)$ now depends on the trinucleon nuclear mass M_{T}, and $F_1(Q)$ and $F_2(Q)$ represent the three-body Dirac and Pauli form factors, respectively. Because the trinucleons are spin-1/2 particles, they only have two independent form factors describing their electromagnetic structure, namely a charge and magnetic form factor. These charge and magnetic form factors are defined as linear combinations of F_1 and F_2 and are explicitly given by

$$F_{\mathrm{C}}(Q) = F_1(Q) - \tau_{\mathrm{T}} F_2(Q), \tag{4.50}$$

$$F_{\mathrm{M}}(Q) = F_1(Q) + F_2(Q). \tag{4.51}$$

Just as for the deuteron, the form factors are related to trinucleon matrix elements of the charge and current operator in the Breit frame, which has an initial and final center-of-mass momentum of $\mathbf{P}_{3\mathrm{N}} = -\mathbf{Q}/2$ and $\mathbf{P}'_{3\mathrm{N}} = \mathbf{Q}/2$. For the triton and the helion these relations are given by

$$F_{\mathrm{C}}(Q) = \frac{1}{Z} \left\langle \mathcal{M}'_{\mathcal{J}} = +1/2 \middle| \hat{\rho}(\mathbf{Q}) \middle| \mathcal{M}_{\mathcal{J}} = +1/2 \right\rangle, \tag{4.52}$$

$$F_{\mathrm{M}}(Q) = \frac{-2m_N}{Q} \left\langle \mathcal{M}'_{\mathcal{J}} = +1/2 \middle| \hat{j}_+(\mathbf{Q}) \middle| \mathcal{M}_{\mathcal{J}} = -1/2 \right\rangle, \tag{4.53}$$

with $\hat{j}_+ \equiv (-\hat{j}_x - i\hat{j}_y)$ the current ladder operator, Z the proton number, and $|\mathcal{M}_{\mathcal{J}} = \pm 1/2\rangle$ either the triton ($\mathcal{M}_{\mathcal{T}} = -1/2$) or the helion state ($\mathcal{M}_{\mathcal{T}} = +1/2$). As a result, there are four independent trinucleon form factors which are normalized as

$$F_{\mathrm{C}}(0) = 1, \qquad F_{\mathrm{M}}(0) = \mu, \tag{4.54}$$

with μ either the triton or the helion magnetic moment in units of μ_N.

4.4.1 Electromagnetic form factors with leading-order currents

The interaction with the external electron changes the center-of-mass momentum of the system and causes the wave function to be probed at higher momenta. This probing of the wave function is proportional to a fraction of the momentum transfer. In the case of a one-body charge or current operator, the interaction happens exclusively with a single particle, which we choose to be the third one:

$$\begin{cases} \mathbf{k}'_1 = \mathbf{k}_1 \\ \mathbf{k}'_2 = \mathbf{k}_2 \\ \mathbf{k}'_3 = \mathbf{k}_3 + \mathbf{Q}. \end{cases} \tag{4.55}$$

Here $\mathbf{k}_i$ describes the single-particle initial and $\mathbf{k}'_i$ final momentum of particle i.

In the Jacobi coordinate system, the electron interacts with the spectator particle only, which we again choose to be the third one. Recall that we have the freedom to select with which particle the interaction occurs because of the antisymmetry of the wave function, see Section 3.2.1. In the Jacobi coordinate system $\mathbf{p}$ represents the relative momentum of subsystem $\{12\}$ and $\mathbf{q}$ that of the spectator particle. Transforming the single-particle momenta to Jacobi momenta, taking into account the Breit frame center-of-mass momenta, yields

$$\mathbf{p}' = \mathbf{p} \quad \text{and} \quad \mathbf{q}' = \mathbf{q} + \frac{2}{3}\mathbf{Q}. \tag{4.56}$$

Thus, also in Jacobi coordinates the shift to the wave function momentum dependence is confined to the spectator particle variable only, i.e., $\phi_\alpha(p, q) \to \phi_\alpha(p', |\mathbf{q} + 2/3\mathbf{Q}|)$. We introduce a shorthand notation for the final spectator momentum by

$$\mathbf{q}_{\frac{2}{3}Q} \equiv \mathbf{q}' = \mathbf{q} + \frac{2}{3}\mathbf{Q}. \tag{4.57}$$

Its magnitude and polar angle are given by

$$|\mathbf{q}_{\frac{2}{3}Q}| = \left(q^2 + \frac{4}{9}Q^2 + \frac{4}{3}p\,Q\cos\theta_{\mathbf{q}_{\frac{2}{3}Q}}\right)^{1/2} \quad \text{and} \quad \theta_{\mathbf{q}_{\frac{2}{3}Q}} = \arccos\frac{q_{\frac{2}{3}Q,z}}{|\mathbf{q}_{\frac{2}{3}Q}|}, \tag{4.58}$$

respectively. This is essentially the same situation as depicted in Fig. 4.4, with changes $\mathbf{p} \to \mathbf{q}$, $\mathbf{p}_Q \to \mathbf{q}_{\frac{2}{3}Q}$, and $1/2\mathbf{Q} \to 2/3\mathbf{Q}$.

Because the external probe interacts with one particle only, the evaluation of the two-body subsystem simplifies considerably, and is the same for both charge and magnetic form factor. Therefore we will first provide the expression describing the two-body subsystem, before specifying final expressions for the charge and magnetic form factor. Recall that the matrix element of a general current operator in the three-body partial-wave basis, defined in Section 3.2.3, is written as[6]

$$\begin{aligned}\langle p'\, q'\, \alpha' |\, J^\mu(\mathbf{Q})\, | p\, q\, \alpha\rangle = &\sum_{M_J M'_J}\sum_{m_j m'_j} \mathcal{C}^{\mathcal{J}'\mathcal{M}'_\mathcal{J}}_{J'M'_J j' m'_j}\, \mathcal{C}^{\mathcal{J}\mathcal{M}_\mathcal{J}}_{JM_J j m_j} \sum_{M_T M'_T}\sum_{m_t m'_t} \mathcal{C}^{\mathcal{T}'\mathcal{M}'_\mathcal{T}}_{T'M'_T t' m'_t}\, \mathcal{C}^{\mathcal{T}\mathcal{M}_\mathcal{T}}_{TM_T t m_t} \\ &\times \mathcal{P}^{M'_J M'_T M_J M_T}_{(L'S')J'T'\,(LS)JT}(\mathbf{Q}, p, p')\, \mathcal{Q}^{m'_j m'_t m_j m_t}_{(\ell' s')j't'\,(\ell s)jt}(\mathbf{Q}, q, q'),\end{aligned} \tag{4.59}$$

with $\mathcal{P}$ and $\mathcal{Q}$ given by

$$\begin{aligned}\mathcal{P}^{M'_J M'_T M_J M_T}_{(L'S')J'T'\,(LS)JT}(\mathbf{Q}, p, p') =& \frac{1}{(2\pi)^3}\int \mathrm{d}\mathbf{p}_1 \int \mathrm{d}\mathbf{p}'_1\, \frac{\delta(p'_1 - p')}{p'_1\, p'} \mathcal{Y}^{*J'M'_J}_{L'S'}(\hat{\mathbf{p}}'_1) \\ &\times \langle \mathbf{p}'_1\, T' M'_T | J^\mu(\mathbf{Q}) | \mathbf{p}_1\, T M_T\rangle\, \frac{\delta(p - p_1)}{p\, p_1} \mathcal{Y}^{JM_J}_{LS}(\hat{\mathbf{p}}_1)\,,\end{aligned} \tag{4.60}$$

$$\begin{aligned}\mathcal{Q}^{m'_j m'_t m_j m_t}_{(\ell' s')j't'\,(\ell s)jt}(\mathbf{Q}, q, q') =& \frac{1}{(2\pi)^3}\int \mathrm{d}\mathbf{q}_1 \int \mathrm{d}\mathbf{q}'_1\, \frac{\delta(q'_1 - q')}{q'_1\, q'} \mathcal{Y}^{*j'm_j}_{\ell' s'}(\hat{\mathbf{q}}'_1) \\ &\times \langle \mathbf{q}'_1\, t' m'_t | J^\mu(\mathbf{Q}) | \mathbf{q}_1\, t m_t\rangle\, \frac{\delta(q - q_1)}{q\, q_1} \mathcal{Y}^{jm_j}_{\ell s}(\hat{\mathbf{q}}_1)\,.\end{aligned} \tag{4.61}$$

The function $\mathcal{P}$ includes all variables and degrees of freedom belonging to the two-body

---

[6] We also remind the reader that lowercase letters denote the spectator particle quantum numbers, capital letters show the two-body subsystem quantum numbers, and calligraphic letters describe the three-body quantum numbers.

subsystem, while $\mathcal{Q}$ describes the spectator particle. Consequently, the one-body charge and current operator act in Eq. (4.61), while Eq. (4.60), because of the orthonormality of the spherical harmonics, reduces to

$$\mathcal{P}^{M_J' M_T' M_J M_T}_{(L'S')J'T'\,(LS)JT}(\mathbf{Q}, p, p') = \sum_{M_L M_S} \mathcal{C}^{J'M_J'}_{L'M_L S'M_S}\, \mathcal{C}^{JM_J}_{LM_L SM_S}\, \delta_{LL'}\delta_{SS'}\delta_{TT'}\delta_{M_T M_T'} \frac{\delta(p-p')}{p'p}. \tag{4.62}$$

This expression holds for both charge and magnetic form factor. Hence, the two-body subsystem is diagonal in all quantum numbers.

The charge and magnetic form factor of the triton and the helion are proportional to specific matrix elements of the charge and current operator as indicated in Eqs. (4.52) and (4.53). The initial and final state of the nucleus are given in a Jj-coupled basis and are solutions of the Faddeev method described in Section 3.2.4. A general expression for the charge form factor is then given by inserting completeness relations of the partial-wave basis between the operator and the wave functions to find

$$F_\mathrm{C}(Q) \propto \sum_{\alpha\alpha'} \int \mathrm{d}p\, p^2 \int \mathrm{d}q\, q^2 \int \mathrm{d}p' p'^2 \int \mathrm{d}q' q'^2\, \phi^*_{\alpha'}(p', q')\, \langle p'\, q'\, \alpha' | \hat{\rho}(\mathbf{Q}) | p\, q\, \alpha \rangle\, \phi_\alpha(p, q). \tag{4.63}$$

To obtain an equivalent expression for the mangetic form factor F_M, a simple change of the operator $\hat{\rho} \to \hat{\mathbf{j}}$ has to be made. The final expression is given by substituting the results of Eqs. (4.59) and (4.62) and examining the one-body charge and magnetic current operator effect on $\mathcal{Q}^{m_j' m_t' m_j m_t}_{(\ell' s')j't'\,(\ell s)jt}(Q, q, q')$. We will consider both separately below.

Charge form factor

The charge operator has the effect to shift the momentum dependence of the spectator particle. This introduces a delta function that enforces the momentum conservation as follows

$$\begin{aligned}
\mathcal{Q}^{m_j' m_t' m_j m_t}_{(\ell' s')j't'\,(\ell s)jt}(Q, q, q') =& \frac{1}{(2\pi)^3} \int \mathrm{d}\mathbf{q}_1 \int \mathrm{d}\mathbf{q}_1'\, \mathcal{Y}^{*j'm_j'}_{\ell' s'}(\hat{\mathbf{q}}_1')\, \frac{\delta(q_1' - q')}{q'\, q_1'} \\
&\times\ (2\pi)^3 \delta(\mathbf{q}_1 - \mathbf{q}_1' - \frac{2}{3}\mathbf{Q}) \frac{\delta(q - q_1)}{q\, q_1} \mathcal{Y}^{jm_j}_{\ell s}(\hat{\mathbf{q}}_1)\ \langle t' m_t' | e_N(Q^2) | t m_t \rangle \\
=& \int \mathrm{d}\hat{\mathbf{q}}\, \mathcal{Y}^{*j'm_j'}_{\ell' s'}(\hat{\mathbf{q}}_{\frac{2}{3}Q})\, \frac{\delta(q' - |\mathbf{q}_{\frac{2}{3}Q}|)}{q'\, |\mathbf{q}_{\frac{2}{3}Q}|} \mathcal{Y}^{jm_j}_{\ell s}(\hat{\mathbf{q}})\ \langle t' m_t' | e_N(Q^2) | t m_t \rangle\,,
\end{aligned} \tag{4.64}$$

where this result is obtained by changing J^μ with the correct one-body charge operator $\hat{\rho}^{(-3)}$. In the last step the integration over $\mathbf{q}_1'$ and q_1 was carried out, and the renaming $\hat{q}_1 \to \hat{q}$ was made. Substituting results Eqs. (4.62) and (4.64) in the expression for the partial-wave expanded matrix element, Eq. (4.59), and adding the correct prefactors, we find the one-body trinucleon charge form factor expression:

$$F_\mathrm{C}(Q) = \frac{3}{Z} \sum_\alpha \tau^{\mathcal{M}_\mathcal{T}}_{\mathrm{E};T}(Q^2) \sum_{m_\ell} \int \mathrm{d}p\, p^2 \int \mathrm{d}\mathbf{q}\, \phi^*_\alpha(p, |\mathbf{q}_{\frac{2}{3}Q}|)\, Y^*_{\ell m_\ell}(\hat{\mathbf{q}}_{\frac{2}{3}Q})\ Y_{\ell m_\ell}(\hat{\mathbf{q}})\ \phi_\alpha(p, q), \tag{4.65}$$

with the isospin factor given by

$$\tau^{\mathcal{M}_\mathcal{T}}_{\mathrm{E/M};T}(Q^2) \equiv \sum_{M_T\, m_t} \mathcal{C}^{\frac{1}{2}\,\mathcal{M}_\mathcal{T}}_{\frac{1}{2} m_t T M_T}\, \mathcal{C}^{\frac{1}{2}\,\mathcal{M}_\mathcal{T}}_{\frac{1}{2} m_t T M_T}\, \frac{G^S_{\mathrm{E/M}}(Q^2) + m_t\, G^V_{\mathrm{E/M}}(Q^2)}{2}. \tag{4.66}$$

Here, the subscript E or M indicates the electric or magnetic nucleon form factor, respectively. It is through this isospin factor that the nucleon substructure is taken into account in the electromagnetic trinucleon one-body form factors. The total isospin of the three-nucleons is $\mathcal{T} = 1/2$, and its projection quantum number determines the nucleus for which the form factor is calculated, i.e., $\mathcal{M}_\mathcal{T} = -1/2$ for the triton and $1/2$ for the helion. The total one-body operator is given by the sum of the interaction with each nucleon, which is accounted for by the prefactor 3 in Eq. (4.65). Note that the expression for the charge form factor is diagonal in all quantum numbers, represented by α, and that the angular integral over $\hat{\mathbf{q}}$ has to be carried out explicitly because of the shift caused in the angle, as was the case for the deuteron. We refer the reader to Appendix B.2 for detailed derivations of (4.64)-(4.66).

Below we present and discuss results for the trinucleon charge form factors F_C obtained with the one-body charge operator, i.e., Eq. (4.65). The integrals are computed by means of the standard Gauss-Legendre method and to calculate the shift in the wave function a global spline interpolation is used, as explained in Section 4.3.3. A sufficiently large mesh for the magnitude, polar, and azimuthal angle of the three momentum variables is chosen, such that variations are below 1% over the entire momentum-transfer range. The trinucleon wave function configurations, obtained with the Faddeev method, are included up to $J_\mathrm{max} = 3$ or 26 channels in total.[7] We use two different combinations of NN + 3N interactions to obtain the wave functions:

- One combination uses the nonlocal EMN NN interaction [23] together with 3N interactions fit to the triton binding energy and nuclear matter saturation properties [32]. These interactions are used at four orders for cutoff values of 420, 450, and 500 MeV, such that the error from truncating the chiral Lagrangian can be estimated. We will denote this interaction as follows: N^{3}LO EMN 500 MeV, for calculations with wave functions obtained from the EMN NN + 3N interaction with a cutoff of 500 MeV at fourth order.

- The second combination uses the nonlocal Entem-Machleidt (EM) NN interaction [189] with a cutoff of 500 MeV at N^{3}LO and SRG-evolved to scale λ_SRG from Ref. [31], together with 3N interactions at N^{2}LO fit to the triton binding energy and the ^{4}He matter radius [31, 139, 214]. The 3N interaction is regularized with a cutoff Λ_3N that is varied separately from the NN cutoff. To denote calculations with this combination we use: EM 500 MeV + 3N(2.0fm^{-1}), for wave functions with an unevolved interaction and with a three-body cutoff $\Lambda_\mathrm{3N} = 2.0$ fm^{-1}, and: $\lambda_\mathrm{SRG}/\Lambda_\mathrm{3N} = 2.2/2.0$ fm^{-1}, for wave functions from interactions evolved to scale $\lambda_\mathrm{SRG} = 2.2$ fm^{-1} with and three-body cutoff $\Lambda_\mathrm{3N} = 2.0$ fm^{-1}.

We note again that the calculations are not consistent according to chiral EFT, because the operator and the interaction are not considered at the same order. However, a calculation

---

[7] This means that the sum over α has 26 terms, where each term has a distinct combination of L, S, J, T, l, and j.

with a one-body operator in combination with a higher-order interaction, functions as a test for the wave functions.

Figure 4.8 shows the truncation error estimate for the triton charge form factor for a momentum transfer up to $Q = 5$ fm^{-1} from calculations with the one-body charge operator and with interactions at NLO, N^{2}LO, and N^{3}LO for the EMN 450 MeV. The isoscalar and isovector nucleon form factors are given by the parametrization from Ref. [179] and the truncation uncertainty is estimated by using the methods developed in Refs. [42, 43]. The hatched area represents the experimental information, given as a parametrization from Ref. [75]. To calculate the truncation error and quantify the DoB intervals, we use the Bayesian model $\mathrm{C}^{650}_{\chi^{-2},0.25-10}$, indicating a breakdown scale of $\Lambda_\mathrm{b} = 650$ MeV and a prior-coefficients which are drawn from a distribution with bounds $0.25 \leqslant \bar{c} \leqslant 10$. We refer again to Section 2.5 for the details about the truncation estimation. The characteristic momentum scale for the trinucleons is given by $2/3Q$, which decreases the range over which chiral EFT is applicable compared to the deuteron. In general, the valid range goes as $(A-1)/A$ for an arbitrary nucleus with mass number A [71], such that the covered momentum-transfer range is maximal for the deuteron. For the trinucleons this translates to a momentum-transfer range of $0 \leqslant Q \leqslant 3/2\Lambda_\mathrm{b}$ MeV, resulting in an upper limit of $Q \approx 4.95$ fm^{-1}. Therefore, we only show results for the truncation error up to that momentum transfer. The Bayesian analysis provides 95% (light shade) and 68% (dark shade) DoB intervals. These intervals grow with increasing momentum transfer, and rapidly expand near the end of the allowed range (see yellow, green, and blue bands between $4.6 - 4.95$ fm^{-1} around halfway the y-axis), as expected. As a result of the smaller characteristic-momentum scale compared to the deuteron, the N^{3}LO band starts to increase rapidly already around 2.8 fm^{-1}. Beware of the logarithmic scale on the y-axis which amplifies the lower bound of the truncation error, causing the impression that the error is much larger there. We observe a systematic order-by-order convergence of the truncation error for increasing orders, each DoB interval overlaps the band from the preceding order.

The central value of the results at each order describe the low Q region well up to ~ 2.5 fm^{-1}, after which they consistently overestimate the experimental results. Consequently, the minimum occurs at too high Q for each order, even pushing the minimum to larger values with each increase in order. This pattern was also observed for the deuteron when the same interaction, without the 3N part, was used. Note that the impact of adding N^{3}LO corrections is larger than only adding N^{2}LO corrections.

A similar order-by-order convergence pattern is observed for the other cutoffs, as well as for the helion. Therefore, we discussed the key features for this specific example such that we can only present N^{3}LO results from here on.

The left and right panel of Fig. 4.9 display the result of the triton and the helion charge form factor, respectively. Both form factors are calculated with the N^{3}LO EMN interaction for cutoffs $\Lambda = 420$, 450, and 500 MeV shown by the dashed-dotted, dashed, and solid lines. Further, the 95% and 68% DoB intervals are shown for the 500 MeV result. The results for different cutoffs start to deviate from each other at 3 fm^{-1} and 2.6 fm^{-1} for the triton and the helion, respectively, yet they all lie within the 68% DoB. In addition, the cutoff dependence is weaker as observed for the deuteron charge form factor, see Fig. 4.6. We observe that a higher cutoff results in a minimum at lower momentum transfer, demonstrating that interactions with a harder cutoff reproduce the high Q region better. However, the central value of the 500 MeV results with minima at ~ 4.2 fm^{-1} (triton) and ~ 3.8 fm^{-1} (helion) still disagree

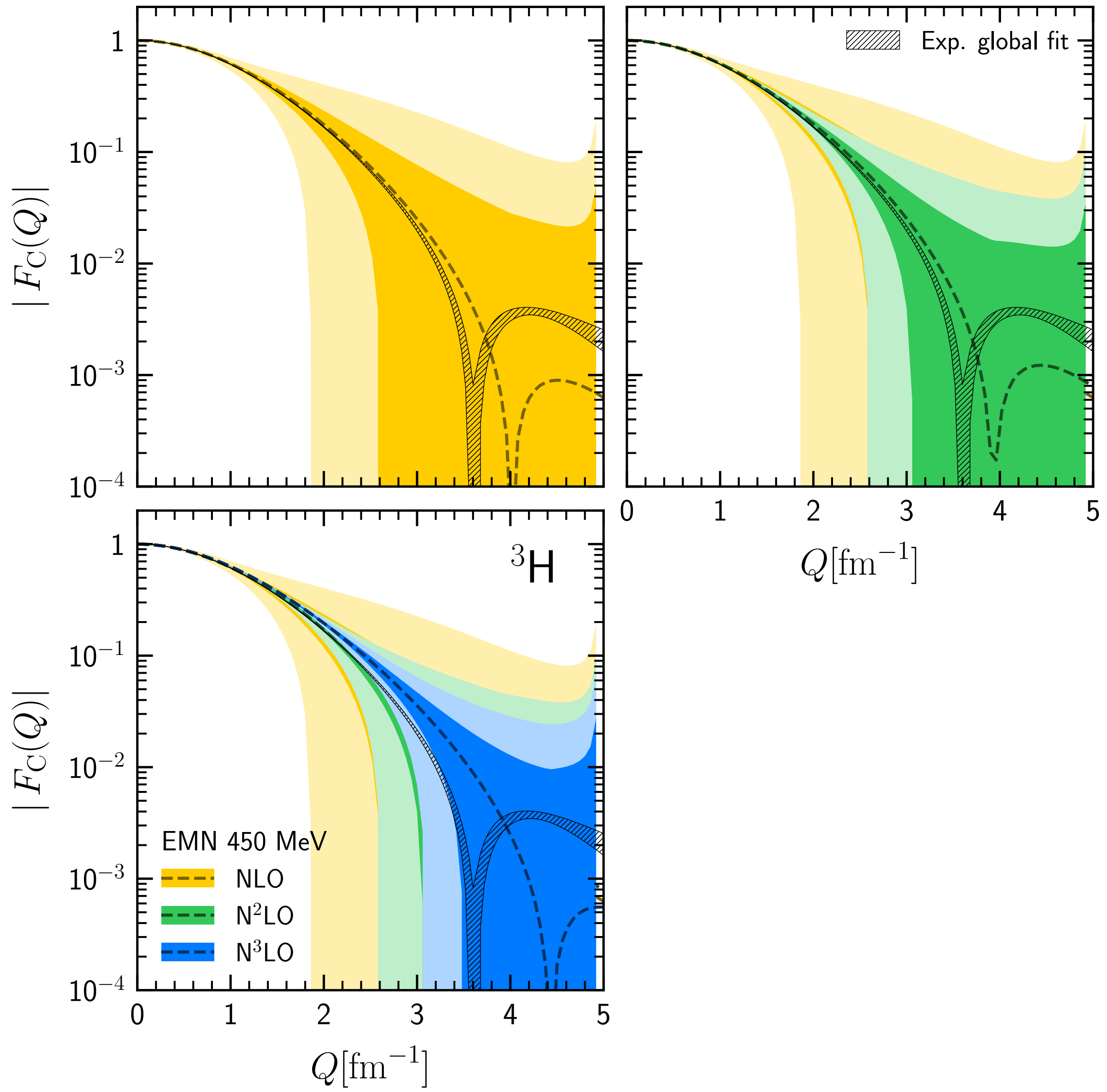

Figure 4.8: Triton charge form factor at different orders of the wave function as a function of the momentum transfer Q compared to an experimental parametrization of the world data. The three panels show the order-by-order convergence of the form factor truncation error estimate obtained by calculating the expectation value of the one-body charge operator for order-by-order improved wave functions. Top left panel: The result for the NLO EMN 450 MeV interaction is given by the dashed dark yellow line. The lightest shade shows the 95% DoB, while the slightly darker shade shows the 68% DoB interval. Top right panel: The dark green line shows the result for the calculation with an interaction at N^{2}LO, and the colored bands are as in the first panel. Bottom left panel: The result for the N^{3}LO calculation is shown by the dark blue line, and the bands illustrate, again, the DoBs. Note that the bands for increasing orders lie inside each other. Experimental results for the charge form factor are given by the hatched area [75].

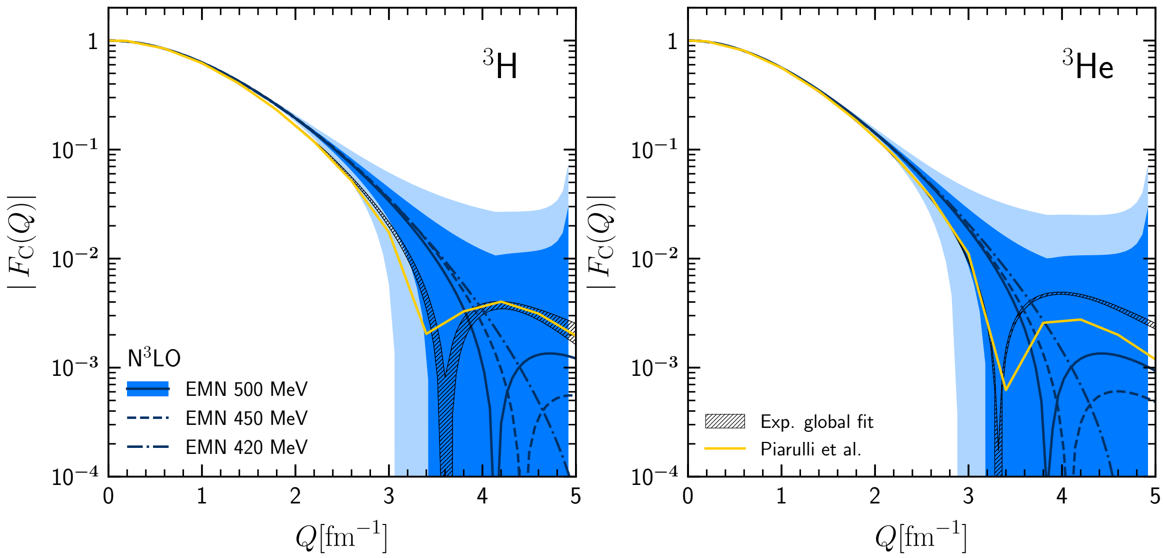

Figure 4.9: Triton (left) and helion (right) charge form factor as a function of the momentum transfer Q, in units of fm^{-1}, compared to an experimental parametrization and other calculations. Both charge form factors are calculated with the one-body charge operator and the N^{3}LO EMN interaction with three different cutoffs of 500 MeV (*solid line*), 450 MeV (*dashed line*), and 420 MeV (*dashed-dotted line*). The light blue bands are as in Fig. 4.8. The hatched area depicts the experimental parametrization from Ref. [75] and results from Ref. [70] are shown by the yellow line, see text for more details about these calculations.

with experiment. At low transfer momenta, the N^{3}LO result agrees with data up to ~ 1.2 fm^{-1} for the triton and ~ 1.5 fm^{-1} for the helion. More importantly, for both the triton and the helion, the experimental results are contained within the 95% DoB over the entire range and within the 68% band in the higher transfer-momentum region, showing the capability and importance of estimating the theoretical error.

Many results exist for form factors obtained with the SNPA. In contrast, charge form factor results for three-nucleon systems from chiral EFT are very scarce. The yellow line in Fig. 4.9 describes results from Piarulli *et al.* [70] obtained with the N^{3}LO EM 500 NN + N^{2}LO 3N [129] interaction and the chiral one-body charge operator, indicated by $\rho^{\text{LO}}/(\text{N}^3\text{LO}/\text{N}^2\text{LO})$.[8] As for the comparison with experiment, the results from this work agree with the central value up to ~ 1.2 fm^{-1} for the triton and 1.5 fm^{-1} for the helion, after which the results from Ref. [70] are consistently lower and in better agreement with experiment. Nevertheless, if we consider the truncation uncertainty intervals and assume that the results from Piarulli *et al.* have a similar uncertainty, then both calculations would agree with each other. Results from Piarulli *et al.* including higher-order operator corrections shift the minimum to lower transfer momenta, as these corrections have an opposite sign compared to the one-body result. Taking into account such a shift, has the consequence that the N^{3}LO EMN results would agree better with experiment. As pointed out in Ref. [71], however, the higher-order corrections beyond the minimum are of the order of the one-body results, suggesting that the chiral expansion is

---

[8] That work presents results for two different interactions: the N^{3}LO EM NN + N^{2}LO 3N [129] with cutoffs set at 500 and 600 MeV, denoted by N^{3}LO/N^{2}LO and N^{3}LO*/N^{2}LO*, respectively. The data are taken from tables X and XI in Ref. [70].

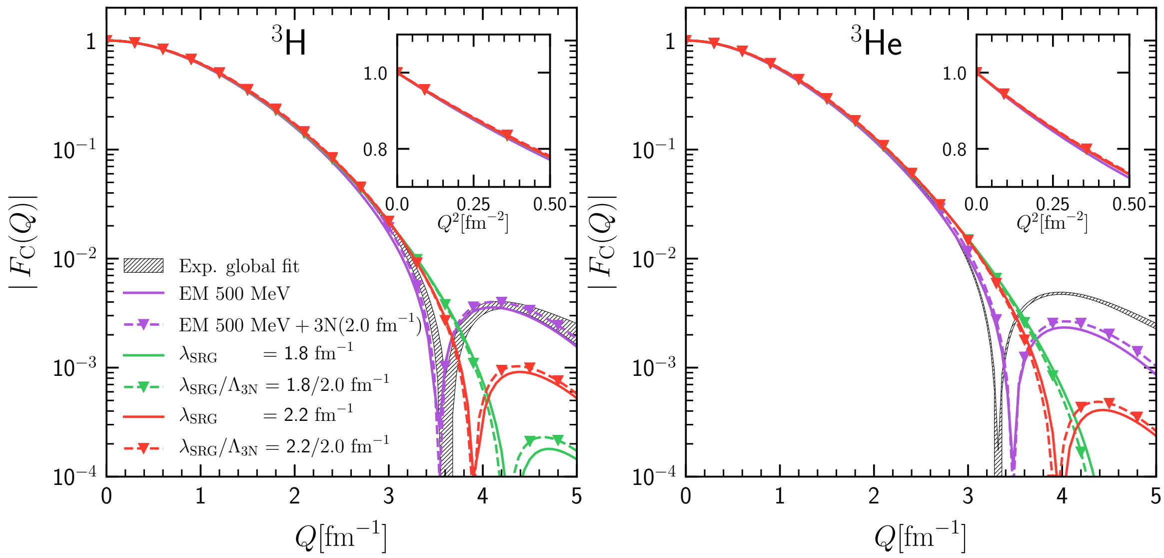

Figure 4.10: Charge form factor of the triton (left) and helion (right) as a function of Q, in units of fm^{-1}, compared to the experimental parametrization from Ref. [75]. The lines show results for calculations with NN interactions only (*solid lines*) and NN + 3N interactions (*dashed lines with downward triangles*) for an unevolved (*purple*), and two different SRG-evolved interactions: One is evolved to a very soft interaction $\lambda_{\mathrm{SRG}} = 1.8$ fm^{-1} (*green*) and the other to a medium scale $\lambda_{\mathrm{SRG}} = 2.2$ fm^{-1} (*red*). The symbol Λ_{3N} represents the three-body regulator scale. The insets display the low momentum-transfer region as a function of Q^2 to amplify the minor differences between results.

not convergent in this region. The large uncertainty bands in this region presumably provide evidence for this argument.

Three-body interactions start to play a role for systems of three or more particles. To investigate their impact on trinucleon form factors, we show in Fig. 4.10 the triton and the helion charge form factor on the left and right, respectively, for results with and without three-body interactions. In addition, we study the impact of interactions at different SRG scales. Using renormalization group methods softens the short-range repulsion, or in other words, it decouples high and low momentum in the interaction. It achieves this with a unitary transformation which leaves the low-momentum observables invariant, such that an effect should be present in the high-momentum-transfer region of the form factor. For more information about the application of SRG in nuclear physics we refer the reader to, e.g., Ref. [215].

The three solid lines correspond to calculations with the one-body charge operator and the N^{3}LO EM 500 MeV NN interaction for three different SRG scales [31]. The purple curve displays an unevolved interaction, the green one a moderate evolution to $\lambda_{\mathrm{SRG}} = 2.2$ fm^{-1}, and the red line corresponds to an evolution until $\lambda_{\mathrm{SRG}} = 1.8$ fm^{-1}. This last interaction has received a lot of attention since it reproduces the empirical saturation point quite well, while simultaneously obtaining ground-state energies of closed-shell nuclei close to experiment, but leaving charge radii underpredicted [216, 217]. It accomplishes these results, even though, the interaction is only fit to few-body data. The three dashed lines with downward triangles present results for the same NN interactions, however, now including the leading 3N interaction at N^{2}LO [31, 139, 214]. We repeat that the 3N interaction uses a different regulator compared to the NN interaction and has a separate cutoff scale denoted by $\Lambda_{3\mathrm{N}}$, which for these calculations is $\Lambda_{3\mathrm{N}} = 2.0\ \mathrm{fm}^{-1}$.

The result for the unevolved NN interaction (purple solid line) is in almost perfect agreement with experiment for the triton, even reproducing the minimum, and is in good agreement for the helion up to $\sim 3\ \mathrm{fm}^{-1}$ to then have a minimum at slightly to high Q. The two SRG-evolved interactions give the same result up until about $Q = 3\ \mathrm{fm}^{-1}$ and then start to deviate from the unevolved result, as well as from each other. Results evolved to smaller and smaller SRG scales, produce a minimum at consecutively higher Q. This is expected since the SRG evolution softens the interaction, i.e., it modifies the high momentum part, which is probed at high Q. A similar effect is observed for the EMN interactions, decreasing the cutoff pushes the minimum further out. In fact, to restore the changes generated by the SRG evolution and to achieve a consistent calculation, the operator should be SRG evolved as well. However, we did not carry out this step for the one-body charge operator, but we will revisit this point in the next chapter, see Section 5.7.

As the figure shows, the difference between the calculations including only NN interactions and with 3N interactions included is minimal, especially considering the logarithmic scale. Essentially, it only scales the NN result. For the two SRG-evolved interactions there is a tiny shift of the zero crossing to lower momentum transfer and after the minimum, the curves 3N results reach a higher maximum. Note that these results employ the same NN interaction, but a different 3N interaction and nucleon form factor, as the yellow line in Fig. 4.9. Indeed, both results have the same qualitative features, where a complete comparison is prevented because of the coarse Q mesh. The fact that the inclusion of the 3N force is so small, even at higher momentum transfers, is noteworthy since they provide important corrections to reproduce correct binding energies and nuclear matter saturation properties [31]. It is not clear why the inclusion of the three-body force does not have an impact on the electromagnetic form factors for the trinucleons. Because of this small impact, we did not pursue a detailed study of the effect caused by changing the three-nucleon couplings c_D and c_E.

In conclusion, the inset in both plots shows the charge form factor as a function of the momentum transfer squared up to $Q = 0.50\ \mathrm{fm}^{-2}$. This is done to amplify any existing variation between the different results. As we will see in the next section, an expansion around $Q^2 = 0$ of the form factor can be made, resulting in a linear dependence at zero momentum transfer. At very small momentum transfers, we can identify the linear behavior, before the quadratic term takes over at $\sim 0.05\ \mathrm{fm}^{-2}$. The insets suggest that the slope of the form factor calculated with the NN + 3N interaction could be slightly reduced, as the dashed line is slightly higher. This would create a smaller radius compared to NN only results. Calculating the radius provides more quantitative information for which we will present results in Section 4.5.

Magnetic form factor

To find the expression for the magnetic form factor, we examine the effect of the current operator in Eq. (4.61). Except for a shift in the momentum dependence of the spectator particle, the current operator also acts on its spin and orbital angular momentum. We substitute the one-body current in Eq. (4.61) to find

$$\begin{aligned}\mathcal{Q}^{m_j' m_t' m_j m_t}_{(\ell' s') j' t'\,(\ell s) j t}(Q, q, q') = &\frac{1}{2m_N} \int \mathrm{d}\hat{\mathbf{q}}\, \mathcal{Y}^{*j' m_j'}_{\ell' s'}(\hat{\mathbf{q}}_{\frac{2}{3}Q}) \Big[2\, \tau^{\mathcal{M}_\mathcal{T}}_{\mathrm{E};T}(Q^2)\, (-q_x - i q_y)\, \delta_{m_s m_s'} \\ &- \tau^{\mathcal{M}_\mathcal{T}}_{\mathrm{M};T}(Q^2)\, i(\boldsymbol{\sigma} \times \mathbf{Q})_+ \Big] \mathcal{Y}^{j m_j}_{\ell s}(\hat{\mathbf{q}})\,, \end{aligned} \tag{4.67}$$

The spin operator, $\boldsymbol{\sigma}$, acts on the spin degree of freedom that is included in the coupled spherical harmonic. This results in the following LO magnetic trinucleon form factor:

$$\begin{aligned}F^{\mathrm{LO}}_{\mathrm{M}}(Q) = &\frac{-3e}{Q} \sum_{\alpha, \{\ell', j'\}} \sum_{\substack{M_J \\ m_j m_j'}} \sum_{\substack{m_\ell m_\ell' \\ m_s m_s'}} \mathcal{C}^{\frac{1}{2}\frac{1}{2}}_{J M_J j' m_j'}\, \mathcal{C}^{\frac{1}{2}-\frac{1}{2}}_{J M_J j m_j} \int \mathrm{d}p\, p^2 \int \mathrm{d}\mathbf{q}\, \phi^*_{\alpha'}(p,\, |\mathbf{q}_{\frac{2}{3}Q}|)\, Y^*_{\ell' m_\ell'}(\hat{\mathbf{q}}_{\frac{2}{3}Q}) \\ &\times \mathcal{C}^{j' m_j'}_{\ell' m_\ell' \frac{1}{2} m_s'}\, \mathcal{C}^{j m_j}_{\ell m_\ell \frac{1}{2} m_s} \Big[2\, \tau^{\mathcal{M}_\mathcal{T}}_{\mathrm{E};T}(Q^2)\, (-q_x - i q_y) \delta_{m_s' m_s} \\ &+ \tau^{\mathcal{M}_\mathcal{T}}_{\mathrm{M};T}(Q^2)\, \langle \tfrac{1}{2} m_s' | i(\boldsymbol{\sigma} \times \mathbf{Q})_+ | \tfrac{1}{2} m_s \rangle \Big] Y_{\ell m_\ell}(\hat{\mathbf{q}})\, \phi_\alpha(p,\, q). \end{aligned} \tag{4.68}$$

Note that the form factor is nondiagonal in ℓ and j only, and that the first term includes the electric isospin factor while the second term the magnetic one, see Eq. (4.66). The superscript LO is added to distinguish between the NLO correction which is calculated below. After introducing the NLO correction in the next section, we discuss the results for the magnetic form factor with one- and two-body operator together. For detailed derivations, we refer the reader to Appendix B.2.

4.4.2 Magnetic form factor with next-to-leading-order currents

For the 2BC it is natural to consider that the interaction occurs between the external probe and the two-body subsystem {12}. In that case, the third particle is left undisturbed, i.e., $\mathbf{k}_3' = \mathbf{k}_3'$. In the Breit frame, this results in the following single-particle momenta, $\mathbf{k}_i$, expressed in Jacobi coordinates, $\tilde{\mathbf{p}}$ and $\tilde{\mathbf{q}}$:

$$\mathbf{q}_1 = \mathbf{k}_1' - \mathbf{k}_1 = -\tilde{\mathbf{p}} - \frac{\tilde{\mathbf{q}}}{2} + \frac{\mathbf{Q}}{3}, \tag{4.69a}$$

$$\mathbf{q}_2 = \mathbf{k}_2' - \mathbf{k}_2 = \tilde{\mathbf{p}} - \frac{\tilde{\mathbf{q}}}{2} + \frac{\mathbf{Q}}{3}, \tag{4.69b}$$

$$\mathbf{q}_3 = \mathbf{k}_3' - \mathbf{k}_3 = 0 = \tilde{\mathbf{q}} + \frac{\mathbf{Q}}{3}, \tag{4.69c}$$

where the tilde over the Jacobi momenta represents the difference between the final and initial momenta, i.e., $\tilde{\mathbf{p}} \equiv \mathbf{p}' - \mathbf{p}$ and $\tilde{\mathbf{q}} \equiv \mathbf{q}' - \mathbf{q}$. Note that the symbols $\mathbf{q}_i$ are not Jacobi momenta, but indicate the momentum transfer between the single-particle momenta themselves. From (4.69a)-(4.69c) we infer the momentum conservation to be

$$\mathbf{q}_{\frac{1}{3}Q} \equiv \mathbf{q}' = \mathbf{q} - \frac{1}{3}\mathbf{Q}, \tag{4.70a}$$

$$\mathbf{q}_1 = -\tilde{\mathbf{p}} + \frac{\mathbf{Q}}{2}, \tag{4.70b}$$

$$\mathbf{q}_2 = \tilde{\mathbf{p}} + \frac{\mathbf{Q}}{2}, \tag{4.70c}$$

where we introduced $\mathbf{q}_{\frac{1}{3}Q}$, similar to Eq. (4.57), such that its magnitude and polar angle are the same as in Eq. (4.58) but with a prefactor 1/3.

As we notice from the momentum conservation, the 2BC has an effect on both the two-body subsystem momentum, Eqs. (4.70b) and (4.70c), and the spectator particle momentum, Eq. (4.70a). On the other hand, the action on the quantum numbers is restricted to the two-body subsystem only, as a result Eq. (4.60) cannot be simplified as before. After performing the radial integrations and changing J^μ for the correct the NLO current operator, i.e., $j_+^{(-1)}$, in Eq. (4.60), we find

$$\mathcal{P}^{M'_J M'_T M_J M_T}_{(L'S')J'T'\,(LS)JT}(\mathbf{Q},p,p') = \int \frac{\mathrm{d}\hat{\mathbf{p}}}{(2\pi)^3} \int \mathrm{d}\hat{\mathbf{p}}\, \mathcal{Y}^{*J'M'_J}_{L'S'}(\hat{\mathbf{p}}')\, \langle \mathbf{p}'\, T' M'_T | \hat{\jmath}_+^{(-1)}(\mathbf{Q}) | \mathbf{p}\, T M_T \rangle\, \mathcal{Y}^{JM_J}_{LS}(\hat{\mathbf{p}})\,, \tag{4.71}$$

where the current operator acts on the two-body momentum, spin, isospin and orbital angular momentum. For the function $\mathcal{Q}$, the effect of the 2BC is given by

$$\mathcal{Q}^{m'_j m'_t m_j m_t}_{(\ell's')j't'\,(\ell s)jt}(\mathbf{Q},q,q') = \int \mathrm{d}\hat{\mathbf{q}}\, \mathcal{Y}^{*j'm'_j}_{\ell's'}(\hat{\mathbf{q}}_{\frac{1}{3}Q})\, \frac{\delta(q' - |\mathbf{q}_{\frac{1}{3}Q}|)}{q'\, |\mathbf{q}_{\frac{1}{3}Q}|}\, \mathcal{Y}^{jm_j}_{\ell s}(\hat{\mathbf{q}})\,, \tag{4.72}$$

where the delta function will introduce the shift in the trinucleon wave function, as before. Substituting these results, we find the three-body partial-wave expanded form factor expression for the NLO 2BC:

$$\begin{aligned} F_{\mathrm{M}}^{\mathrm{NLO}}(Q) =& \frac{3\sqrt{2}m_N}{Q(2\pi)^3} \frac{e\, g_a^2}{(2F_\pi)^2}\, G_{\mathrm{E}}^V(Q^2) \sum_{\alpha\alpha'} \int \mathrm{d}\mathbf{p} \int \mathrm{d}\mathbf{q} \int \mathrm{d}\mathbf{p}'\, \phi^*_{\alpha'}(p',\, |\mathbf{q}_{\frac{1}{3}Q}|)\, \phi_\alpha(p,\, q) \\ & \times \sum_{M_J M'_J} \sum_{m_j m'_j} \mathcal{C}^{\frac{1}{2}\,\frac{1}{2}}_{J'M'_J j'm'_j}\, \mathcal{C}^{\frac{1}{2}\,-\frac{1}{2}}_{JM_J jm_j} \sum_{m_\ell m'_\ell} \sum_{m_s} \mathcal{C}^{j'm'_j}_{\ell'm'_\ell \frac{1}{2}\, m_s}\, \mathcal{C}^{jm_j}_{\ell m_\ell \frac{1}{2}\, m_s}\, Y^*_{\ell'm'_\ell}(\hat{\mathbf{q}}_{\frac{1}{3}Q})\, Y_{\ell m_\ell}(\hat{\mathbf{q}}) \\ & \times \sum_{M_L M'_L} \sum_{M_S M'_S} \mathcal{C}^{J'M'_J}_{L'M'_L S'M'_S}\, \mathcal{C}^{JM_J}_{LM_L SM_S}\, Y^*_{L'M'_L}(\hat{\mathbf{p}}')\, Y_{LM_L}(\hat{\mathbf{p}})\, \Gamma^{\mathcal{M}_\mathcal{T}}_{T'T}\, \Sigma^{M'_S M_S}_{S'S}(\mathbf{Q},\mathbf{p}',\mathbf{p}). \end{aligned} \tag{4.73}$$

The isospin dependence is accounted for in the function $\Gamma^{\mathcal{M}_\mathcal{T}}_{T'T}$, which is given by

$$\Gamma^{\mathcal{M}_\mathcal{T}}_{T'T} = \sum_{M_T M'_T} \sum_{m_t} \mathcal{C}^{\frac{1}{2}\mathcal{M}_\mathcal{T}}_{T'M'_T \frac{1}{2} m_t}\, \mathcal{C}^{\frac{1}{2}\,\mathcal{M}_\mathcal{T}}_{TM_T \frac{1}{2}\, m_t}\, \langle T'M'_T |\, i(\boldsymbol{\tau}_1 \times \boldsymbol{\tau}_2)_z\, | TM_T \rangle\,, \tag{4.74}$$

and the spin and momentum operator action is summarized in $\Sigma^{M'_S M_S}_{S'S}(\mathbf{q}_1, \mathbf{q}_2)$, which is defined by

$$\begin{aligned} \Sigma^{M'_S M_S}_{S'S}(\mathbf{Q},\mathbf{p}',\mathbf{p}) = & \sum_{\{m_{s_i} m'_{s_i}\}} \mathcal{C}^{S'M'_S}_{\frac{1}{2}\, m'_{s_1}\, \frac{1}{2}\, m'_{s_2}}\, \mathcal{C}^{SM_S}_{\frac{1}{2}\, m_{s_1}\, \frac{1}{2}\, m_{s_2}} \\ & \times \langle \mathbf{p}'\, \tfrac{1}{2} m'_{s_1} \tfrac{1}{2} m'_{s_2} | \left(\sigma_{1+} - q_{1+} \frac{\boldsymbol{\sigma}_1 \cdot \mathbf{q}_1}{\omega^2_{q_1}} \right) \frac{\boldsymbol{\sigma}_2 \cdot \mathbf{q}_2}{\omega^2_{q_2}} + 1 \leftrightharpoons 2 | \mathbf{p}\, \tfrac{1}{2} m_{s_1} \tfrac{1}{2} m_{s_2} \rangle, \end{aligned} \tag{4.75}$$

where $\omega^2_{q_i} = q_i^2 + m_\pi^2$. This result for the trinucleon NLO magnetic form factor requires a few remarks. First, the Q dependence of the two-body subsystem is not as explicit as for the one-body form factor result, but is included in $\mathbf{q}_i$, see Eqs. (4.70b) and (4.70c). Second, compared to the one-body form factor there is an extra integration over $\mathbf{p}'$, and over the angular part of $\mathbf{p}$, resulting in a nine-dimensional integral. This implies a substantial increase in computational cost, as the integrals are still solved using the Gauss-Legendre method, see Section 4.3.3. Even though the integration could be sped up with adaptive methods, the calculation time was still acceptable. Finally, the expression is completely nondiagonal in α, and there are many sums over projection quantum numbers, which grow if configurations up to a high two-body angular momentum J are considered. We refer again to Appendix B.2 for detailed derivations of the expressions of the 2BC correction to the magnetic form factor.

The two-body NLO current operator depends on the nucleon axial coupling g_A, the pion decay amplitude F_π, the averaged pion mass m_π, and the nucleon mass m_N for which we adopt the following values 1.27, 92.3 MeV, 138.039 MeV, and 938.918 MeV, respectively. The first combination of interactions (EMN), as described above, is used to calculate the magnetic form factor results. We do not show results for the second combination of interactions, as their results for the magnetic form factor provide the same qualitative observations made for the charge form factor, see Fig. 4.10 and the corresponding discussion.

In Fig. 4.11 we show the triton (left column) and the helion (right column) magnetic form factor, in units of μ_N, for calculations with the one-body current operator (top row) and with NLO or 2BC corrections (bottom row) as a function of the momentum transfer Q, in units of fm^{-1}. The results are, again, given for the N^{3}LO EMN interaction for cutoffs $\Lambda = 420$, 450, and 500 MeV by the dashed-dotted, dashed and solid lines, together with the DoBs for the 500 MeV result. As for the charge form factor results, we compare to one-body current operator (yellow line) and NLO corrected (green line) results from Ref. [70].

The magnetic form factor results for all cutoffs disagree with experiment over the entire momentum-transfer region and underestimates the data until the minimum, even when the truncation uncertainty is considered. At $Q = 0$, the result deviates from the experimental value and for the low momentum transfer this offset appears constant. Compared to the one-body charge form factor, for which higher-order corrections vanish at $Q = 0$, the higher-order magnetic form factor corrections are sizeable at $Q = 0$, and adjust the offset at low momentum transfers.

The bottom row shows results with 2BC corrections included. Values at low momentum transfer are shifted up for both nuclei, but still disagree with experiment. This statement is made more quantitative in the next chapter, where we study magnetic moments in more detail. Note that the DoB intervals of the one-body and two-body results do not overlap at low momentum transfers, which results from the inconsistent inclusion of the operators compared to the order of the interaction. At higher Q, the minimum is shifted to higher momentum transfers, such that the central value of the triton result reproduces the minimum and the central value of the helion result is slightly too low, confirming once again that 2BC provide essential corrections to the one-body current operator. Nevertheless, within the truncation uncertainty, the higher Q region overlaps experimental data completely. The cutoff variation is slightly reduced with respect to the one-body result. If we again assume a similar truncation uncertainty for the results from Piarulli *et al.* [70], then they agree with our results and with experiment. Stronger conclusion could be made if a smaller uncertainty is realized by including higher-order operators in the calculation.

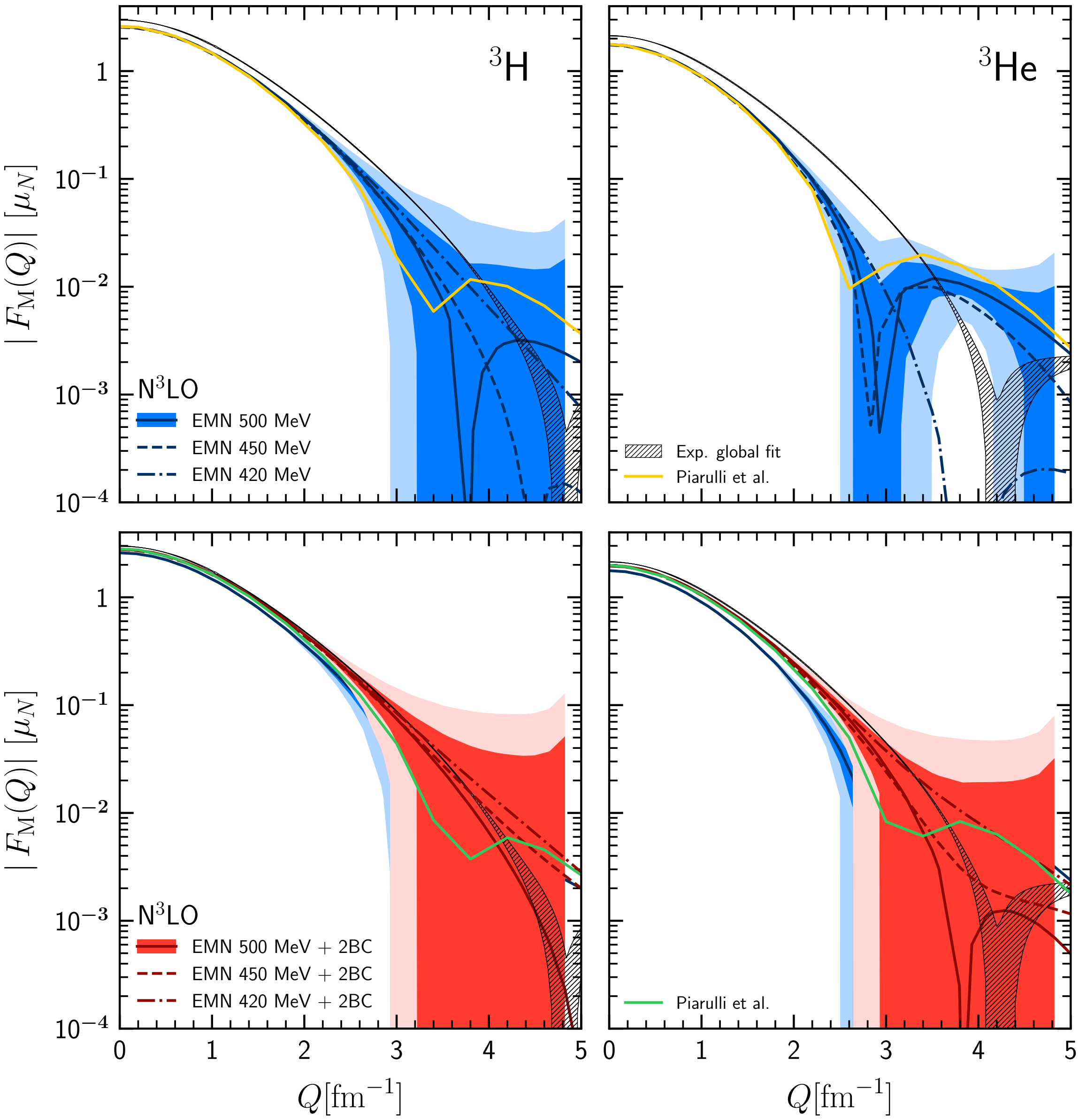

Figure 4.11: Triton (left column) and helion (right column) magnetic form factor, in units of μ_N, as a function of Q, in units of fm^{-1}, compared to experimental results and other calculations. Top row: Calculations with the one-body current operator and the N^{3}LO EMN interaction for three different cutoffs: 500 MeV (*solid line*), 450 MeV (*dashed line*), 420 MeV (*dashed-dotted line*). The blue bands are as in Fig. 4.9. Note that the experimental normalization value, i.e., $F_{\mathrm{M}}(0)$, is not reproduced. The hatched bands are the magnetic form factor parametrization from Ref. [75] and the yellow line are one-body current operator calculations from Ref. [70]. Bottom row: Magnetic form factor calculations including the NLO current operator correction, denoted by 2BC, for the same cutoffs. The light red band represents the 95% DoB of the 500 MeV result and the darker red band the 68% DoB. The green line shows the NLO result from Ref. [70].

4.5 CHARGE AND MAGNETIC RADIUS DETERMINATION

At low- and zero-momentum transfer, the electron probes the long-range behavior of the wave function, and thus, is sensitive to the radius. Extracting the radius from the electromagnetic form factors is done by determining the slope at zero momentum transfer. As stated before, nuclear form factors are Fourier transforms of the spatial charge and current distributions:[9]

$$F_{\mathrm{X}}(Q) = \frac{4\pi}{QZ}\int \mathrm{d}\mathbf{r}\,\rho_{\mathrm{X}}(\mathbf{r})\,e^{i\mathbf{Q}\cdot\mathbf{r}}, \tag{4.76}$$

where X denotes the charge (C) or magnetic (M) form factor, such that $\rho_{\mathrm{X}}(\mathbf{r})$ is either the charge or magnetic spatial density. For small momentum transfers, the exponential can be expanded in even powers of $q\mathbf{r}$, such that Eq. (4.76) becomes

$$F_{\mathrm{X}}(Q) = 1 - \frac{1}{6}Q^2\langle r_{\mathrm{X}}^2\rangle + \frac{1}{5!}Q^4\langle r_{\mathrm{X}}^4\rangle + ..., \tag{4.77}$$

with $\langle r_{\mathrm{X}}^2\rangle$ the mean-square radius of density $\rho_{\mathrm{X}}(\mathbf{r})$. Hence, the derivative of Eq. (4.77) at zero momentum transfer determines the mean-square electromagnetic radius:

$$\langle r_{\mathrm{X}}^2\rangle = -6\left.\frac{\mathrm{d}F_{\mathrm{X}}(Q^2)}{\mathrm{d}Q^2}\right|_{Q^2=0}. \tag{4.78}$$

A few remarks are in order: First, the result in Eq. (4.78) strictly speaking only determines the nuclear charge radius. However, the same value is extracted from the magnetic form factor. Even though a magnetic radius definition in terms of only the wave functions does not exist, the Q^2-dependent term at $Q = 0$ can be considered a genuine magnetic radius which can be compared to the same value from experiment. Second, the slope of the form factor determines the radius only to the degree that higher-order effects are negligible. Equation (4.78) is also used to determine experimental radii. Because experiments measure form factors at finite momentum transfer, assumptions have to be made to extrapolate results to $Q^2 = 0$, resulting in model dependent uncertainties for the radii. Finally, by including nucleon form factors in our calculations, we account for the proton and the neutron size. See Section 4.2 for details about the electromagnetic nucleon radii and the nucleon form factor parametrization that we use.

4.5.1 Deuteron electromagnetic radii

The deuteron is a loosely bound system, indicating that it is an extended nucleus. As a result, the deuteron rms radius is rather independent of the NN interaction details, and instead, depends on the binding energy. There are two quantities commonly quantifying the deuteron size: the point-proton radius, r_{pt}, and the charge radius, r_{ch}. The latter is obtained by calculating the slope of the charge form factor, as described above, while the former depends on the wave functions only. They are related by

$$r_{\mathrm{ch}}^2 = r_{\mathrm{pt}}^2 + r_{\mathrm{p}}^2 + r_{\mathrm{n}}^2 + \frac{3}{4m_{\mathrm{p}}^2}, \tag{4.79}$$

---

[9] For the deuteron, the symbol G_{X} is implied instead of F_{X}.

Table 4.1: Cumulative contributions to the deuteron root-mean-square charge and magnetic radius obtained with the one-body charge and current operator at LO, NLO, N^2LO, and N^3LO for the EMN NN interaction with cutoffs $\Lambda = 450$, 500, and 550 MeV. The quoted errors show the estimated truncation uncertainty for each order. Experimental values for the rms charge and magnetic radius from e-d scattering are 2.130(10) fm [218] and 2.072(18) fm [218], respectively.

	r_{ch} [fm]			r_{m} [fm]		
	450 MeV	500 MeV	550 MeV	450 MeV	500 MeV	550 MeV
LO	2.069	2.075	2.082	2.029	2.041	2.052
NLO	2.129(20)	2.129(20)	2.128(19)	2.094(21)	2.095(19)	2.095(17)
N^2LO	2.127(3)	2.127(3)	2.126(3)	2.100(3)	2.097(3)	2.098(3)
N^3LO	2.125(1)	2.129(1)	2.128(1)	2.095(1)	2.098(1)	2.098(1)

where r_{p}^2 is the proton mean-square charge radius, r_{n}^2 the neutron mean-square charge radius, m_{p} the proton mass, and the last term is known as the *Darwin-Foldy* correction and is of relativistic origin. As we can see from Eq. (4.79), the charge radius consists of the deuteron internal structure, r_{pt}^2, with contributions from the individual nucleons, $r_{\mathrm{p,n}}^2$. Essentially, this corresponds to including the individual nucleon structure by folding the nucleon form factors into the charge operator. It is important to make this distinction as experimental and theoretical results provide both quantities. In this thesis, we only quote results for the deuteron rms charge radius obtained with Eq. (4.78) from the form factor G_{C}.

The experimental and theoretical deuteron rms magnetic radius are also extracted from the slope of the magnetic form factor, G_{M}, at zero momentum transfer. They are typically less studied than the rms charge radius. However, new muonic experiments on light nuclei will also provide precise magnetic radii, such that the importance of 2BC effects on the magnetic radius can be studied in detail [219].

The deuteron rms charge and magnetic radius obtained with the chiral EMN NN interaction at four different orders and cutoffs $\Lambda = 450$, 500, and 550 MeV are presented in Table 4.1. For the nucleon form factors, the parametrization from Ref. [179] was used and for orders $i \geqslant 2$ truncation uncertainties are given. The rms charge radius results are well within the experimental error, and even close to the central value. On the other hand, the rms magnetic radii slightly overestimate the experimental value. These two observations are traced back to the fact that higher-order charge operators have a negligible effect on the charge radius [70], because their corrections vanish at $Q = 0$, whereas higher-order current operators do change the zero- and low-momentum transfer region of the magnetic form factor. As the 2BC corrections for the deuteron are of order 10^{-3} [70], they are expected to have a rather minor effect on the rms magnetic radius. In general, the cutoff dependence is below 1% for both radii at all orders, except the magnetic radius at LO, confirming the observation about the cutoff dependence made for the form factor results, see Section 4.3. All results show a systematic order-by-order convergence with overlapping errors. Truncation errors following the EKM approach [96] were also calculated and are of the same size.

To revisit the deuteron-radius puzzle mentioned in Section 4.1.1, current chiral EFT calculations are still not precise enough to differentiate between the muonic and atomic deuterium results for which the error is one order-of-magnitude smaller. However, nuclear structure calculations can help to reduce nuclear uncertainties which are important in the

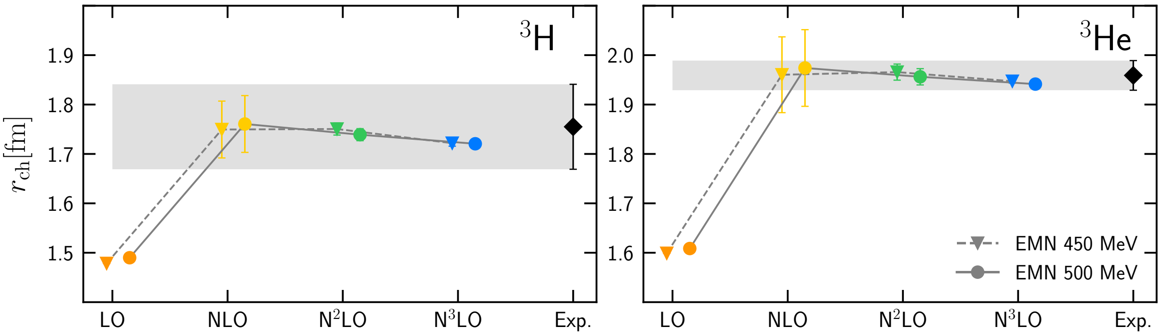

Figure 4.12: Trinucleon rms charge radius, in units of fm, at different orders of the chiral expansion compared to the experimental radius. The four different orders of the EMN NN + 3N interaction are denoted by orange (LO), yellow (NLO), green (N^{2}LO), and blue (N^{3}LO). The dashed and dotted lines connect results with a cutoff of 450 MeV and 500 MeV, respectively. Truncation uncertainty estimates are shown by the error bars. Left panel: Results for the triton. Right panel: Results for the helion. The experimental values are 1.755(86) fm and 1.959(30) fm for the triton and helion, respectively, from Ref. [75].

analysis, see, e.g., Refs. [220, 221]. We refer again to Appendix E for more information about the deuteron-radius puzzle and for the experimental values. If we consider the range of the charge radii resulting from the different cutoffs, then we notice that the CODATA-2018 [65] and the muonic spectroscopy value [66] lie within.

4.5.2 Trinucleon electromagnetic radii

In this section we present and discuss the trinucleon electromagnetic radii results, obtained with the two different combinations for the interactions, as outlined in Section 4.4.1. The electromagnetic radii are extracted from Eq. (4.78) from the charge, i.e., F_C, and magnetic form factor, i.e., F_M.

Figure 4.12 displays the results for the triton and the helion charge radius, calculated at different chiral orders of the EMN NN + 3N interaction for cutoffs 450 and 500 MeV and with the one-body charge operator. The cumulative contributions to the charge radius are presented by showing the order-by-order increased result, which at NLO already agrees well with experimental radii. In addition, the truncation uncertainty at each order, except LO, is given by the error bars. At N^{3}LO, the errors are smaller than the symbols. Equivalently to the form factor results, the radii show a systematic order-by-order convergence with overlapping errors and exhibit only minor cutoff dependence. The values at N^{3}LO are given by 1.722(8) fm and 1.721(6) fm for the EMN 450 and 500 MeV triton charge radius, and 1.947(8) fm and 1.941(8) fm for the EMN 450 and 500 MeV helion charge radius. The triton results agree within error bars with values by Piarulli *et al.* [70], which are 1.750 – 1.762 fm, obtained with the N^{3}LO*/N^{2}LO* (first value) and N^{3}LO/N^{2}LO (second value) interactions, see Section 4.4.1 for details about the notation. To the contrary, the helion results which are given by 1.958 – 1.955 fm [70] are somewhat higher. The experimental values are not precise enough to distinguish between the impact of the interaction on the radius. A recent *ab initio* study of medium-mass properties based on the same interactions found too large charge radii, and underbound ground-state energies [161]. More results for light and heavy

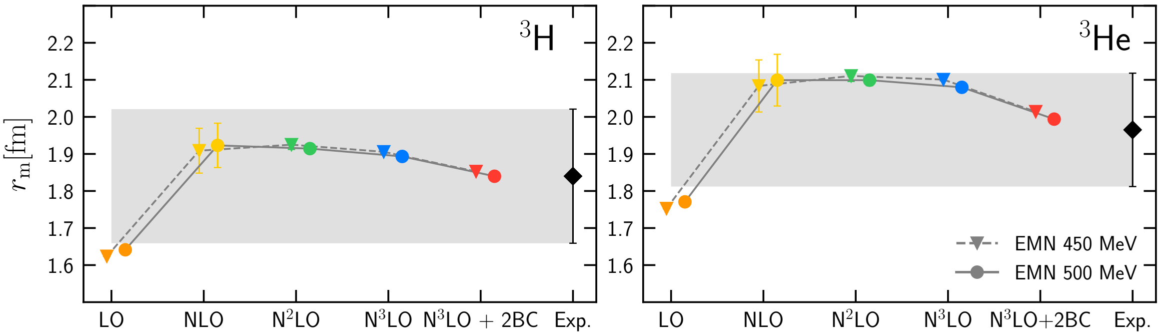

Figure 4.13: Trinucleon rms magnetic radius, in units of fm, at different orders of the chiral expansion compared to the experimental radius. The colors and lines are as in Fig. 4.12, with the addition of red symbols to represent results which include NLO 2BC corrections. Left panel: Results for the triton. Right panel: Results for the helion. The experimental values are 1.840(181) fm and 1.965(153) fm for the triton and helion, respectively, from Ref. [75].

nuclei are necessary to make firm conclusions about the systematics of this new family of interactions.

We present results for the trinucleon magnetic radii in Fig. 4.13, obtained with the same interactions as described for the charge radii above, with additionally results that include NLO 2BC corrections in red. Recall that these corrections to the form factor are obtained by adding Eq. (4.73) to Eq. (4.68). Note that the 2BCs are not included at the correct order according to chiral EFT. Two-body current corrections substantially reduce the values, shifting them towards the central experimental results. They are the dominant correction to the magnetic radius, with an effect up to 5% [70], and are essential for agreement with experiment. This case in particular, the large error of the experimental results prevent a clear conclusion about the 2BC contributions. The magnetic radii at N^{3}LO with 2BCs are 1.853(7) fm 1.840(6) fm for the triton and 2.014(7) fm 1.994(6) fm for the helion, where the former value is for $\Lambda = 450$ MeV and the latter $\Lambda = 500$ MeV, and show a slightly larger cutoff spread that the charge radii. Again, the triton values agree within error with $1.845 - 1.854$ fm [70], and disagree with the helion results, $1.983 - 1.990$ fm [70], which are somewhat higher than our results.

Table 4.2 contains results for the trinucleon rms charge and magnetic radii, obtained with unevolved and SRG-evolved EM NN 500 MeV and NN + 3N interactions, see Fig. 4.10 for charge form factor results of the same interactions. The results are ordered at increasing SRG-scale.

The trinucleon rms charge radii agree with experiment within error bars. Both the triton and the helion show the same trends for the different interactions: the biggest correction from inclusion of 3N interactions is seen for the unevolved potential and is $\sim 3\%$, while the SRG-evolved interactions show corrections of $\leqslant 1\%$. This confirms the qualitative observation made in Section 4.4.1 that the slope is slightly decreased if 3N interactions are included. In general, accounting for 3N interactions moves the result closer to the central value of the experimental result. The observed trend that charge radii are somewhat too small for nuclei ranging to ^{100}Sn [216, 217] is not confirmed by the trinucleon charge radii. Presumably, the reason being that they are too much correlated with the helium-4 charge radius and the triton binding energy which are used to fit these interactions. Finally, the results for the EM

Table 4.2: Root-mean-square charge and magnetic radii in fm for the triton (^{3}H) and the helion (^{3}He), obtained with NN EM 500 MeV and NN + 3N interactions evolved to different scales as introduced in the text. The arrow depicts the addition of 2BC corrections in going from the left to the right column (for magnetic radii). Experimental values for the triton and helion rms charge and magnetic radius are from Ref. [75].

	r_{ch} [fm]		r_{m} [fm]			
Interaction	^{3}H	^{3}He	^{3}H		^{3}He	
Exp.	1.755(86)	1.959(30)	1.840(181)		1.965(153)	
			$\xrightarrow{\text{2BC}}$		$\xrightarrow{\text{2BC}}$	
EM 500 MeV	1.795	2.022	1.917	1.872	2.153	2.068
EM 500 MeV + 3N(2.0 fm^{-1})	1.746	1.961	1.917	1.864	2.097	2.011
$\lambda_{\mathrm{SRG}} = 2.2\ \mathrm{fm}^{-1}$	1.766	1.979	1.922	1.873	2.097	2.010
$\lambda_{\mathrm{SRG}}/\Lambda_{\mathrm{3N}} = 2.2/2.0\ \mathrm{fm}^{-1}$	1.753	1.964	1.910	1.860	2.087	2.007
$\lambda_{\mathrm{SRG}} = 1.8\ \mathrm{fm}^{-1}$	1.770	1.979	1.919	1.873	2.091	2.017
$\lambda_{\mathrm{SRG}}/\Lambda_{\mathrm{3N}} = 1.8/2.0\ \mathrm{fm}^{-1}$	1.760	1.969	1.911	1.864	2.085	2.010

interactions are slightly larger compared to the results obtained with the EMN interactions, see Fig. 4.12. Again, the too large experimental error prevents to make solid conclusions.

The rms magnetic radii in Table 4.2 include 2BC corrections, denoted by the arrow. Similar trends for the 3N dependence and the SRG evolution are observed as for the charge radii. Although, the inclusion of 3N interactions has a slightly smaller effect on the magnetic radii. The dominant correction comes from the 2BCs and is of the order of $\sim 5\%$. Their effect brings the theory results, again, closer to experimental values and is of the same size as observed in Ref. [70]. Unquestionably, the magnetic radii and form factor results show the importance of 2BCs for mangetic observables of the trinucleons.

5

MAGNETIC PROPERTIES OF LIGHT NUCLEI

Static moments and electromagnetic transitions are important observables from nuclear structure theory to study nuclear interactions. These observables are sensitive to details of the wave function, providing an ideal testing ground for our understanding of the nucleus. Magnetic observables, in particular, depend heavily on the dynamics between nucleons in the form of many-body currents, which are derived from the chiral Lagrangian. In this chapter we introduce the formalism to calculate magnetic moments and transitions, and we present results for several light nuclei using currents and interactions from chiral EFT.

The chapter is organized as follows: in Section 5.1 we briefly mention the status of theoretical calculations of magnetic observables with currents derived from chiral EFT. Then, in Section 5.2 we restate the electromagnetic interaction Hamiltonian and, in contrast to the previous chapter, we make a multipole expansion of the radiation field. The resulting electromagnetic operators can be classified according to their behavior under parity. In addition, we present the operators in the long-wavelength limit and their connection with conventional multipole operators. Having shown this connection, the conventional multipole operators can then be used to calculate magnetic moments and magnetic transitions. In fact, the normalization of the form factor, which we primarily discussed in the previous chapter, also provides the nuclear magnetic moment, and in Section 5.3 we demonstrate this statement. Then, we include corrections to the conventional magnetic moment operator arising from 2BCs in Section 5.4. After introducing these two possibilities to calculate the magnetic moment, we present results for the magnetic moment of the deuteron and the trinucleons obtained from the form factor normalization in Section 5.5.

In Section 5.6, as a preparation to embed the operator in many-body calculations we make a transformation of the magnetic moment operator matrix elements to a single-particle HO basis and benchmark the transformation by calculating magnetic moments for the trinucleons and comparing them to the form factor normalization. Finally, in Section 5.7 we present results for the magnetic moment and magnetic $M1$ transition strength for ^{6}Li, which for the first time are completely calculated within chiral EFT, and compare them to measurements from a new experiment in Section 5.8. These results have been presented in our paper, which is available as a preprint Ref. [222].

5.1 CURRENT THEORETICAL STATUS

Except for the two- and three-nucleon electromagnetic form factor calculations from Refs. [70, 186], which we presented in the previous chapter, there are presently no full chiral EFT results for magnetic observables of higher-mass nuclei. Therefore, we summarize calculations for magnetic moments and electromagnetic transitions obtained with a hybrid approach that include corrections beyond the one-body operator.

Pioneering hybrid calculations for the magnetic moment of two- and three-nucleon systems were performed in Refs. [223, 224], where the authors included currents up to N^3LO in the magnetic moment operator. Using this approach, they found agreement for the isoscalar and isovector trinucleon magnetic moments with experimental values at the $2-3\%$ level. The most comprehensive study of magnetic moments and electromagnetic transitions with currents from chiral EFT and wave functions from realistic nuclear Hamiltonians for $A \leqslant 9$ nuclei was carried out in Ref. [51]. In that work, Green's function Monte-Carlo (GFMC) methods were used to solve the many-body problem. As can be observed, both magnetic moments and transitions are in good agreement with experimental data once 2BCs are included, i.e., red diamonds are closer to the black stars. Although the agreement with experiment is good, the hybrid approach fails to understand the nuclear dynamics from a microscopic point of view. Therefore, in the rest of this chapter, we present the required steps to extend the calculation of magnetic moments and magnetic transitions from few-nucleon systems to light nuclei with currents and interactions from chiral EFT.

5.2 ELECTROMAGNETIC INTERACTION

We begin by stating the electromagnetic interaction Hamiltonian, which describes the interaction between an external probe and the nucleus [225]:

$$H_{\mathrm{int}} = -e_{\mathrm{p}} \int \mathrm{d}\mathbf{r}\, \mathbf{j}(\mathbf{r}) \cdot \mathbf{A}(\mathbf{r}) + \frac{e_{\mathrm{p}}^2}{8\pi} \int \mathrm{d}\mathbf{r} \int \mathrm{d}\mathbf{r}'\, \frac{\rho(\mathbf{r})\rho(\mathbf{r}')}{|\mathbf{r}-\mathbf{r}'|}, \tag{5.1}$$

where $\mathbf{j}(\mathbf{r})$ represents the nuclear current density in coordinate space and $\rho(\mathbf{r})$ the nuclear charge density. Here $\mathbf{A}(r)$ is the vector potential of the quantized radiation field, which is given by

$$\mathbf{A}(\mathbf{r}) = \sum_{\mathbf{q}} \sum_{\rho=1,2} \frac{1}{(2\omega_q \Omega)^{1/2}} \left[\mathbf{e}_{\mathbf{q}\rho}\, a_{\mathbf{q}\rho}\, e^{i\mathbf{q}\cdot\mathbf{r}} + \mathrm{h.c.}\right], \tag{5.2}$$

where $\mathbf{q}$ represents the momentum carried by the photon, $\omega_q = |\mathbf{q}|$ is the photon or momentum transfer magnitude, $\mathbf{e}_{\mathbf{q}\rho}$, with $\rho = (1,2)$, defines two unit vectors transverse to the momentum transfer, $a_{\mathbf{q}\rho}$ represents the field operators, and h.c. denotes the Hermitian conjugate. So far, the interaction in Eq. (5.1) does not make specific assumptions about the target, except for the presence of local current and charge densities $\mathbf{j}(\mathbf{r})$ and $\rho(\mathbf{r})$: it can include corrections like two-body operators. Note that the sum over $\mathbf{q}$ represents a quantized integral, with periodic boundary conditions in a large box of volume Ω. We define circularly polarized unit vectors,

$\mathbf{e}_{\mathbf{q}\lambda}$, and field operators, $a_{\mathbf{q}\lambda}$, by

$$\begin{aligned} \mathbf{e}_{\mathbf{q}\pm1} &\equiv \mp\frac{1}{\sqrt{2}}(\mathbf{e}_{q1} \pm i\mathbf{e}_{q2}), \qquad \mathbf{e}_0 \equiv \frac{q}{|\mathbf{q}|}, \text{ and} \\ a_{\mathbf{q}\pm1} &\equiv \mp\frac{1}{\sqrt{2}}(a_{q1} \mp i a_{q2}). \end{aligned} \tag{5.3}$$

Furthermore, we let $\mathbf{q}$ define the z-axis. With these definitions the vector potential can be rewritten as

$$\mathbf{A}(\mathbf{r}) = \sum_{\mathbf{q}} \sum_{\lambda=\pm1} \frac{1}{(2\omega_q\Omega)^{1/2}} \left[\mathbf{e}_{\mathbf{q}\lambda}\, a_{\mathbf{q}\lambda}\, e^{i\mathbf{q}\cdot\mathbf{r}} + \text{h.c.}\right]. \tag{5.4}$$

5.2.1 Multipole expansion

The nuclear matrix element of an electromagnetic process where a photon is absorbed or emitted is given by [225][1]

$$\langle J_f M_f\, \mathbf{q}\lambda | \hat{H}' | J_i M_i\rangle = \frac{-e_{\mathrm{p}}}{(2\omega_q\Omega)^{1/2}} \langle J_f M_f\, \mathbf{q}\lambda | \int \mathrm{d}\mathbf{r}\, e^{i\mathbf{q}\cdot\mathbf{r}} \mathbf{e}_{\mathbf{q}\lambda}\, \mathbf{j}(\mathbf{r})\, | J_i M_i\rangle\,, \tag{5.5}$$

where $e^{i\mathbf{q}\cdot\mathbf{r}}\mathbf{e}_{\mathbf{q}\lambda}$ represents the photons as circularly polarized plane waves, $|\mathbf{q}\lambda\rangle = a^\dagger_{\mathbf{q}\lambda}\,|0\rangle$, and where it is assumed that the nuclear state, $|JM\rangle$, is an eigenstate of total angular momentum. Note that we denoted the term linear in the vector potential by

$$\hat{H}' \equiv \int \mathrm{d}\mathbf{r}\, e^{i\mathbf{q}\cdot\mathbf{r}} \mathbf{e}_{\mathbf{q}\lambda}\, \mathbf{j}(\mathbf{r}). \tag{5.6}$$

The goal is to make a multipole expansion of this expression to decompose the current density into operators that commute with total angular momentum. This eventually will reduce the calculation complexity.

We continue by expanding the plane wave in Eq. (5.5) into partial waves and coupling the polarization vector with the resulting spherical harmonics:

$$\mathbf{e}_{\mathbf{q}\lambda} e^{i\mathbf{q}\cdot\mathbf{r}} = \sum_\ell \sum_J \sqrt{4\pi(2\ell+1)}\, j_\ell(qx)\, \mathcal{C}^{J\lambda}_{l01\lambda}\, \mathcal{Y}^{J\lambda}_{\ell 1}(\hat{\mathbf{r}})\,. \tag{5.7}$$

Through the properties of Clebsch-Gordan coefficients and spherical Bessel functions we can rewrite the expansion to finally arrive at [58, 225]

$$\frac{-e_{\mathrm{p}}}{\sqrt{2\omega_q\Omega}} \int \mathrm{d}\mathbf{r}\, e^{-i\mathbf{q}\cdot\mathbf{r}}\, \mathbf{e}^\dagger_{\mathbf{q}\lambda} \cdot \hat{\boldsymbol{\jmath}}(\mathbf{r}) = e_{\mathrm{p}} \sum_{J\geq1} (-1)^J \sqrt{\frac{2\pi(2J+1)}{2\omega_q\Omega}}\, \left[\hat{T}^{\mathrm{el}}_{J-\lambda}(q) + \hat{T}^{\mathrm{mag}}_{J-\lambda}(q)\right]. \tag{5.8}$$

Here, J is the angular momentum carried by the photon. The transverse *electric* and *magnetic*

---

[1] The photon described here is allowed to be either a real photon, i.e., $|\mathbf{k}| = \omega$, or a virtual photon, denoted by $\mathbf{q}$ with $\mathbf{q}^2 < \omega^2$. Recall that the virtual photon is exchanged between the probe and the target during the scattering event. To connect with the previous chapter and to keep the notation consistent we use $q = |\mathbf{q}|$ instead of $k = |\mathbf{k}|$.

multipole operators are defined by [58, 225]

$$\hat{T}^{\mathrm{el}}_{JM}(q) \equiv \frac{1}{q}\int \mathrm{d}\mathbf{r} \left[\boldsymbol{\nabla} \times j_J(qx)\,\mathcal{Y}^{JM}_{J1}(\hat{\mathbf{r}})\right] \cdot \hat{\boldsymbol{\jmath}}(\mathbf{r}), \tag{5.9}$$

$$\hat{T}^{\mathrm{mag}}_{JM}(q) \equiv \int \mathrm{d}\mathbf{r} \left[j_J(qx)\,\mathcal{Y}^{JM}_{J1}(\hat{\mathbf{r}})\right] \cdot \hat{\boldsymbol{\jmath}}(\mathbf{r}). \tag{5.10}$$

Up to now, the expressions are general in that the form of the target current density is left unspecified. It can consist of one-, two-, or many-body operators.

Tensor structure of transverse operators

The results obtained in Eqs. (5.9) and (5.10) are classified as *spherical tensor operators of rank J*. Their evaluation between angular momentum eigenstates is considerably reduced by applying the Wigner-Eckart theorem, which states that the dependence of any spherical tensor operator matrix element on the projection quantum number can be entirely accounted for by Clebsch-Gordan coefficients [166]:

$$\langle j'm'|\hat{T}_{k\kappa}|jm\rangle = \frac{(-1)^{2k}}{\sqrt{2j'+1}}\,\mathcal{C}^{j'm'}_{jmk\kappa}\;\langle j'||\hat{T}_k||j\rangle\,, \tag{5.11}$$

where $\hat{T}_{k\kappa}$ is a spherical tensor of rank k with projection κ and $\langle j'||\hat{T}_k||j\rangle$ defines the so-called *reduced matrix element*. Basically, the action of the tensor operator adds a state with angular momentum k to the state with angular momentum j, which is accounted for by the Clebsch-Gordan coefficient.

Angular momentum selection rules for the matrix elements can be obtained by applying the Wigner-Eckart theorem to the transverse operators:

$$\langle J_f M_f|\hat{T}_{JM}|J_i M_i\rangle = \frac{(-1)^{2J}}{\sqrt{2J_f+1}}\,\mathcal{C}^{J_f M_f}_{J_i M_i J M}\;\langle J_f||\hat{T}_J||J_i\rangle\,. \tag{5.12}$$

The Clebsch-Gordan coefficients restrict the multipole operators that contribute to a transition matrix element by the triangle inequality, i.e., $|J_f - J_i| \leqslant J \leqslant J_f + J_i$. As such, the multipole expansion expands the electromagnetic interaction in terms of exchanged angular momentum. Together with the resulting tensor operators in Eq. (5.8), the Clebsch-Gordan coefficients imply that $M_f = M_i - \lambda$. Furthermore, given that the sum starts at $J = 1$, real one-photon transitions $J = 0 \to J = 0$ are forbidden.

The behavior of the transverse operators under parity is deduced from the individual components that make up the operator. Given the parity of the coupled spherical harmonics,[2] $\hat{\Pi}\,\mathcal{Y}^{JM}_{J1}(\hat{\mathbf{r}})\;\hat{\Pi}^{-1} = (-1)^J \mathcal{Y}^{JM}_{J1}(\hat{\mathbf{r}})$, and the gradient, $\hat{\Pi}\,\boldsymbol{\nabla}\,\hat{\Pi}^{-1} = -\boldsymbol{\nabla}$, we find the transformation relations for the transverse operators

$$\hat{\Pi}\,\hat{T}^{\mathrm{el}}_{JM}\,\hat{\Pi}^{-1} = (-1)^J\,\hat{T}^{\mathrm{el}}_{JM}, \qquad \hat{\Pi}\,\hat{T}^{\mathrm{mag}}_{JM}\,\hat{\Pi}^{-1} = (-1)^{J+1}\,\hat{T}^{\mathrm{mag}}_{JM}. \tag{5.13}$$

These parity selection rules dictate if only parity-conserving or parity-changing operators contribute to a specific transition, depending on the initial and final state of the matrix element.

---

[2] The parity operator is denoted by $\hat{\Pi}$ and changes the sign of spatial coordinates. Note that $\hat{\Pi}^2 = 1$ such that its eigenvalues are ±1.

One-body current densities

We now consider the transverse multipole operators for the one-body current density. To a first approximation, the electromagnetic interaction between probe and target nucleus happens both with the *convection current density*, which originates from the motion of the individual charged particles, and with the *intrinsic magnetization density* coming from the magnetic moments of the individual nucleons. Accordingly, the following change can be made for the interaction term

$$\begin{aligned}-e_{\mathrm{p}}\int \mathrm{d}\mathbf{r}\,\hat{\boldsymbol{\jmath}}(\mathbf{r})\cdot\mathbf{A}(\mathbf{r}) \to -e_{\mathrm{p}}\int\mathrm{d}\mathbf{r}\,\hat{\boldsymbol{\jmath}}_c(\mathbf{r}) - e_{\mathrm{p}}\int\mathrm{d}\mathbf{r}\,\hat{\boldsymbol{\mu}}(\mathbf{r})\cdot[\boldsymbol{\nabla}\times\mathbf{A}(\mathbf{r})]\\ = -e_{\mathrm{p}}\int\mathrm{d}\mathbf{r}\,[\hat{\boldsymbol{\jmath}}_c(\mathbf{r})+\boldsymbol{\nabla}\times\hat{\boldsymbol{\mu}}(\mathbf{r})]\cdot\mathbf{A}(\mathbf{r}),\end{aligned} \tag{5.14}$$

where the coordinate-space expressions for the convection current density and intrinsic magnetization density are, respectively, given by [58, 225]

$$\hat{\boldsymbol{\jmath}}_c(\mathbf{r}) = \sum_{i=1}^{Z}\delta(\mathbf{r}-\mathbf{r}_i)\,\frac{\mathbf{p}_i}{m_{\mathrm{p}}} \quad \text{and} \quad \hat{\boldsymbol{\mu}}(\mathbf{r}) = \frac{\mu_N}{e}\sum_{i=1}^{A}\lambda_i\,\boldsymbol{\sigma}_i\,\delta(\mathbf{r}-\mathbf{r}_i), \tag{5.15}$$

with m_{p} the proton mass, λ_i the magnetic moment of the ith nucleon in units of nuclear magnetons, and $\boldsymbol{\sigma}_i$ the vector of Pauli matrices $(\sigma_x, \sigma_y, \sigma_z)$. This substitution allows one to rewrite the multipole operators in terms of the individual contributions to the one-body current density [58, 225]:

$$\hat{T}^{\mathrm{el}}_{JM}(q) \equiv \frac{1}{q}\int\mathrm{d}\mathbf{r}\left([\boldsymbol{\nabla}\times j_J(qr)\,\mathcal{Y}^{JM}_{J1}(\hat{\mathbf{r}})\,]\cdot\hat{\boldsymbol{\jmath}}_c(\mathbf{r}) + q^2\, j_J(qr)\,\mathcal{Y}^{JM}_{J1}(\hat{\mathbf{r}})\,\cdot\hat{\boldsymbol{\mu}}(\mathbf{r})\right), \tag{5.16}$$

$$\hat{T}^{\mathrm{mag}}_{JM}(q) \equiv \int\mathrm{d}\mathbf{r}\left(j_J(qr)\,\mathcal{Y}^{JM}_{J1}(\hat{\mathbf{r}})\,\cdot\hat{\boldsymbol{\jmath}}_c(\mathbf{r}) + [\boldsymbol{\nabla}\times j_J(qr)\,\mathcal{Y}^{JM}_{J1}(\hat{\mathbf{r}})\,]\cdot\hat{\boldsymbol{\mu}}(\mathbf{r})\right). \tag{5.17}$$

For low momentum transfers, the spherical Bessel function can be expanded such that only a few multipoles are necessary to reach a given accuracy. We discuss this limit below.

5.2.2 Long-wavelength limit

The momentum transfer in many electromagnetic processes is small. Therefore, as a result of $qR \ll 1$, where R is the typical nuclear size, only a few multipoles will contribute to the sums in Eqs. (5.9) and (5.10). In this case, the asymptotic spherical Bessel function can be written in its asymptotic form:[3]

$$\lim_{qr\to 0} j_J(qr) = \frac{(qr)^J}{(2J+1)!!}. \tag{5.18}$$

Taking into account the leading term and rewriting the transverse electric and magnetic multipole operators, Eqs. (5.16) and (5.17), their long-wavelength limit takes the form [58,

---

[3] The double factorial is given by $(2J+1)!! = 1\times 3\times \ldots \times (2J+1)$.

225]

$$\hat{T}^{\mathrm{el}}_{JM}(q) \approx \frac{q^J}{(2J+1)!!}\sqrt{\frac{J+1}{J}}\int \mathrm{d}\mathbf{r}\left[r^J Y_{JM}(\hat{\mathbf{r}})\,\hat{\rho}(\mathbf{r}) - \frac{iq}{J+1}\hat{\boldsymbol{\mu}}(\mathbf{r})\cdot(\mathbf{r}\times\boldsymbol{\nabla} r^J\,Y_{JM}(\hat{\mathbf{r}})\,)\right], \tag{5.19}$$

$$\hat{T}^{\mathrm{mag}}_{JM}(q) \approx i\frac{q^J}{(2J+1)!!}\sqrt{\frac{J+1}{J}}\int \mathrm{d}\mathbf{r}\left[\hat{\boldsymbol{\mu}}(\mathbf{r}) + \frac{1}{J+1}\mathbf{r}\times\hat{\boldsymbol{\jmath}}_c(\mathbf{r})\right]\cdot\boldsymbol{\nabla} r^J\,Y_{JM}(\hat{\mathbf{r}})\,. \tag{5.20}$$

These results are, except for a factor and power of q, equal to the static electric and magnetic multipole operators. Note that the second term in Eq. (5.19) is small considering the extra factor of q and the fact that the integration is over the nuclear volume. Therefore, this term is negligible for low momentum transfers and is usually left out.

To make the connection with the conventional multipole operators more explicit, we state the definitions of the electric and magnetic multipole operators. The *nuclear electric multipole operator* is defined by [226]

$$\hat{Q}_{\ell m} = \int \mathrm{d}\mathbf{r}\, r^\ell Y_{\ell m}(\hat{\mathbf{r}})\,\hat{\rho}(\mathbf{r}), \tag{5.21}$$

and determines the static multipole moments of multipolarity ℓ and projection m of the electric charge density by taking expectation values of the operator with respect to nuclear states $|\psi\rangle = |\xi J M_J\rangle$, where ξ collects all quantum numbers except the total angular momentum J and its porjection M_J. Usually, the static moments are defined in terms of maximal projection, i.e., $M_J = J$. For instance, the nuclear quadrupole moment is defined by

$$Q \equiv \sqrt{\frac{16\pi}{5}}\,\langle \xi J M = J|\hat{Q}_{20}|\xi J M = J\rangle = \int \mathrm{d}\mathbf{r}(3z^2 - r^2)\rho(\mathbf{r}), \tag{5.22}$$

where the prefactor cancels the normalization of the spherical harmonic in Eq. (5.21), such that Q matches the definition of its classical analog. In this case, the nuclear density is given by the absolute square of the wave functions $\rho(\mathbf{r}) = |\psi(\mathbf{r})|^2$. Note that the first term of the electric transverse operator in Eq. (5.19) is, except for a factor and power of q, equal to Eq. (5.21).

The *nuclear magnetic multipole operator* is given by [226]

$$\hat{\mathcal{M}}^{\mathrm{mag}}_{\ell m} = \frac{1}{\ell+1}\int \mathrm{d}\mathbf{r}\,\mathbf{r}\times\hat{\boldsymbol{\jmath}}(\mathbf{r})\cdot\boldsymbol{\nabla} r^\ell Y_{\ell m}(\mathbf{r})\,, \tag{5.23}$$

which, again, equals the result in Eq. (5.20) up to a factor and powers in q. The $\ell = 1$ multipole equals, up to a factor, the magnetic dipole moment operator:[4]

$$\hat{\boldsymbol{\mu}} = \frac{1}{2}\int \mathrm{d}\mathbf{r}\,\mathbf{r}\times\hat{\boldsymbol{\jmath}}(\mathbf{r}). \tag{5.24}$$

In addition to the connection with the transverse magnetic multipole operator, this result shows the dependence of the magnetic dipole moment operator on the nuclear current operator.

From here on, we denote the magnetic dipole moment operator simply with *magnetic moment operator*. As $\hat{\boldsymbol{\jmath}}(\mathbf{r})$ can be expanded as a sum of many-body operators, the magnetic moment operator exhibits the same feature given Eq. (5.24). In a future section we examine the corrections to the magnetic moment operator due to the the NLO 2BCs in more detail.

---

[4] The spherical harmonics in Eq. (5.23) provide a factor of $\sqrt{\frac{3}{4\pi}}$.

To summarize, many electromagnetic processes involve low momentum transfers such that the spherical Bessel function can be expanded and the transverse operators rewritten. This leads to the result and conclusion that both transverse multipole operators are equal to, except for a factor and power of q, the conventional electric and magnetic multipole operators, which are used to define the nuclear static moments. In the next section we demonstrate the connection between these general results, the form factor normalization, and the static operators. Then, in Section 5.4 we examine the magnetic dipole moment operator and its corrections in greater detail.

5.3 Magnetic moment from form factor

As we observed in Chapter 4, the Born approximation of the electron scattering process naturally introduces two form factors $F_1(Q)$ and $F_2(Q)$ associated with the vertex. The former is related to the electromagnetic coupling of the Dirac type, while the latter to a Pauli-type coupling, hence their labeling as Dirac and Pauli form factors. These form factors do not permit a direct physical interpretation. In Ref. [227], however, it was determined for a spin-1/2 particle with internal structure, that a linear combination of them can be connected to the distribution of charge and magnetization inside the particle by calculating moments of the expectation value of the current operator. A generalization of this statement for particles with a spin up to $J = 3/2$ was given in Ref. [228]. For particles with spin 1, an extra form factor for the quadrupole charge distribution is introduced, and particles with spin 3/2 have an additional octopole magnetic form factor. Interestingly, employing these physical form factors in the analysis of scattering experiments, as opposed to $F_1(Q)$ and $F_2(Q)$, turns out to be more straightforward due to the elimination of the interference term in the cross-section expression, recall the discussion in Section 4.2.

Given that form factors are related to the distribution of charge and magnetization it is of interest to calculate moments of the various distributions, as they give insights into the shape of the distribution itself. Particularly, the normalization of the form factors is of interest. A classical interpretation of the form factors follows from their connection with the definition of classical multipole moments and from the observation that their normalization coincides with static electromagnetic moments, which we illustrate below. First, we discuss the normalization of the magnetic form factor of a spin-1/2 particle, to then show the normalization of the three form factors of a spin-1 particle.

5.3.1 Spin-1/2 nucleus

We show that the normalization of the magnetic form factor of a spin-1/2 particle equals the magnetic moment, following Refs. [227, 228], by calculating the expectation value of Eq. (5.24). As a reminder, we restate the matrix element of the current operator between particle states $|P\lambda\rangle$, with four-momentum P and helicity λ:

$$\langle P'\lambda'|J_\mu(0)|P\lambda\rangle = ie\,\bar{v}(P',\lambda')\left[\gamma^\mu F_1(Q^2) + \kappa_j \frac{i\sigma^{\mu\nu}q_\nu}{2m_T}F_2(Q^2)\right]v(P,\lambda), \tag{5.25}$$

where m_T is the target particle mass and where the current operator is evaluated at $x = 0$, see Section 4.2 for more details. The matrix element of the current operator between momentum states can be written as

$$\langle P'|J_\mu(x)|P\rangle = \mathrm{e}^{-i(P'-P)\cdot x}\,\langle P'|J_\mu(0)|P\rangle\,. \tag{5.26}$$

To find the normalization, we use a wave packet $\int \mathrm{d}\mathbf{P}\, a(\mathbf{P})\,|P\lambda\rangle$, where $a(\mathbf{P})$ is the amplitude of the wave packet. The expectation value of the magnetic moment operator with respect to the wave packets becomes [227]

$$\begin{aligned}\langle \boldsymbol{\mu}\rangle =& \frac{1}{2}\int \mathrm{d}\mathbf{P}'\, a^*(P')\int \mathrm{d}\mathbf{P}\, a(P)\int \mathrm{d}\mathbf{r}\, e^{-i(P'-P)\cdot x}\,\mathbf{r}\times\langle P'\,s'|\mathbf{j}(0)|P\,s\rangle\\ =&-(2\pi)^3\frac{i}{2}\int \mathrm{d}\mathbf{P}'\, a^*(P')\int \mathrm{d}\mathbf{P}\, a(P)\,\delta(\mathbf{P}'-\mathbf{P})\,\boldsymbol{\nabla}_P\times\langle P'\,\lambda'|\mathbf{j}(0)|P\,\lambda\rangle\, e^{i(P'_0-P_0)\cdot t},\end{aligned} \tag{5.27}$$

where in the last line the exponential was written as a Dirac delta function and the change $\mathbf{r}\to -i\boldsymbol{\nabla}_P$ was made. Substituting the expression for the matrix element, Eq. (5.25), performing an integration by parts, and choosing a specific wave packet $|a(\mathbf{P})|^2 = \delta(\mathbf{P})$, yields the final result

$$\langle \boldsymbol{\mu}\rangle = e\Big[F_1(0)+F_2(0)\Big]\bar{v}_{\lambda'}(0)\boldsymbol{\sigma}v_\lambda(0) = e\,F_{\mathrm{M}}(0)\,\bar{v}_{\lambda'}(0)\,\boldsymbol{\sigma}\,v_\lambda(0). \tag{5.28}$$

The magnetic moment follows by selecting the z-component of the operator and the helicities in their maximal projection.

5.3.2 Spin-1 nucleus

Because the deuteron has an integer spin of 1, its electromagnetic distribution is described by three form factors: the charge, the quadrupole, and the magnetic form factor, whose normalization give the total charge, the quadrupole moment, and the magnetic moment. In the following we present how the normalization of each form factor is obtained using the impulse approximation, i.e., one-body operators only, and the deuteron wave functions, defined in Section 3.1.4. The steps follow the same ideas discussed in Section 5.2, however, for the deuteron in particular an elegant solution can be found by starting from the one-body operators instead of the general multipole expressions.

The effect of the momentum transfer is given by $\exp(i/2\mathbf{Q}\cdot\mathbf{r})$, where $\mathbf{Q}=\mathbf{P}'-\mathbf{P}$ and where $\mathbf{Q}$ is chosen along the positive z-direction. We restate the expression for the charge form factor, this time with the exponential which enforces the momentum conservation:

$$G_{\mathrm{C}}(Q) = \frac{1}{3}\sum_{M_J}\langle M_J|\mathrm{e}^{i\frac{1}{2}\mathbf{Q}\cdot\mathbf{r}}|M_J\rangle\,. \tag{5.29}$$

Inserting complete sets of coordinate states and making a multipole expansion of the exponential yields

$$G_{\mathrm{C}}(Q) = \int \mathrm{d}\mathbf{r}\,\psi^*_{\mathrm{d}}(\mathbf{r})\sum_{\lambda=0}^{\infty}(2\lambda+1)i^\lambda j_\lambda(Qr)P_\lambda(\cos\theta)\psi_{\mathrm{d}}(\mathbf{r}). \tag{5.30}$$

Next, we expand the deuteron wave functions into partial waves, use Clebsch-Gordan and spherical-harmonic properties, and perform the angular integration, so that the final result of the form factor expressed in coordinate space is given by [229]

$$G_{\mathrm{C}}(Q) = \int \mathrm{d}r \, \left[u^2(r) + w^2(r)\right] j_0\left(\frac{Qr}{2}\right). \tag{5.31}$$

The normalization follows immediately by using the asymptotic form of the spherical Bessel function given in Eq. (5.18).

For the quadrupole form factor, retrieving the normalization is accomplished along the same lines as for the charge form factor. If we fill out the $\exp(i/2\mathbf{Q}\cdot\mathbf{r})$ in the definition for the quadrupole form factor and perform the same steps as outlined above, then we find [229]

$$\begin{aligned} G_{\mathrm{Q}}(Q) =& \frac{1}{2\eta}\left[\langle M_J = 0|\mathrm{e}^{i\frac{1}{2}\mathbf{Q}\cdot\mathbf{r}}|M_J = 0\rangle - \langle M_J = 1|\mathrm{e}^{i\frac{1}{2}\mathbf{Q}\cdot\mathbf{r}}|M_J = 1\rangle\right] \\ =& \frac{3\sqrt{2}}{2\eta}\int \mathrm{d}r \left[u^2(r)w^2(r) + \frac{w^2(r)}{2\sqrt{2}}\right] j_2\left(\frac{Qr}{2}\right). \end{aligned} \tag{5.32}$$

The asymptotic form of the spherical Bessel function for $J = 2$ equals $(qr)^2/15$, such that the normalization of the previous equation provides the quadrupole moment:

$$G_{\mathrm{Q}}(0) = M_{\mathrm{d}}^2 Q_{\mathrm{d}} = M_{\mathrm{d}}^2 \frac{1}{\sqrt{50}} \int \mathrm{d}r \, r^2 \left[u^2(r)w^2(r) + \frac{w^2(r)}{2\sqrt{2}}\right]. \tag{5.33}$$

Finally, the magnetic form factor normalization is, again, obtained through the same procedure. The coordinate space expression is given by [229]

$$\begin{aligned} G_{\mathrm{M}}(Q) = \int \mathrm{d}r \Big\{ & \left[\mu_s(u^2(r) + w^2(r)) - \frac{3}{2}(\mu_s - \frac{1}{2})w^2(r)\right] j_0\left(\frac{Qr}{2}\right) \\ & + \frac{1}{\sqrt{2}}w(r)\left[\mu_s(u(r) + \frac{1}{\sqrt{2}}w(r)) + \frac{3}{\sqrt{8}}w(r)\right] j_2\left(\frac{Qr}{2}\right)\Big\}, \end{aligned} \tag{5.34}$$

such that the expansion of the spherical Bessel functions and the limit of zero momentum transfer yields the following result

$$G_{\mathrm{M}}(0) = \mu_{\mathrm{s}} - \frac{3}{2}\left(\mu_{\mathrm{s}} - \frac{1}{2}\right) P_{\mathrm{D}}, \tag{5.35}$$

which is exactly the expression given in Section 3.1.4.

5.4 Magnetic moment operator

5.4.1 NLO magnetic moment operator from current operator

The magnetic moment operator is given in Eq. (5.24), where $\mathbf{j}(\mathbf{r})$ is the coordinate-space implementation of the nuclear current density. Fourier transforming Eq. (5.24) yields the magnetic moment operator in momentum space [89]:

$$\hat{\boldsymbol{\mu}} = -\frac{i}{2} \lim_{\mathbf{q}\to 0} \boldsymbol{\nabla}_{\mathbf{q}} \times \hat{\boldsymbol{\jmath}}(\mathbf{Q}), \tag{5.36}$$

where the gradient operator with respect to $\mathbf{Q}$ is given by $\boldsymbol{\nabla}_{\mathbf{Q}} = (\partial_{Q_x}, \partial_{Q_y}, \partial_{Q_z})$. Recall from Chapter 1 that the current operator can be expanded as a sum of one- and many-body operators. As a result the magnetic moment operator has an identical expansion. The one-, two-, and many-body expansion of the magnetic moment operator is given by

$$\hat{\boldsymbol{\mu}} = \sum_{i}^{A} \hat{\boldsymbol{\mu}}_{1\mathrm{b},i} + \sum_{ij}^{A} \hat{\boldsymbol{\mu}}_{2\mathrm{b},ij} + ..., \tag{5.37}$$

where $\hat{\boldsymbol{\mu}}_{1\mathrm{b},i}$ is the single-nucleon contribution, $\hat{\boldsymbol{\mu}}_{2\mathrm{b},ij}$ the two-body part, and the ellipsis denotes the many-body operators. If the expansion is terminated after the two-body part, then the total operator is obtained by summing over all individual nucleons and all pairs.

Because 2BC operators are translationally invariant with respect to the two-body center-of-mass $\mathbf{R}_{\mathrm{NN}}$, the center-of-mass motion can be factored out:

$$\hat{\boldsymbol{\jmath}}_{2\mathrm{b}}(\mathbf{Q}, \mathbf{R}_{\mathrm{NN}}) = e^{i\mathbf{Q}\cdot\mathbf{R}_{\mathrm{NN}}} \hat{\boldsymbol{\jmath}}_{2\mathrm{b}}(\mathbf{Q}). \tag{5.38}$$

Accordingly, Eq. (5.36) splits into two parts, where one term depends on the relative position between the two particles and the other on the center of mass. The former is the so-called *intrinsic* magnetic moment operator and is given by [89]

$$\hat{\boldsymbol{\mu}}_{2\mathrm{b}}^{\mathrm{int}} = -\frac{i}{2} \lim_{\mathbf{Q}\to 0} \boldsymbol{\nabla}_{\mathbf{Q}} \times \hat{\boldsymbol{\jmath}}_{2\mathrm{b}}(\mathbf{Q}). \tag{5.39}$$

The other term is the *Sachs* contribution [230]:

$$\hat{\boldsymbol{\mu}}_{2\mathrm{b}}^{\mathrm{Sachs}} = \frac{1}{2} \mathbf{R}_{\mathrm{NN}} \times \hat{\boldsymbol{\jmath}}_{2\mathrm{b}}(\mathbf{Q}). \tag{5.40}$$

This division into two parts is a general result valid for 2BC operators at any order.

Similar to the treatment of the magnetic form factor in the previous chapter, we continue by considering the NLO correction to the magnetic moment operator. The total NLO correction to the magnetic operator is given by

$$\hat{\boldsymbol{\mu}}_{2\mathrm{b}}^{\mathrm{NLO}} = \hat{\boldsymbol{\mu}}_{2\mathrm{b}}^{\mathrm{NLO,\ int}} + \hat{\boldsymbol{\mu}}_{2\mathrm{b}}^{\mathrm{NLO,\ Sachs}}. \tag{5.41}$$

In the next two subsections we proceed by first Fourier transforming the momentum-space 2BC expressions to then show the explicit coordinate-space form of the intrinsic and Sachs contribution to the NLO magnetic moment operator.

5.4.2 Two-body current Fourier transform

As we have seen in Section 2.4.3, the NLO 2BC momentum-space expressions can be linked to two separate diagrams. One is the so-called *seagull* $\mathbf{j}^{\mathrm{s}}$ and the other the *pion-in-flight* diagram $\mathbf{j}^{\pi}$, see Fig. 2.2. Their sum constitutes the NLO correction to the current operator and is given by

$$\mathbf{j}_{2\mathrm{b}}^{(-1)} = \mathbf{j}^{\mathrm{s}} + \mathbf{j}^{\pi}, \tag{5.42}$$

where we introduced a notation for both terms. We restate the momentum-space expression for both [70]:

$$\mathbf{j}^{\mathrm{s}}(\mathbf{q}_1,\mathbf{q}_2) = -ie\frac{g_A^2}{F_\pi^2}\,G_{\mathrm{E}}^V(Q^2)\,(\boldsymbol{\tau}_1\times\boldsymbol{\tau}_2)_z\left[\boldsymbol{\sigma}_1\frac{\boldsymbol{\sigma}_2\cdot\mathbf{q}_2}{\omega_{q_2}^2}-\boldsymbol{\sigma}_2\frac{\boldsymbol{\sigma}_1\cdot\mathbf{q}_1}{\omega_{q_1}^2}\right], \tag{5.43}$$

$$\mathbf{j}^{\pi}(\mathbf{q}_1,\mathbf{q}_2) = -ie\frac{g_A^2}{F_\pi^2}\,G_{\mathrm{E}}^V(Q^2)\,(\boldsymbol{\tau}_1\times\boldsymbol{\tau}_2)_z(\mathbf{q}_2-\mathbf{q}_1)\frac{\boldsymbol{\sigma}_1\cdot\mathbf{q}_1}{\omega_{q_1}^2}\frac{\boldsymbol{\sigma}_2\cdot\mathbf{q}_2}{\omega_{q_2}^2}, \tag{5.44}$$

where $\mathbf{q}_i=\mathbf{k}_i'-\mathbf{k}_i$, $\omega_{q_i}^2=q_i^2+m_\pi^2$, m_π is the pion mass, and $\boldsymbol{\tau}_i$ are the nucleon isospin Pauli matrices. Their Fourier transforms provide the coordinate-space expressions,

$$\mathbf{j}^{\mathrm{s}}(\mathbf{Q},\mathbf{r},\mathbf{R}_{\mathrm{NN}}) = e\frac{g_A^2m_\pi^2}{4\pi F_\pi^2}(\boldsymbol{\tau}_1\times\boldsymbol{\tau}_2)_z\,e^{i\mathbf{Q}\cdot\mathbf{R}_{\mathrm{NN}}}\left[e^{i\frac{\mathbf{Q}}{2}\cdot\mathbf{r}}\boldsymbol{\sigma}_1(\boldsymbol{\sigma}_2\cdot\hat{r})+e^{-i\frac{\mathbf{Q}}{2}\cdot\mathbf{r}}\boldsymbol{\sigma}_2(\boldsymbol{\sigma}_1\cdot\hat{r})\right]f(r), \tag{5.45}$$

$$\mathbf{j}^{\pi}(\mathbf{Q},\mathbf{r},\mathbf{R}_{\mathrm{NN}}) = e\frac{2\,g_A^2}{F_\pi^2}(\boldsymbol{\tau}_1\times\boldsymbol{\tau}_2)_z\,e^{i\mathbf{Q}\cdot\mathbf{R}_{\mathrm{NN}}}\left[\boldsymbol{\sigma}_1\cdot\left(\frac{\mathbf{Q}}{2}-i\boldsymbol{\nabla}_{\mathbf{r}}\right)\right]\left[\boldsymbol{\sigma}_2\cdot\left(\frac{\mathbf{Q}}{2}+i\boldsymbol{\nabla}_r\right)\right]\boldsymbol{\nabla}_{\mathbf{r}}I(\mathbf{r},\mathbf{Q}), \tag{5.46}$$

where $r=|\mathbf{r}|$, $\hat{r}=\frac{\mathbf{r}}{r}$ is the unit vector defined by the relative coordinate $\mathbf{r}=\mathbf{x}_1-\mathbf{x}_2$, and $\boldsymbol{\nabla}_{\mathbf{r}}$ the gradient with respect to that coordinate. The functions $f(r)$ and $I(\mathbf{Q},\mathbf{r})$ are given by

$$f(r)\equiv\left(1+\frac{1}{m_\pi r}\right)\frac{e^{-m_\pi r}}{m_\pi r}, \tag{5.47}$$

$$I(\mathbf{Q},\mathbf{r})\equiv\int_{\mathbf{p}}\frac{e^{i\mathbf{p}\cdot\mathbf{r}}}{\left[m_\pi^2+(\mathbf{p}-\frac{\mathbf{Q}}{2})^2\right]\left[m_\pi^2+(\mathbf{p}+\frac{\mathbf{Q}}{2})^2\right]}. \tag{5.48}$$

By examining Eqs. (5.45) and (5.46), we can easily observe that the two-body center-of-mass dependence of the NLO 2BC factorizes. A step-by-step derivation of the Fourier transforms is given in Appendix C.1.

5.4.3 Intrinsic and Sachs operators

The NLO magnetic moment operator in coordinate-space is given by substituting the NLO 2BC operator in Eq. (5.36), which yields

$$\boldsymbol{\mu}_{2\mathrm{b}}^{\mathrm{NLO}}(\mathbf{r}) = -\frac{i}{2}\lim_{\mathbf{Q}\to 0}\boldsymbol{\nabla}_{\mathbf{q}}\times\left(e^{i\mathbf{Q}\cdot\mathbf{R}_{\mathrm{NN}}}\mathbf{j}_{2\mathrm{b}}^{(-1)}(\mathbf{Q},\mathbf{r})\right), \tag{5.49}$$

where we have explicitly showed the factorization of the center-of-mass dependence. Employing the vector identity $\boldsymbol{\nabla}\times(\psi\mathbf{A})=\psi(\boldsymbol{\nabla}\times\mathbf{A})+(\boldsymbol{\nabla}\psi)\times\mathbf{A}$ in Eq. (5.49) we find the NLO intrinsic and Sachs [230] contributions to the magnetic moment operator:

$$\boldsymbol{\mu}_{2\mathrm{b}}^{\mathrm{NLO,\ int}}(\mathbf{r}) = -\frac{i}{2}\lim_{\mathbf{Q}\to 0}e^{i\mathbf{Q}\cdot\mathbf{R}_{\mathrm{NN}}}\left(\boldsymbol{\nabla}_{\mathbf{Q}}\times\mathbf{j}_{2\mathrm{b}}^{(-1)}(\mathbf{Q},\mathbf{r})\right), \tag{5.50}$$

$$\boldsymbol{\mu}_{2\mathrm{b}}^{\mathrm{NLO,\ Sachs}}(\mathbf{r}) = \frac{1}{2}\lim_{\mathbf{Q}\to 0}e^{i\mathbf{Q}\cdot\mathbf{R}_{\mathrm{NN}}}\,\mathbf{R}_{\mathrm{NN}}\times\mathbf{j}_{2\mathrm{b}}^{(-1)}(\mathbf{Q}). \tag{5.51}$$

The result for the Sachs term is given by

$$\boldsymbol{\mu}_{2\mathrm{b}}^{\mathrm{NLO,\ Sachs}}(\mathbf{r}) = -\frac{1}{2}(\boldsymbol{\tau}_1\times\boldsymbol{\tau}_2)_z\,V_{1\pi}(r)\,\mathbf{R}_{\mathrm{NN}}\times\mathbf{r}, \tag{5.52}$$

where $V_{1\pi}(r)$ is the coordinate-space one-pion-exchange potential:

$$V_{1\pi}(r) = \frac{m_\pi^2}{12\pi}\frac{g_A^2}{F_\pi^2}(\boldsymbol{\tau}_1\cdot\boldsymbol{\tau}_2)\left\{\left[S_{12}\left(1+\frac{3}{m_\pi r}+\frac{3}{(m_\pi r)^2}\right)+\boldsymbol{\sigma}_1\cdot\boldsymbol{\sigma}_2\right]\frac{e^{-m_\pi r}}{r}-\frac{4\pi}{3}\boldsymbol{\sigma}_1\cdot\boldsymbol{\sigma}_2\delta(r)\right\}, \tag{5.53}$$

with $S_{12} = 3\hat{r}\cdot\boldsymbol{\sigma}_1\hat{r}\cdot\boldsymbol{\sigma}_2 - \boldsymbol{\sigma}_1\cdot\boldsymbol{\sigma}_2$. Remarkably, the NLO Sachs term is uniquely determined by the one-pion-exchange potential only and does not depend on the current operator.[5]

The intrinsic magnetic moment operator is obtained by substituting the expressions for the seagull and pion-in-flight diagrams, Eqs. (5.45) and (5.46), into Eq. (C.10). For the seagull term this results in

$$\boldsymbol{\mu}_{\text{2b}}^{\text{int, s}}(\mathbf{r}) = e\frac{g_A^2 m_\pi}{16\pi F_\pi^2}(\boldsymbol{\tau}_1\times\boldsymbol{\tau}_2)_z\left[\hat{r}\times\boldsymbol{\sigma}_1(\boldsymbol{\sigma}_2\cdot\hat{r})-\hat{r}\times\boldsymbol{\sigma}_2(\boldsymbol{\sigma}_1\cdot\hat{r})\right] m_\pi r\, f(r). \tag{5.54}$$

Substituting the pion-in-flight current yields

$$\boldsymbol{\mu}_{\text{2b}}^{\text{int, }\pi}(\mathbf{r}) = e\frac{2\,g_A^2}{F_\pi^2}(\boldsymbol{\tau}_1\times\boldsymbol{\tau}_2)_z\lim_{\mathbf{Q}\to 0}\boldsymbol{\nabla}_{\mathbf{Q}}\times\left[\boldsymbol{\sigma}_1\cdot\left(\frac{\mathbf{Q}}{2}-i\boldsymbol{\nabla}_r\right)\right]\left[\boldsymbol{\sigma}_2\cdot\left(\frac{\mathbf{Q}}{2}+i\boldsymbol{\nabla}_r\right)\right]\boldsymbol{\nabla}_r I(\mathbf{r},\mathbf{Q}). \tag{5.55}$$

Three distinct terms are identified before applying the curl to the expression:

$$\boldsymbol{\nabla}_{\mathbf{Q}}\times\left(\boldsymbol{\sigma}_1\cdot\frac{\mathbf{Q}}{2}\right)\left(\boldsymbol{\sigma}_2\cdot\frac{\mathbf{Q}}{2}\right)\boldsymbol{\nabla}_r I(\mathbf{r},\mathbf{Q}), \tag{5.56a}$$

$$\boldsymbol{\nabla}_{\mathbf{Q}}\times\left(-\boldsymbol{\sigma}_1\cdot i\boldsymbol{\nabla}_r\right)\left(\boldsymbol{\sigma}_2\cdot i\boldsymbol{\nabla}_r\right)\boldsymbol{\nabla}_r I(\mathbf{r},\mathbf{Q}), \tag{5.56b}$$

$$\boldsymbol{\nabla}_{\mathbf{Q}}\times\left[\left(\boldsymbol{\sigma}_1\cdot\frac{\mathbf{q}}{2}\right)\left(\boldsymbol{\sigma}_2\cdot i\boldsymbol{\nabla}_r\right)\boldsymbol{\nabla}_r I(\mathbf{r},\mathbf{Q})-\left(\boldsymbol{\sigma}_1\cdot i\boldsymbol{\nabla}_r\right)\left(\boldsymbol{\sigma}_2\cdot\frac{\mathbf{Q}}{2}\right)\boldsymbol{\nabla}_r I(\mathbf{r},\mathbf{Q})\right]. \tag{5.56c}$$

A detailed examination of each term can be found in Appendix C.2. Consequently, the result for the intrinsic pion-in-flight term is given by

$$\begin{aligned}\boldsymbol{\mu}_{\text{2b}}^{\text{int, }\pi}(\mathbf{r}) = &\frac{e g_A^2 m_\pi}{16\pi F_\pi^2}(\boldsymbol{\tau}_1\times\boldsymbol{\tau}_2)_z\left\{\left[(\hat{r}\cdot\boldsymbol{\sigma}_2)(\boldsymbol{\sigma}_1\times\hat{r})-(\hat{r}\cdot\boldsymbol{\sigma}_1)(\boldsymbol{\sigma}_2\times\hat{r})\right]\left(1+\frac{1}{m_\pi r}\right)\right.\\ &\left.-\frac{2}{m_\pi r}(\boldsymbol{\sigma}_1\times\boldsymbol{\sigma}_2)\right\}e^{-m_\pi r}.\end{aligned} \tag{5.57}$$

Summing the seagull, Eq. (5.54), and the pion-in-flight, Eq. (5.57), contributions yields the total intrinsic operator

$$\begin{aligned}\boldsymbol{\mu}_{\text{2b}}^{\text{NLO, int}}(\mathbf{r}) &= \boldsymbol{\mu}_{\text{2b}}^{\text{int, s}}(\mathbf{r})+\boldsymbol{\mu}_{\text{2b}}^{\text{int, }\pi}(\mathbf{r})\\ &= -\frac{g_A^2 m_\pi}{8\pi F_\pi^2}(\boldsymbol{\tau}_1\times\boldsymbol{\tau}_2)_z\left\{\left(1+\frac{1}{m_\pi r}\right)\left[(\boldsymbol{\sigma}_1\times\boldsymbol{\sigma}_2)\cdot\hat{r}\right]\hat{r}-(\boldsymbol{\sigma}_1\times\boldsymbol{\sigma}_2)\right\}e^{-m_\pi r}.\end{aligned} \tag{5.58}$$

The total NLO magnetic moment operator that is used in this work is given by the sum of the intrinsic, Eq. (5.58), and the Sachs contribution, Eq. (5.52):

$$\boldsymbol{\mu}_{\text{2b}}^{\text{NLO}}(\mathbf{r}) = \boldsymbol{\mu}_{\text{2b}}^{\text{NLO, int}}(\mathbf{r})+\boldsymbol{\mu}_{\text{2b}}^{\text{NLO, Sachs}}(\mathbf{r}). \tag{5.59}$$

---

[5] Given that the potential between the nucleons uniquely defines the Sachs term [89], higher-order Sachs contributions depend on higher-order parts of the NN potential. For example, the N^{3}LO Sachs term depends on two-pion-exchange parts of the potential entering the chiral expansion at that order.

Table 5.1: Deuteron magnetic moment in units of the nuclear magneton μ_N. Results are obtained with the one-body current operator at LO, NLO, N^2LO, and N^3LO (rows) of the EMN NN interaction for cutoffs $\Lambda = 450$, 500, and 550 MeV (columns). Values between brackets represent the truncation uncertainty. The experimental deuteron magnetic moment is given by 0.8574382338(22) μ_N [65].

	μ_d $[\mu_N]$		
	450 MeV	500 MeV	550 MeV
LO	0.843	0.838	0.835
NLO	0.861(12)	0.860(13)	0.859(13)
N^2LO	0.857(2)	0.854(2)	0.852(2)
N^3LO	0.854(1)	0.856(0)	0.856(1)

5.5 DEUTERON AND TRINUCLEON MAGNETIC MOMENTS

Deuteron

In Table 5.1 we present results for the deuteron magnetic moment obtained from the normalization of the magnetic form factor. The three columns correspond to values from three different cutoffs for the EMN NN interaction and each row contains results for increasing orders of the chiral expansion. Starting at NLO, truncation uncertainty estimates from the Bayesian analysis are displayed, see Section 4.3.4 for details. Results for all cutoffs exhibit systematic convergence, where each result at successive chiral order is contained in the interval of the previous one and at N^3LO there is only a very small cutoff dependence of $\leq 1\%$. Remarkably, one-body current calculations with the N^3LO interaction are within 1% of the experimental deuteron magnetic moment, which equals 0.8574382338(22) μ_N [65]. As previously noted, the NLO 2BC operator is isovector and, therefore, has no effect on the deuteron ground-state magnetic moment.

Higher-order isoscalar current operators introduce new LECs that have to be fixed. The deuteron magnetic moment is the observable of choice to constrain these new LECs [70, 89, 223, 224]. As a result, calculations that include higher-order corrections to the current operator always agree with experiment and results from other light nuclei are necessary to test the impact of these corrections.

Trinucleons

For the trinucleons we present results for the two combinations of interactions introduced in Section 4.4.1. Figure 5.1 displays the trinucleon magnetic moments in μ_N obtained from $F_\mathrm{M}(0)$ as a function of increasing chiral order for cutoffs 450 MeV, indicated by downward triangles and connected by dashed lines, and 500 MeV, indicated by circles and solid lines. Additionally, results for the unevolved interaction of the second combination are shown by purple squares and solid lines. They are compared to the experimental values of 2.9789624659(59) μ_N and $-2.127625307(25)$ μ_N for the triton and the helion, respectively.

The sign of magnetic moments can be understood to be driven by the valence nucleon. Therefore, given that the triton has a valence proton it is situated in the positive region, while the helion, which has a valence neutron, in the negative region. We observe that increasing the order of the interaction has almost no effect on the magnetic moment of the trinucleons.

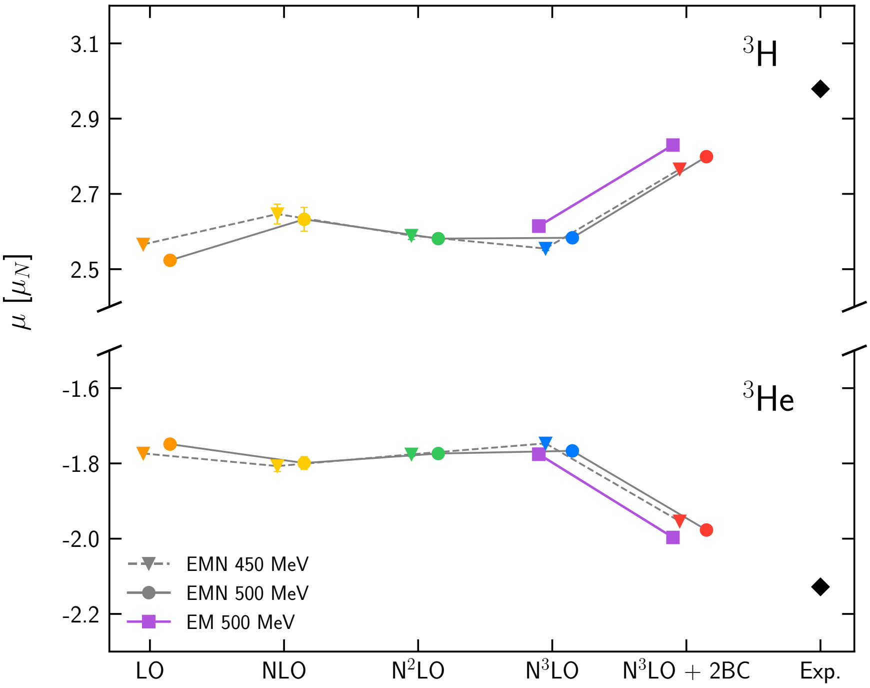

Figure 5.1: Triton and helion magnetic moments in units of μ_N as a function of increasing order of the chiral expansion for the EMN NN + 3N interaction at cutoffs 450 MeV (*downward triangles* and *dashed lines*) and 500 MeV (*circles* and *solid lines*). Results from calculations with LO, NLO, N^{2}LO, and N^{3}LO interactions are shown in orange, yellow, green, and blue, respectively. The inclusion of 2BCs in the operator is shown by the red symbols. Purple squares show the result of calculations with the N^{3}LO EM NN + N^{2}LO 3N interaction.

However, adding NLO 2BC corrections, shown by N^{3}LO + 2BC and red symbols, adjusts the value by $\sim 10\%$, making the agreement with experiment better. Similarly to the higher-order isoscalar current operators, their isovector counterparts also introduce new LECs that have to be fixed. Different strategies exist, however, commonly the isovector combination μ_V of the trinucleon magnetic moments is chosen to constrain these LECs [70, 89].[6] This has again the effect that the experimental magnetic moment is exactly reproduced if these higher-order corrections to the operator are taken into account. Therefore, one has to consider other light nuclei, i.e., $A > 3$, to study the effects of both higher-order isoscalar and isovector corrections.

Table 5.2 displays the results for calculations performed with the second combination of interactions. They include the N^{3}LO NN EM + N^{2}LO 3N for an unevolved interaction and for two SRG-evolved interactions to scales $\lambda_{\text{SRG}} = 2.2$ fm^{-1} and $\lambda_{\text{SRG}} = 1.8$ fm^{-1}. Additionally, results with and without 3N interactions are shown individually to evaluate their impact on the magnetic moment. For both nuclei, the left column shows results for the one-body current operator, while the right column shows results with NLO 2BC corrections. This addition is demonstrated by the arrow above the columns.

We start by discussing the impact of the SRG evolution. Going from the top of the columns to the bottom corresponds to starting with an unevolved interaction and ending with a fairly

---

[6] The isoscalar (μ_S) and isovector (μ_V) combinations of the trinucleon magnetic moments are defined by $\mu_S \equiv \mu_{\text{t}} + \mu_{\text{h}}$ and $\mu_V \equiv \mu_{\text{t}} - \mu_{\text{h}}$.

Table 5.2: Magnetic moments in units of μ_N for the triton and the helion, obtained with NN EM 500 MeV and NN + 3N interactions evolved to different SRG-scales as introduced in the text. The arrow depicts the addition of 2BC corrections in going from the left to the right column.

	μ [μ_N]			
Interaction	^{3}H		^{3}He	
Exp.	2.9789624659(59)		$-2.127625307(25)$	
		$\xrightarrow{\text{2BC}}$		$\xrightarrow{\text{2BC}}$
EM 500 MeV	2.579	2.793	-1.773	-1.983
EM 500 MeV + 3N(2.0 fm^{-1})	2.575	2.798	-1.772	-1.991
$\lambda_{\text{SRG}} = 2.2$ fm^{-1}	2.646	2.840	-1.808	-1.999
$\lambda_{\text{SRG}}/\Lambda_{\text{3N}} = 2.2/2.0$ fm^{-1}	2.640	2.839	-1.805	-2.000
$\lambda_{\text{SRG}} = 1.8$ fm^{-1}	2.672	2.852	-1.821	-1.999
$\lambda_{\text{SRG}}/\Lambda_{\text{3N}} = 1.8/2.0$ fm^{-1}	2.666	2.851	-1.818	-2.000

large SRG-evolved interaction. The trend is clear: SRG-evolving the interaction generates larger magnetic moments (in absolute values), shifting the values towards the experimental one in the case for the trinucleons. We expect that a consistent evolution of the operator restores the values from the evolved interactions to the value from the unevolved one. In Section 5.7 we will present results for ^{6}Li with consistently evolved operators to observe the effect of the evolution.

The impact of the 3N interaction contribution can be examined for each SRG-evolved scale by inspecting the each group of two rows. For each of the three interactions, the addition of 3N forces is almost negligible. This is in contrast to the effect observed for the magnetic radius where the value changed up to $\sim 2\%$, see Section 4.5.2.

Finally, we discuss the effect on the magnetic moment by including NLO 2BCs to the operator. As was seen in calculations with the first combination of interactions, here 2BCs change the magnetic moment up to 10% and substantially improve agreement with experiment. The observations made about 2BC effects on the magnetic moment in Fig. 5.1 and Table 5.2, and similarly on the magnetic form factor and magnetic radius, see Sections 4.4.2 and 4.5.2, are proof of their importance in a chiral framework.

5.6 Current matrix elements in harmonic-oscillator basis

Many basis-expansion methods rely on operator representations with respect to a single-particle basis. One example of such a basis which is often used is the HO basis, as it covers the relevant physics and is able to exploit symmetries of the operators. The goal of this section is to obtain a description of current operator matrix elements in terms of single-particle HO basis states.

Until now, we have expanded matrix elements of the current operator with respect to partial waves, either in a two-body or three-body angular-momentum coupled basis. These basis states allow for a direct transformation to relative HO basis states. Here, 'relative' indicates that this basis too is defined in terms of Jacobi coordinates, i.e., it is defined with respect to the relative and the center-of-mass motion. As both bases have the same angular dependence, only the radial component has to be transformed.

After a transformation to the relative HO basis, a second transformation is necessary to obtain single-particle basis states. This crucial step is achieved by performing the so-called *Talmi-Moshinsky transformation* [231, 232], which connects single-particle states to relative and center-of-mass states. The resulting current operator matrix elements with respect to single-particle HO basis states can then be used to construct many-body states, which are the key component in many-body calculations.

In Section 5.6.1 we lay the foundation by examining the transformation of the two-body basis and in Section 5.6.2 we consider the three-body basis. Note that the transformation of the matrix elements is unrelated to the deuteron or the trinucleon wave functions, but enables the use of partial-wave expanded matrix elements in calculations of observables for other light- and medium-mass nuclei. To finish the section, we present benchmark results in Section 5.6.3 of the trinucleon magnetic moments obtained from the expectation value of the magnetic moment operator between single-particle HO states.

5.6.1 Two-body harmonic-oscillator transformation

A general relative two-body HO basis state with relative orbital angular momentum L and total spin S coupled to relative angular momentum J is given by

$$|N(LS)JM_J\rangle = \sum_{M_L M_S} \mathcal{C}^{JM_J}_{LM_L SM_S}\, |N\, LM_L\, SM_S\rangle\,, \tag{5.60}$$

where N is the HO radial quantum number related to the relative coordinate and where we suppressed the isospin dependence. Considering only the relative orbital angular momentum part of these HO basis states, they can be expressed in terms of the relative momentum $\mathbf{p}$ by inserting a complete set of relative momentum states,

$$|NLM_L\rangle = \int \frac{\mathrm{d}\mathbf{p}}{(2\pi)^3}\, |\mathbf{p}\rangle\, \langle \mathbf{p}|NLM_L\rangle\,. \tag{5.61}$$

The overlap defines the HO wave function:

$$\langle \mathbf{p}|N\, LM_L\rangle \equiv \sqrt{(2\pi)^3} R_{NL}(p) Y_{LM_L}(\hat{\mathbf{p}})\,. \tag{5.62}$$

Here, the radial part of the overlap is given by [233]

$$R_{NL}(p) = (-1)^N \sqrt{\frac{2n!\, b^3}{\Gamma(n+l+\frac{3}{2})}}\, (pb)^L\, e^{-\frac{1}{2}p^2b^2}\, L_N^{(L+\frac{1}{2})}(p^2b^2), \tag{5.63}$$

where $b^{-1} = \sqrt{m_N \Omega}$ is the oscillator parameter with oscillator frequency Ω which sets the width of the HO potential, $L_n^{(\alpha)}(x)$ represents the *generalized Laguerre polynomials*, and $\Gamma(x)$ the well-known gamma function. Note that the spherical harmonic contains the angular dependence, equivalent to the partial-wave states we discussed in Section 3.1.2.

By inserting a complete set of partial waves, defined in Section 3.1.2, in Eq. (5.61) and using the definition of the overlap from Eq. (5.62), we find the connection between the HO basis states and the partial-wave basis states as follows

$$\begin{aligned}|NLM_L\rangle &= \int \frac{\mathrm{d}\mathbf{p}}{(2\pi)^3}\sqrt{(2\pi)^3}R_{NL}(p)Y_{LM_L}(\hat{\mathbf{p}}) \sum_{L'M'_L}\int \mathrm{d}p'\,p'^2\sqrt{(2\pi)^3}\frac{\delta(p-p')}{p\,p'}Y^*_{L'M'_L}(\hat{\mathbf{p}}')\,|p'L'M'_L\rangle \\ &= \int \mathrm{d}p\,p^2\,R_{NL}(p)\,|pLM_L\rangle\,. \end{aligned} \tag{5.64}$$

This result allows us to express the relative two-body HO current operator matrix elements in terms of two-body partial-wave expanded matrix elements:

$$\begin{aligned}\langle N'(L'S')J'M'_J\,T'M'_T|J^\mu|N(LS)JM_J\,TM_T\rangle &= \int \mathrm{d}p'\,p'^2\,R_{N'L'}(p')\int \mathrm{d}p\,p^2\,R_{NL}(p) \\ &\quad\times \langle p'(L'S')J'M'_J\,T'M'_T|J^\mu|p(LS)JM_J\,TM_T\rangle\,,\end{aligned} \tag{5.65}$$

where we accounted for spin and isospin degrees of freedom and coupled orbital angular momentum L and spin S to the total angular momentum $\mathbf{J}=\mathbf{L}+\mathbf{S}$. This HO transformation of the two-body partial waves concludes the first step in obtaining a matrix element expansion in terms of single-particle HO basis states. In the following we continue by transforming the relative HO basis to a single-particle basis.

The basis states presented in Eq. (5.61) are formulated in terms of the coordinate system introduced in Section 3.1.1. With respect to this coordinate system, the HO Hamiltonian is given by

$$\hat{H}_{\mathrm{HO}} = \frac{\hat{\mathbf{P}}^2_{\mathrm{NN}}}{2M} + \frac{1}{2}M\Omega^2\hat{\mathbf{R}}^2_{\mathrm{NN}} + \frac{\hat{\mathbf{r}}^2}{2\mu} + \frac{1}{2}\mu\Omega^2\hat{\mathbf{r}}^2, \tag{5.66}$$

where, for particles with equal mass, the total mass is given by $M = m_1 + m_2 = 2m$ and the reduced mass by $\mu = m/2$. However, different conventions exist for the center-of-mass coordinate system. For example, an alternative and more symmetric choice for the relative and center-of-mass momentum is given by

$$\tilde{\mathbf{p}} = 1/\sqrt{2}(\mathbf{k}_1-\mathbf{k}_2), \qquad \tilde{\mathbf{P}}_{\mathrm{NN}} = 1/\sqrt{2}(\mathbf{k}_1+\mathbf{k}_2), \tag{5.67}$$

where the tilde over the variable labels the coordinate system. As a result, the oscillator parameters from both representations are related by $\tilde{b}=\sqrt{2}b$. This distinction is important given that the transformation to single-particle states, which we discuss next, assumes the symmetric definition of the coordinate system while partial-wave states assume the normal one.

In the following, we derive the transformation that takes relative two-body HO states to jj-coupled single-particle HO states. As mentioned above, the crucial step in this process is given by the so-called Talmi-Moshinsky transformation, which connects the two nucleon single-particle state to the center-of-mass and relative state of the two-body system. Other steps in the derivation exclusively involve recoupling of angular momenta. The ultimate goal is then to express the current operator matrix elements in terms of the acquired single-particle states.

Before we start, we remark that we only show those quantum numbers relevant to the specific step. To find an expression for the transformation to single-particle HO basis states $\{|n_k(l_k s_k)j_k m_{j_k} t_k m_{t_k}\rangle\}$, we begin by coupling two single-particle states to total angular momentum J_tot and total isospin T:[7]

$$\begin{aligned}|1,2\rangle &\equiv |n_1(l_1s_1)j_1m_{j_1}t_1m_{t_1}, n_2(l_2s_2)j_2m_{j_2}t_2m_{t_2}\rangle \\ &= \sum_{J_\text{tot}M_{J_\text{tot}}}\sum_{TM_T} \mathcal{C}^{J_\text{tot}M_{J_\text{tot}}}_{j_1m_{j_1}j_2m_{j_2}}\,\mathcal{C}^{TM_T}_{t_1m_{t_1}t_2m_{t_2}}\,|[n_1(l_1s_1)j_1, n_2(l_2s_2)j_2]J_\text{tot}M_{J_\text{tot}}\,(t_1t_2)TM_T\rangle\,.\end{aligned} \tag{5.68}$$

As a second step, we recouple from a j_1j_2-coupling to a ΛS-coupling, where Λ is the total orbital angular momentum and S the total spin, by using a $9j$-symbol:

$$|[(l_1s_1)j_1,(l_2s_2)j_2]J_\text{tot}M_{J_\text{tot}}\rangle = \sum_{\Lambda S}\hat{j}_1\,\hat{j}_2\,\hat{\Lambda}\,\hat{S}\begin{Bmatrix} l_1 & s_1 & j_1\\ l_2 & s_2 & j_2\\ \Lambda & S & J_\text{tot}\end{Bmatrix}|[n_1(l_1l_2)\Lambda,(s_1s_2)S]J_\text{tot}M_{J_\text{tot}}\rangle\,, \tag{5.69}$$

where we adopted the notation $\hat{a} \equiv \sqrt{2a+1}$. In a next step, we transform the single-particle momenta $\mathbf{k}_1$ and $\mathbf{k}_2$ to the relative and center-of-mass momenta, as given in Eq. (5.67), via the following orthogonal matrix [234]

$$\begin{pmatrix}\tilde{\mathbf{P}}_\text{NN}\\ \tilde{\mathbf{p}}\end{pmatrix} = \begin{pmatrix}\sqrt{\frac{d}{d+1}} & \sqrt{\frac{d}{d+1}}\\ \sqrt{\frac{d}{d+1}} & -\sqrt{\frac{d}{d+1}}\end{pmatrix}\begin{pmatrix}\mathbf{k}_1\\ \mathbf{k}_2\end{pmatrix}, \tag{5.70}$$

with $d=1$ for a two-body system. This transformation is represented by a Talmi-Moshinsky bracket or *HO bracket*, which is specified by

$$\begin{aligned}|[n_1l_1(\mathbf{k}_1),n_2l_2(\mathbf{k}_2)]\Lambda\rangle = &\sum_{\substack{N_\text{NN}\,L_\text{NN}\\ N\,L}}\langle N_\text{NN}N(L_\text{NN}L)\Lambda|n_1\,n_2(l_1\,l_2)\Lambda\rangle_{d=1}\\ &\times|[N_\text{NN}L_\text{NN}(\tilde{\mathbf{P}}_\text{NN})NL(\tilde{\mathbf{p}})]\Lambda\rangle\,.\end{aligned} \tag{5.71}$$

A modern and simple implementation of the HO bracket is given in Ref. [234]. The last step involves recoupling of angular momenta: the relative orbital angular momentum L is coupled with the total spin S to the relative angular momentum J, which is successively coupled with the center-of-mass orbital angular momentum L_NN to the total angular momentum J_tot:

$$|[(L_\text{NN}L)\Lambda S]J_\text{tot}\rangle = \sum_J(-1)^{L_\text{NN}+L+S+J}\,\hat{\Lambda}\,\hat{J}\begin{Bmatrix}L_\text{NN} & L & \Lambda\\ S & J_\text{tot} & J\end{Bmatrix}|[L_\text{NN}(LS)J]J_\text{tot}\rangle\,, \tag{5.72}$$

where the recoupling was achieved by a $6j$-symbol [166], which is represented by $\{...\}$. Combining the outcomes of Eqs. (5.68), (5.69), (5.71), and (5.72) and decoupling the center-of-mass

---

[7] Note that the total angular momentum $\mathbf{J}_\text{tot} = \mathbf{j}_1 + \mathbf{j}_2$ does not coincide with the relative two-body angular momentum $\mathbf{J} = \mathbf{L} + \mathbf{S}$, which emerges from the coupling of the relative orbital angular momentum L and the total spin S. We use the notation J_tot and distinguish with J to keep everything consistent with previous notation.

orbital momentum L_{NN} and the relative angular momentum J yields the final result

$$\begin{aligned}
|1,2\rangle = &\sum_{J_{\mathrm{tot}} M_{J_{\mathrm{tot}}}} \sum_{T M_T} \sum_{\Lambda S} \sum_{\substack{N_{\mathrm{NN}} L_{\mathrm{NN}} \\ N\, L}} \sum_{J} \sum_{M_{L_{\mathrm{NN}}} M_J} (-1)^{L_{\mathrm{NN}}+L+S+J}\, \hat{j}_1\, \hat{j}_2\, \hat{\Lambda}^2\, \hat{S}\, \hat{J} \\
&\times \mathcal{C}^{J_{\mathrm{tot}} M_{J_{\mathrm{tot}}}}_{j_1 m_{j_1} j_2 m_{j_2}}\, \mathcal{C}^{T M_T}_{t_1 m_{t_1} t_2 m_{t_2}} \begin{Bmatrix} l_1 & s_1 & j_1 \\ l_2 & s_2 & j_2 \\ \Lambda & S & J_{\mathrm{tot}} \end{Bmatrix} \\
&\times \langle N_{\mathrm{NN}} N (L_{\mathrm{NN}} L)\Lambda | n_1\, n_2 (l_1\, l_2)\Lambda\rangle_{d=1} \begin{Bmatrix} L_{\mathrm{NN}} & L & \Lambda \\ S & J_{\mathrm{tot}} & J \end{Bmatrix} \\
&\times \mathcal{C}^{J_{\mathrm{tot}} M_{J_{\mathrm{tot}}}}_{L_{\mathrm{NN}} M_{L_{\mathrm{NN}}} J M_J}\, |N_{\mathrm{NN}} L_{\mathrm{NN}} M_{L_{\mathrm{NN}}}; N(LS) J M_J T M_T\rangle\,. \qquad (5.73)
\end{aligned}$$

This expression is the full transformation that has to be carried out to obtain single-particle HO states, which can be used in many-body frameworks, from center-of-mass and relative HO states.

The matrix element of a general current operator with respect to a general center-of-mass and relative HO state is given by

$$\begin{aligned}
\langle N'_{\mathrm{NN}} L'_{\mathrm{NN}} M'_{L_{\mathrm{NN}}}; N'(L'S')J'M'_J T' M'_T | J^{\mu}\, |N_{\mathrm{NN}} L_{\mathrm{NN}} M_{L_{\mathrm{NN}}}; N(LS) J M_J T M_T\rangle& \\
= \delta_{N_{\mathrm{NN}} N'_{\mathrm{NN}}}\, \delta_{L_{\mathrm{NN}} L'_{\mathrm{NN}}}\, \delta_{M_{L_{\mathrm{NN}}} M'_{L_{\mathrm{NN}}}}& \\
\times \langle N'(L'S')J'M'_J T' M'_T|\, J^{\mu}\, |N(LS) J M_J T M_T\rangle\,.& \\
(5.74)&
\end{aligned}$$

In words, the current operator does not act on the center-of-mass quantum numbers. In the last line of the expression we recognize the matrix element as the one given in Eq. (5.64). Finally, the matrix element with respect to single-particle states is found by placing the current operator between two single-particle states and substituting the result from Eq. (5.73).

5.6.2 Three-body Jacobi harmonic-oscillator states

In this section we outline the necessary steps to obtain single-particle states starting from three-body Jacobi partial waves, but without going into the same detail as for the two-body case. The relative three-body Jacobi HO basis states are given by

$$|N\, n\, \alpha\rangle = |N\, n\, [(LS)J\, (\ell s)j]\mathcal{J}\mathcal{M}_{\mathcal{J}}\, (Tt)\mathcal{T}\mathcal{M}_{\mathcal{T}}\rangle\,, \qquad (5.75)$$

where N is the radial HO quantum number related to the $\{12\}$ subsystem and n to the spectator particle. Note that the notation for the quantum numbers corresponds to the one introduced in Section 3.2.1. As the HO transformation only affects the spatial part of the state, we decouple total angular momentum and, subsequently, orbital angular momentum from spin for both the subsystem and the spectator particle, which leads to

$$|N\, n\, \alpha\rangle = \sum_{\substack{M_L M_S M_J \\ m_\ell m_s m_j}} \mathcal{C}^{\mathcal{J}\mathcal{M}_{\mathcal{J}}}_{J M_J j m_j}\, \mathcal{C}^{J M_J}_{L M_L S M_S}\, \mathcal{C}^{j m_j}_{\ell m_\ell s m_s}\, |N\, n\, L M_L\, S M_S\, \ell m_\ell\, s m_s\rangle\,, \qquad (5.76)$$

where we suppressed the isospin dependence. In analogy to the two-body case, the transformation for the three-body current operator matrix elements from the partial-wave basis to the three-body Jacobi HO basis is given by[8]

$$\langle N'n'\alpha'|J^\mu|Nn\alpha\rangle = \int \mathrm{d}p'\, p'^2\, R_{N'L'}(p') \int \mathrm{d}q\, q'^2\, R_{n'l'}(q') \int \mathrm{d}p\, p^2\, R_{NL}(p) \int \mathrm{d}q\, q^2\, R_{nl}(q) \times \langle p'q'\alpha'|J^\mu|pq\alpha\rangle\,, \tag{5.78}$$

where $R_{NL}(p)$ and $R_{nl}(q)$ are the radial wave functions defined in Eq. (5.63) with oscillator parameters b_p and b_q, respectively.

Similar to the relative HO two-body states, the definition of Jacobi momenta used in the derivation to obtain single-particle states is given by the symmetric choice:[9]

$$\tilde{\mathbf{p}} = \frac{\mathbf{k}_1 - \mathbf{k}_2}{\sqrt{2}}, \qquad \tilde{\mathbf{q}} = \sqrt{\frac{2}{3}}\Big(\mathbf{k}_3 - \frac{1}{2}(\mathbf{k}_1 - \mathbf{k}_2)\Big), \qquad \tilde{\mathbf{P}}_{3\mathrm{N}} = \frac{\mathbf{k}_1 + \mathbf{k}_2 + \mathbf{k}_3}{\sqrt{3}}. \tag{5.79}$$

This results in a change $\tilde{b}_p = \sqrt{2}b_p$ for the oscillator parameter related to the two-body subsystem, $\tilde{b}_q = \sqrt{3/2}b_q$ for the oscillator parameter connected to the spectator particle, and $\tilde{b}_{3\mathrm{N}} = 1/\sqrt{3}b_{3\mathrm{N}}$ for the center-of-mass oscillator parameter.

The derivation of the transformation for three-body Jacobi HO states largely follows the same steps as for the two-body case, with the extra difficulty that the two-body center-of-mass motion and the spectator motion have to be related to the three-body center-of-mass $\mathbf{P}_{3\mathrm{N}}$ and the second Jacobi momentum $\mathbf{q}$, i.e., a second Talmi-Moshinsky transformation. Given that the derivation is rather lengthy and cluttered we have kept it for the appendices: we present the full transformation in Appendix D. Here we only state the final result, which is given by

$$\begin{aligned} |1\,2\,3\rangle &\equiv |n_1(l_1s_1)j_1m_{j_1}t_1m_{t_1}, n_2(l_2s_2)j_2m_{j_2}t_2m_{t_2}, n(ls)jm_jtm_t\rangle \\ &= \sum_{J_\mathrm{tot}\mathcal{J}_\mathrm{tot}} \sum_{T\mathcal{T}} \sum_{N_{3\mathrm{N}}L_{3\mathrm{N}}} \sum_{\beta} \sum_{ML_{3\mathrm{N}}M_{J_3}} \mathcal{C}^{J_\mathrm{tot}M_{J_\mathrm{tot}}}_{j_1m_{j_1}j_2m_{j_2}} \mathcal{C}^{\mathcal{J}_\mathrm{tot}\mathcal{M}_{\mathcal{J}_\mathrm{tot}}}_{J_\mathrm{tot}M_{J_\mathrm{tot}}jm_j} \mathcal{C}^{TM_T}_{t_1m_{t_1}t_2m_{t_2}} \mathcal{C}^{\mathcal{T}\mathcal{M}_\mathcal{T}}_{TM_Ttm_t} \\ &\quad \times T\,\mathcal{C}^{\mathcal{J}_\mathrm{tot}\mathcal{M}_{\mathcal{J}_\mathrm{tot}}}_{L_{3\mathrm{N}}M_{L_{3\mathrm{N}}}J_3M_{J_3}}\, |N_{3\mathrm{N}}L_{3\mathrm{N}}\rangle\, |\beta M_{J_3}\rangle\,, \end{aligned} \tag{5.80}$$

where T represents the overlap between relative and center-of-mass states, and angular-momentum coupled single-particle states. Evidently, the three-body transformation amounts to finding an expression for this overlap, which is given in the appendix mentioned above.

5.6.3 Magnetic moment operator benchmark

The results presented here are the outcome from a collaboration with Ref. [235]. They consist of a benchmark of the trinucleon magnetic moments obtained from the magnetic moment operator, as presented in Section 5.4, evaluated between single-particle HO states, as outlined above. These values are then compared to the magnetic moments obtained from the form factor normalization.

---

[8] The overlap between three-body momentum states in Jacobi coordinates $|\mathbf{pq}\rangle$ and three-body HO states $|N\,n\,(L\ell)\mathcal{L}\mathcal{M}_\mathcal{L}\rangle$, where only the relevant orbital angular momenta are shown, is given by

$$\langle \mathbf{p}\,\mathbf{q}|N\,n\,(L\ell)\mathcal{L}\mathcal{M}_\mathcal{L}\rangle = (2\pi)^3 R_{NL}(p)\, R_{nl}(q)\, \mathcal{Y}^{\mathcal{L}\mathcal{M}_\mathcal{L}}_{L\ell}(p,q)\,. \tag{5.77}$$

Here, the momentum-space radial wave functions R_{NL} contain the radial part of the two-body subsystem and R_{nl} that of the spectator particle.

[9] This is compared to the definition of the Jacobi momenta given in (3.22a)-(3.22c).

Table 5.3: Magnetic moment of the triton (μ_t) and the helion (μ_h) in units of μ_N from the form factor normalization $F_\mathrm{M}(0)$ and the magnetic moment operator $\hat{\boldsymbol{\mu}} = \hat{\boldsymbol{\mu}}_{1\mathrm{b}}^{\mathrm{LO}} + \hat{\boldsymbol{\mu}}_{2\mathrm{b}}^{\mathrm{NLO}}$. Calculations with the magnetic moment operator use the HO formalism, see text for details. The values between brackets represent the uncertainties from the HO model-space truncation. The experimental values are taken from Ref. [65].

	μ_t $[\mu_N]$		μ_h $[\mu_N]$	
	$F_\mathrm{M}(0)$	$\hat{\boldsymbol{\mu}}$	$F_\mathrm{M}(0)$	$\hat{\boldsymbol{\mu}}$
LO	2.622	2.622	−1.783	−1.783
NLO	2.836	2.833(4)	−1.993	−1.989(4)
intrinsic	-	0.192	-	−0.189
Sachs	-	0.018(4)	-	−0.017(4)
Exp.	2.979		−2.128	

Table 5.3 shows the magnetic moments obtained from both formalisms for the N^{3}LO EM NN interaction with $\Lambda = 500$ MeV.[10] The first row presents results from calculations with the one-body operator only ('LO'), while the second row shows results with the NLO 2BCs included ('NLO'). Contributions from the latter to the magnetic moment are shown separately by the rows indicated with 'intrinsic' and 'Sachs'. As noted in Section 5.4, this separation cannot be made for the form factor calculation, hence only the total values can be compared. Bracketed values represent numerical uncertainties from the HO model-space truncation: calculations were performed for $N_\mathrm{max} = 10, 20$, and 30 with HO frequencies $\Omega = 20, 30$, and 40 MeV, where the nominal value was taken from the converged result at $N_\mathrm{max} = 30$ and the uncertainty was determined by calculating the standard deviation from values for the different oscillator frequencies.

The effect on the ground state magnetic moment of the $\hat{\boldsymbol{\mu}}_{2\mathrm{b}}^{\mathrm{NLO,\ intrinsic}}$ operator is an improvement of the value around 10%, while the Sachs operator has a small effect of $0.5\% - 1\%$. Clearly, the intrinsic term accounts for the bulk of the correction. Total results from both methods agree with each other within uncertainties. As a result, the matrix elements of the magnetic moment operator in the HO basis can be safely used in other calculations, which we will discuss in the next section.

5.7 Magnetic properties of ^{6}Li

As a first step towards calculating magnetic properties of other light nuclei $A \geqslant 4$, we consider ^{6}Li, which is the next stable light nucleus with a nonzero nuclear spin: the ^{4}He nucleus is spinless and, therefore, has no magnetic properties. The ^{6}Li nucleus is essentially a ^{4}He core with a deuteron halo. As a result, ground state magnetic properties of ^{6}Li are approximately given by the deuteron properties. Similar to the deuteron, ^{6}Li is an isoscalar nucleus such that isovector two-body NLO contributions to the magnetic moment operator have no effect, see Sections 4.1.1 and 4.3.4. Nevertheless, two-body NLO corrections to the operator can be studied through isovector radiative processes involving the absorption or emission of photons.

---

[10] Note that the 3N interaction is left out for these results.

The study of these radiative processes is largely equivalent to the study of the ground state properties, which have been the main focus in this thesis, with the distinction that initial and final nuclear state differ. Hence, we can use the framework presented in Section 5.2. We start in Section 5.7.1 by introducing transition probabilities and linking them to the decay width, which is measured experimentally. Then, in Section 5.7.2, we briefly describe the IT-NCSM, the many-body method of choice for the *ab initio* calculations of the magnetic moment and transition of ^{6}Li. Finally, we present results in Section 5.7.3, which are taken from a publication that is available as a preprint [222].

5.7.1 Magnetic transition probabilities

The probability of an initial state of the nucleus to emit or absorb a photon is given by Fermi's golden rule:

$$\Gamma_{\gamma,i\to f} = 2\pi |\langle f|\hat{H}'|i\rangle|^2 \rho(E_f), \tag{5.81}$$

where $\rho(E_f)$ is the density of final states with energy E_f and $\hat{H}'$ is the interaction Hamiltonian as defined in Eq. (5.6). Suppose that the emitted photons originate from an unoriented source,[11] then the total transition probability is given by summing over final states and averaging over initial spins [225],[12]

$$\Gamma_{\gamma,i\to f} = 2\pi \sum_{\lambda}\sum_{M_f} \frac{1}{2J_i+1} \sum_{M_i} \int \frac{\mathrm{d}\mathbf{q}}{(2\pi)^3}\, |\langle J_f M_f \mathbf{k}\lambda|\hat{H}'|J_i M_i\rangle|^2\, \delta(E_f+\omega_k-E_i), \tag{5.82}$$

where the delta function ensures energy conservation and where we specified the initial and final nuclear state to be eigenstates of angular momentum. Using the result from the multipole expansion, Eq. (5.8), and applying the Wigner-Eckart theorem to the nuclear matrix elements, Eq. (5.12), results in a squared matrix element of the form

$$|\langle J_f M_f||\hat{T}^{\mathrm{el}}_J + \hat{T}^{\mathrm{mag}}_J||J_i M_i\rangle|^2. \tag{5.83}$$

Because parity conservation dictates that one or the other multipole must vanish, it follows that the cross term is evidently zero:

$$|\langle J_f M_f||\hat{T}^{\mathrm{el}}_J + \hat{T}^{\mathrm{mag}}_J||J_i M_i\rangle|^2 = |\langle J_f M_f||\hat{T}^{\mathrm{el}}_J||J_i M_i\rangle|^2 + |\langle J_f M_f||\hat{T}^{\mathrm{mag}}_J||J_i M_i\rangle|^2. \tag{5.84}$$

Clebsch-Gordan orthonormality properties eliminate sums over M_f and M_i such that, together with the previous result, Eq. (5.82) can be written as [225]

$$\Gamma_{\gamma,i\to f} = 8\pi\,\alpha\,k\, \frac{1}{2J_i+1} \sum_{J\geqslant 1} \Big[|\langle J_f||\hat{T}^{\mathrm{el}}_J(q)||J_i\rangle|^2 + |\langle J_f||\hat{T}^{\mathrm{mag}}_J(q)||J_i\rangle|^2 \Big]. \tag{5.85}$$

This outcome is general in the sense that it is valid for any localized quantum mechanical system. It contains both electric and magnetic transverse operators at every allowed multipole order.

---

[11] Experiments measuring transition probabilities detect radiation from a polarized or an unpolarized source, where the quantity that is polarized is the nuclear spin. The difference between these two kinds of experiments is accounted for by selecting a spcific initial spin state or by averaging over the initial spin states.

[12] Note that now $k = |\mathbf{k}|$ is used to denote the *real* photon momentum, given that the discussion is about transitions induced by real photons.

In reality, the wavelength of the photon will be large compared to size of the target, such that only one or few multipoles have to be taken into account, as we showed in Section 5.2.2. Substituting the long wavelength limit of the transverse operators, Eqs. (5.19) and (5.20), into Eq. (5.85) and only regarding a single multipole yields [236]

$$\Gamma_{\gamma,i\to f} = \sum_{J\geqslant 1} \frac{8\pi\,\alpha\,k^{2J+1}(J+1)}{J\big[(2J+1)!!\big]^2} B(E/M\,J; J_i \to J_f), \tag{5.86}$$

where the last factor defines the *transition strength*

$$B(E/M\,J; J_i \to J_f) \equiv \frac{1}{2J_i+1} |\, \langle J_f M_f || \hat{O}_J^{E/M} || J_i M_i \rangle \,|^2. \tag{5.87}$$

Here, $\hat{O}_J^{E/M}$ represents the remaining part of the electric or magnetic multipole operator in the long-wavelength limit. Note that the transition strength contains all the nuclear structure information.

In the following, we are interested in calculating the magnetic dipole $(J = 1)$ transition strength of the first excited state to the ground state of ^{6}Li, i.e., $B(M1; 0^+_{T=1} \to 1^+_{T=0})$, where $M1$ denotes the magnetic dipole operator and I^π_T denotes a specific nuclear state with spin I, parity π, and isospin T. Given that the long-wavelength limit of the multipole operators differs from the magnetic moment operator only by a factor and power in k, we can substitute the magnetic moment operator for $\hat{O}_J^{E/M}$ in Eq. (5.87). Accordingly, we can use the conventional LO magnetic moment operator with corrections from the NLO two-body operator, for which we obtained expressions in Section 5.4. From now on we will denote the magnetic moment operator with $M1$, which refers to the magnetic dipole character of the transition.

5.7.2 Importance-truncated no-core shell model

In order to calculate observables of atomic nuclei with more than four constituents, different techniques from those discussed in Chapter 3 are required. A common approach to solving the many-body problem is to use basis-expansion methods, where the eigenstate of the Hamiltonian is expanded in terms of a suitable many-body basis. In particular, the *configuration interaction* (CI) typically employs A-body *Slater determinants* constructed from single-particle states to represent the eigenstate and, in principle, provides an exact solution of the Schrödinger equation in A-body space. However, in practice one has to reduce the basis size due to computational limitations: the large dimension of the A-body basis generates a Hamiltonian too large to store. As a result of this basis truncation, only upper bounds to the ground state energy can be obtained.

A restriction of the infinite basis is provided by, for example, the so-called *no-core shell model* (NCSM) which constrains the allowed excitations with respect to a chosen reference state, allowing one to calculate nuclei up to $A \sim 12$ [237, 238]. Even though the computational cost is reduced by employing the NCSM, further extensions have to be considered to tackle the computation of higher-mass nuclei. To this end, the *importance-truncated NCSM* (IT-NCSM) provides a physics-driven method to select individual many-body basis states according to their importance, extending calculations to the medium-mass range up to $A \sim 24$ [26].

The CI and its variations are powerful many-body methods as they provide solutions which are intrinsically variational, i.e., enlarging the basis results in solutions that approach the exact one from above. Furthermore, they are versatile, in the sense that, any observable can be calculated and they can address open- and closed-shell nuclei on equal footing. In the following, we briefly describe the general CI framework, then introduce the NCSM, and finally specify the approach employed in the IT-NCSM.

Configuration interaction

The CI ansatz is given by

$$|\Psi_n\rangle = \sum_i c_i^{(n)} |\Phi_i\rangle = \sum_i \langle\Phi_i|\Psi_n\rangle |\Phi_i\rangle \,, \tag{5.88}$$

where n denotes the labeling of excited states of the nucleus and where the expansion of the nuclear eigenstate is given in terms of A-body Slater determinants $|\Phi_i\rangle$. In general, Slater determinants are constructed from any suitable single-particle basis, e.g., HO, natural orbitals, or HF, using the M-scheme approach, i.e., the total angular momentum projection is given by $M = \sum_i^A m_i$ such that Slater determinants are eigenstates of $\hat{J}_z$. In the following we assume Slater determinants to be constructed from HO single-particle states $\{|n(\ell s)jm_j tm_t\rangle\}$, given that the results in this thesis are obtained with such a basis.

By employing an expansion as in Eq. (5.88), the typical eigenvalue problem $\hat{H}|\Psi_n\rangle = E_n|\Psi_n\rangle$ becomes

$$\sum_i \langle\Phi_j|\hat{H}|\Phi_i\rangle \langle\Phi_i|\Psi_n\rangle = E_n \langle\Phi_j|\Psi_n\rangle \,, \tag{5.89}$$

where we multiplied $\langle\Phi_j|$ from the left and where E_n represent eigenenergies corresponding to state n. Equation (5.89) demonstrates that the Hamiltonian in the CI framework is composed of matrix elements $\langle\Phi_j|\hat{H}|\Phi_i\rangle$. They do not correspond to two-body interaction matrix elements, and they can be derived using *Slater-Condon rules* [239].[13] A diagonalization of the Hamiltonian then determines the eigenvalues and the eigenstates, hence, obtaining the energies E_n and the coefficients $c_i^{(n)}$. Mostly, one is only interested in a few low-lying eigenvalues, such that merely a part of the matrix needs to be diagonalized. This is achieved with the *Lanczos algorithm*, which efficiently calculates extremal eigenvalues and eigenstates for matrices with a linear dimension up to 10^{10} [240]. Consequently, the eigenstates allow one to calculate any observable by determining the expectation value of any operator of interest:

$$\langle\Psi_n'|\hat{O}|\Psi_n\rangle \,. \tag{5.90}$$

The matrix elements can again be obtained with Slater-Condon rules and, in principle, create the possibility to calculate transitions given that the final and initial state can differ.

Commonly, the determinants $|\Phi_i\rangle$ are organized according to a reference state $|\Phi\rangle$ with particle-hole (p-h) excitations built on top of it:

$$|\Psi_n\rangle = |\Phi\rangle + \sum_{a,p} c_{n,a}^{p} |\Phi_a^p\rangle + \sum_{\substack{a<b\\p<q}} c_{n,ab}^{pq} |\Phi_{ab}^{pq}\rangle + \sum_{\substack{a<b<c\\p<q<r}} c_{n,abc}^{pqr} |\Phi_{abc}^{pqr}\rangle + \ldots, \tag{5.91}$$

---

[13] The Slater-Condon rules express many-body matrix elements as integrals in terms of single-particle orbitals to exploit the orthogonality of the single-particle basis. The nonvanishing many-body matrix elements depend on the operator structure: one-body operators can connect many-body states which differ by one single-particle state, whereas two-body operators can connect at most many-body states differing by two single-particle states (and so on for n-body operators). This reduces the cost of matrix element calculations, since the vanishing matrix elements can be easily predicted and need not be computed.

where $a, b, c, \ldots$ represent single-particle hole states which are obtained by exciting a particle to a single-particle particle state, represented by $p, q, r, \ldots$. A full CI calculation of a nucleus with mass A would include all combinations of Ap-Ah excitations. In reality, the single-particle basis is truncated by restricting the single-particle states available to construct the many-body basis. The truncated basis spans the model space $\mathcal{M}$ and, as a result, eigenvalues are no longer exact but yield an upper bound. The dimension of the CI space exhibits factorial growth for both the single-particle basis dimension and the particle number A, limiting CI calculations to the lightest nuclei only. Further truncations have to be made to push calculations to higher nuclear-mass regions, introducing variations of the CI method like the NCSM [241, 242] which we discuss next.

No-core shell model

The truncation scheme adopted in the NCSM is based on only including many-body states which have a certain maximal excitation compared to the reference determinant $|\Phi\rangle$. For HO single-particle states the energy is given by

$$\epsilon = \left(2n + l + \frac{3}{2}\right)\hbar\Omega. \tag{5.92}$$

Then, the restriction of the model space is achieved by the so-called N_{max} truncation, which allows a maximum of HO excitation energy above the reference:

$$\sum_{i=1}^{A} (\epsilon_i - \epsilon_{0,i}) \leqslant N_{\text{max}}\Omega, \tag{5.93}$$

where the sum runs over the single-particle energies of the occupied particle states in the many-body state and where $\sum_{i=1}^{A} \epsilon_{0,i}$ defines the energy of the reference.

NCSM calculations are typically performed for a range of N_{max} values to assess the convergence of observables with respect to the model-space size. Converged results should be independent of the HO frequency Ω, which would show as a flat trend of the observable as a function of Ω. In practical calculations, however, converged results are often not realized. One possibility to obtain an estimate is to resort to choosing the optimal Ω as the value which minimizes the energy.

Importance-truncated no-core shell model

Because of the combinatorial growth of the model space as a function of basis size and N_{max} truncation, many NCSM calculations still do not fully converge. The observation that a large fraction of many-body states have an almost negligible contribution to the expansion of the eigenstate, i.e., certain coefficients $c_i^{(n)}$ are small, led to the formulation of the IT-NCSM [243, 244]. The main idea behind the IT-NCSM is to select important basis states based upon a predefined *importance measure* without solving the many-body problem in the full model space. Subsequently, the importance-truncated model space is determined by imposing a threshold on the importance measure.

The importance measure is defined as the first-order perturbative correction of a reference state which approximates the desired eigenstate. This reference state is given by

$$|\Psi^{(n)}_{\mathrm{ref}}\rangle = \sum_{i\in\mathcal{M}_{\mathrm{ref}}} c^{(n)}_{i,\mathrm{ref}}\,|\Phi_i\rangle\,, \tag{5.94}$$

and is obtained by diagonalizing the Hamiltonian in a smaller model space $\mathcal{M}_{\mathrm{ref}}$. The definition of the importance measure $\kappa_i^{(n)}$ for basis states not included in $\mathcal{M}_{\mathrm{ref}}$ is given by

$$\begin{aligned}\kappa_i^{(n)} &\equiv -\frac{\langle\Phi_i|\hat{H}|\Psi^{(n)}_{\mathrm{ref}}\rangle}{\Delta\epsilon_i}\\ &= \sum_{j\in\mathcal{M}_{\mathrm{ref}}} c^{(n)}_{j,\mathrm{ref}}\frac{\langle\Phi_i|\hat{H}|\Phi_j\rangle}{\Delta\epsilon_i},\end{aligned} \tag{5.95}$$

which is the first-order perturbative correction to $|\Psi^{(n)}_{\mathrm{ref}}\rangle$ and where $\Delta\epsilon_i = \epsilon_i - \epsilon_{\mathrm{ref}}$. Constructing the importance-truncated model space $\mathcal{M}_{\mathrm{IT}}$ is done by selecting those states for which the absolute value of the importance measure is larger than a predefined threshold

$$|\kappa_i^{(n)}| \geqslant \kappa_{\mathrm{min}}, \tag{5.96}$$

such that the full NCSM model space is retrieved in the limit $\kappa_{\mathrm{min}} \to 0$. Final results for observables are determined by extrapolating calculations obtained with several different values for κ_{min} to a vanishing threshold. For reviews on the subject of the NCSM and the IT-NCSM we refer to, e.g., Refs. [238, 244].

5.7.3 ^{6}Li magnetic dipole strength and magnetic moment

Significant progress has been made in chiral EFT [23, 125]. In addition, the *ab initio* solution of the quantum many-body problem for light nuclei has also seen much progress in the last decade, making precision calculations possible [8, 238]. Recently, the attention has been on the consistent inclusion of electroweak transition operators [81], with a focus on the impact of 2BCs. For EM transitions in light nuclei, calculations with traditional 2BCs and potentials were performed in Ref. [245], while calculations with 2BCs from chiral EFT used in conjunction with wave functions derived from traditional potentials were performed in Ref. [51], reaching a precision at the few percent level. In this section, we will present the first calculations obtained with both 2BCs and interactions consistently derived from chiral EFT. In the case of weak β decays, this has been shown to lead to a systematic improvement between experiment and theory [148].

We present results for the ground-state magnetic moment $\mu(1^+_{T=0})$ and the transition strength of the first excited state to the ground state $B(M1; 0^+_{T=1} \to 1^+_{T=0})$ of ^{6}Li, obtained with the LO, SRG evolved LO, and SRG evolved NLO $M1$ operator. For the *ab initio* calculations, the IT-NCSM, introduced in the previous section, was employed as a state-of-the-art many-body method. Within the IT-NCSM, NN and 3N interactions derived within chiral EFT were used. Four different Hamiltonians were considered which are denoted by Roman numerals I-IV. They include (I) the EM NN interaction at N^{3}LO, introduced in Section 4.4.1, complemented with a local 3N interaction (cutoff Λ = 500 MeV, c_D = 0.8) at N^{2}LO, which is fitted to reproduce the binding energy as well as the β-decay half-life of ^{3}H [50]. Furthermore, Hamiltonians (II- IV) use the EMN NN interactions at N^{2}LO, N^{3}LO, and N^{4}LO with $\Lambda = 500$ MeV [23] complemented with consistent nonlocal 3N interactions up to N^{2}LO, N^{3}LO, and N^{3}LO, respectively. The NN interactions were only fitted to NN scattering data and the deuteron binding energy, while the 3N interactions were fitted to reproduce the triton binding energy and to optimize the ground-state energy and radius of ^{4}He, which led to the values $c_D = -1$, $c_D = 2$, and $c_D = 3$, for cases II, III and IV, respectively. The SRG was employed at the NN and 3N level with a flow parameter of $\alpha = 0.08$ fm^4 [246, 247]. The SRG transformation provides interactions that result in faster convergence when they are used in many-body calculations [215].

Using an SRG-transformed Hamiltonian requires a consistent SRG transformation of the $M1$ operator. In previous studies, this consistent treatment was neglected. Here SRG corrections of the $M1$ operator were included at the two-body level. In addition to the SRG corrections, the NLO 2BC contributions to the $M1$ operator were included as well. At NLO, these are commonly expressed as a sum of two contributions, the intrinsic term and the Sachs term, see Eqs. (5.52) and (5.58). The Sachs term only depends on the potential between the two nucleons, whereas the translationally invariant intrinsic term is given by the spatial part of the 2BC.

For each interaction, an IT-NCSM calculation was carried out with $N_{\max}$ from 2 to 12 with harmonic-oscillator frequencies $\Omega = 16$, 20, and 24 MeV. For the resulting value of the magnetic moment and the transition strength, the central value for the highest $N_{\max}$ was used as the nominal result, and the neighboring results as an estimate for the many-body uncertainties. Results of the calculations are listed in Table 5.4, which also lists results of quantum Monte Carlo (QMC) calculations from Refs. [51, 245]. Calculations in Ref. [245] were performed using the SNPA, with wave functions obtained from the Argonne v_{18} NN [248] and the Illinois-2 3N potential [249]. Two-body MECs were constructed from the NN potential by satisfying the continuity equation, recall the discussion from Section 4.1.1. The second set of QMC calculations generated the wave functions from the Argonne v_{18} NN [248] and the improved Illinois-7 3N potential [250]. In this case, results from the SNPA 2BC operators (same operator as in Ref. [245]) were compared to results obtained with 2BCs derived within chiral EFT. The latter approach is commonly called a hybrid approach, again, see Section 4.1.1.

The LO results for the magnetic moment and the transition strength are consistently higher compared to the LO QMC results. The SRG evolution decreases the values by about 2% and 4% for μ and $B(M1)$, respectively. Adding two-body NLO corrections leads to a large increase of $\sim$9% for the transition strength. This observation is comparable to the effect for the trinucleons presented in Fig. 5.1 and Table 5.2, once more indicating the 2BC importance for magnetic observables. Due to ^{6}Li being isoscalar, the magnetic moment value is practically unaffected by adding the NLO corrections.

Even for results from complete calculations (total QMC hybrid and SRG evolved NLO), there is disagreement between the two approaches. This could originate from two possible sources: the QMC results take higher-order corrections to the operator, up to N^{3}LO, into account or the mismatch between the short-range behavior of the interaction and the operator, inherent to the hybrid approach, causes inconsistencies which can lead to incorrect results. Further studies are necessary to gain more insight into this disagreement. In the next section we compare the results to experimental values.

Table 5.4: Results of the calculations for $B(M1; 0^+_{T=1} \to 1^+_{T=0})$, in units of μ_N^2, and $\mu(1^+_{T=0})$, in units of μ_N, of ^{6}Li. They employ four different Hamiltonians (I-IV), which are introduced in the text, and values between brackets represent the estimated many-body uncertainties. Calculations are sorted by the type of $M1$ operator used, i.e., LO, LO SRG evolved, and NLO SRG evolved. For comparison, results of QMC calculations from Refs. [51, 245] are shown in the second part of the table. The SNPA for the operator in Ref. [245] was complemented by a 'Hybrid' approach in Ref. [51]. Here 'LO' refers to one-body currents and 'Total' to the inclusion of 2BCs. Table adapted from Ref. [222].

	μ $[\mu_N]$			$B(M1)$ $[\mu_N^2]$		
	LO	LO SRG ev.	NLO SRG ev.	LO	LO SRG ev.	NLO SRG ev.
I	0.8399(22)	0.8221(28)	0.8240(34)	15.02(10)	14.44(8)	15.74(12)
II	0.8374(24)	0.8195(29)	0.8216(34)	14.92(13)	14.36(11)	15.48(15)
III	0.8344(21)	0.8188(26)	0.8217(32)	14.68(10)	14.13(8)	15.15(13)
IV	0.8388(18)	0.8236(23)	0.8261(28)	14.81(10)	14.32(8)	15.32(13)

	QMC LO	QMC Total	QMC LO	QMC Total
SNPA [245]	0.810(1)	0.800(1)	12.84(11)	15.00(11)
SNPA [51]	0.817(1)	0.807(1)	-	-
Hybrid [51]	0.817(1)	0.837(1)	13.18(4)	16.07(6)

5.8 COMPARISON AGAINST NEW S-DALINAC EXPERIMENT

Nuclear structure physics has entered an era of precision studies, both in experiment and theory. For light nuclei, *ab initio* theory based on interactions from chiral effective field theory [125] is reaching an accuracy at which corrections to EM operators that emerge naturally in the chiral expansion become relevant. A recent review [81] indicates that precision measurements of EM transition rates with uncertainties of a few percent or better are required to explore and validate the effects of these subleading corrections. For few-nucleon systems, direct measurements of strong transition rates with such precision are often challenging experimentally owing to the very short lifetimes involved.

Therefore, to test the above obtained results and reduce experimental uncertainties, a precision experiment with a new technique was carried out at the *Superconducting Darmstadt Electron Linear Accelerator* (S-DALINAC) [252, 253], which measured the dominant internal EM decay branch of the first excited 0^+_1 state of ^{6}Li at $E_{0^+_1} = 3562.88(10)$ keV [251] to its 1^+_1 ground state. The extremely short half-life of the excited state of about 80 as [251] makes a direct measurement of its decay rate impossible [254].[14] The potentially competing parity-forbidden decay via α emission has not been observed, and it is at least a million times weaker than the γ decay [255]. Because of its occurrence as stable matter (compared to the lighter hypernuclei [256]) and the low nucleon number of ^{6}Li, the decay of its 0^+_1 state is the EM transition of the most simple hadronic system simultaneously accessible by precision studies in theory and experiment. It is, therefore, ideally suited for testing our understanding of nuclear forces and electromagnetic currents in a many-nucleon system.

The experiment was performed at the *Darmstadt High-Intensity Photon Setup* (DHIPS) [257],

---

[14] One attosecond (as) equals 10^{-18} of a second.

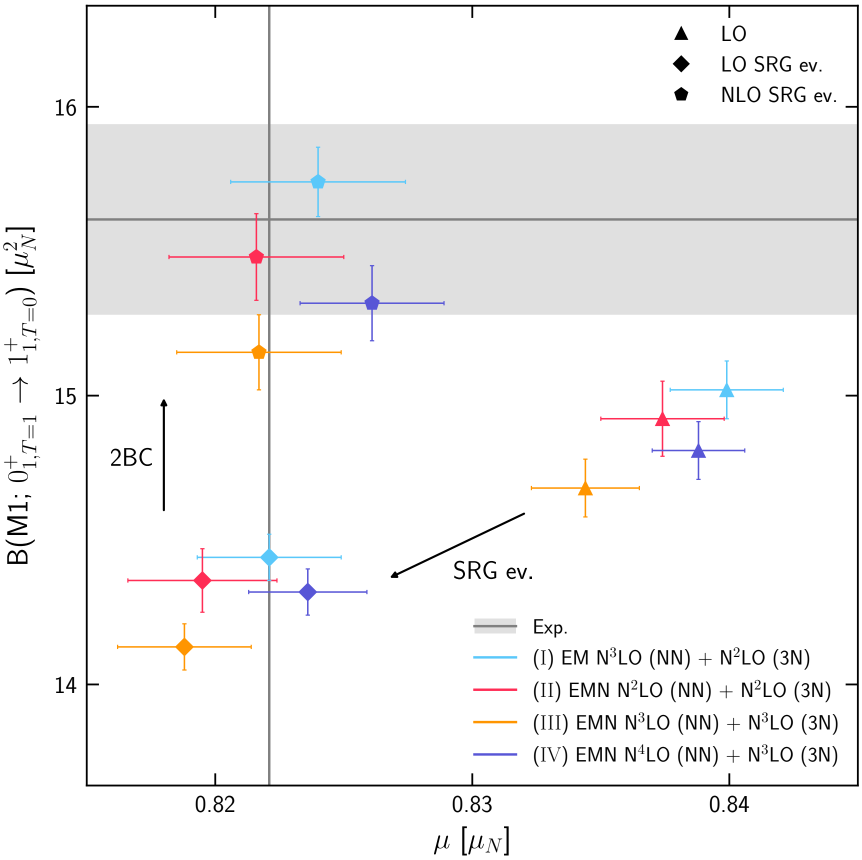

Figure 5.2: Results for $B(M1; 0^+_{T=1} \to 1^+_{T=0})$ and $\mu(1^+_{T=0})$ from calculations based on Hamiltonians I-IV, see also Table 5.4. As shown in the upper legend, upward triangles indicate calculations with the unevolved (LO) one-body transition operator, diamonds indicate calculations with the consistently SRG-transformed operator (LO SRG ev.), and pentagonal markers indicate the calculations with a consistently SRG-transformed operator including contributions from NLO 2BCs (NLO SRG ev.). The labeled arrows illustrate the impact of the two aforementioned improvements. The experimental 68% confidence interval for $B(M1)$ is indicated by the shaded area, and the central values for $B(M1)$ and μ [251] by a solid line (the confidence interval of μ is not visible at this scale). Figure adapted from Ref. [222].

with continuous energy photon beams generated by bremsstrahlung processes of the 7.1(2) MeV electron beam of the S-DALINAC on a copper radiator. To achieve the high precision necessary, the new nuclear resonance fluorescence (NRF) based relative self-absorption (SAbs) method [258, 259] was employed. The measurements and analysis of systematic effects produced a value for the γ-decay width $\Gamma_{\gamma,0^+_{T=1}\to 1^+_{T=0}} = 8.17^{+0.14}_{-0.13}$ (stat.)$^{+0.10}_{-0.11}$ (syst.) eV, which corresponds to a strength $B(M1; 0^+_{T=1} \to 1^+_{T=0}) = 15.61^{+0.27}_{-0.25}$ (stat.)$^{+0.19}_{-0.21}$ (syst.) μ_N^2 [222]. The 68.3% confidence interval is divided into statistical (stat.) and systematic (syst.) parts, where the latter accounts for uncertainties of the target dimensions as well as atomic and condensed-matter contributions. Since both contributions are uncorrelated and the confidence intervals are almost symmetric, a symmetrized and quadratically summed uncertainty of 15.61(33) μ_N^2 is used in Fig. 5.2 to compare against the theoretical results.

Figure 5.2 shows the results obtained in the previous section, compared to the new experimental constraint and the magnetic moment $\mu(1^+_{1,T=0}) = 0.82205667(26)\ \mu_N$ [251] of the ground state of ^{6}Li. The four different Hamiltonians are denoted by four colors, teal, pink, orange, and indigo for I, II, III, and IV, while the different operators are shown by three distinct symbols, an upward triangle, a diamond, and a pentagon for the LO, SRG evolved LO, and SRG evolved NLO operators, respectively. Remarkably, the results of the most complete calculations, including contributions from the 2BC to the $M1$ operator, exhibit excellent agreement with the new experimental constraints. This indicates once again the importance of 2BCs for a correct description of the ^{6}Li nucleus. Such tests of chiral EFT would not have been possible on the basis of the pre-2019 data. The increase of the $B(M1)$ is also found in QMC calculations when 2BCs are included [51, 245], see also Table 5.4 and the discussion in the previous section.

The situation encountered here may remind the reader of the ^{6}He beta-decay half-life discrepancy that existed in the literature before 2012 and was resolved by a high-precision measurement of Knecht *et al.* [260] in that year. Similar to the weak-interaction sector, the new experiment improves the validation on the corresponding EM-analog transition by remeasuring the γ-decay half-life of the first excited state of ^{6}Li with isospin $T = 1$. In total, a relative uncertainty of 2% with balanced contributions by statistics and systematics was achieved. This translates into an uncertainty of about 2 as for the half-life of the 0_1^+ state of ^{6}Li. In addition, chiral EFT nuclear structure calculations were performed that, for the first time, take 2BCs at NLO, combined with chiral interactions at various orders, into account. The high degree of agreement between experiment and theory is a result of the recent progress in both areas.

6

CONCLUSIONS AND OUTLOOK

In this thesis, we examined the effect of the leading 2BC operators on electromagnetic observables of $A = 2$, 3, and 6 nuclei. They are essential in describing electromagnetic properties, especially magnetic ones, and they arise from the exchange of a pion between a pair of nucleons. To study them, we have used chiral EFT as the nuclear framework of choice to provide nuclear interactions and electromagnetic nuclear current operators. This framework allows a systematically improvable calculation scheme to describe interactions between nucleons and with external probes at low energies in close connection to the underlying theory of QCD. We obtained results with associated uncertainty estimates from calculations with high-precision NN and 3N chiral interactions developed in an order-by-order manner.

The main focus of this thesis was the analysis of the electromagnetic deuteron and trinucleon form factors. For the deuteron, we presented results for the charge, quadrupole, and magnetic form factors obtained with the one-body operator. The leading 2BC contributions vanish for the isoscalar deuteron due to its isovector structure. In order to obtain the form factors, we expanded the one-body charge and current operators with respect to a relative momentum-space partial-wave basis. The form factors were then obtained by computing specific linear combinations of deuteron matrix elements, where we made use of the EMN NN interactions [23] up to fourth order to determine the deuteron wave functions. As the chiral interactions are consistently developed order by order, we were able to compute reliable truncation uncertainty DoB intervals at each order by employing a Bayesian model. We observed a systematic order-by-order convergence of the uncertainty intervals with successively overlapping bands. Given that the uncertainty depends on the characteristic momentum scale of the process, the DoB intervals grow as the momentum transfer increases. This generated rather large intervals in the kinematic region where the first minimum occurs for both the charge and magnetic form factors. Consequently, the majority of experimental data was consistent with the 68% DoB interval, while the 95% interval covered essentially all data. This suggests that the requirement to exactly reproduce the experimental minimum might be too strict given that chiral EFT's predictive power in this kinematic region diminishes as the expansion parameter is momentum dependent, and hence inherently results in larger uncertainties. Finally, as an extra verification, we extracted the magnetic moment from the magnetic form factor normalization. Its value confirmed our findings on the form factor and almost exactly agreed with the experimental value.

The analysis of the deuteron form factors laid the foundation for our examination of the trinucleons, for which we provided charge and magnetic form factor results. Similar to the two-body case, we started by expanding the charge and current operators with respect to a relative three-body momentum-space partial-wave basis, where the three particles are described in terms of Jacobi momenta. We determined the form factors using two different combinations of NN + 3N interactions: the first combination used the same NN interaction as for the deuteron calculations but complemented with 3N interactions at fourth order which are fit to the triton binding energy and nuclear matter [32], while the second combination used unevolved as well as SRG-evolved EM NN interactions [189] with 3N interactions at third order which are fit to few-nucleon systems only [31]. The latter combination was used to investigate the effect of 3N and SRG-evolved interactions on the form factors. As the SRG-evolution softens the interaction, a difference in the form factor at higher-momentum transfers is expected. This effect was indeed confirmed by our observations: a softer interaction pushes the minimum to higher momentum transfers. On the other hand, the omission or addition of 3N interactions had an almost negligible effect upon qualitative inspection of the form factor. The main goal of our study with the first combination of interactions was to assess the impact of 2BCs. If 2BC corrections are included, we observed that the form factor curve is shifted up at low transfer momenta, while the minimum is simultaneously shifted to higher momentum transfers. Both trends bring the theoretical result to better agreement with experimental data and the overlap of the truncation uncertainty DoB intervals with the experimental bands is also improved when 2BCs are included, especially for helion.

The effect of 2BCs on the trinucleon form factors is well known on a qualitative level, whereas the form factor curves do not allow to conclusively determine the effect of SRG-evolving or including 3N interactions, especially in the regime of low momentum transfers. To quantify possible effects and to analyze them in more detail, we studied the electromagnetic radii and magnetic moments of trinucleons. First of all, we observed that SRG-evolved interactions increased the absolute value of the magnetic moment and of the charge radius, while the magnetic radius stayed nearly constant. Second, the effect of including 3N interactions on the magnetic moment is almost negligible, yet the charge and magnetic radius both reduced in size by up to 3%, shifting the result towards the central experimental value. Finally, incorporation of 2BC corrections resulted in a decrease of the magnetic radius of about 5% and a large increase of the absolute value of the magnetic moment by as much as 10%, leading to better agreement with the experimental value in both cases. Experimental values for the electromagnetic radii are, however, not precise enough to allow decisive conclusions about the necessity of 3N interactions or even 2BCs. The magnetic moments on the other hand are known very precisely and the leading 2BCs are found to produce significant corrections to the theoretical result such that they are in better agreement.

As we demonstrated for trinucleons: magnetic observables are very sensitive to the exchange dynamics between the nucleons. In order to extend our study of the leading 2BC effects on magnetic observables, we considered the next light nucleus after the trinucleons with nonvanishing magnetic properties, ^{6}Li, as a first exploration of light nuclei. To this end, we calculated the magnetic moment and an isovector magnetic transition from an excited state to the ground state. To simplify the analysis, we examined the magnetic dipole moment operator which equals the zero-momentum-transfer limit of the curl of the current operator. Which allowed us to include the 2BC contributions to the magnetic moment operator. These contributions constitute the well-known intrinsic and Sachs corrections. In order to compute the magnetic properties, we employed the IT-NCSM to solve the many-body problem and obtain the ^{6}Li wave functions. We used four different Hamiltonians to assess interaction systematics. The Hamiltonians were SRG-evolved in order to accomplish a better convergence of the calculation. Furthermore, the magnetic moment operator needed to be represented in a single-particle basis before it could be incorporated into the IT-NCSM calculations. To achieve this, we performed a basis transformation of the relative partial-wave basis to a HO single-particle basis and successfully benchmarked the transformation against the trinucleon magnetic moments obtained from form factor calculations. The result for the magnetic moment and the transition strength led to two main findings. First, 2BC contributions caused a large correction to the isovector transition strength result, leading to an improved agreement with experiment. Second, a consistent SRG evolution of the operator is key in order to obtain agreement with the experimental magnetic moment and transition strength. These conclusions and further high-precision tests of chiral EFT were only possible by a recent measurement performed at the S-DALINAC based on a new experimental technique to measure the magnetic transition strength.

Our studies can be extended in future work by including higher-order two-body charge and current operators in the few-nucleon form factor calculations. In this way, a consistent calculation with operators and interactions at the same order can be performed. Such an approach may lead to insights in the convergence behavior of the observables at high momentum transfers. In relation to this, it will be interesting to see the effect on the truncation uncertainty intervals of the form factors, especially in the high momentum transfer region.

As some of the higher-order operators are associated with new LECs which have to be fixed to few-nucleon observables, one approach to further investigate 2BCs is by studying other light nuclei or even medium-mass nuclei. To achieve this, the technique we used for ^{6}Li has to be extended to other nuclei showing interesting electromagnetic properties. This would result in an improvement over existing calculations of light nuclei which use a hybrid approach, i.e., current operators from chiral EFT in combination with phenomenological interactions, to obtain electromagnetic properties. In addition, the impact of 2BCs on electromagnetic transitions, magnetic moments, and electromagnetic form factors of medium-mass nuclei is completely unexplored. For example, an interesting phenomenon worthwhile studying is given by the unexpectedly large charge radii of neutron-rich calcium isotopes [30]. These radii cannot be reproduced by conventional methods. This may result from truncations in the many-body calculations or from important higher-order operator effects which are presently not included. To conclude, this thesis provides a basis for calculations with chiral 2BCs in the electromagnetic sector beyond light nuclei.

A

DEUTERON, TRITON, AND HELION PARTIAL-WAVE CONFIGURATIONS

Making a partial-wave expansion of the deuteron and trinucleon wave functions results in several possible configurations which depend on the total two- and three-body quantum numbers. Below we list these configurations for the deuteron and the trinucleons.

Two-body configurations

There are only two configurations of the two-body partial-wave basis states that contribute to the deuteron wave function. For completeness and to show the similarity with the three-body basis, we specify these two configurations in Table A.1.

Table A.1: Deuteron two-body partial-wave quantum numbers. The leftmost column shows the nuclear spectroscopic notation.

${}^{(2S+1)}L_J$	L	S	J	T
${}^3\mathrm{S}_1$	0	1	1	0
${}^3\mathrm{D}_1$	2	1	1	0

Three-body configurations

In this thesis we investigate the triton and the helion. Their three-body quantum numbers $\mathcal{J} = \mathcal{T} = \frac{1}{2}$, together with positive parity $\mathcal{P} = +1$ and an antisymmetric two-body subsystem, i.e., $(-1)^{L+S+T} = -1$, determine the possible configurations of the Jj-coupled basis. All the different possibilities for a two-body angular momentum of $J \leqslant 8$ are listed in Table A.2.

Table A.2: Possible three-body configurations for quantum numbers in $\alpha = \{L, S, J, T, \ell, j\}$ satisfying total angular momentum and total isospin $\mathcal{J} = \mathcal{T} = \frac{1}{2}$, positive parity $\mathcal{P} = +1$ up to $J = 8$. Table adapted from [33].

	L	S	J	T	ℓ	j
1	0	0	0	1	0	$\frac{1}{2}$
2	1	1	0	1	1	$\frac{1}{2}$
3	1	0	1	0	1	$\frac{1}{2}$
4	1	0	1	0	1	$\frac{3}{2}$
5	0	1	1	0	0	$\frac{1}{2}$
6	0	1	1	0	2	$\frac{3}{2}$
7	1	1	1	1	1	$\frac{1}{2}$
8	1	1	1	1	1	$\frac{3}{2}$
9	2	1	1	0	0	$\frac{1}{2}$
10	2	1	1	0	2	$\frac{3}{2}$
11	2	0	2	1	2	$\frac{3}{2}$
12	2	0	2	1	2	$\frac{5}{2}$
13	1	1	2	1	1	$\frac{3}{2}$
14	1	1	2	1	3	$\frac{5}{2}$
15	2	1	2	0	2	$\frac{3}{2}$
16	2	1	2	0	2	$\frac{5}{2}$
17	3	1	2	1	1	$\frac{3}{2}$
18	3	1	2	1	3	$\frac{5}{2}$
19	3	0	3	0	3	$\frac{5}{2}$
20	3	0	3	0	3	$\frac{7}{2}$
21	2	1	3	0	2	$\frac{5}{2}$
22	2	1	3	0	4	$\frac{7}{2}$
23	3	1	3	1	3	$\frac{5}{2}$
24	3	1	3	1	3	$\frac{7}{2}$
25	4	1	3	0	2	$\frac{5}{2}$
26	4	1	3	0	4	$\frac{7}{2}$
27	4	0	4	1	4	$\frac{7}{2}$
28	4	0	4	1	4	$\frac{9}{2}$
29	3	1	4	1	3	$\frac{7}{2}$
30	3	1	4	1	5	$\frac{9}{2}$
31	4	1	4	0	4	$\frac{7}{2}$
32	4	1	4	0	4	$\frac{9}{2}$
33	5	1	4	1	3	$\frac{7}{2}$
34	5	1	4	1	5	$\frac{9}{2}$
35	5	0	5	0	5	$\frac{9}{2}$
36	5	0	5	0	5	$\frac{11}{2}$
37	4	1	5	0	4	$\frac{9}{2}$
38	4	1	5	0	6	$\frac{11}{2}$
38	5	1	5	1	5	$\frac{9}{2}$
40	5	1	5	1	5	$\frac{11}{2}$
41	6	1	5	0	4	$\frac{9}{2}$
42	6	1	5	0	6	$\frac{11}{2}$
43	6	0	6	1	6	$\frac{11}{2}$
44	6	0	6	1	6	$\frac{13}{2}$
45	5	1	6	1	5	$\frac{11}{2}$
46	5	1	6	1	7	$\frac{13}{2}$
47	6	1	6	0	6	$\frac{11}{2}$
48	6	1	6	0	6	$\frac{13}{2}$
49	7	1	6	1	5	$\frac{11}{2}$
50	7	1	6	1	7	$\frac{13}{2}$
51	7	0	7	0	7	$\frac{13}{2}$
52	7	0	7	0	7	$\frac{15}{2}$
53	6	1	7	0	6	$\frac{13}{2}$
54	6	1	7	0	8	$\frac{15}{2}$
55	7	1	7	1	7	$\frac{13}{2}$
56	7	1	7	1	7	$\frac{15}{2}$
57	8	1	7	0	6	$\frac{13}{2}$
58	8	1	7	0	8	$\frac{15}{2}$
59	8	0	8	1	8	$\frac{15}{2}$
60	8	0	8	1	8	$\frac{17}{2}$
61	7	1	8	1	7	$\frac{15}{2}$
62	7	1	8	1	9	$\frac{17}{2}$
63	8	1	8	0	8	$\frac{15}{2}$
64	8	1	8	0	8	$\frac{17}{2}$
65	9	1	8	1	7	$\frac{15}{2}$
66	9	1	8	1	9	$\frac{17}{2}$

B

PARTIAL-WAVE EXPANDED FORM FACTORS

Because we represent the deuteron and trinucleon wave functions in a two- and three-body partial-wave basis, respectively, we have to expand the charge and current operators in the respective partial-wave basis. In this chapter, we represent the detailed derivation of each form factor. In the first section, we address the deuteron form factors and in the second section we consider the trinucleon form factors.

B.1 Deuteron form factors

B.1.1 One-body charge and quadrupole form factor

Charge form factor

In the following we show the step-by-step derivation of the deuteron charge form factor. The notation we use here employs the one that we introduced in Section 4.3.2. We begin by restating the charge form factor expression we obtained in Section 4.3.1, which was given in terms of the independent deuteron matrix elements,

$$G_{\mathrm{C}}(Q) = \frac{1}{3\sqrt{1+\eta_{\mathrm{d}}}}(g_0 + 2g_{-1}) = \frac{1}{3\sqrt{1+\eta_{\mathrm{d}}}} \sum_{M_J=\pm 1,0} \langle M_J\, \mathbf{Q}/2 |\, \hat{\rho}^{(-3)}\, | M_J\, - \mathbf{Q}/2 \rangle \,. \tag{B.1}$$

As a first step, we insert two relative-momentum completeness relations between the one-body charge operator and the deuteron states and decouple the total angular momentum $J = 1$ into orbital angular momentum L and spin S:

$$\begin{aligned} G_{\mathrm{C}}(Q) =& \frac{1}{3\sqrt{1+\eta_{\mathrm{d}}}} \sum_{M_J=\pm 1,0} \sum_{\substack{L'M'_L \\ S'M'_S}} \sum_{\substack{LM_L \\ SM_S}} \mathcal{C}^{1M_J}_{L'M'_L S'M'_S}\, \mathcal{C}^{1M_J}_{LM_L SM_S} \int_{\mathbf{p}'} \int_{\mathbf{p}} \phi^*_{L'}(p')\, Y^*_{L'M'_L}(\hat{\mathbf{p}}') \\ & \times \langle S'\, M'_S | S\, M_S \rangle\, \langle \mathbf{Q}/2\, \mathbf{p}' |\, \hat{\rho}^{(-3)}\, | - \mathbf{Q}/2\, \mathbf{p} \rangle\; Y_{LM_L}(\hat{\mathbf{p}})\; \phi_L(p) \,. \end{aligned} \tag{B.2}$$

Evaluating the one-body charge operator between momentum states yields

$$\begin{aligned} G_{\mathrm{C}}(Q) =& \frac{1}{3\sqrt{1+\eta_{\mathrm{d}}}} \sum_{M_J=\pm1,0} \sum_{\substack{L'M'_L \\ S'M'_S}} \sum_{\substack{LM_L \\ SM_S}} \mathcal{C}^{1M_J}_{L'M'_LS'M'_S}\, \mathcal{C}^{1M_J}_{LM_LSM_S} \int_{\mathbf{p}'}\int_{\mathbf{p}} \phi^*_{L'}(p')\, Y^*_{L'M'_L}(\hat{\mathbf{p}}') \\ & \times \delta_{SS'}\, \delta_{M_SM'_S}\, G^S_{\mathrm{E}}(Q^2)\, (2\pi)^3 \delta(\mathbf{p}-\mathbf{p}'-\mathbf{Q}/2)\, Y_{LM_L}(\hat{\mathbf{p}})\; \phi_L(p), \end{aligned} \tag{B.3}$$

where the isoscalar electric nucleon form factor $G^S_{\mathrm{E}}(Q^2)$ arises from

$$\begin{aligned} \langle T'M'_T|\, e_{N,i}(Q^2)\, |TM_T\rangle =& \sum_{i=1,2} \sum_{m'_{t_i} m_{t_i}} \mathcal{C}^{00}_{\frac{1}{2}m'_{t_1}\frac{1}{2}m'_{t_2}}\, \mathcal{C}^{00}_{\frac{1}{2}m_{t_1}\frac{1}{2}m_{t_2}} \\ & \times \langle \tfrac{1}{2}m'_{t_1}\, \tfrac{1}{2}m'_{t_2}| \frac{G^S_{\mathrm{E}}(Q^2)+G^V_{\mathrm{E}}(Q^2)\hat{\tau}_{i,z}}{2} |\tfrac{1}{2}m_{t_1}\, \tfrac{1}{2}m_{t_2}\rangle \\ =& G^S_{\mathrm{E}}(Q^2). \end{aligned}$$

Integrating over $\mathbf{p}'$ eliminates the delta function and yields

$$\begin{aligned} G_{\mathrm{C}}(Q) =& \frac{G^S_{\mathrm{E}}(Q^2)}{3\sqrt{1+\eta_{\mathrm{d}}}} \sum_{M_J=\pm1,0} \sum_{L'M'_L} \sum_{\substack{LM_L \\ SM_S}} \mathcal{C}^{1M_J}_{L'M'_LS'M'_S}\, \mathcal{C}^{1M_J}_{LM_LSM_S} \\ & \times \int_{\mathbf{p}} \phi^*_{L'}(|\mathbf{p}_Q|)\, Y^*_{L'M'_L}(\hat{\mathbf{p}}_Q)\, Y_{LM_L}(\hat{\mathbf{p}})\; \phi_L(p), \end{aligned} \tag{B.4}$$

where we introduced the notation $\mathbf{p}_Q = \mathbf{p} - \mathbf{Q}/2$. In a next step, we use the fact that $S = 1$ for the deuteron and the following Clebsch-Gordan property [166]

$$\sum_{\alpha\gamma} \mathcal{C}^{c\gamma}_{a\alpha b\beta}\, \mathcal{C}^{c\gamma}_{a\alpha b'\beta'} = \frac{2c+1}{2b+1} \delta_{bb'}\, \delta_{\beta\beta'}, \tag{B.5}$$

so that we find

$$\begin{aligned} G_{\mathrm{C}}(Q) =& \frac{G^S_{\mathrm{E}}(Q^2)}{3\sqrt{1+\eta_{\mathrm{d}}}} \sum_{L'M'_L} \sum_{\substack{LM_L \\ SM_S}} \frac{2J+1}{2L+1} \delta_{LL'}\, \delta_{M_LM'_L} \\ & \times \int_{\mathbf{p}} \phi^*_{L'}(|\mathbf{p}_Q|)\, Y^*_{L'M'_L}(\hat{\mathbf{p}}_Q)\; Y_{LM_L}(\hat{\mathbf{p}})\; \phi_L(p). \end{aligned} \tag{B.6}$$

Performing the sum over the delta functions and rewriting the result provides the final expression for the one-body deuteron charge form factor:

$$G_{\mathrm{C}}(Q) = \frac{G^S_{\mathrm{E}}(Q^2)}{3\sqrt{1+\eta_{\mathrm{d}}}} \sum_{LM_L} \frac{2\cdot 1+1}{2L+1} \int_{\mathbf{p}} \phi^*_L(|\mathbf{p}_Q|)\, Y^*_{LM_L}(\hat{\mathbf{p}}_Q)\; Y_{LM_L}(\hat{\mathbf{p}})\; \phi_L(p) \tag{B.7}$$

$$\begin{aligned} =& \frac{G^S_{\mathrm{E}}(Q^2)}{\sqrt{1+\eta_{\mathrm{d}}}} \sum_{LM_L} \frac{1}{2L+1} \\ & \times \int_0^\infty \frac{\mathrm{d}p}{(2\pi)^3}\, p^2 \int_0^\pi \mathrm{d}\theta_p\, \sin\theta_p \int_0^{2\pi} \mathrm{d}\varphi_p\, \phi^*_L(|\mathbf{p}_Q|)\, Y^*_{LM_L}(\hat{\mathbf{p}}_Q)\; Y_{LM_L}(\hat{\mathbf{p}})\; \phi_L(p). \end{aligned} \tag{B.8}$$

The last step explicitly shows the integration over each variable of the three-dimensional integral that we have to solve. To calculate this integral, we use the techniques explained in

Section 4.3.3. Note that the expression for the charge form factor is completely diagonal in its quantum numbers.

Quadrupole form factor

Because the steps we need to carry out to obtain the quadrupole form factor are practically the same as the ones we showed for the charge form factor, we present all them one after another without a detailed explanation. The deuteron quadrupole form factor expression due to the one-body charge operator is found by

$$\begin{aligned}
G_{\mathrm{Q}}(Q) =& \frac{2\,M_{\mathrm{d}}^2}{Q^2\,\sqrt{1+\eta_{\mathrm{d}}}}\Big[\,\langle 0\,\mathbf{Q}/2|\,\hat{\rho}^{(-3)}\,|0\,-\mathbf{Q}/2\rangle - \langle 1\,\mathbf{Q}/2|\,\hat{\rho}^{(-3)}\,|1\,-\mathbf{Q}/2\rangle\,\Big] \\
=& \frac{2\,M_{\mathrm{d}}^2}{Q^2\,\sqrt{1+\eta_{\mathrm{d}}}} \sum_{\substack{L'M'_L\\ S'M'_S}} \sum_{\substack{LM_L\\ SM_S}} \Big(\mathcal{C}^{10}_{L'M'_LS'M'_S}\,\mathcal{C}^{10}_{LM_LSM_S} - \mathcal{C}^{11}_{L'M'_LS'M'_S}\,\mathcal{C}^{11}_{LM_LSM_S}\Big)\int_{\mathbf{p}'}\int_{\mathbf{p}} \\
&\times \phi^*_{L'}(p')\,Y^*_{L'M'_L}(\hat{\mathbf{p}}')\;\langle S'\,M'_S|S\,M_S\rangle\,\langle \mathbf{Q}/2\,\mathbf{p}'|\,\hat{\rho}^{(-3)}\,|-\mathbf{Q}/2\,\mathbf{p}\rangle\;Y_{LM_L}(\hat{\mathbf{p}})\;\phi_L(p) \qquad \text{(B.9)} \\
=& \frac{2\,M_{\mathrm{d}}^2}{Q^2\,\sqrt{1+\eta_{\mathrm{d}}}} \sum_{\substack{L'M'_L\\ S'M'_S}} \sum_{\substack{LM_L\\ SM_S}} \Big(\mathcal{C}^{10}_{L'M'_LS'M'_S}\,\mathcal{C}^{10}_{LM_LSM_S} - \mathcal{C}^{11}_{L'M'_LS'M'_S}\,\mathcal{C}^{11}_{LM_LSM_S}\Big)\int_{\mathbf{p}'}\int_{\mathbf{p}} \\
&\times \phi^*_{L'}(p')\,Y^*_{L'M'_L}(\hat{\mathbf{p}}')\;\delta_{SS'}\,\delta_{M_SM'_S}\;G^S_{\mathrm{E}}(Q^2)\,(2\pi)^3\delta(\mathbf{p}-\mathbf{p}'-\mathbf{Q}/2)\,Y_{LM_L}(\hat{\mathbf{p}})\;\phi_L(p) \qquad \text{(B.10)} \\
=& \frac{2\,M_{\mathrm{d}}^2\,G^S_{\mathrm{E}}(Q^2)}{Q^2\,\sqrt{1+\eta_{\mathrm{d}}}} \sum_{L'M'_L} \sum_{\substack{LM_L\\ SM_S}} \Big(\mathcal{C}^{10}_{L'M'_LSM_S}\,\mathcal{C}^{10}_{LM_LSM_S} - \mathcal{C}^{11}_{L'M'_LSM_S}\,\mathcal{C}^{11}_{LM_LSM_S}\Big) \\
&\times \int_{\mathbf{p}} \phi^*_L(|\mathbf{p}_Q|)\,Y^*_{L'M'_L}(\hat{\mathbf{p}}_Q)\;Y_{LM_L}(\hat{\mathbf{p}})\;\phi_L(p) \qquad \text{(B.11)} \\
=& \frac{2\,M_{\mathrm{d}}^2\,G^S_{\mathrm{E}}(Q^2)}{Q^2\,\sqrt{1+\eta_{\mathrm{d}}}} \sum_{L'M'_L} \sum_{\substack{LM_L\\ M_S}} \Big(\mathcal{C}^{10}_{L'M'_L1M_S}\,\mathcal{C}^{10}_{LM_L1M_S} - \mathcal{C}^{11}_{L'M'_L1M_S}\,\mathcal{C}^{11}_{LM_L1M_S}\Big) \\
&\times \int_0^\infty \frac{\mathrm{d}p}{(2\pi)^3}\,p^2 \int_0^\pi \mathrm{d}\theta_p\,\sin\theta_p \int_0^{2\pi} \mathrm{d}\varphi_p\,\phi^*_{L'}(|\mathbf{p}_Q|)\,Y^*_{L'M'_L}(\hat{\mathbf{p}}_Q)\;Y_{LM_L}(\hat{\mathbf{p}})\;\phi_L(p), \qquad \text{(B.12)}
\end{aligned}$$

where in the last step we made explicit that $S = 1$. Compared to the charge form factor expression, the quadrupole form factor expression is nondiagonal in orbital angular momentum and still depends on Clebsch-Gordan coefficients.

B.1.2 One-body magnetic form factor

The one-body current operator consists of two terms. Therefore, we can split the magnetic form factor calculation into two parts as follows

$$G_{\mathrm{M}}(Q^2) = G_{\mathrm{M},1}(Q^2) + G_{\mathrm{M},2}(Q^2). \qquad \text{(B.13)}$$

Below, we consider both terms separately.

Magnetic form factor first term

The detailed derivation of the first term of the magnetic form factor expression is given by

$$\begin{aligned}
G_{\mathrm{M},1}(Q^2) =&\frac{-2\,M_\mathrm{d}}{Q\,\sqrt{1+\eta_\mathrm{d}}}\,\langle +1\,\mathbf{Q}/2|\,e_{N,i}(Q^2)\frac{\hat{p}_+}{2\,m_N}\,|0\;-\mathbf{Q}/2\rangle &\text{(B.14)}\\
=&\frac{-2\,M_\mathrm{d}}{Q\,\sqrt{1+\eta_\mathrm{d}}}\sum_{\substack{L'M_L'\\S'M_S'}}\sum_{\substack{LM_L\\SM_S}}\mathcal{C}^{11}_{L'M_L'S'M_S'}\,\mathcal{C}^{10}_{LM_LSM_S}\int_{\mathbf{p}'}\int_{\mathbf{p}}\phi^*_{L'}(p')\,Y^*_{L'M_L'}(\hat{\mathbf{p}}')\\
&\times\langle S'\,M_S'|S\,M_S\rangle\,\langle\mathbf{Q}/2\,\mathbf{p}'|\,e_{N,i}(Q^2)\frac{\hat{p}_+}{2\,m_N}\,|-\mathbf{Q}/2\,\mathbf{p}\rangle\;Y_{LM_L}(\hat{\mathbf{p}})\;\phi_L(p) &\text{(B.15)}\\
=&\frac{-M_\mathrm{d}}{Q\,m_N\,\sqrt{1+\eta_\mathrm{d}}}\sum_{\substack{L'M_L'\\S'M_S'}}\sum_{\substack{LM_L\\SM_S}}\mathcal{C}^{11}_{L'M_L'S'M_S'}\,\mathcal{C}^{10}_{LM_LSM_S}\int_{\mathbf{p}'}\int_{\mathbf{p}}\phi^*_{L'}(p')\,Y^*_{L'M_L'}(\hat{\mathbf{p}}')\\
&\times\delta_{S'S}\,\delta_{M_S'M_S}\,G^S_\mathrm{E}(Q^2)\,(2\pi)^3\delta(\mathbf{p}'-\mathbf{p}-\mathbf{Q}/2)\,(p^f_++p^i_+)\,Y_{LM_L}(\hat{\mathbf{p}})\;\phi_L(p) &\text{(B.16)}\\
=&\frac{-M_\mathrm{d}\,G^S_\mathrm{E}(Q^2)}{Q\,m_N\,\sqrt{1+\eta_\mathrm{d}}}\sum_{L'M_L'}\sum_{\substack{LM_L\\SM_S}}\mathcal{C}^{11}_{L'M_L'SM_S'}\,\mathcal{C}^{10}_{LM_LSM_S}\int_{\mathbf{p}}\phi^*_{L'}(|\mathbf{p}_Q|)\,Y^*_{L'M_L'}(\hat{\mathbf{p}}_Q)\\
&\times(2p_++Q_++P_+)\,Y_{LM_L}(\hat{\mathbf{p}})\;\phi_L(p) &\text{(B.17)}\\
=&\frac{-2\,M_\mathrm{d}\,G^S_\mathrm{E}(Q^2)}{Q\,m_N\,\sqrt{1+\eta_\mathrm{d}}}\sum_{L'M_L'}\sum_{\substack{LM_L\\M_S}}\mathcal{C}^{11}_{L'M_L'1M_S'}\,\mathcal{C}^{10}_{LM_L1M_S}\int_0^\infty\frac{\mathrm{d}p}{(2\pi)^3}\,p^2\int_0^\pi\mathrm{d}\theta_p\,\sin\theta_p\\
&\times\int_0^{2\pi}\mathrm{d}\varphi_p\,\phi^*_{L'}(|\mathbf{p}_Q|)\,Y^*_{L'M_L'}(\hat{\mathbf{p}}_Q)\;p_+\,Y_{LM_L}(\hat{\mathbf{p}})\;\phi_L(p). &\text{(B.18)}
\end{aligned}$$

The momentum operator $\hat{p}_+$ has the effect to generate the extra factor $(2p_+ + Q_+ + P_+)$. In the end this factor will only contribute p_+, because in the Breit frame we have $\mathbf{P} = -\mathbf{Q}/2$ and we chose $\mathbf{Q}$ along the positive z direction so that $Q_+ = -Q/\sqrt{2}(\sin\theta\cos\varphi + i\sin\theta\sin\varphi) = 0$. The factor p_+ is given by

$$p_+ = -\frac{p_x + i\,p_y}{\sqrt{2}} = \frac{-p}{\sqrt{2}}(\sin\theta_p\cos\varphi_p + i\sin\theta_p\sin\varphi_p). \tag{B.19}$$

It acts as a ladder operator on the orbital angular momentum quantum number L.

Magnetic form factor second term

We continue with the second term of the magnetic moment operator which is found by

$$\begin{aligned}
G_{\mathrm{M},2}(Q^2) =&\frac{2\,M_\mathrm{d}}{Q\,\sqrt{1+\eta_\mathrm{d}}}\,\langle +1\,\mathbf{Q}/2|\,\mu_{N,i}(Q^2)\frac{i(\boldsymbol{\sigma}\times\mathbf{Q})_+}{2m_N}\,|0\;-\mathbf{Q}/2\rangle &\text{(B.20)}\\
=&\frac{2\,M_\mathrm{d}}{Q\,\sqrt{1+\eta_\mathrm{d}}}\sum_{\substack{L'M_L'\\S'M_S'}}\sum_{\substack{LM_L\\SM_S}}\mathcal{C}^{11}_{L'M_L'S'M_S'}\,\mathcal{C}^{10}_{LM_LSM_S}\int_{\mathbf{p}'}\int_{\mathbf{p}}\phi^*_{L'}(p')\,Y^*_{L'M_L'}(\hat{\mathbf{p}}')\\
&\times G^S_\mathrm{M}(Q^2)\,(2\pi)^3\delta(\mathbf{p}'-\mathbf{p}-\mathbf{Q}/2)\\
&\times\frac{1}{2m_N}\,\langle S'\,M_S'|\,i(i\,Q_z\,\hat{\sigma}_{+,i}+i\,Q_+\,\hat{\sigma}_z)\,|S\,M_S\rangle\;Y_{LM_L}(\hat{\mathbf{p}})\;\phi_L(p), &\text{(B.21)}
\end{aligned}$$

where we worked out the cross product between the spin operator and the momentum transfer. Carrying out the integration over $\mathbf{p}'$ reduces the expression to

$$\begin{aligned}
G_{\mathrm{M},2}(Q^2) = & \frac{M_\mathrm{d}\, G_\mathrm{M}^S(Q^2)}{\cancel{Q}\, m_N \sqrt{1+\eta_\mathrm{d}}} \sum_{\substack{L'M_L' \\ S'M_S'}} \sum_{\substack{LM_L \\ SM_S}} \mathcal{C}^{11}_{L'M_L'S'M_S'} \, \mathcal{C}^{10}_{LM_LSM_S} \\
& \times \int_{\mathbf{p}} \phi^*_{L'}(|\mathbf{p}_Q|)\, Y^*_{L'M_L'}(\hat{\mathbf{p}}_Q) \sum_{i=1,2} \sum_{\substack{m_1'm_2' \\ m_1m_2}} \mathcal{C}^{S'M_S'}_{\frac{1}{2}\,m_1'\,\frac{1}{2}\,m_2'} \, \mathcal{C}^{SM_S}_{\frac{1}{2}\,m_1\,\frac{1}{2}\,m_2} \\
& \times \langle \tfrac{1}{2} m_1' \; \tfrac{1}{2} m_2' | \, \cancel{Q}_z \, \hat{\sigma}_{+,i} \, | \tfrac{1}{2} m_1 \; \tfrac{1}{2} m_2 \rangle \; Y_{LM_L}(\hat{\mathbf{p}}) \; \phi_L(p),
\end{aligned} \tag{B.22}$$

where $Q_z = Q$ cancels the momentum transfer in the denominator of the prefactor. By employing the index notation, we simplified the calculation of the cross product $\mathbf{Q} \times \boldsymbol{\sigma}$. We treat the spin part separately as follows

$$\mathcal{S}^{S'S}_{M_S'M_S} = \sum_{i=1,2} \sum_{\substack{m_1'm_2' \\ m_1m_2}} \mathcal{C}^{S'M_S'}_{\frac{1}{2}\,m_1'\,\frac{1}{2}\,m_2'} \, \mathcal{C}^{SM_S}_{\frac{1}{2}\,m_1\,\frac{1}{2}\,m_2} \; \langle \tfrac{1}{2} m_1' \; \tfrac{1}{2} m_2' | \, \hat{\sigma}_{+,i} \, | \tfrac{1}{2} m_1 \; \tfrac{1}{2} m_2 \rangle \tag{B.23}$$

$$\begin{aligned}
= & \sum_{\substack{m_1'\,m_2' \\ m_1\,m_2}} \mathcal{C}^{S'M_S'}_{\frac{1}{2}\,m_1'\,\frac{1}{2}\,m_2'} \, \mathcal{C}^{SM_S}_{\frac{1}{2}\,m_1\,\frac{1}{2}\,m_2} \left[\sqrt{\frac{3}{4} - m_1(m_1+1)}\, \delta_{m_1'(m_1+1)}\, \delta_{m_2'm_2} \right. \\
& \left. + \sqrt{\frac{3}{4} - m_2(m_2+1)}\, \delta_{m_1'm_1}\, \delta_{m_2'(m_2+1)} \right]
\end{aligned} \tag{B.24}$$

$$\begin{aligned}
= & \sum_{m_1\,m_2} \left[\sqrt{\frac{3}{4} - m_1(m_1+1)}\, \mathcal{C}^{S'M_S'}_{\frac{1}{2}\,m_1+1\,\frac{1}{2}\,m_2} \, \mathcal{C}^{SM_S}_{\frac{1}{2}\,m_1\,\frac{1}{2}\,m_2} \right. \\
& \left. + \sqrt{\frac{3}{4} - m_2(m_2+1)}\, \mathcal{C}^{S'M_S'}_{\frac{1}{2}\,m_1\,\frac{1}{2}\,m_2+1} \, \mathcal{C}^{SM_S}_{\frac{1}{2}\,m_1\,\frac{1}{2}\,m_2} \right].
\end{aligned} \tag{B.25}$$

Note that we decoupled the spin part into its components, i.e., the spin of the neutron and proton, in order to evaluate the matrix elements involving the spin operator. With this result, we obtain the final expression of the second term as

$$\begin{aligned}
G_{\mathrm{M},2}(Q^2) = & \frac{M_\mathrm{d}\, G_\mathrm{M}^S(Q^2)}{\sqrt{1+\eta_\mathrm{d}}} \sum_{\substack{L'M_L' \\ S'M_S'}} \sum_{\substack{LM_L \\ SM_S}} \mathcal{C}^{11}_{L'M_L'S'M_S'} \, \mathcal{C}^{10}_{LM_LSM_S} \; \mathcal{S}^{S'S}_{M_S'M_S} \\
& \times \int_{\mathbf{p}} \phi^*_{L'}(|\mathbf{p}_Q|)\, Y^*_{L'M_L'}(\hat{\mathbf{p}}_Q) \; Y_{LM_L}(\hat{\mathbf{p}}) \; \phi_L(p)
\end{aligned} \tag{B.26}$$

$$\begin{aligned}
= & \frac{M_\mathrm{d}\, G_\mathrm{M}^S(Q^2)}{\sqrt{1+\eta_\mathrm{d}}} \sum_{\substack{L'M_L' \\ M_S'}} \sum_{\substack{LM_L \\ M_S}} \mathcal{C}^{11}_{L'M_L'1M_S'} \, \mathcal{C}^{10}_{LM_L1M_S} \; \mathcal{S}^{1\,1}_{M_S'M_S} \\
& \times \int_0^\infty \frac{\mathrm{d}p}{(2\pi)^3}\, p^2 \int_0^\pi \mathrm{d}\theta_p \, \sin\theta_p \int_0^{2\pi} \mathrm{d}\varphi_p \, \phi^*_{L'}(|\mathbf{p}_Q|)\, Y^*_{L'M_L'}(\hat{\mathbf{p}}_Q) \; Y_{LM_L}(\hat{\mathbf{p}}) \; \phi_L(p).
\end{aligned} \tag{B.27}$$

This final expression concludes the detailed derivation for the deuteron form factors represented in a two-body partial-wave basis.

B.2 TRINUCLEON FORM FACTORS

In this section we provide detailed derivations and expressions for the trinucleon charge and magnetic form factors. Particularly, we employ the one-body charge operator to obtain the charge form factor, and the one- and two-body current operators to calculate the magnetic form factor. Because we use Jacobi momenta, the action of the one-body operator is isolated to the separate particle, while the two-body subsystem is left invariant (see Section 3.2.1). On the other hand, the two-body operator acts on the quantum numbers of the two-body subsystem and causes a shift only to the relative momentum of the separate particle. Therefore, we can identify general parts of the expression that do not change regardless of which electromagnetic form factor we investigate.

General current operator partial-wave expansion

Before we show the detailed form factor expressions expanded with respect to a three-body partial-wave basis, we restate the expansion of a general current operator. We find it by inserting complete sets of momentum states,

$$\begin{aligned}
&\langle p'\, q'\, \alpha'\, \mathcal{J}'\mathcal{M}'_{\mathcal{J}}\, \mathcal{T}'\mathcal{M}'_{\mathcal{T}}|\, \hat{J}^{\mu}\, |p\, q\, \alpha\, \mathcal{J}\mathcal{M}_{\mathcal{J}}\, \mathcal{T}\mathcal{M}_{\mathcal{T}}\rangle \\
&\qquad = \int_{\mathbf{p}'_1}\int_{\mathbf{q}'_1}\int_{\mathbf{p}_1}\int_{\mathbf{q}_1} \langle p'\, q'\, \alpha'\, \mathcal{J}'\mathcal{M}'_{\mathcal{J}}\, \mathcal{T}'\mathcal{M}'_{\mathcal{T}}|\mathbf{p}'_1\, \mathbf{q}'_1\rangle\, \langle \mathbf{p}'_1\, \mathbf{q}'_1|\, \hat{J}^{\mu}\, |\mathbf{p}_1\, \mathbf{q}_1\rangle \\
&\qquad\quad \times \langle \mathbf{p}_1\, \mathbf{q}_1|p\, q\, \alpha\, \mathcal{J}\mathcal{M}_{\mathcal{J}}\, \mathcal{T}\mathcal{M}_{\mathcal{T}}\rangle\,.
\end{aligned} \tag{B.28}$$

Then, we decouple total angular momentum $\mathcal{J}$ and total isospin $\mathcal{T}$, and write the overlap between the partial-wave states and the momentum states as coupled spherical harmonics to obtain

$$\begin{aligned}
= \int_{\mathbf{p}'_1}\int_{\mathbf{q}'_1}\int_{\mathbf{p}_1}\int_{\mathbf{q}_1} &\sum_{\substack{M'_J m'_j \\ M_J m_j}} \mathcal{C}^{\mathcal{J}'\mathcal{M}'_{\mathcal{J}}}_{J'M'_J j' m j'}\, \mathcal{C}^{\mathcal{J}\mathcal{M}_{\mathcal{J}}}_{JM_J j m_j} \sum_{\substack{M'_T m'_t \\ M_T m_t}} \mathcal{C}^{\mathcal{T}'\mathcal{M}'_{\mathcal{T}}}_{T'M'_T t' m'_t}\, \mathcal{C}^{\mathcal{T}\mathcal{M}_{\mathcal{T}}}_{TM_T t m_t} \\
&\times \mathcal{Y}^{*J'M'_J}_{L'S'}(\hat{\mathbf{p}}'_1)\, \sqrt{(2\pi)^3}\, \frac{\delta(p'_1 - p')}{p'_1\, p'}\, \mathcal{Y}^{*j'm_j}_{\ell' s'}(\hat{\mathbf{q}}'_1)\, \sqrt{(2\pi)^3}\, \frac{\delta(q'_1 - q')}{q'_1\, q'} \\
&\times \mathcal{Y}^{JM_J}_{LS}(\hat{\mathbf{p}}_1)\, \sqrt{(2\pi)^3}\, \frac{\delta(p - p_1)}{p\, p_1}\, \mathcal{Y}^{jm_j}_{\ell s}(\hat{\mathbf{q}}_1)\, \sqrt{(2\pi)^3}\, \frac{\delta(q - q_1)}{q\, q_1} \\
&\times \langle \mathbf{p}'_1 \mathbf{q}'_1\, t' m'_t\, T M_T|\, \hat{J}^{\mu}\, |\mathbf{p}_1 \mathbf{q}_1\, t m_t\, T M_T\rangle\,.
\end{aligned} \tag{B.29}$$

We identify and isolate the parts of the separate particle and the two-body subsystem as follows

$$\begin{aligned}
= \sum_{\substack{M'_J m'_j \\ M_J m_j}} &\mathcal{C}^{\mathcal{J}'\mathcal{M}'_{\mathcal{J}}}_{J'M'_J j' m'_j}\, \mathcal{C}^{\mathcal{J}\mathcal{M}_{\mathcal{J}}}_{JM_J j m_j} \sum_{\substack{M'_T m'_t \\ M_T m_t}} \mathcal{C}^{\mathcal{T}'\mathcal{M}'_{\mathcal{T}}}_{T'M'_T t' m'_t}\, \mathcal{C}^{\mathcal{T}\mathcal{M}_{\mathcal{T}}}_{TM_T t m_t} \int_{\mathbf{p}'_1}\int_{\mathbf{q}'_1}\int_{\mathbf{p}_1}\int_{\mathbf{q}_1} \\
&\times (2\pi)^3\, \frac{\delta(p'_1 - p')}{p'_1\, p'}\, \mathcal{Y}^{*J'M'_J}_{L'S'}(\hat{\mathbf{p}}'_1)\, \langle \mathbf{p}'_1\, T'M'_T|\, \hat{J}^{\mu}\, |\mathbf{p}_1\, TM_T\rangle\, \frac{\delta(q'_1 - q')}{q'_1\, q'}\, \mathcal{Y}^{JM_J}_{LS}(\hat{\mathbf{p}}_1) \\
&\times (2\pi)^3\, \frac{\delta(p - p_1)}{p\, p_1}\, \mathcal{Y}^{*j'm'_j}_{\ell' s'}(\hat{\mathbf{q}}'_1)\, \langle \mathbf{q}'_1\, t'\, m'_t|\, \hat{J}^{\mu}\, |\mathbf{q}_1\, t\, m_t\rangle\, \frac{\delta(q - q_1)}{q\, q_1}\, \mathcal{Y}^{jm_j}_{\ell s}(\hat{\mathbf{q}}_1)\,.
\end{aligned} \tag{B.30}$$

In a next step, we introduce the functions $\mathcal{P}$ and $\mathcal{Q}$

$$
\begin{aligned}
&= \sum_{\substack{M'_J m'_j \\ M_J m_j}} \mathcal{C}^{\mathcal{J}'\mathcal{M}'_{\mathcal{J}}}_{J'M'_J j' m'_j}\, \mathcal{C}^{\mathcal{J}\mathcal{M}_{\mathcal{J}}}_{JM_J j m_j} \sum_{\substack{M'_T m'_t \\ M_T m_t}} \mathcal{C}^{\mathcal{T}'\mathcal{M}'_{\mathcal{T}}}_{T'M'_T t' m'_t}\, \mathcal{C}^{\mathcal{T}\mathcal{M}_{\mathcal{T}}}_{TM_T t m_t} \\
&\quad \times \mathcal{P}^{M'_J M'_T M_J M_T}_{(L'S')J'T'\,(LS)JT}(p,p')\, \mathcal{Q}^{m'_j m'_t m_j m_t}_{(\ell' s')j't'\,(\ell s)jt}(q,q'). \qquad \text{(B.31)}
\end{aligned}
$$

They are given by

$$
\begin{aligned}
\mathcal{P}^{M'_J M'_T M_J M_T}_{(L'S')J'T'\,(LS)JT}(p,p') \equiv& \frac{1}{(2\pi)^3} \int \mathrm{d}\mathbf{p}'_1 \int \mathrm{d}\mathbf{p}_1\, \frac{\delta(p'_1 - p')}{p'_1\, p'}\, \mathcal{Y}^{*J'M'_J}_{L'S'}(\hat{\mathbf{p}}'_1) \\
&\times \langle \mathbf{p}'_1\, T'M'_T |\, \hat{J}^\mu \,| \mathbf{p}_1\, TM_T \rangle\, \frac{\delta(p - p_1)}{p\, p_1}\, \mathcal{Y}^{JM_J}_{LS}(\hat{\mathbf{p}}_1)\,, \qquad \text{(B.32)} \\
\mathcal{Q}^{m'_j m'_t m_j m_t}_{(\ell' s')j't'\,(\ell s)jt}(q,q') \equiv& \frac{1}{(2\pi)^3} \int \mathrm{d}\mathbf{q}'_1 \int \mathrm{d}\mathbf{q}_1\, \frac{\delta(q'_1 - q')}{q'_1\, q'}\, \mathcal{Y}^{*j'm'_j}_{\ell' s'}(\hat{\mathbf{q}}'_1) \\
&\times \langle \mathbf{q}'_1\, t'\, m'_t |\, \hat{J}^\mu \,| \mathbf{q}_1\, t\, m_t \rangle\, \frac{\delta(q - q_1)}{q\, q_1}\, \mathcal{Y}^{jm_j}_{\ell s}(\hat{\mathbf{q}}_1). \qquad \text{(B.33)}
\end{aligned}
$$

These two functions parametrize the action of the operator on the quantum numbers and momentum of the separate particle, $\mathcal{Q}$, or of the two-body subsystem, $\mathcal{P}$. In the following we give explicit forms of these functions once we replace the general current operator with specific expressions for the charge and current operators.

B.2.1 One-body charge and magnetic form factor

The one-body charge and current operators act on the separate particle only. As a result, we can simplify $\mathcal{P}$ and use the outcome for both the charge and magnetic form factor. To find the simplified expression, we begin by decoupling the two-body angular momentum J into its components:

$$
\begin{aligned}
\mathcal{P}^{M'_J M'_T M_J M_T}_{(L'S')J'T'\,(LS)JT}(p,p') =& \frac{1}{(2\pi)^3} \int \mathrm{d}\mathbf{p}'_1 \int \mathrm{d}\mathbf{p}_1\, \frac{\delta(p'_1 - p')}{p'_1\, p'} \mathcal{Y}^{*J'M'_J}_{L'S'}(\hat{\mathbf{p}}'_1) \\
&\times \langle \mathbf{p}'_1\, T'M'_T | \mathbf{p}_1\, TM_T \rangle\, \frac{\delta(p - p_1)}{p\, p_1} \mathcal{Y}^{JM_J}_{LS}(\hat{\mathbf{p}}_1) \qquad \text{(B.34)} \\
=& \frac{1}{(2\pi)^3} \int \mathrm{d}\mathbf{p}'_1 \int \mathrm{d}\mathbf{p}_1\, \frac{\delta(p'_1 - p')}{p'_1\, p'} \sum_{M'_L M'_S} \mathcal{C}^{J'M'_J}_{L'M'_L S'M'_S}\, Y^*_{L'M'_L}(\hat{\mathbf{p}}'_1) \\
&\times (2\pi)^3 \delta(\mathbf{p}_1 - \mathbf{p}'_1)\, \delta_{TT'}\, \delta_{M_T M'_T} \frac{\delta(p - p_1)}{p\, p_1} \\
&\times \sum_{M_L M_S} \mathcal{C}^{JM_J}_{LM_L SM_S}\, Y_{LM_L}(\hat{\mathbf{p}}_1)\, \langle S'M'_S | SM_S \rangle\,. \qquad \text{(B.35)}
\end{aligned}
$$

In a next step we perform the integration over $\mathbf{p}'_1$, which yields

$$
\begin{aligned}
\mathcal{P}^{M'_J M'_T M_J M_T}_{(L'S')J'T'\,(LS)JT}(p,p') = \int \mathrm{d}\mathbf{p}_1\, \frac{\delta(p_1 - p')}{p_1\, p'} \sum_{M'_L M'_S} \mathcal{C}^{J'M'_J}_{L'M'_L S'M_S}\, Y^*_{L'M'_L}(\hat{\mathbf{p}}_1)\, \frac{\delta(p - p_1)}{p\, p_1} \\
\times \sum_{M_L M_S} \mathcal{C}^{JM_J}_{LM_L SM_S}\, Y_{LM_L}(\hat{\mathbf{p}}_1)\, \delta_{SS'}\, \delta_{M_S M'_S}\, \delta_{TT'}\, \delta_{M_T M'_T}. \qquad \text{(B.36)}
\end{aligned}
$$

Integrating over p_1 removes one of the delta functions and the angular integration over $\hat{\mathbf{p}}_1$, due to $\int \mathrm{d}\hat{\mathbf{x}}\, Y^*_{\ell' m'_\ell}(\hat{\mathbf{x}})\, Y_{\ell m_\ell}(\hat{\mathbf{x}}) \ = \delta_{\ell\ell'}\, \delta_{m_\ell m'_\ell}$, eliminates the spherical harmonics, so that we obtain

$$\begin{aligned}
\mathcal{P}^{M'_J M'_T M_J M_T}_{(L'S')J'T'\,(LS)JT}(p,p') =& \frac{\delta(p-p')}{p\,p'} \sum_{M'_L} \mathcal{C}^{J'M'_J}_{L'M'_L S'M_S} \sum_{M_L M_S} \mathcal{C}^{JM_J}_{LM_L SM_S}\, \delta_{LL'}\, \delta_{M_L M'_L} \\
& \times \delta_{SS'}\, \delta_{TT'}\, \delta_{M_T M'_T} \qquad \text{(B.37)} \\
=& \sum_{M_L M_S} \mathcal{C}^{J'M'_J}_{L'M_L S'M_S}\, \mathcal{C}^{JM_J}_{LM_L SM_S}\, \delta_{LL'}\, \delta_{SS'}\, \delta_{TT'}\, \delta_{M_T M'_T}\, \frac{\delta(p-p')}{p'p}. \qquad \text{(B.38)}
\end{aligned}$$

This last expression is the final result for $\mathcal{P}$ in case the operator is of the one-body type. Note that the two-body subsystem is diagonal in its quantum numbers.

The isospin part of the one-body operators is practically the same for both form factors except for a different type of nucleon form factor. That is, the trinucleon charge form factors depend on the electric nucleon form factors, while the magnetic form factors depend on the magnetic nucleon form factors. The operator only acts on the isospin quantum number of the separate particle. Therefore, we address it separately and parametrize it as follows

$$\begin{aligned}
\tau^{\mathcal{M}_\mathcal{T}}_{\mathrm{E/M};T}(Q^2) =& \langle (T'\tfrac{1}{2})\mathcal{T}\mathcal{M}_\mathcal{T}|\, \frac{G^S_{\mathrm{E/M}}(Q^2) + G^V_{\mathrm{E/M}}(Q^2)\, \tau_{3,z}}{2}\, |(T\tfrac{1}{2})\mathcal{T}\mathcal{M}_\mathcal{T}\rangle \qquad \text{(B.39)} \\
=& \sum_{\substack{M'_T m'_t \\ M_T m_t}} \mathcal{C}^{\mathcal{T}\mathcal{M}_\mathcal{T}}_{\frac{1}{2}\,m'_t T'M'_T}\, \mathcal{C}^{\mathcal{T}\mathcal{M}_\mathcal{T}}_{\frac{1}{2}\,m_t TM_T} \\
& \times \langle \tfrac{1}{2}\, m'_t\, T'M'_T|\, \frac{G^S_{\mathrm{E/M}}(Q^2) + G^V_{\mathrm{E/M}}(Q^2)\, \tau_{3,z}}{2}\, |TM_T\, \tfrac{1}{2}\, m_t\rangle \qquad \text{(B.40)} \\
=& \sum_{\substack{M'_T m'_t \\ M_T m_t}} \mathcal{C}^{\mathcal{T}\mathcal{M}_\mathcal{T}}_{\frac{1}{2}\,m'_t T'M'_T}\, \mathcal{C}^{\mathcal{T}\mathcal{M}_\mathcal{T}}_{\frac{1}{2}\,m_t TM_T}\, \delta_{TT'}\, \delta_{M_T M'_T}\, \delta_{m_t m'_t} \\
& \times \frac{G^S_{\mathrm{E/M}}(Q^2) + m_t\, G^V_{\mathrm{E/M}}(Q^2)}{2} \qquad \text{(B.41)} \\
=& \sum_{M_T\, m_t} \mathcal{C}^{\frac{1}{2}\,\mathcal{M}_\mathcal{T}}_{\frac{1}{2}\,m_t T'M_T}\, \mathcal{C}^{\frac{1}{2}\,\mathcal{M}_\mathcal{T}}_{\frac{1}{2}\,m_t TM_T}\, \delta_{TT'}\, \frac{G^S_{\mathrm{E/M}}(Q^2) + m_t\, G^V_{\mathrm{E/M}}(Q^2)}{2}, \qquad \text{(B.42)}
\end{aligned}$$

where the subscript E/M denotes the use of the electric or magnetic nucleon form factors and where we assumed that the isospin of the initial and final state are equal, i.e., $\mathcal{T}' = \mathcal{T}$ and $\mathcal{M}'_\mathcal{T} = \mathcal{M}_\mathcal{T}$. Note that we employed $t = 1/2$ for the nucleon isospin, $\mathcal{T} = 1/2$ for the trinucleon isospin, and that $\mathcal{M}_\mathcal{T} = 1/2$ or $-1/2$ determines if the nucleus is a helion or a triton, respectively. If we make the point particle assumption, then $G^S_\mathrm{E}(Q^2) = G^V_\mathrm{E}(Q^2) = 1$ and $G^S_\mathrm{M}(Q^2) = 0.880\mu_N$ $G^V_\mathrm{M}(Q^2) = 4.706\mu_N$.

Charge form factor

The charge form factor due to the one-body charge operator expanded in a partial-wave basis is given by

$$F_\mathrm{C}(Q) = \frac{1}{Z}\, \langle \mathcal{M}'_\mathcal{J} = +1/2|\hat{\rho}^{(-3)}(\mathbf{Q})|\mathcal{M}_\mathcal{J} = +1/2\rangle\,. \qquad \text{(B.43)}$$

As a first step, we insert complete sets of partial-wave states:

$$F_{\mathrm{C}}(Q) = \frac{3}{Z}\sum_{\alpha'\alpha}\int \mathrm{d}p'\, p'^2 \int \mathrm{d}q'\, q'^2 \int \mathrm{d}p p^2 \int \mathrm{d}q q^2\, \phi^*_{\alpha'}(p', q')\, \langle p'\, q'\, \alpha' | \hat{\rho}^{(-3)}(\mathbf{Q}) | p\, q\, \alpha\rangle\, \phi_\alpha(p, q) \tag{B.44}$$

$$\begin{aligned} &= \frac{3}{Z}\sum_{\alpha'\alpha}\int \mathrm{d}p'\, p'^2 \int \mathrm{d}q'\, q'^2 \int \mathrm{d}p p^2 \int \mathrm{d}q q^2\, \phi^*_{\alpha'}(p', q') \\ &\quad\times \sum_{\substack{M'_J m'_j \\ M_J m_j}} \mathcal{C}^{\frac{1}{2}\,\frac{1}{2}}_{J' M'_J j' m'_j}\, \mathcal{C}^{\frac{1}{2}\,\frac{1}{2}}_{J M_J j m_j} \sum_{\substack{M'_T m'_t \\ M_T m_t}} \mathcal{C}^{\frac{1}{2}\,\mathcal{M}_\mathcal{T}}_{T' M'_T \frac{1}{2}\, m'_t}\, \mathcal{C}^{\frac{1}{2}\,\mathcal{M}_\mathcal{T}}_{T M_T \frac{1}{2}\, m_t} \\ &\quad\times \mathcal{P}^{M'_J M'_T M_J M_T}_{(L'S')J'T'\,(LS)JT}(p, p')\, \mathcal{Q}^{m'_j m'_t m_j m_t}_{(\ell' s')j'\frac{1}{2}\;(\ell s)j\frac{1}{2}}(q, q')\, \phi_\alpha(p, q), \end{aligned} \tag{B.45}$$

where the factor 3 originates from the antisymmetry of the wave functions and $\mathcal{P}$ is given by Eq. (B.38). The effect of the one-body charge operator on $\mathcal{Q}$ is given by

$$\begin{aligned} \mathcal{Q}^{m'_j m'_t m_j m_t}_{(\ell' s')j'\frac{1}{2}\;(\ell s)j\frac{1}{2}}(Q, q, q') &= \frac{1}{(2\pi)^3}\int \mathrm{d}\mathbf{q}'_1 \int \mathrm{d}\mathbf{q}_1\, \mathcal{Y}^{*j' m'_j}_{\ell' s'}(\hat{\mathbf{q}}'_1)\, \frac{\delta(q'_1 - q')}{q'\, q'_1} \\ &\quad\times (2\pi)^3 \delta(\mathbf{q}_1 - \mathbf{q}'_1 - \frac{2}{3}\mathbf{Q})\, \frac{\delta(q - q_1)}{q\, q_1}\, \mathcal{Y}^{j m_j}_{\ell s}(\hat{\mathbf{q}}_1)\,. \end{aligned} \tag{B.46}$$

Performing the integration over $\mathbf{q}'_1$ and q_1 yields

$$\begin{aligned} \mathcal{Q}^{m'_j m'_t m_j m_t}_{(\ell' s')j'\frac{1}{2}\;(\ell s)j\frac{1}{2}}(Q, q, q') &= \sum_{\substack{m'_\ell m'_s \\ m_\ell m_s}} \mathcal{C}^{j' m'_j}_{\ell' m'_\ell s' m'_s}\, \mathcal{C}^{j m_j}_{\ell m_\ell s m_s} \int \mathrm{d}\hat{\mathbf{q}}_1\, Y^*_{\ell' m'_\ell}(\widehat{q\hat{q}_1 - \frac{2}{3}\mathbf{Q}})\, \langle s' m'_s | s m_s\rangle \\ &\quad\times \frac{\delta(|q\hat{q}_1 + \frac{2}{3}\mathbf{Q}| - q')}{q'\, |q\hat{q}_1 + \frac{2}{3}\mathbf{Q}|} Y_{\ell m_\ell}(\hat{\mathbf{q}}_1) \end{aligned} \tag{B.47}$$

$$\begin{aligned} &= \sum_{\substack{m'_\ell \\ m_\ell m_s}} \mathcal{C}^{j' m'_j}_{\ell' m'_\ell s' m_s}\, \mathcal{C}^{j m_j}_{\ell m_\ell s m_s}\, \delta_{ss'} \\ &\quad\times \int \mathrm{d}\hat{\mathbf{q}}\, Y^*_{\ell' m'_\ell}(\hat{\mathbf{q}}_{\frac{2}{3}Q})\, \frac{\delta(q' - |\mathbf{q}_{\frac{2}{3}Q}|)}{q'\, |\mathbf{q}_{\frac{2}{3}Q}|} Y_{\ell m_\ell}(\hat{\mathbf{q}})\,. \end{aligned} \tag{B.48}$$

Combining this result with the outcomes of Eq. (B.38) and Eq. (B.42) yields the expression for the trinucleon charge form factor

$$F_{\mathrm{C}}(Q) = \frac{3}{Z}\sum_{\alpha} \tau^{\mathcal{M}_\mathcal{T}}_{\mathrm{E};T}(Q^2) \sum_{m_\ell} \int \mathrm{d}p\, p^2 \int \mathrm{d}\mathbf{q}\, \phi^*_\alpha(p, |\mathbf{q}_{\frac{2}{3}Q}|)\, Y^*_{\ell m_\ell}(\hat{\mathbf{q}}_{\frac{2}{3}Q})\; Y_{\ell m_\ell}(\hat{\mathbf{q}})\; \phi_\alpha(p, q), \tag{B.49}$$

where the value of $\mathcal{M}_\mathcal{T}$ determines which trinucleon is calculated. Note that the expression is diagonal in all quantum numbers.

Magnetic form factor

We continue by deriving the expression for the magnetic form factor. The trinucleon magnetic form factor resulting from the one-body current operator expanded in a partial-wave basis is defined by

$$F_{\mathrm{M}}^{\mathrm{LO}}(Q) = \frac{-2m_N}{Q} \langle \mathcal{M}'_{\mathcal{J}} = +1/2 | \hat{\jmath}_{+}^{(-2)}(\mathbf{Q}) | \mathcal{M}_{\mathcal{J}} = -1/2 \rangle \,. \tag{B.50}$$

To start, we insert complete sets of partial-wave states and parametrize the resulting expression with the functions $\mathcal{P}$ and $\mathcal{Q}$

$$\begin{aligned} F_{\mathrm{M}}^{\mathrm{LO}}(Q) =& \frac{-2m_N}{Q} 3 \sum_{\alpha'\alpha} \int \mathrm{d}p'\, p'^2 \int \mathrm{d}q'\, q'^2 \int \mathrm{d}p p^2 \int \mathrm{d}q q^2\, \phi^*_{\alpha'}(p', q') \\ & \times \sum_{\substack{M'_J m'_j \\ M_J m_j}} \mathcal{C}^{\frac{1}{2}\,\frac{1}{2}}_{J' M'_J j' m'_j}\, \mathcal{C}^{\frac{1}{2}\,-\frac{1}{2}}_{J M_J j m_j} \sum_{\substack{M'_T m'_t \\ M_T m_t}} \mathcal{C}^{\frac{1}{2}\,\mathcal{M}_{\mathcal{T}}}_{T' M'_T \frac{1}{2}\, m'_t}\, \mathcal{C}^{\frac{1}{2}\,\mathcal{M}_{\mathcal{T}}}_{T M_T \frac{1}{2}\, m_t} \\ & \times \mathcal{P}^{M'_J M'_T M_J M_T}_{(L'S')J'T'\,(LS)JT}(p, p')\, \mathcal{Q}^{m'_j m'_t m_j m_t}_{(\ell' s')j' \frac{1}{2}\;(\ell s)j \frac{1}{2}}(q, q')\, \phi_{\alpha}(p, q), \end{aligned} \tag{B.51}$$

with $\mathcal{P}$ given by Eq. (B.38). The impact on the form of $\mathcal{Q}$ due to the one-body magnetic operator is given by

$$\begin{aligned} \mathcal{Q}^{m'_j m'_t m_j m_t}_{(\ell' s')j' \frac{1}{2}\;(\ell s)j \frac{1}{2}}(Q, q, q') =& \frac{1}{(2\pi)^3} \int \mathrm{d}\mathbf{q}'_1 \int \mathrm{d}\mathbf{q}_1\, \frac{\delta(q'_1 - q')}{q'_1\, q'} \mathcal{Y}^{*j'm'_j}_{\ell' s'}(\hat{\mathbf{q}}'_1) \\ & \times \langle \mathbf{q}'_1\, t'\, m'_t | \hat{\jmath}_{+}^{(-2)} | \mathbf{q}_1\, t\, m_t \rangle\, \frac{\delta(q - q_1)}{q\, q_1} \mathcal{Y}^{jm_j}_{\ell s}(\hat{\mathbf{q}}_1) \end{aligned} \tag{B.52}$$

$$\begin{aligned} =& \frac{e}{2m_N} \frac{1}{(2\pi)^3} \int \mathrm{d}\mathbf{q}'_1 \int \mathrm{d}\mathbf{q}_1\, \frac{\delta(q'_1 - q')}{q'_1\, q'} \mathcal{Y}^{*j'm'_j}_{\ell' s'}(\hat{\mathbf{q}}'_1) \\ & \times (2\pi)^3 \delta(\mathbf{q}_1 - \mathbf{q}'_1 - \frac{2}{3}\mathbf{Q}) \Big[2\, \tau^{\mathcal{M}_{\mathcal{T}}}_{\mathrm{E};T}(Q^2)\, \hat{q}_{+} + \tau^{\mathcal{M}_{\mathcal{T}}}_{\mathrm{M};T}(Q^2)\, i(\boldsymbol{\sigma} \times \mathbf{Q})_{+} \Big] \\ & \times \frac{\delta(q - q_1)}{q\, q_1} \mathcal{Y}^{jm_j}_{\ell s}(\hat{\mathbf{q}}_1) \,. \end{aligned} \tag{B.53}$$

Note that the first term depends on the electric isospin function $\tau^{\mathcal{M}_{\mathcal{T}}}_{\mathrm{e};T}(Q^2)$, while the second term depends on the magnetic isospin function $\tau^{\mathcal{M}_{\mathcal{T}}}_{\mathrm{M};T}(Q^2)$. In the next step, we perform the integrations over $\mathbf{q}'_1$ and q_1:

$$\begin{aligned} \mathcal{Q}^{m'_j m'_t m_j m_t}_{(\ell' s')j' \frac{1}{2}\;(\ell s)j \frac{1}{2}}(Q, q, q') =& \frac{e}{2m_N} \int \mathrm{d}\hat{\mathbf{q}}_1\, \mathcal{Y}^{*j'm'_j}_{\ell' s'}(\widehat{q\hat{q}_1 - \frac{2}{3}\mathbf{Q}})\, \frac{\delta(|q\hat{q}_1 + \frac{2}{3}\mathbf{Q}| - q')}{q'\, |q\hat{q}_1 + \frac{2}{3}\mathbf{Q}|} \\ & \times \Big[2\, \tau^{\mathcal{M}_{\mathcal{T}}}_{\mathrm{E};T}(Q^2)\, \hat{q}_{+} + \tau^{\mathcal{M}_{\mathcal{T}}}_{\mathrm{M};T}(Q^2)\, Q\hat{\sigma}_{+} \Big] \mathcal{Y}^{jm_j}_{\ell s}(\hat{\mathbf{q}}) \,. \end{aligned} \tag{B.54}$$

Using the notation $\mathbf{q}_{\frac{2}{3}Q}$ and decoupling the coupled spherical harmonics gives

$$\begin{aligned} =& \frac{e}{2m_N} \sum_{\substack{m'_\ell m'_s \\ m_\ell m_s}} \mathcal{C}^{j'm'_j}_{\ell' m'_\ell s' m'_s}\, \mathcal{C}^{jm_j}_{\ell m_\ell s m_s} \int \mathrm{d}\hat{\mathbf{q}}\, Y^*_{\ell' m'_\ell}(\hat{\mathbf{q}}_{\frac{2}{3}Q}) \\ & \times \Big[\frac{2}{\sqrt{2}}\, \tau^{\mathcal{M}_{\mathcal{T}}}_{\mathrm{E};\mathcal{T}T}(Q^2)(-q_x - iq_y)\, \delta_{m_s m'_s} + \tau^{\mathcal{M}_{\mathcal{T}}}_{\mathrm{M};\mathcal{T}T}(Q^2)\, Q\, \langle \frac{1}{2} m'_s |\, \hat{\sigma}_{+}\, | \frac{1}{2} m_s \rangle \Big] Y_{\ell m_\ell}(\hat{\mathbf{q}}) \,. \end{aligned} \tag{B.55}$$

Substituting this result, together with the result obtained in Eq. (B.38) into Eq. (B.51) we find the final expression for the LO magnetic form factor,

$$\begin{aligned}
F_{\mathrm{M}}^{\mathrm{LO}}(Q) = & \frac{-3e}{Q} \sum_{\alpha,\{\ell',j'\}} \sum_{\substack{m_j' \\ M_J m_j}} \sum_{\substack{m_\ell' m_s' \\ m_\ell m_s}} \mathcal{C}^{\frac{1}{2}\,\frac{1}{2}}_{JM_J j' m_j'} \, \mathcal{C}^{\frac{1}{2}\,-\frac{1}{2}}_{JM_J j m_j} \int \mathrm{d}p\, p^2 \int \mathrm{d}\mathbf{q}\, \phi^*_{\alpha'}(p,\, |\mathbf{q}_{\frac{2}{3}Q}|)\, Y^*_{\ell' m_\ell'}(\hat{\mathbf{q}}_{\frac{2}{3}Q}) \\
& \times \mathcal{C}^{j' m_j'}_{\ell' m_\ell' \frac{1}{2}\, m_s'} \, \mathcal{C}^{j m_j}_{\ell m_\ell \frac{1}{2}\, m_s} \Big[\sqrt{2}\, \tau^{\mathcal{M}_\mathcal{T}}_{\mathrm{E};T}(Q^2)\, (-q_x - i q_y)\, \delta_{m_s' m_s} \\
& \qquad + \tau^{\mathcal{M}_\mathcal{T}}_{\mathrm{M};T}(Q^2)\, Q \, \langle \frac{1}{2} m_s' |\, \hat{\sigma}_+ \,| \frac{1}{2} m_s \rangle \Big] Y_{\ell m_\ell}(\hat{\mathbf{q}})\, \phi_\alpha(p,\, q). \qquad \text{(B.56)}
\end{aligned}$$

We denote this result with LO to distinguish between the correction to the magnetic form factor arising from the leading 2BCs.

B.2.2 Two-body magnetic form factor

The correction to the trinucleon magnetic form factor arising from the NLO 2BC operators is found by replacing $\hat{\jmath}_+^{(-2)}(\mathbf{Q})$ with $\hat{\jmath}_+^{(-1)}(\mathbf{Q})$ in Eq. (B.50), and hence calculating the effect of this operator on $\mathcal{Q}$ and $\mathcal{P}$. For the two-body current, the impact on $\mathcal{Q}$ is limited to a shift in the momentum of the separate particle,

$$\begin{aligned}
\mathcal{Q}^{m_j' m_t' m_j m_t}_{(\ell' s') j' t' \, (\ell s) j t}(\mathbf{Q}, q, q') = & \frac{1}{(2\pi)^3} \int \mathrm{d}\mathbf{q}_1' \int \mathrm{d}\mathbf{q}_1 \, \frac{\delta(q_1' - q')}{q_1'\, q'} \sum_{m_\ell' m_s'} \mathcal{C}^{j' m_j'}_{\ell' m_\ell' s' m_s'} \, Y^*_{\ell' m_\ell'}(\hat{\mathbf{q}}_1') \, \langle s' m_s' | \\
& \times (2\pi)^3 \delta(\mathbf{q}_1' - \mathbf{q}_1 - \frac{1}{3}\mathbf{Q}) \frac{\delta(q - q_1)}{q\, q_1} \sum_{m_\ell m_s} \mathcal{C}^{j m_j}_{\ell m_\ell s m_s} \, Y_{\ell m_\ell}(\hat{\mathbf{q}}_1) \, | s m_s \rangle \, .
\end{aligned}$$
$$\text{(B.57)}$$

Integrating over $\mathbf{q}_1'$ gives

$$\begin{aligned}
\mathcal{Q}^{m_j' m_t' m_j m_t}_{(\ell' s') j' t' \, (\ell s) j t}(\mathbf{Q}, q, q') = & \int \mathrm{d}\mathbf{q}_1 \, \frac{\delta(|\mathbf{q}_1 - 1/3\mathbf{Q}| - q')}{q_1\, q'} \sum_{m_\ell' m_s'} \mathcal{C}^{j' m_j'}_{\ell' m_\ell' s' m_s'} \, Y^*_{\ell' m_\ell'}(\widehat{\mathbf{q}_1 - \frac{1}{3} Q}) \\
& \times \frac{\delta(q - q_1)}{q\, q_1} \sum_{m_\ell m_s} \mathcal{C}^{j m_j}_{\ell m_\ell s m_s} \, Y_{\ell m_\ell}(\hat{\mathbf{q}}_1) \, \delta_{s s'} \, \delta_{m_s m_s'} \qquad \text{(B.58)} \\
= & \sum_{\substack{m_\ell' \\ m_\ell m_s}} \mathcal{C}^{j' m_j'}_{\ell' m_\ell' s' m_s'} \, \mathcal{C}^{j m_j}_{\ell m_\ell s m_s} \, \delta_{s s'} \\
& \times \int \mathrm{d}\hat{\mathbf{q}}_1 \, Y^*_{\ell' m_\ell'}(\widehat{q \hat{\mathbf{q}}_1 - \frac{1}{3} Q}) \, \frac{\delta(|q \hat{\mathbf{q}}_1 - 1/3\mathbf{Q}| - q')}{q\, q'} \, Y_{\ell m_\ell}(\hat{\mathbf{q}}_1) \qquad \text{(B.59)} \\
= & \sum_{\substack{m_\ell' \\ m_\ell m_s}} \mathcal{C}^{j' m_j'}_{\ell' m_\ell' s' m_s'} \, \mathcal{C}^{j m_j}_{\ell m_\ell s m_s} \, \delta_{s s'} \\
& \times \int \mathrm{d}\hat{\mathbf{q}} \, Y^*_{\ell' m_\ell'}(\hat{\mathbf{q}}_{\frac{1}{3}Q}) \, \frac{\delta(q' - |\mathbf{q}_{\frac{1}{3}Q}|)}{q' \, |\mathbf{q}_{\frac{1}{3}Q}|} Y_{\ell m_\ell}(\hat{\mathbf{q}}) \, , \qquad \text{(B.60)}
\end{aligned}$$

where in the last step we introduced the notation $\mathbf{q}_{\frac{1}{3}Q} = \mathbf{q} - \mathbf{Q}$. On the other hand, the 2BC operator acts on the quantum numbers of the two-body subsystem so that $\mathcal{P}$ does not simplify as in the one-body operator case. We find

$$\mathcal{P}^{M'_J M'_T M_J M_T}_{(L'S')J'T'\,(LS)JT}(\mathbf{Q},p,p') = \frac{1}{(2\pi)^3}\int \mathrm{d}\mathbf{p}'_1 \int \mathrm{d}\mathbf{p}_1\, \frac{\delta(p'_1-p')}{p'_1\,p'} \mathcal{Y}^{*J'M'_J}_{L'S'}(\hat{\mathbf{p}}'_1) \\ \times \langle \mathbf{p}'_1\, T' M'_T |\, \hat{\jmath}^{(-1)}_{+}(\mathbf{Q})\, | \mathbf{p}_1\, T M_T\rangle\, \frac{\delta(p-p_1)}{p\,p_1} \mathcal{Y}^{JM_J}_{LS}(\hat{\mathbf{p}}_1)\,. \tag{B.61}$$

Substituting the expression for the NLO 2BC yields

$$= \frac{1}{(2\pi)^3} \sum_{\substack{M'_L M'_S\\ M_L M_S}} \mathcal{C}^{J'M'_J}_{L'M'_L S'M'_S}\, \mathcal{C}^{JM_J}_{LM_L SM_S} \int \mathrm{d}\mathbf{p}'_1 \int \mathrm{d}\mathbf{p}_1\, \frac{\delta(p'_1-p')}{p'_1\,p'} Y^{*}_{L'M'_L}(\hat{\mathbf{p}}'_1) \\ \times \langle \mathbf{p}'_1\, S' M'_S |\left(\sigma_{1+} - q_{1+}\frac{\boldsymbol{\sigma}_1\cdot\mathbf{q}_1}{\omega^2_{q_1}}\right)\frac{\boldsymbol{\sigma}_2\cdot\mathbf{q}_2}{\omega^2_{q_2}} + 1 \leftrightharpoons 2\, |\mathbf{p}_1\, S M_S\rangle \\ \times \langle T' M'_T |\, i(\boldsymbol{\tau}_1\times\boldsymbol{\tau}_2)_z\, | T M_T\rangle\, \frac{\delta(p-p_1)}{p\,p_1} Y_{LM_L}(\hat{\mathbf{p}}_1) \tag{B.62}$$

$$= \frac{1}{(2\pi)^3} \sum_{\substack{M'_L M'_S\\ M_L M_S}} \mathcal{C}^{J'M'_J}_{L'M'_L S'M'_S}\, \mathcal{C}^{JM_J}_{LM_L SM_S} \int \mathrm{d}\hat{\mathbf{p}}' \int \mathrm{d}\hat{\mathbf{p}}\, Y^{*}_{L'M'_L}(\hat{\mathbf{p}}') \\ \times \Sigma^{M'_S M_S}_{S'S}(\mathbf{Q},\mathbf{p}',\mathbf{p})\, \langle T' M'_T |\, i(\boldsymbol{\tau}_1\times\boldsymbol{\tau}_2)_z\, | T M_T\rangle\, Y_{LM_L}(\hat{\mathbf{p}})\,, \tag{B.63}$$

where we introduced the following function

$$\Sigma^{M'_S M_S}_{S'S}(\mathbf{Q},\mathbf{p}',\mathbf{p}) = \sum_{\substack{m'_{s_1} m'_{s_2}\\ m_{s_1} m_{s_2}}} \mathcal{C}^{S'M'_S}_{\frac{1}{2}\, m'_{s_1}\, \frac{1}{2}\, m'_{s_2}}\, \mathcal{C}^{SM_S}_{\frac{1}{2}\, m_{s_1}\, \frac{1}{2}\, m_{s_2}} \\ \times \langle \mathbf{p}'\, \tfrac{1}{2} m'_{s_1}\, \tfrac{1}{2} m'_{s_2} |\left(\sigma_{1+} - q_{1+}\frac{\boldsymbol{\sigma}_1\cdot\mathbf{q}_1}{\omega^2_{q_1}}\right)\frac{\boldsymbol{\sigma}_2\cdot\mathbf{q}_2}{\omega^2_{q_2}} + 1 \leftrightharpoons 2\, |\mathbf{p}\, \tfrac{1}{2} m_{s_1}\, \tfrac{1}{2} m_{s_2}\rangle, \tag{B.64}$$

which summarizes the action of the spin and momentum operators. Recall that $\mathbf{q}_1 = -\mathbf{p}' + \mathbf{p} + \mathbf{Q}/2$ and $\mathbf{q}_2 = \mathbf{p}' - \mathbf{p} + \mathbf{Q}/2$. If we combine the results from Eq. (B.60) and Eq. (B.63), then the trinucleon magnetic form factor at NLO becomes

$$F^{\mathrm{NLO}}_{\mathrm{M}}(Q) = \frac{3\sqrt{2}m_N}{Q(2\pi)^3}\frac{e\,g_a^2}{(2F_\pi)^2}\, G^V_{\mathrm{E}}(Q^2) \sum_{\alpha'\alpha} \sum_{\substack{M'_J m'_j\\ M_J m_j}} \mathcal{C}^{\frac{1}{2}\,\frac{1}{2}}_{J'M'_J j'm'_j}\, \mathcal{C}^{\frac{1}{2}\,-\frac{1}{2}}_{JM_J jm_j} \sum_{\substack{m'_\ell\\ m_\ell m_s}} \mathcal{C}^{j'm'_j}_{\ell'm'_\ell \frac{1}{2}\, m_s}\, \mathcal{C}^{jm_j}_{\ell m_\ell \frac{1}{2}\, m_s} \\ \times \sum_{\substack{M'_L M'_S\\ M_L M_S}} \mathcal{C}^{J'M'_J}_{L'M'_L S'M'_S}\, \mathcal{C}^{JM_J}_{LM_L SM_S} \int \mathrm{d}\mathbf{p}' \int \mathrm{d}\mathbf{p} \int \mathrm{d}\mathbf{q}\, \phi^*_{\alpha'}(p',\, |\mathbf{q}_{\frac{1}{3}Q}|) Y^*_{L'M'_L}(\hat{\mathbf{p}}') \\ \times Y^*_{\ell'm'_\ell}(\hat{\mathbf{q}}_{\frac{1}{3}Q})\, \Gamma^{\mathcal{M}_\mathcal{T}}_{T'T}\, \Sigma^{M'_S M_S}_{S'S}(\mathbf{Q},\mathbf{p}',\mathbf{p})\, Y_{\ell m_\ell}(\hat{\mathbf{q}})\, Y_{LM_L}(\hat{\mathbf{p}})\, \phi_\alpha(p,\, q). \tag{B.65}$$

Note that now we employed NLO to denote the correction to the magnetic form factor from the leading 2BCs. The isospin dependence is accounted for in the function $\Gamma^{\mathcal{M}_\mathcal{T}}_{T'T}$, which is given by

$$\Gamma^{\mathcal{M}_\mathcal{T}}_{T'T} = \sum_{M'_T M_T} \sum_{m_t} \mathcal{C}^{\frac{1}{2}\mathcal{M}_\mathcal{T}}_{T'M'_T \frac{1}{2} m_t} \, \mathcal{C}^{\frac{1}{2}\,\mathcal{M}_\mathcal{T}}_{T M_T \frac{1}{2}\, m_t} \, \langle T'M'_T |\, i(\boldsymbol{\tau}_1 \times \boldsymbol{\tau}_2)_z \,| T M_T \rangle \, . \tag{B.66}$$

Compared to the expression resulting from the one-body current operator, the result in Eq. (B.65) is much more costly to calculate numerically: the expression is nondiagonal in all the quantum numbers represented by the index α and involves a nine-dimensional integral over the momenta $\mathbf{p}$, $\mathbf{p}'$, and $\mathbf{q}$.

C

NLO MAGNETIC MOMENT OPERATOR

The following two sections are devoted to the detailed derivations to the equations presented in Sections 5.4.2 and 5.4.3. In the first section, we calculate the Fourier transform of the seagull and pion-in-flight contribution to the NLO 2BC. Then in the second section, we proceed by calculating the NLO corrections to the magnetic moment operator with the expressions obtained in the first section.

C.1 Fourier transform of NLO current operator

In the following, we provide the derivations for the Fourier transform of the seagull $\mathbf{j}^{\mathrm{s}}$ and pion-in-flight $\mathbf{j}^{\pi}$ contributions to the NLO current operator. We start with the pion-in-flight contribution. Its Fourier transform is given by

$$\begin{aligned}
\mathbf{j}^{\pi}(\mathbf{Q},\mathbf{r},\mathbf{R}_{\mathrm{NN}}) =& \int_{\mathbf{q}_1} e^{i\mathbf{q}_1\cdot\mathbf{r}_1} \int_{\mathbf{q}_2} e^{i\mathbf{q}_2\cdot\mathbf{r}_2}\, \mathbf{j}^{\pi}(\mathbf{Q},\mathbf{q}_1,\mathbf{q}_2)\,(2\pi)^3\delta(\mathbf{q}_1+\mathbf{q}_2-\mathbf{Q}) \\
=& -ie\frac{g_A^2}{F_\pi^2}\,G_{\mathrm{E}}^{V}(Q^2)\,(\boldsymbol{\tau}_1\times\boldsymbol{\tau}_2)_z \int_{\mathbf{q}_1} e^{i\mathbf{q}_1\cdot\mathbf{r}_1} \int_{\mathbf{q}_2} e^{i\mathbf{q}_2\cdot\mathbf{r}_2}\,(2\pi)^3\delta(\mathbf{q}_1+\mathbf{q}_2-\mathbf{Q}) \\
&\times(\mathbf{q}_2-\mathbf{q}_1)\,\frac{\boldsymbol{\sigma}_1\cdot\mathbf{q}_1}{\omega_{q_1}^2}\,\frac{\boldsymbol{\sigma}_2\cdot\mathbf{q}_2}{\omega_{q_2}^2},
\end{aligned}\tag{C.1}$$

where the delta function enforces momentum conservation. Carrying out the integration over the delta function yields

$$\begin{aligned}
\mathbf{j}^{\pi}(\mathbf{Q},\mathbf{r},\mathbf{R}_{\mathrm{NN}}) =& -ie\frac{g_A^2}{F_\pi^2}\,G_{\mathrm{E}}^{V}(Q^2)\,(\boldsymbol{\tau}_1\times\boldsymbol{\tau}_2)_z \int_{\mathbf{q}_1} e^{i\mathbf{q}_1\cdot\mathbf{r}_1}\, e^{i(\mathbf{Q}-\mathbf{q}_1)\cdot\mathbf{r}_2}\left[(\mathbf{Q}-\mathbf{q}_1)-\mathbf{q}_1\right] \\
&\times\frac{\boldsymbol{\sigma}_1\cdot\mathbf{q}_1}{\omega_{q_1}^2}\,\frac{\boldsymbol{\sigma}_2\cdot(\mathbf{Q}-\mathbf{q}_1)}{m_\pi^2+(\mathbf{Q}-\mathbf{q}_1)^2}.
\end{aligned}\tag{C.2}$$

We rewrite the exponentials to express them in terms of relative and center-of-mass coordinates as follows

$$\begin{aligned}
e^{i\mathbf{q}_1\cdot\mathbf{r}_1}e^{i(\mathbf{Q}-\mathbf{q}_1)\cdot\mathbf{r}_2} =& e^{i\mathbf{q}_1\cdot(\mathbf{r}_1-\mathbf{r}_2)}e^{i\mathbf{Q}\cdot\mathbf{r}_2} \\
=& e^{i\mathbf{q}_1\cdot\mathbf{r}}e^{i\mathbf{Q}\cdot(\mathbf{R}_{\mathrm{NN}}-\frac{\mathbf{r}}{2})} \\
=& e^{i(\mathbf{q}_1-\frac{\mathbf{Q}}{2})\cdot\mathbf{r}}e^{i\mathbf{Q}\cdot\mathbf{R}_{\mathrm{NN}}}.
\end{aligned}$$

Inserting this result and making the substitution $\mathbf{p} = \mathbf{q}_1 - \mathbf{Q}/2$ yields

$$\begin{aligned}\mathbf{j}^{\pi}(\mathbf{Q}, \mathbf{r}, \mathbf{R}_{\mathrm{NN}}) =& -2ie\,\frac{g_A^2}{F_\pi^2}\,G_{\mathrm{E}}^{V}(Q^2)\,(\boldsymbol{\tau}_1 \times \boldsymbol{\tau}_2)_z\,e^{i\mathbf{Q}\cdot\mathbf{R}_{\mathrm{NN}}} \int_{\mathbf{p}} \mathbf{p}\,\frac{\boldsymbol{\sigma}_1 \cdot (\mathbf{p} + \frac{\mathbf{Q}}{2})}{m_\pi^2 + (\mathbf{p} + \frac{\mathbf{Q}}{2})^2}\,\frac{\boldsymbol{\sigma}_2 \cdot (\mathbf{p} - \frac{\mathbf{Q}}{2})}{m_\pi^2 + (\mathbf{p} - \frac{\mathbf{Q}}{2})^2} \\ =& 2e\,\frac{g_A^2}{F_\pi^2}\,G_{\mathrm{E}}^{V}(Q^2)\,(\boldsymbol{\tau}_1 \times \boldsymbol{\tau}_2)_z\,e^{i\mathbf{Q}\cdot\mathbf{R}_{\mathrm{NN}}}\left[\boldsymbol{\sigma}_1 \cdot \left(\frac{\mathbf{Q}}{2} - i\boldsymbol{\nabla}_{\mathbf{r}}\right)\right] \\ & \times \left[\boldsymbol{\sigma}_2 \cdot \left(\frac{\mathbf{Q}}{2} + i\boldsymbol{\nabla}_{\mathbf{r}}\right)\right]\boldsymbol{\nabla}_{\mathbf{r}} I(\mathbf{r}, \mathbf{Q}),\end{aligned} \tag{C.3}$$

where we used $\mathbf{p} \to -i\boldsymbol{\nabla}_{\mathbf{r}}$ to obtain the last equality and defined

$$I(\mathbf{r}, \mathbf{Q}) \equiv \int_{\mathbf{p}} \frac{e^{i\mathbf{p}\cdot\mathbf{r}}}{[m_\pi^2 + (\mathbf{p} - \frac{\mathbf{Q}}{2})^2]\,[m_\pi^2 + (\mathbf{p} + \frac{\mathbf{Q}}{2})^2]}. \tag{C.4}$$

The result in Eq. (C.3) is the Fourier transformed pion-in-flight current in terms of relative and center-of-mass coordinates.

We continue by evaluating the Fourier transform of the seagull term. It is given by

$$\begin{aligned}\mathbf{j}^{\mathrm{s}}(\mathbf{Q}, \mathbf{r}, \mathbf{R}_{\mathrm{NN}}) =& \int_{\mathbf{q}_1} e^{i\mathbf{q}_1\cdot\mathbf{r}_1} \int_{\mathbf{q}_2} e^{i\mathbf{q}_2\cdot\mathbf{r}_2}\,\mathbf{j}^{\mathrm{s}}(\mathbf{Q}, \mathbf{q}_1, \mathbf{q}_2)\,(2\pi)^3\delta(\mathbf{q}_1 + \mathbf{q}_2 - \mathbf{Q}) \\ =& -ie\frac{g_A^2}{F_\pi^2}\,G_{\mathrm{E}}^{V}(Q^2)\,(\boldsymbol{\tau}_1 \times \boldsymbol{\tau}_2)_z \int_{\mathbf{q}_1} e^{i\mathbf{q}_1\cdot\mathbf{r}_1} \int_{\mathbf{q}_2} e^{i\mathbf{q}_2\cdot\mathbf{r}_2}\,(2\pi)^3\delta(\mathbf{q}_1 + \mathbf{q}_2 - \mathbf{Q}) \\ & \times \left[\boldsymbol{\sigma}_1\frac{\boldsymbol{\sigma}_2 \cdot \mathbf{q}_2}{\omega_{q_2}^2} - \boldsymbol{\sigma}_2\frac{\boldsymbol{\sigma}_1 \cdot \mathbf{q}_1}{\omega_{q_1}^2}\right].\end{aligned} \tag{C.5}$$

Performing the integration over the delta function yields two terms:

$$\begin{aligned}\mathbf{j}^{\mathrm{s}}(\mathbf{Q}, \mathbf{r}, \mathbf{R}_{\mathrm{NN}}) =& -ie\frac{g_A^2}{F_\pi^2}\,G_{\mathrm{E}}^{V}(Q^2)\,(\boldsymbol{\tau}_1 \times \boldsymbol{\tau}_2)_z\bigg[e^{i\mathbf{Q}\cdot\mathbf{r}_1} \int_{\mathbf{q}_2} e^{-i\mathbf{q}_2\cdot\mathbf{r}}\boldsymbol{\sigma}_1\frac{\boldsymbol{\sigma}_2 \cdot \mathbf{q}_2}{\omega_{q_2}^2} \\ & - e^{i\mathbf{Q}\cdot\mathbf{r}_2} \int_{\mathbf{q}_1} e^{i\mathbf{q}_1\cdot\mathbf{r}}\boldsymbol{\sigma}_2\frac{\boldsymbol{\sigma}_1 \cdot \mathbf{q}_1}{\omega_{q_1}^2}\bigg] \\ =& -ie\frac{g_A^2}{F_\pi^2}\,G_{\mathrm{E}}^{V}(Q^2)\,(\boldsymbol{\tau}_1 \times \boldsymbol{\tau}_2)_z\bigg[-ie^{i\mathbf{Q}\cdot\mathbf{r}_1}\boldsymbol{\sigma}_1(\boldsymbol{\sigma}_2 \cdot \boldsymbol{\nabla}_{\mathbf{r}}) \int_{\mathbf{q}_2} \frac{e^{-i\mathbf{q}_2\cdot\mathbf{r}}}{\omega_{q_2}^2} \\ & + ie^{i\mathbf{Q}\cdot\mathbf{r}_2}\boldsymbol{\sigma}_2(\boldsymbol{\sigma}_1 \cdot \boldsymbol{\nabla}_{\mathbf{r}}) \int_{\mathbf{q}_1} \frac{e^{i\mathbf{q}_1\cdot\mathbf{r}}}{\omega_{q_1}^2}\bigg] \\ =& e\frac{g_A^2}{4\pi F_\pi^2}\,G_{\mathrm{E}}^{V}(Q^2)\,(\boldsymbol{\tau}_1 \times \boldsymbol{\tau}_2)_z\left[e^{i\mathbf{Q}\cdot\mathbf{r}_1}\boldsymbol{\sigma}_1(\boldsymbol{\sigma}_2 \cdot \boldsymbol{\nabla}_{\mathbf{r}}) + e^{i\mathbf{Q}\cdot\mathbf{r}_2}\boldsymbol{\sigma}_2(\boldsymbol{\sigma}_1 \cdot \boldsymbol{\nabla}_{\mathbf{r}})\right]\frac{e^{-mr}}{r} \\ =& e\frac{g_A^2 m^2}{4\pi F_\pi^2}\,G_{\mathrm{E}}^{V}(Q^2)\,(\boldsymbol{\tau}_1 \times \boldsymbol{\tau}_2)_z\,e^{i\mathbf{Q}\cdot\mathbf{R}_{\mathrm{NN}}}\left[e^{i\frac{\mathbf{Q}}{2}\cdot\mathbf{r}}\boldsymbol{\sigma}_1(\boldsymbol{\sigma}_2 \cdot \hat{r}) + e^{-i\frac{\mathbf{Q}}{2}\cdot\mathbf{r}}\boldsymbol{\sigma}_2(\boldsymbol{\sigma}_1 \cdot \hat{r})\right]f(r),\end{aligned} \tag{C.6}$$

where we used $\mathbf{q}_1 \to -i\boldsymbol{\nabla}_{\boldsymbol{r}}$ and $\mathbf{q}_2 \to -i\boldsymbol{\nabla}_{\boldsymbol{r}}$ to obtain the second equality and where $\hat{r} = \frac{\mathbf{r}}{|\mathbf{r}|}$. Furthermore, we defined

$$f(r) \equiv \left(1 + \frac{1}{mr}\right)\frac{e^{-mr}}{mr}. \tag{C.7}$$

The final expression given by Eq. (C.6) provides the Fourier transformed seagull current.

Both Fourier transforms of the seagull and pion-in-flight current are split into a center-of-mass and relative part. This allows us to separate out the center-of-mass motion of the two-body system as follows

$$\mathbf{j}^{(-1)}(\mathbf{Q},\mathbf{r},\mathbf{R}_{\mathrm{NN}}) \to e^{i\mathbf{Q}\cdot\mathbf{R}_{\mathrm{NN}}}\mathbf{j}^{(-1)}(\mathbf{Q},\mathbf{r}). \tag{C.8}$$

In fact, this observation is true, not only for the NLO 2BC, but for any 2BC operator as a result of its translational invariance with respect to the two-body center of mass.

C.2 INTRINSIC MAGNETIC MOMENT OPERATOR

As a result of the separation of the 2BC operators into a part that only depends on the relative or center-of-mass coordinate, the magnetic moment operator splits into two terms: the intrinsic and Sachs term (see Section 5.4.3). It turns out that, for the NLO contribution to the magnetic moment operator, the Sachs term only depends on the one-pion-exchange potential. On the other hand, the intrinsic term is determined by the NLO 2BC operator. The contributions to the magnetic moment operator beyond leading order coming from the NLO 2BC are thus given by

$$\boldsymbol{\mu}_{2\mathrm{b}}^{\mathrm{NLO}}(\mathbf{r}) = \boldsymbol{\mu}_{2\mathrm{b}}^{\mathrm{NLO,\ int}}(\mathbf{r}) + \boldsymbol{\mu}_{2\mathrm{b}}^{\mathrm{NLO,\ Sachs}}(\mathbf{r}). \tag{C.9}$$

In the following we will derive the expression for the intrinsic magnetic moment operator at NLO. This is obtained by filling out the expression for the NLO 2BC into

$$\boldsymbol{\mu}_{2\mathrm{b}}^{\mathrm{NLO,\ int}}(\mathbf{r}) = -\frac{i}{2}\lim_{\mathbf{Q}\to 0} e^{i\mathbf{Q}\cdot\mathbf{R}_{\mathrm{NN}}}\Big(\boldsymbol{\nabla}_{\mathbf{Q}}\times\mathbf{j}^{(-1)}(\mathbf{Q},\mathbf{r})\Big). \tag{C.10}$$

Because the NLO 2BC operator consists of two terms, the seagull and pion in flight, the intrinsic part of the magnetic moment operator will be made up of two terms:

$$\boldsymbol{\mu}_{2\mathrm{b}}^{\mathrm{NLO,\ int}}(\mathbf{r}) = \boldsymbol{\mu}_{2\mathrm{b}}^{\mathrm{int,\ s}}(\mathbf{r}) + \boldsymbol{\mu}_{2\mathrm{b}}^{\mathrm{int,\ }\pi}(\mathbf{r}), \tag{C.11}$$

where the first term is obtained by substituting Eq. (C.6) and the second by substituting Eq. (C.3).

We start with the seagull term. Substituting the expression for the seagull term, Eq. (C.6), into Eq. (C.10) gives

$$\begin{aligned}
\boldsymbol{\mu}_{2\mathrm{b}}^{\mathrm{int,\ s}}(\mathbf{r}) =& -e\,\frac{i}{2}\,\frac{g_A^2 m^2}{4\pi F_\pi^2}(\boldsymbol{\tau}_1\times\boldsymbol{\tau}_2)_z \\
&\times \lim_{\mathbf{Q}\to 0} e^{i\mathbf{Q}\cdot\mathbf{R}_{\mathrm{NN}}}\left[\boldsymbol{\nabla}_{\mathbf{Q}}\times e^{i\frac{\mathbf{Q}}{2}\cdot\mathbf{r}}\boldsymbol{\sigma}_1(\boldsymbol{\sigma}_2\cdot\hat{r}) + \boldsymbol{\nabla}_{\mathbf{Q}}\times e^{-i\frac{\mathbf{Q}}{2}\cdot\mathbf{r}}\boldsymbol{\sigma}_2(\boldsymbol{\sigma}_1\cdot\hat{r})\right]f(r) \\
=& -e\,\frac{i}{2}\,\frac{g_A^2 m^2}{4\pi F_\pi^2}(\boldsymbol{\tau}_1\times\boldsymbol{\tau}_2)_z \\
&\times \lim_{\mathbf{Q}\to 0} e^{i\mathbf{Q}\cdot\mathbf{R}_{\mathrm{NN}}}\left[\frac{i}{2}e^{i\frac{\mathbf{Q}}{2}\cdot\mathbf{r}}\mathbf{r}\times\boldsymbol{\sigma}_1(\boldsymbol{\sigma}_2\cdot\hat{r}) + \frac{-i}{2}e^{-i\frac{\mathbf{Q}}{2}\cdot\mathbf{r}}\mathbf{r}\times\boldsymbol{\sigma}_2(\boldsymbol{\sigma}_1\cdot\hat{r})\right]f(r) \\
=& -e\,\frac{g_A^2 m^2}{16\pi F_\pi^2}(\boldsymbol{\tau}_1\times\boldsymbol{\tau}_2)_z\Big[\hat{r}\times\boldsymbol{\sigma}_1(\boldsymbol{\sigma}_2\cdot\hat{r}) - \hat{r}\times\boldsymbol{\sigma}_2(\boldsymbol{\sigma}_1\cdot\hat{r})\Big]r\,f(r).
\end{aligned} \tag{C.12}$$

Which can be rewritten as

$$\boldsymbol{\mu}_{\text{2b}}^{\text{int, s}}(\mathbf{r}) = -e\frac{g_A^2 m^2}{16\pi F_\pi^2}(\boldsymbol{\tau}_1 \times \boldsymbol{\tau}_2)_z \Big\{ \hat{r}\left[\hat{r} \cdot (\boldsymbol{\sigma}_1 \times \boldsymbol{\sigma}_2)\right] - \boldsymbol{\sigma}_1 \times \boldsymbol{\sigma}_2 \Big\} r\, f(r), \tag{C.13}$$

to give the final result for the intrinsic seagull contribution to the magnetic moment operator.

The calculation of the pion-in-flight term requires more work. Substituting expression Eq. (C.3), into Eq. (C.10) gives

$$\begin{aligned}\boldsymbol{\mu}_{\text{2b}}^{\text{int, }\pi}(\mathbf{r}) =& 2\, e\frac{g_A^2}{F_\pi^2}(\boldsymbol{\tau}_1 \times \boldsymbol{\tau}_2)_z \\ & \times \lim_{\mathbf{Q}\to 0} e^{i\mathbf{Q}\cdot\mathbf{R}_{\text{NN}}} \boldsymbol{\nabla}_{\mathbf{Q}} \times \left[\boldsymbol{\sigma}_1 \cdot \left(\frac{\mathbf{Q}}{2} - i\boldsymbol{\nabla}_{\mathbf{r}}\right)\right]\left[\boldsymbol{\sigma}_2 \cdot \left(\frac{\mathbf{Q}}{2} + i\boldsymbol{\nabla}_{\mathbf{r}}\right)\right]\boldsymbol{\nabla}_{\mathbf{r}} I(\mathbf{r},\mathbf{Q}). \end{aligned}\tag{C.14}$$

Simplifying this expression comes down to calculating the effect of the curl on the three factors:

$$\boldsymbol{\nabla}_{\mathbf{Q}} \times \left[\boldsymbol{\sigma}_1 \cdot \left(\frac{\mathbf{Q}}{2} - i\boldsymbol{\nabla}_{\mathbf{r}}\right)\right]\left[\boldsymbol{\sigma}_2 \cdot \left(\frac{\mathbf{Q}}{2} + i\boldsymbol{\nabla}_{\mathbf{r}}\right)\right]\boldsymbol{\nabla}_{\mathbf{r}} I(\mathbf{r},\mathbf{Q}). \tag{C.15}$$

Therefore, we can identify three separate parts before we calculate the curl,

$$F_1(\mathbf{r},\mathbf{Q}) = \boldsymbol{\nabla}_{\mathbf{Q}} \times \left(\boldsymbol{\sigma}_1 \cdot \frac{\mathbf{Q}}{2}\right)\left(\boldsymbol{\sigma}_2 \cdot \frac{\mathbf{Q}}{2}\right)\boldsymbol{\nabla}_r I(\mathbf{r},\mathbf{Q}), \tag{C.16a}$$

$$F_2(\mathbf{r},\mathbf{Q}) = \boldsymbol{\nabla}_{\mathbf{Q}} \times \Big(- \boldsymbol{\sigma}_1 \cdot i\boldsymbol{\nabla}_r\Big)\Big(\boldsymbol{\sigma}_2 \cdot i\boldsymbol{\nabla}_r\Big)\boldsymbol{\nabla}_r I(\mathbf{r},\mathbf{Q}), \tag{C.16b}$$

$$F_3(\mathbf{r},\mathbf{Q}) = \boldsymbol{\nabla}_{\mathbf{Q}} \times \left[\left(\boldsymbol{\sigma}_1 \cdot \frac{\mathbf{Q}}{2}\right)\Big(\boldsymbol{\sigma}_2 \cdot i\boldsymbol{\nabla}_r\Big)\boldsymbol{\nabla}_r I(\mathbf{r},\mathbf{Q}) - \Big(\boldsymbol{\sigma}_1 \cdot i\boldsymbol{\nabla}_r\Big)\left(\boldsymbol{\sigma}_2 \cdot \frac{\mathbf{Q}}{2}\right)\boldsymbol{\nabla}_r I(\mathbf{r},\mathbf{Q})\right]. \tag{C.16c}$$

The first term gives

$$\begin{aligned}F_1(\mathbf{r},\mathbf{Q}) =& \boldsymbol{\nabla}_{\mathbf{Q}}\left(\boldsymbol{\sigma}_1 \cdot \frac{\mathbf{Q}}{2}\right)\left(\boldsymbol{\sigma}_2 \cdot \frac{\mathbf{Q}}{2}\right) \times \boldsymbol{\nabla}_r I(\mathbf{r},\mathbf{Q}) + \mathcal{O}(Q^2) \\ =& \left(\boldsymbol{\sigma}_1 \cdot \frac{\mathbf{Q}}{2}\right)\boldsymbol{\sigma}_2 \times \boldsymbol{\nabla}_r I(\mathbf{r},\mathbf{Q}) + \left(\boldsymbol{\sigma}_2 \cdot \frac{\mathbf{Q}}{2}\right)\boldsymbol{\sigma}_1 \times \boldsymbol{\nabla}_r I(\mathbf{r},\mathbf{Q}) + \mathcal{O}(Q^2). \end{aligned}\tag{C.17}$$

This last expression trivially gives zero when taking the limit $\mathbf{Q} \to 0$. The second term evaluates to

$$F_2(\mathbf{r},\mathbf{Q}) = \Big(- \boldsymbol{\sigma}_1 \cdot i\boldsymbol{\nabla}_r\Big)\Big(\boldsymbol{\sigma}_2 \cdot i\boldsymbol{\nabla}_r\Big)\boldsymbol{\nabla}_{\mathbf{Q}} \times \boldsymbol{\nabla}_r I(\mathbf{r},\mathbf{Q}), \tag{C.18}$$

which also vanishes in the limit $\mathbf{Q} \to 0$ because of

$$\begin{aligned}\lim_{\mathbf{Q}\to 0} \boldsymbol{\nabla}_{\mathbf{Q}} \boldsymbol{\nabla}_{\mathbf{r}} I(\mathbf{r},\mathbf{Q}) =& \lim_{\mathbf{Q}\to 0} \int_{\mathbf{p}} \boldsymbol{\nabla}_{\mathbf{Q}}\, \mathbf{p}\, \frac{e^{i\mathbf{p}\cdot\mathbf{r}}}{[m_\pi^2 + (\mathbf{p} - \frac{\mathbf{Q}}{2})^2]\,[m_\pi^2 + (\mathbf{p} + \frac{\mathbf{Q}}{2})^2]} \\ =& \frac{1}{2} \lim_{\mathbf{Q}\to 0} \int_{\mathbf{p}} \mathbf{p}\, e^{i\mathbf{p}\cdot\mathbf{r}} \left[\frac{-\mathbf{p} - \frac{\mathbf{Q}}{2}}{[m_\pi^2 + (\mathbf{p} + \frac{\mathbf{Q}}{2})^2]^2\,[m_\pi^2 + (\mathbf{p} - \frac{\mathbf{Q}}{2}]^2)} \right. \\ & \left. + \frac{\mathbf{p} - \frac{\mathbf{Q}}{2}}{[m_\pi^2 + (\mathbf{p} - \frac{\mathbf{Q}}{2})^2]^2\,[m_\pi^2 + (\mathbf{p} + \frac{\mathbf{Q}}{2})^2]} \right], \end{aligned}\tag{C.19}$$

(C.20)

which straithforwardly gives

$$=\frac{1}{2}\int_{\mathbf{p}} \mathbf{p}\, e^{i\mathbf{p}\cdot\mathbf{r}}\left[\frac{-\mathbf{p}}{\left(m_\pi^2+\mathbf{p}^2\right)^3}+\frac{\mathbf{p}}{\left(m_\pi^2+\mathbf{p}^2\right)^3}\right]=0.$$

Finally, the third term yields

$$F_3(\mathbf{r},\mathbf{Q}) = \boldsymbol{\sigma}_1 \times \Big(\boldsymbol{\sigma}_2 \cdot i\boldsymbol{\nabla}_{\mathbf{r}}\Big)\boldsymbol{\nabla}_{\mathbf{r}} I(\mathbf{r},\mathbf{Q}) - \boldsymbol{\sigma}_2 \times \Big(\boldsymbol{\sigma}_1 \cdot i\boldsymbol{\nabla}_{\mathbf{r}}\Big)\boldsymbol{\nabla}_{\mathbf{r}} I(\mathbf{r},\mathbf{Q}) + \mathcal{O}(\mathbf{Q}). \tag{C.21}$$

The terms linear in $\mathbf{Q}$ will vanish upon taking the limit to zero momentum transfer. What is still left, is the double derivative of the integral represented by $I(\mathbf{r},\mathbf{Q})$. The integral simplifies after taking the limit, such that we perform this as a first step:

$$\lim_{\mathbf{Q}\to 0} I(\mathbf{r},\mathbf{Q}) = I(\mathbf{r}) = \frac{\pi^2}{m_\pi} e^{-m_\pi r}. \tag{C.22}$$

Taking a first gradient gives

$$\boldsymbol{\nabla}_{\mathbf{r}} \frac{\pi^2}{m_\pi} e^{-m_\pi r} = -\pi^2 e^{-m_\pi r}\hat{r}. \tag{C.23}$$

We use this result to take the second derivative as follows

$$\Big(\boldsymbol{\sigma}_i \cdot \boldsymbol{\nabla}_{\mathbf{r}}\Big)\boldsymbol{\nabla}_{\mathbf{r}} \frac{\pi^2}{m_\pi} e^{-m_\pi r} = \Big(\sigma_x \frac{\partial}{\partial x} + \sigma_y \frac{\partial}{\partial y} + \sigma_z \frac{\partial}{\partial z}\Big)(-\pi^2) e^{-m_\pi r}\hat{r}, \tag{C.24}$$

which is easier to calculate if we regard the x coordinate only:

$$\begin{aligned}
\Rightarrow \frac{\partial}{\partial x}(e^{-m_\pi r}\hat{r}) &= e^{-m_\pi r}\frac{\partial}{\partial x}\left(\frac{\mathbf{r}}{r}\right) + \hat{r}\,\frac{\partial}{\partial x}(e^{-m_\pi r}) \\
&= e^{-m_\pi r}\left[\frac{\partial \mathbf{r}}{\partial x}\frac{1}{r} + \mathbf{r}\frac{\partial}{\partial x}\left(\frac{1}{r}\right)\right] + \hat{r}\,\frac{\partial}{\partial x}(e^{-m_\pi r}) \\
&= e^{-m_\pi r}\left[\frac{\hat{i}}{r} - \frac{\mathbf{r}\,x}{r^3}\right] - \frac{m_\pi x}{r}\,\hat{r}\, e^{-m_\pi r}.
\end{aligned}$$

If we perform the same steps for the other two coordinates and write everything in terms of vectors again, we find

$$\begin{aligned}
\Big(\boldsymbol{\sigma}_i \cdot \boldsymbol{\nabla}_{\mathbf{r}}\Big)\boldsymbol{\nabla}_{\mathbf{r}} \frac{\pi^2}{m_\pi} e^{-m_\pi r} =& \left[\boldsymbol{\sigma}_i \frac{e^{-m_\pi r}}{r} - (\boldsymbol{\sigma}_i \cdot \hat{r})\hat{r}\frac{1}{r}e^{-m_\pi r} - m_\pi(\boldsymbol{\sigma}_i \cdot \hat{r})\hat{r}e^{-m_\pi r}\right](-\pi)^2 \\
=& m_\pi \pi^2\left[\left(1 + \frac{1}{m_\pi r}\right)(\hat{r}\cdot\boldsymbol{\sigma}_i)\hat{r} - \frac{1}{m_\pi r}\boldsymbol{\sigma}_i\right]e^{-m_\pi r}.
\end{aligned} \tag{C.25}$$

Hence, the final result for $F_3(\mathbf{r},\mathbf{Q})$ in the limit of zero momentum transfer is given by

$$\begin{aligned}
\lim_{\mathbf{Q}\to 0} F_3(\mathbf{r},\mathbf{Q}) =& m_\pi \pi^2 [(\hat{r}\cdot\boldsymbol{\sigma}_2)(\boldsymbol{\sigma}_1 \times \hat{r}) - (\hat{r}\cdot\boldsymbol{\sigma}_1)(\boldsymbol{\sigma}_2 \times \hat{r}] m_\pi\, r\, f(r) \\
&- 2 m_\pi \pi^2 (\boldsymbol{\sigma}_1 \times \boldsymbol{\sigma}_2)\left(\frac{e^{-m_\pi r}}{m_\pi r}\right).
\end{aligned} \tag{C.26}$$

Combining all the results yields the expression for the pion-in-flight magnetic moment operator

$$\begin{aligned}\boldsymbol{\mu}_{\text{2b}}^{\text{int, }\pi}(\mathbf{r}) =& \frac{eg_A^2 m_\pi}{16\pi F_\pi^2}(\boldsymbol{\tau}_1 \times \boldsymbol{\tau}_2)_z\left[(\hat{r}\cdot\boldsymbol{\sigma}_2)(\boldsymbol{\sigma}_1\times\hat{r}) - (\hat{r}\cdot\boldsymbol{\sigma}_1)(\boldsymbol{\sigma}_2\times\hat{r})\right] m_\pi\, r\, f(r) \\ &- \frac{eg_A^2 m_\pi}{8\pi F_\pi^2}(\boldsymbol{\tau}_1 \times \boldsymbol{\tau}_2)_z(\boldsymbol{\sigma}_1\times\boldsymbol{\sigma}_2)\frac{e^{-m_\pi r}}{m_\pi r}.\end{aligned} \tag{C.27}$$

We can find a final expression for the total intrinsic magnetic moment operator by using the identity

$$\mathbf{A}\cdot(\mathbf{B}\times\mathbf{C})\mathbf{D} = (\mathbf{A}\cdot\mathbf{D})(\mathbf{B}\times\mathbf{C}) + (\mathbf{B}\cdot\mathbf{D})(\mathbf{C}\times\mathbf{A}) + (\mathbf{C}\cdot\mathbf{D})(\mathbf{A}\times\mathbf{B}), \tag{C.28}$$

such that it becomes

$$\begin{aligned}\boldsymbol{\mu}_{\text{2b}}^{\text{NLO, int}}(\mathbf{r}) &= \boldsymbol{\mu}_{\text{2b}}^{\text{int, }\pi}(\mathbf{r}) + \boldsymbol{\mu}_{\text{2b}}^{\text{int, s}}(\mathbf{r}) \\ &= -\frac{g_A^2 m_\pi}{8\pi F_\pi^2}(\boldsymbol{\tau}_1 \times \boldsymbol{\tau}_2)_z\left[\left(1+\frac{1}{m_\pi r}\right)((\boldsymbol{\sigma}_1\times\boldsymbol{\sigma}_2)\cdot\hat{r})\hat{r} - (\boldsymbol{\sigma}_1\times\boldsymbol{\sigma}_2)\right]e^{-m_\pi r}.\end{aligned} \tag{C.29}$$

This result is the final expression for the intrinsic magnetic moment operator at NLO.

D

THREE-BODY TALMI-MOSHINSKY TRANSFORMATION

In the following we derive the transformation that takes three-body Jacobi HO states to single-particle HO states. To achieve this goal, we follow the discussions presented in Refs. [261, 262].

We begin with j-coupled HO single-particle states and couple the angular momentum of particle 1 and 2 to J_{tot}, and, successively, couple the resulting angular momentum of the two-body subsystem with the angular momentum of the third particle (and equivalently for the isospin):

$$\begin{aligned} |1\,2\,3\rangle &\equiv |n_1(l_1s_1)j_1m_{j_1}t_1m_{t_1}, n_2(l_2s_2)j_2m_{j_2}t_2m_{t_2}, n(ls)jm_jtm_t\rangle \\ &= \sum_{J_{\text{tot}}\mathcal{J}_{\text{tot}}}\sum_{T\mathcal{T}} \mathcal{C}^{J_{\text{tot}}M_{J_{\text{tot}}}}_{j_1m_{j_1}j_2m_{j_2}}\,\mathcal{C}^{\mathcal{J}_{\text{tot}}\mathcal{M}_{\mathcal{J}_{\text{tot}}}}_{J_{\text{tot}}M_{J_{\text{tot}}}jm_j}\,\mathcal{C}^{TM_T}_{t_1m_{t_1}t_2m_{t_2}}\,\mathcal{C}^{\mathcal{T}\mathcal{M}_{\mathcal{T}}}_{TM_Ttm_t} \\ &\quad\times |\{[n_1(l_1s_1)j_1n_2(l_2s_2)j_2]J_{\text{tot}}M_{J_{\text{tot}}}n(ls)j\}\mathcal{J}_{\text{tot}}\mathcal{M}_{\mathcal{J}_{\text{tot}}}\{[t_1t_2]Tt\}\mathcal{T}\mathcal{M}_{\mathcal{T}}\rangle\,, \end{aligned} \tag{D.1}$$

with $\mathcal{M}_{J_{\text{tot}}} = m_{j_1} + m_{j_2} + m_j$ and $\mathcal{M}_{T_{\text{tot}}} = m_{t_1} + m_{t_2} + m_t$. Note that the subscript 'tot' distinguishes J_{tot} from the total relative angular momentum J, which arises from $\mathbf{J} = \mathbf{L} + \mathbf{S}$. In what follows we define the ket appearing in the last line of Eq. (D.1) as

$$\begin{aligned} &\{\{|1\rangle\,|2\rangle\}^{J_{\text{tot}}}\,|3\rangle\,\}^{\mathcal{J}_{\text{tot}}\mathcal{M}_{\mathcal{J}_{\text{tot}}}} \\ &\qquad\equiv |\{[n_1(l_1s_1)j_1n_2(l_2s_2)j_2]J_{\text{tot}}M_{J_{\text{tot}}}n(ls)j\}\mathcal{J}_{\text{tot}}\mathcal{M}_{\mathcal{J}_{\text{tot}}}\{[t_1t_2]Tt\}\mathcal{T}\mathcal{M}_{\mathcal{T}}\rangle\,. \end{aligned} \tag{D.2}$$

The completeness of the three-body center-of-mass and the relative motion in the Jacobi HO basis is given by

$$\sum_{N_{3\text{N}}L_{3\text{N}}M_{L_{3\text{N}}}}\sum_{\beta} |N_{3\text{N}}L_{3\text{N}}M_{L_{3\text{N}}}\beta\rangle\,\langle N_{3\text{N}}L_{3\text{N}}M_{L_{3\text{N}}}\beta| = 1, \tag{D.3}$$

where the index collects the quantum numbers $\beta = \{N, L, S, J, n, l, j, \mathcal{J}, \mathcal{M}_{\mathcal{J}}, T, \mathcal{T}, \mathcal{M}_{\mathcal{T}}\}$ and where $|\beta\rangle$ is the state defined in Eq. (5.75). Recoupling these states to total angular momentum $\mathcal{J}_{\text{tot}}$ yields

$$\sum_{N_{3\text{N}}L_{3\text{N}}}\sum_{\beta}\sum_{\mathcal{J}_{\text{tot}}\mathcal{M}_{\mathcal{J}_{\text{tot}}}} \{\,|N_{3\text{N}}L_{3\text{N}}\rangle\,|\beta\rangle\,\}^{\mathcal{J}_{\text{tot}}\mathcal{M}_{\mathcal{J}_{\text{tot}}}}\{\,\langle N_{3\text{N}}L_{3\text{N}}|\,\langle\beta|\,\}^{\mathcal{J}_{\text{tot}}\mathcal{M}_{\mathcal{J}_{\text{tot}}}} = 1, \tag{D.4}$$

where the collective index β no longer contains $\mathcal{M}_{\mathcal{J}}$. Inserting this set of complete states in

Eq. (D.1) gives

$$\begin{aligned}|1\,2\,3\rangle &\equiv |n_1(l_1 s_1)j_1 m_{j_1} t_1 m_{t_1}, n_2(l_2 s_2)j_2 m_{j_2} t_2 m_{t_2}, n(ls)j m_j t m_t\rangle \\ &= \sum_{J_{\text{tot}}\mathcal{J}_{\text{tot}}} \sum_{T\mathcal{T}} \mathcal{C}^{J_{\text{tot}} M_{J_{\text{tot}}}}_{j_1 m_{j_1} j_2 m_{j_2}} \, \mathcal{C}^{\mathcal{J}_{\text{tot}} \mathcal{M}_{\mathcal{J}_{\text{tot}}}}_{J_{\text{tot}} M_{J_{\text{tot}}} j m_j} \, \mathcal{C}^{T M_T}_{t_1 m_{t_1} t_2 m_{t_2}} \, \mathcal{C}^{\mathcal{T}\mathcal{M}_{\mathcal{T}}}_{T M_T t m_t} \\ &\quad \times T \left\{ |N_{3\text{N}} L_{3\text{N}}\rangle \, |\beta\rangle \right\}^{\mathcal{J}_{\text{tot}} \mathcal{M}_{\mathcal{J}_{\text{tot}}}} , \end{aligned} \tag{D.5}$$

with the overlap T defined by

$$T \equiv \left\{ \langle N_{3\text{N}} L_{3\text{N}}| \, \langle\beta| \right\}^{\mathcal{J}_{\text{tot}} \mathcal{M}_{\mathcal{J}_{\text{tot}}}} \left\{ \{|1\rangle \, |2\rangle\}^{J_{\text{tot}}} \, |3\rangle \right\}^{\mathcal{J}_{\text{tot}} \mathcal{M}_{\mathcal{J}_{\text{tot}}}} . \tag{D.6}$$

Accordingly, the transformation to singe-particle states amounts to finding an expression for the overlap T. This can be done by considering the quantum numbers of the two-body subsystem and the spectator particle separately. Consequently, we have to perform two Talmi-Moshinsky transformations: one transformation applies to the two nucleon single-particle state constructed from particle 1 and 2, and the two-body center-of-mass and relative motion, while the second transfromation applies to the single-particle state of the third particle and the two-body state to the three-body center-of-mass and relative motion.

We start by examining the two-body subsystem. As a first step, we recouple to a ΛS-coupling:

$$|[(l_1 s_1)j_1 (l_1 s_1)j_1] J_{\text{tot}}\rangle = \sum_{\Lambda\, S} \hat{\jmath}_1 \, \hat{\jmath}_2 \, \hat{\Lambda} \, \hat{S} \begin{Bmatrix} l_1 & s_1 & j_1 \\ l_2 & s_2 & j_2 \\ \Lambda & S & J_{\text{tot}} \end{Bmatrix} |[(l_1 l_2)\Lambda (s_1 s_2) S] J_{\text{tot}}\rangle \, . \tag{D.7}$$

Then, we perform the Talmi-Moshinsky transformation for the single-particle momenta $\mathbf{k}_1$ and $\mathbf{k}_1$ to the center-of-mass $\mathbf{P}_{\text{NN}}$ and relative momenta $\mathbf{p}$

$$\begin{aligned}|[n_1 l_1(\mathbf{k}_1), n_2 l_2(\mathbf{k}_2)]\Lambda\rangle &= \sum_{\substack{N_{\text{NN}}\, L_{\text{NN}} \\ N\, L}} \langle N_{\text{NN}} N (L_{\text{NN}} L)\Lambda | n_1 \, n_2 (l_1 \, l_2)\Lambda\rangle_{d=1} \\ &\qquad \times |[N_{\text{NN}} L_{\text{NN}}(\tilde{\mathbf{P}}_{\text{NN}}) N L(\tilde{\mathbf{p}})]\Lambda\rangle \, . \end{aligned} \tag{D.8}$$

These two steps conclude the first part with respect to the two-body subsystem.

Before we make the Talmi-Moshinsky transformation for the spectator particle, we have to perform two angular-momenta recouplings. The first one consists of decoupling the angular momentum of the spectator particle j and coupling its orbital angular momentum l with the total orbital angular momentum of the two-body subsystem Λ to the total orbital angular momentum $\mathcal{L}$, and similar for the spins, so that

$$|[(\Lambda S) J_{\text{tot}} (ls) j] \mathcal{J}_{\text{tot}}\rangle = \sum_{\mathcal{L}\mathcal{S}} \hat{J}_{\text{tot}} \, \hat{\jmath} \, \hat{\mathcal{L}} \, \hat{\mathcal{S}} \begin{Bmatrix} \Lambda & S & J_{\text{tot}} \\ l & s & j \\ \mathcal{L} & \mathcal{S} & \mathcal{J}_{\text{tot}} \end{Bmatrix} |[(\Lambda l)\mathcal{L} (S s)\mathcal{S}] \mathcal{J}_{\text{tot}}\rangle \, . \tag{D.9}$$

Subsequently, we recouple the orbital angular momenta L_{NN} and l to I, to then couple I and L to the total orbital angular momentum $\mathcal{L}$:

$$|[(L_{\text{NN}} L)\Lambda l]\mathcal{L}\rangle = \sum_{I} (-1)^{L+l+\Lambda+I} \, \hat{\Lambda} \, \hat{I} \begin{Bmatrix} l & L_{\text{NN}} & I \\ L & \mathcal{L} & \Lambda \end{Bmatrix} |[(L_{\text{NN}} l) I L]\mathcal{L}\rangle \, . \tag{D.10}$$

The second Talmi-Moshinsky transformation relates the center-of-mass momentum of the two-body subsystem and the spectator momentum to the second Jacobi momentum $\mathbf{q}$ and the three-body center-of-mass momentum through

$$\begin{pmatrix} \mathbf{P}_{3\mathrm{N}} \\ \mathbf{q} \end{pmatrix} = \begin{pmatrix} \sqrt{\frac{d}{d+1}} & \sqrt{\frac{d}{d+1}} \\ \sqrt{\frac{d}{d+1}} & -\sqrt{\frac{d}{d+1}} \end{pmatrix} \begin{pmatrix} \mathbf{P}_{\mathrm{NN}} \\ \mathbf{k}_3 \end{pmatrix}, \tag{D.11}$$

with $d = 2$, which in HO brackets becomes

$$\begin{aligned} |[N_{\mathrm{NN}} L_{\mathrm{NN}} (\mathbf{P}_{\mathrm{NN}}) nl(\mathbf{k}_3)] I\rangle = &\sum_{\substack{N_{3\mathrm{N}} L_{3\mathrm{N}} \\ n_3 l_3}} \langle N_{3\mathrm{N}} n_3 (L_{3\mathrm{N}} l_3) I | N_{\mathrm{NN}}\, n (L_{\mathrm{NN}}\, l) I\rangle_{d=2} \\ &\times |[N_{3\mathrm{N}} L_{3\mathrm{N}} (\mathbf{P}_{3\mathrm{N}}) n_3 l_3 (\mathbf{q})] I\rangle\,. \end{aligned} \tag{D.12}$$

The next two steps eliminate the orbital angular momentum of the center-of-mass momentum $L_{3\mathrm{N}}$, given that $\{\, \langle N_{\mathrm{NN}} L_{\mathrm{NN}} |\, \langle \beta |\, \}^{\mathcal{J}_{\mathrm{tot}} \mathcal{M}_{\mathcal{J}_{\mathrm{tot}}}}$ is independent of it. First, we couple the orbital angular momenta L and l_3 to L_3 and, successively, couple L_3 and $L_{3\mathrm{N}}$ to the total orbital angular momentum $\mathcal{L}$:

$$|[(L_{3\mathrm{N}} l_3) I L] \mathcal{L}\rangle = \sum_{L_3} (-1)^{L_{3\mathrm{N}} + l_3 + L + \mathcal{L}}\, \hat{I}\, \hat{L}_3 \begin{Bmatrix} L_{3\mathrm{N}} & l_3 & I \\ L & \mathcal{L} & L_3 \end{Bmatrix} |[L_{3\mathrm{N}} (l_3 L) L_3] \mathcal{L}\rangle\,. \tag{D.13}$$

Additionally, the order of the coupling is reversed from $(l_3 L) L_3$ to $(L l_3) L_3$, which adds a phase $(-1)^{l_3 + L - L_3}$ according to the Clebsch-Gordan symmetry relations. Second, we separate the center-of-mass orbital angular momentum $L_{3\mathrm{N}}$ from L_3 and couple L_3 with the total spin S to the total relative angular momentum J_3, which yields

$$|[(L_{3\mathrm{N}} L_3) \mathcal{L} \mathcal{S}] \mathcal{J}_{\mathrm{tot}}\rangle = \sum_{J_3} (-1)^{L_{3\mathrm{N}} + L_3 + S + \mathcal{J}_{\mathrm{tot}}}\, \hat{\mathcal{L}}\, \hat{J}_3 \begin{Bmatrix} L_{3\mathrm{N}} & L_3 & \mathcal{L} \\ \mathcal{S} & \mathcal{J}_{\mathrm{tot}} & J_3 \end{Bmatrix} |[L_{3\mathrm{N}} (L_3 \mathcal{S}) J_3] \mathcal{J}_{\mathrm{tot}}\rangle\,. \tag{D.14}$$

In the final step before collecting all terms, we change from a $\Lambda\mathcal{S}$-coupling to a $J j_3$-coupling, which introduces the relative angular momenta J and j_3:

$$|[(\Lambda l_3) L_3 (S s) \mathcal{S}] J_3\rangle = \sum_{J\, j_3} \hat{L}_3\, \hat{\mathcal{S}}\, \hat{J}\, \hat{j}_3 \begin{Bmatrix} L & l_3 & L_3 \\ S & s & \mathcal{S} \\ J & j_3 & J_3 \end{Bmatrix} |[(\Lambda S) J (l_3 s) j_3] J_3\rangle\,. \tag{D.15}$$

The transformation from a three-body Jacobi HO basis to a single-particle HO basis is then given by combining all results obtained above into

$$
\begin{aligned}
\{\{|1\rangle\,|2\rangle\}^{J_{\text{tot}}}\,|3\rangle\,\}^{\mathcal{J}_{\text{tot}}\mathcal{M}_{\mathcal{J}_{\text{tot}}}} = &\sum_{\Lambda S}\sum_{\substack{N_{\text{NN}}L_{\text{NN}}\\ NL}}\sum_{\mathcal{L}\mathcal{S}}\sum_{I}\sum_{\substack{N_{3\text{N}}L_{3\text{N}}\\ n_3\,l_3}}\sum_{L_3}\sum_{J_3}\sum_{J\,j_3} \\
&\times \hat{j}_1\,\hat{j}_2\,\hat{\Lambda}\,\hat{S}\begin{Bmatrix} l_1 & s_1 & j_1 \\ l_2 & s_2 & j_2 \\ \Lambda & S & J_{\text{tot}} \end{Bmatrix} \\
&\times \langle N_{\text{NN}}N(L_{\text{NN}}L)\Lambda|n_1\,n_2(l_1\,l_2)\Lambda\rangle_{d=1} \\
&\times \hat{J}_{\text{tot}}\,\hat{j}\,\hat{\mathcal{L}}\,\hat{\mathcal{S}}\begin{Bmatrix} \Lambda & S & J_{\text{tot}} \\ l & s & j \\ \mathcal{L} & \mathcal{S} & \mathcal{J}_{\text{tot}} \end{Bmatrix} \\
&\times (-1)^{L+l+\Lambda+I}\,\hat{\Lambda}\,\hat{I}\begin{Bmatrix} l & L_{\text{NN}} & I \\ L & \mathcal{L} & \Lambda \end{Bmatrix} \\
&\times \langle N_{3\text{N}}n_3(L_{3\text{N}}l_3)I|N_{\text{NN}}\,n(L_{\text{NN}}\,l)I\rangle_{d=2} \\
&\times (-1)^{L_{3\text{N}}+l_3+L+\mathcal{L}}\,\hat{I}\,\hat{L}_3\begin{Bmatrix} L_{3\text{N}} & l_3 & I \\ L & \mathcal{L} & L_3 \end{Bmatrix}(-1)^{l_3+L-L_3} \\
&\times (-1)^{L_{3\text{N}}+L_3+S+\mathcal{J}_{\text{tot}}}\,\hat{\mathcal{L}}\,\hat{J}_3\begin{Bmatrix} L_{3\text{N}} & L_3 & \mathcal{L} \\ \mathcal{S} & \mathcal{J}_{\text{tot}} & J_3 \end{Bmatrix} \\
&\times \hat{L}_3\,\hat{\mathcal{S}}\,\hat{J}\,\hat{j}_3\begin{Bmatrix} L & l_3 & L_3 \\ S & s & \mathcal{S} \\ J & j_3 & J_3 \end{Bmatrix} \\
&\times \{\,|N_{\text{NN}}L_{\text{NN}}\rangle\,|\beta\rangle\,\}^{\mathcal{J}_{\text{tot}}\mathcal{M}_{\mathcal{J}_{\text{tot}}}}. \qquad \text{(D.16)}
\end{aligned}
$$

Multiplying the state $\{\,\langle N'_{\text{NN}}L'_{\text{NN}}|\,\langle\beta|'\,\}^{\mathcal{J}_{\text{tot}}\mathcal{M}_{\mathcal{J}_{\text{tot}}}}$ from the left to the above result creates the following Kronecker deltas

$$
\delta_{N_{3\text{N}}N'_{3\text{N}}}\delta_{L_{3\text{N}}L'_{3\text{N}}}\delta_{NN'}\delta_{LL'}\delta_{SS'}\delta_{jj'}\delta_{n_3n'_3}\delta_{l_3l'_3}\delta_{j_3j'_3}\delta_{J_3J'_3}, \qquad \text{(D.17)}
$$

such that the overlap T becomes

$$\begin{aligned}
T = & \sum_{\Lambda} \sum_{N_{\mathrm{NN}} L_{\mathrm{NN}}} \sum_{\mathcal{L}\mathcal{S}} \sum_{I} \sum_{L_3} \\
& \times \hat{j}_1\, \hat{j}_2\, \hat{\Lambda}\, \hat{S} \begin{Bmatrix} l_1 & s_1 & j_1 \\ l_2 & s_2 & j_2 \\ \Lambda & S & J_{\mathrm{tot}} \end{Bmatrix} \\
& \times \langle N_{\mathrm{NN}} N (L_{\mathrm{NN}} L) \Lambda | n_1\, n_2 (l_1\, l_2) \Lambda \rangle_{d=1} \\
& \times \hat{J}_{\mathrm{tot}}\, \hat{j}\, \hat{\mathcal{L}}\, \hat{\mathcal{S}} \begin{Bmatrix} \Lambda & S & J_{\mathrm{tot}} \\ l & s & j \\ \mathcal{L} & \mathcal{S} & \mathcal{J}_{\mathrm{tot}} \end{Bmatrix} \\
& \times (-1)^{L+l+\Lambda+I}\, \hat{\Lambda}\, \hat{I} \begin{Bmatrix} l & L_{\mathrm{NN}} & I \\ L & \mathcal{L} & \Lambda \end{Bmatrix} \\
& \times \langle N_{3\mathrm{N}} n_3 (L_{3\mathrm{N}} l_3) I | N_{\mathrm{NN}}\, n (L_{\mathrm{NN}}\, l) I \rangle_{d=2} \\
& \times (-1)^{L_{3\mathrm{N}}+l_3+L+\mathcal{L}}\, \hat{I}\, \hat{L}_3 \begin{Bmatrix} L_{3\mathrm{N}} & l_3 & I \\ L & \mathcal{L} & L_3 \end{Bmatrix} (-1)^{l_3+L-L_3} \\
& \times (-1)^{L_{3\mathrm{N}}+L_3+S+\mathcal{J}_{\mathrm{tot}}}\, \hat{\mathcal{L}}\, \hat{J}_3 \begin{Bmatrix} L_{3\mathrm{N}} & L_3 & \mathcal{L} \\ \mathcal{S} & \mathcal{J}_{\mathrm{tot}} & J_3 \end{Bmatrix} \\
& \times \hat{L}_3\, \hat{\mathcal{S}}\, \hat{J}\, \hat{j}_3 \begin{Bmatrix} L & l_3 & L_3 \\ S & s & \mathcal{S} \\ J & j_3 & J_3 \end{Bmatrix} .
\end{aligned} \tag{D.18}$$

We restate Eq. (D.5) and decouple the angular momentum $\mathcal{J}_{\mathrm{tot}}$, to find the final transformation relation

$$\begin{aligned}
|1\,2\,3\rangle \equiv & |n_1 (l_1 s_1) j_1 m_{j_1} t_1 m_{t_1}, n_2 (l_2 s_2) j_2 m_{j_2} t_2 m_{t_2}, n (l s) j m_j t m_t \rangle \\
= & \sum_{J_{\mathrm{tot}} \mathcal{J}_{\mathrm{tot}}} \sum_{T \mathcal{T}} \sum_{N_{3\mathrm{N}} L_{3\mathrm{N}}} \sum_{\beta} \sum_{M L_{3\mathrm{N}} M_{J_3}} \mathcal{C}^{J_{\mathrm{tot}} M_{J_{\mathrm{tot}}}}_{j_1 m_{j_1} j_2 m_{j_2}}\, \mathcal{C}^{\mathcal{J}_{\mathrm{tot}} \mathcal{M}_{\mathcal{J}_{\mathrm{tot}}}}_{J_{\mathrm{tot}} M_{J_{\mathrm{tot}}} j m_j}\, \mathcal{C}^{T M_T}_{t_1 m_{t_1} t_2 m_{t_2}}\, \mathcal{C}^{\mathcal{T} \mathcal{M}_{\mathcal{T}}}_{T M_T t m_t} \\
& \times T\, \mathcal{C}^{\mathcal{J}_{\mathrm{tot}} \mathcal{M}_{\mathcal{J}_{\mathrm{tot}}}}_{L_{3\mathrm{N}} M_{L_{3\mathrm{N}}} J_3 M_{J_3}}\, |N_{3\mathrm{N}} L_{3\mathrm{N}}\rangle\, |\beta M_{J_3}\rangle .
\end{aligned} \tag{D.19}$$

E

EXPERIMENTAL QUANTITIES OF A =2, 3, AND 6 NUCLEI

In this chapter, we list experimental quantities that are relevant to our discussion of the nuclei under investigation. In that regard, these quantities include either input values to calculations or values of observables we compute.

E.1 Deuteron experimental results

The deuteron binding energy is measured by observing gamma rays originating from the radiative capture of thermal neutrons on ^{1}H, i.e., the reaction ^{1}H(n, γ)^{2}H. Additionally, the neutron mass can be extracted by summing the binding energy and the mass difference ^{2}H$-^1$H [263].

Atomic masses are determined to very high precision with *Penning trap* measurements. To obtain the deuteron mass, cyclotron frequencies of two ions are compared yielding a mass ratio. This technique reaches relative accuracies of the order of $\sim 10^{-11}$, resulting in some of the most precise measurements in physics. Very recently, a new measurement of the deuteron mass found a difference of 4.8 standard deviations from the CODATA-2018 [65] value, see Ref. [264]. However, this difference has no significant effect on results in this thesis since other inputs to the calculation are less precise. Both the new and the CODATA-2018 value are presented in Table E.1 in atomic mass units (AMU), while the mass in MeV is only given for the CODATA-2018 determination.

The deuteron magnetic moment is obtained by measuring the electronic and nuclear Zeeman level splitting in a deuterium atom. This measurement then provides the ratio of deuteron to electron magnetic moment [60].

Measuring the electric-quadrupole-interaction constant eqQ_d/h, which is measured by the hyperfine splitting in HD or D$_2$ molecules, allows one to extract the deuteron quadrupole moment. A theoretical calculation of the electric field gradient, i.e., q, for these molecules then determines the quadrupole moment Q_d. This calculation has been performed resulting in a value $Q_\mathrm{d} = 0.2860(15)$ fm^2 [168]. Later work argued that the high quality analysis of [168] demands a readjustment [169]. Consequently, they readjusted the value to $Q_\mathrm{d} = 0.2859(3)$ fm^2, stating that even after the readjustment the error estimate remains too conservative [169]. Theoretical results for Q_d compare to this last value.

The determination of the deuteron root-mean-square (rms) charge radius is accomplished using three different methods:

Table E.1: Experimental results for the static properties of the deuteron. The deuteron mass is the only value used as an input in calculations, while the rest of the quantities function as a cross-check for results. See text for a short explanation how each result is obtained.

Quantity	Symbol	Numerical Value	Ref.
Binding energy	$\epsilon_{\rm d}$	2.22456612(48) MeV	[263]
Mass	$\mathrm{M_d}$		
energy equivalent		1875.612928(12) MeV	[65]
AMU: CODATA 2018		2.013553212745(40) u	[65]
AMU: MPIK 2020		2.013553212535(17) u	[264]
Magnetic dipole moment	$\mu_{\rm d}$	0.8574382338(22) μ_N	[65]
Electric quadrupole moment	$\mathrm{Q_d}$	0.2859(3) fm^2	[168, 169]
rms Charge radius	$\langle r^2_{\rm ch}\rangle^{1/2}_{\rm d}$		
e-d scattering		2.130(10) fm	[218]
d spectroscopy		2.1415(45) fm	[67]
μd spectroscopy		2.12562(78) fm	[66]
CODATA 2014		2.1413(25) fm	[60]
CODATA 2018		2.12799(74) fm	[65]
rms Magnetic radius	$\langle r^2_{\rm m}\rangle^{1/2}_{\rm d}$		
e-d scattering		2.072(18) fm	[218]

1. **electron-deuteron (e-d) elastic scattering**: Elastic scattering of electrons on deuteron nuclei measures its charge distribution. The mean-square (ms) charge radius is defined by the slope at zero momentum transfer of this charge distribution, i.e.,

$$\langle r^2_{\rm ch}\rangle_{\rm d} = -6\frac{{\rm d}G_{\rm ch}(Q^2)}{{\rm d}Q^2}\bigg|_{Q^2=0}. \tag{E.1}$$

   The most complete and precise determination of the deuteron charge radius was performed by fitting the world e-d scattering data with a parametrization for the form factor. This analysis results in a value $\langle r^2_{\rm ch}\rangle^{1/2}_{\rm d} = 2.130(10)$ fm [218].

2. **atomic deuterium spectroscopy**: Two different methods determine the deuteron charge rms radius with precision spectroscopy of deuterium (D) atoms. First, one can study internal transitions in D to deduce the rms charge radius. This is because atomic S-state energy levels contain a correction term which accounts for the finite size of nuclei which is denoted by $E_{\rm NS}$. The leading-order term of $E_{\rm NS}$ is proportional to the ms charge radius:

$$E \propto E_{\rm NS} \propto \langle r^2_{\rm d}\rangle. \tag{E.2}$$

   Examining several transitions between energy levels in atomic deuterium results in $\langle r^2_{\rm ch}\rangle^{1/2}_{\rm d} = 2.1415(45)$ fm [67].

   Alternatively, the hydrogen-deuterium isotope shift of the 1S - 2S transition is measured. From this measurement the deuteron-proton ms charge-radius difference can be inferred very accurately [265]:

$$\langle r^2_{\rm ch}\rangle_{\rm d} - \langle r^2_{\rm ch}\rangle_{\rm p} = 3.82007(65)\text{fm}. \tag{E.3}$$

Using the proton rms charge radius from the latest CODATA-2018 update, i.e., $\langle r^2_{\text{ch}}\rangle_{\text{p}} = 0.8414(19)$ fm [65], leads to a value of $\langle r^2_{\text{ch}}\rangle^{1/2}_{\text{d}} = 2.1279(20)$ fm.

3. **muonic deuterium spectroscopy**: This experimental method relies on the same measurement techniques as just described, however, in this case a negative muon orbits the nucleus instead of an electron. Because the muon is roughly 200 times heavier than the electron its muonic Bohr radius is much smaller than the electronic Bohr radius. Therefore, the overlap of the muonic wave function with the nuclear charge distribution is much larger. In particular, the overlap scales as $(m_{\text{red}}/m_e)^3$, with $m_{\text{red}} \equiv (m_\mu m_d)/(m_\mu + m_d)$ which for the muon approximately equals $m_{\text{red}} \approx 196 m_e$, causing a $\sim 10^7$ times bigger overlap for muonic deuterium. Hence, measuring the Lamb shift, which is the energy difference between 2P - 2S, results in an extreme sensitivity to the deuteron ms charge radius. The measurement in muonic deuterium finds a radius of $\langle r^2_{\text{ch}}\rangle^{1/2}_{\text{d}} = 2.12562(13)$ fm [66], which is very precise and disagrees with the scattering and atomic spectroscopy measurements. In this sense, there is a deuteron-radius puzzle in analogy to the proton-radius puzzle.

The three methods described above provide uncorrelated results for the deuteron rms charge radius. From the electronic deuterium results the CODATA determines the internationally recomended value. They calculate a combined least-squares adjusted value of the e-d scattering and H - D spectroscopy results, omitting the muonic deuterium value from their 2018 revision [60]. Moreover, the deuteron-radius puzzle and the proton-radius puzzle are connected through Eq. (E.3). Therefore, new information about one affects the other and vice versa.

Recently, two atomic hydrogen measurements [63, 64] and an e-p scattering experiment [62] obtained values for the proton rms charge radius that agree with the observed radius from muonic experiments possibly clarifying the proton-radius puzzle. Although they support the smaller radius found by muonic experiments, they are unable to explain the difference observed in pre-2010 data, withholding a universal acceptance of the apparent solution. Nevertheless, the CODATA changed their recommended value for the proton rms charge radius to $r_p = 0.8414(19)$ fm in their latest update [65].[1] As stated, this affects the deuteron rms charge radius value which was updated accordingly, see table Table E.1. The updated result is still 1.9σ larger than the muonic deuterium value and 2.9σ smaller than the value from electronic deuterium. Obviously, the possible clarification of the proton-radius puzzle did not settle the deuteron-radius puzzle yet. New muon-nucleon and muon-nuclei scattering experiments are under construction to obtain form factors from the interaction with a different lepton than the electron [266, 267]. These results will contribute to the understanding of the radius puzzles.

The last experimental result in the table represents the deuteron rms magnetic radius which is equivalent to the rms charge radius in the sense that it describes the Q^2 dependence of the magnetic form factor at $Q^2 = 0$. In this case, the magnetic form factor is again obtained by fitting a parametrization to the world e-d scattering data. Calculating the slope of the magnetic form factor yields an rms magnetic radius of $\langle r^2_{\text{m}}\rangle^{1/2}_{\text{d}} = 2.072(18)$ fm [59].

---

[1] The latest update is not published yet but can be accessed through a web-based database, see Ref. [65].

Table E.2: Experimental results for the static properties of the triton and the helion. See text for a short explanation how each value is obtained.

		triton	helion	
Quantity	Symbol	Numerical Value	Numerical Value	Ref.
Magnetic dipole moment	$\mu_{\mathrm{t/h}}$	2.9789624659(59) μ_N	−2.127625307(25) μ_N	[65]
rms Charge radius	$\langle r^2_{\mathrm{ch}}\rangle^{1/2}_{\mathrm{t/h}}$	1.755(86) fm	1.959(30) fm	[75]
rms Magnetic radius	$\langle r^2_{\mathrm{m}}\rangle^{1/2}_{\mathrm{t/h}}$	1.840(181) fm	1.965(153) fm	[75]

E.2 TRITON AND HELION EXPERIMENTAL RESULTS

The triton and helion rms radii are obtained by determining the Q^2 dependence of the form factor at $Q^2 = 0$. Obtaining the form factors is done by fitting a general parametrization to the elastic electron scattering world data [59, 75]. This approach ensures that the parametrization contains the complete experimental information. Subsequently, the charge and magnetic rms radii are extracted by calculating the slope, see Eq. (E.1). The results for the triton and the helion radii from Ref. [75] are summarized in Table E.2. Later determinations of the radii from Ref. [59], which were based on the same approach, give identical results.

Unfortunately, the precision of electron scattering experiments, which is around 5% for charge and 10% for magnetic radii, proves to be insufficient for chiral EFT's precise results which have less than a 1% cutoff spread at N^{3}LO, see Section 4.5. As such no clear conclusions can be made about, for example, 2BC contributions to the radii. At the moment, there are ongoing efforts of the *Charge Radius Experiment with Muonic Atoms* (CREMA) collaboration to measure the Lamb shift of several light muonic atoms, including μ^3He, which will result in more precise radii determinations. Of course, these efforts were triggered by the proton- and deuteron-radius puzzles as a way to acquire more information. The data analysis to determine the helion rms charge radius is being carried out right now and a result will be published soon [74, 268]. The higher precision will allow tests for 2BC and 3N force contributions to the radii. As an additional benefit, these experiments also provide rms magnetic radii of the different light nuclei the CREMA collaboration investigates [219].

The magnetic dipole moment of the trinucleons is obtained with nuclear magnetic resonance (NMR) experiments, which measure resonance frequencies of a reference atom and the atom under investigation. The ratio of these resonance frequencies then yields the magnetic moment of the nucleus with respect to the reference nucleus [60].

E.3 ^{6}LI EXPERIMENTAL RESULTS

The excitation energy of the first excited state of ^{6}Li is obtained using NRF. This experimental technique uses a photon beam to irradiate the target of interest and subsequently investigates the decay of the resonantly excited states. The excitation energy of the first excited state of ^{6}Li was determined by resonantly scattering gamma rays from a ^{6}Li target and subsequently comparing their energies to known lines from a ^{56}Co reference source [269].

The isovector magnetic dipole transition strength between the first excited state 0^+ to the ground state 1^+ is impossible to determine with a direct measurement due to its short

Table E.3: Experimental results for static properties of ^{6}Li relevant to our work. See text for a short explanation how each value is obtained.

Quantity	Symbol	Numerical Value	Ref.
Magnetic dipole moment	μ_{Li}	0.82205667(26) μ_N	[270]
0^+ Excited state	E_{0^+}	3562.88(10) keV	[251, 269]
Transition Strength	$B(M1 : 0^+ \to 1^+)$	15.61(33) μ_N^2	[222]

half-life of about 80 as [251]. There exist multiple determinations of the transition strength which are measured using different techniques, and they are either not very precise or rely on model-dependent extrapolations, see the discussion in Ref. [222]. Therefore, a new experiment was performed at the S-DALINAC which used the newly developed NRF-based relative SAbs method [258, 259] in order to provide a model-independent and precise measurement of the transition.

The magnetic dipole moment of ^{6}Li is obtained with NMR experiments where the deuteron is used as a reference isotope [270]. Experimental values for the properties of ^{6}Li we mentioned here are summarized in Table E.3.

ACKNOWLEDGEMENTS

During my doctoral studies I learned much about physics and myself. Clearing my tallest hurdle so far would not have been possible without a great deal of support. Therefore, I would like to express my gratitude towards the people who helped me along the way.

First of all, I would like to thank my advisor Achim Schwenk for welcoming me in his group. The ever kind and patient encouragements together with his excellent guidance through physics have helped me to find my way in this project. I am also very grateful for the many encouragements and possibilities to participate in summer schools, workshops, and conferences in Germany and abroad. Thank you for creating an atmosphere that allows for scientific and personal growth.

During my research, I have benefited a lot from the help and expertise of Kai Hebeler and Sebastian König. Their doors were always open and they always found time to answer physics or programming related questions. Thank you Kai for your insights and for agreeing to review my thesis. Thank you Sebastian to guide me through the 'world of programming', everyday I am fascinated by your coding skills.

I would like to thank Jan Hoppe, Alexander Tichai, Lars Zurek, Matthias Heinz, and Marc Leonhardt for their tedious work of proofreading this thesis and for providing useful feedback. In this regard, I would also like to thank Achim, Kai, and Sebastian again for their valuable comments.

I would like to acknowledge my office mates, Jan Hoppe, Philipp Klos, Marco Knöll, Julius Müller, Stefan Shulz, Klaus Vobig, and Lars Zurek for creating a fun environment over the years. Besides physics and IT related questions there was always time to discuss other topics which made the time in the office very enjoyable. Jan and Lars, I will never forget the great times we spent together in China and Vancouver, xièxiè.

I would also like to thank my current and former *strongint*-group colleagues, Catharina Brase, Arianna Carbone, Toño Coello Pérez, Christian Drischler, Victoria Durant, Svenja Greif, Matthias Heinz, Jan Hoppe, Lukas Huth, Sabrina Huth, Jonas Keller, Philipp Klos, Yeunhwan Lim, Joel Lynn, Mirko Plößer, Marc Schönborn, Johannes Simonis, Alexander Tichai, Corbinian Wellenhofer, Lars Zurek for the stimulating group atmosphere.

I am very grateful for having received funding from the "International Max Planck Research School for Precision Tests of Fundamental Symmetries" and for being supported by the Deutsche Forschungsgemeinschaft (DFG, German Research Foundation) – Project-ID 279384907 – SFB 1245.

I would also like to thank the *coffee crew*, Christian Appel, Thorsten Haase, Sabrina Klos, Philipp Klos, Marc Leonhardt, Martin Pospiech, and Lukas Rammelmüller for the many lively discussions over coffee and Milchreis on Fridays and for being friends beyond that. Thank you Philipp to introduce me to such a great group of people.

Charlotte en Ruben, ik heb altijd veel energie geput uit het delen van onze vreugde en frustraties over het maken van een doktoraat in het 'bijzondere' Duitsland. Bedankt dat jullie deur altijd open staat.

Bij deze wil ik ook mijn ouders bedanken voor hun onvoorwaardelijke ondersteuning in alles wat ik doe en onderneem. Zonder hun ontelbare uren tijdsinvestering en (on)gedwongen aanmoedigingen in de juiste richting had ik nooit gestaan waar ik nu sta. Julie, Yves, Katrin, en Bernard bedankt om er altijd te zijn wanneer ik het nodig heb.

Liefste Laurine, duizendmaal bedankt voor je steun tijdens de afgelopen maanden. Ik weet dat ik het je niet makkelijk gemaakt heb en dat je, zonder er ooit voor te kiezen, deel was van dit thesis-project, maar zonder jou had het eindresultaat er heel anders uit gezien of er zelfs helemaal niet geweest. Bedankt dat ik altijd op je kan rekenen! Ik vind dat we een uitstekend team zijn.

BIBLIOGRAPHY

[1] J. Erler, N. Birge, M. Kortelainen, W. Nazarewicz, E. Olsen, A. M. Perhac, and M. Stoitsov, “The limits of the nuclear landscape,” Nature **486**, 509 (2012).

[2] R. Gupta, “Introduction to lattice QCD,” (1997), arXiv:hep-lat/9807028.

[3] S. Dürr *et al.*, “Ab Initio Determination of Light Hadron Masses,” Science **322**, 1224 LP (2008).

[4] S. R. Beane, W. Detmold, K. Orginos, and M. J. Savage, “Nuclear physics from lattice QCD,” Prog. Part. Nucl. Phys. **66**, 1 (2011).

[5] S. R. Beane, E. Chang, S. D. Cohen, W. Detmold, H. W. Lin, T. C. Luu, K. Orginos, A. Parreño, M. J. Savage, and A. Walker-Loud (NPLQCD Collaboration), “Light nuclei and hypernuclei from quantum chromodynamics in the limit of SU(3) flavor symmetry,” Phys. Rev. D **87**, 034506 (2013).

[6] K. Orginos, A. Parreño, M. J. Savage, S. R. Beane, E. Chang, and W. Detmold (NPLQCD Collaboration), “Two nucleon systems at $m_\pi \sim 450$ MeV from lattice QCD,” Phys. Rev. D **92**, 114512 (2015).

[7] W. Detmold, R. G. Edwards, J. J. Dudek, M. Engelhardt, H.-W. Lin, S. Meinel, K. Orginos, and P. Shanahan (USQCD Collaboration), “Hadrons and nuclei,” Eur. Phys. J. A **55**, 193 (2019).

[8] J. Carlson, S. Gandolfi, F. Pederiva, S. C. Pieper, R. Schiavilla, K. E. Schmidt, and R. B. Wiringa, “Quantum Monte Carlo methods for nuclear physics,” Rev. Mod. Phys. **87**, 1067 (2015).

[9] S. Weinberg, “Dynamical Approach to Current Algebra,” Phys. Rev. Lett. **18**, 188 (1967).

[10] S. Weinberg, “Nonlinear Realizations of Chiral Symmetry,” Phys. Rev. **166**, 1568 (1968).

[11] L.-F. Li and H. Pagels, “Perturbation Theory about a Goldstone Symmetry,” Phys. Rev. Lett. **26**, 1204 (1971).

[12] S. Weinberg, “Phenomenological Lagrangians,” Physica A **96**, 327 (1979).

[13] H. Georgi, “Effective Field Theory,” Ann. Rev. Nucl. Part. Sci. **43**, 209 (1993).

[14] S. Willenbrock and C. Zhang, “Effective Field Theory Beyond the Standard Model,” Ann. Rev. Nucl. Part. Sci. **64**, 83 (2014).

[15] R. A. Porto, “The effective field theorist’s approach to gravitational dynamics,” Phys. Rep. **633**, 1 (2016).

[16] J. Polchinski, “Effective Field Theory and the Fermi Surface,” (1992), arXiv:hep-th/9210046.

[17] R. E. Tribble, L. Trache, and S. Stoica, "The Frontiers of Nuclear Science: A New Long Range Plan for the United States," AIP Conf. Proc. **972**, 17 (2008).

[18] S. Weinberg, "Nuclear forces from chiral lagrangians," Phys. Lett. B **251**, 288 (1990).

[19] S. Weinberg, "Effective chiral lagrangians for nucleon-pion interactions and nuclear forces," Nucl. Phys. B **363**, 3 (1991).

[20] S. Weinberg, "Three-body interactions among nucleons and pions," Phys. Lett. B **295**, 114 (1992).

[21] S. Weinberg, "What is Quantum Field Theory, and What Did We Think It Is?" (1996), arXiv:hep-th/9702027.

[22] E. Epelbaum, H. Krebs, and U.-G. Meißner, "Precision Nucleon-Nucleon Potential at Fifth Order in the Chiral Expansion," Phys. Rev. Lett. **115**, 122301 (2015).

[23] D. R. Entem, R. Machleidt, and Y. Nosyk, "High-quality two-nucleon potentials up to fifth order of the chiral expansion," Phys. Rev. C **96**, 024004 (2017).

[24] P. Reinert, H. Krebs, and E. Epelbaum, "Semilocal momentum-space regularized chiral two-nucleon potentials up to fifth order," Eur. Phys. J. A **54**, 86 (2018).

[25] T. Otsuka, T. Suzuki, J. D. Holt, A. Schwenk, and Y. Akaishi, "Three-Body Forces and the Limit of Oxygen Isotopes," Phys. Rev. Lett. **105**, 032501 (2010).

[26] H. Hergert, S. Binder, A. Calci, J. Langhammer, and R. Roth, "Ab Initio Calculations of Even Oxygen Isotopes with Chiral Two-Plus-Three-Nucleon Interactions," Phys. Rev. Lett. **110**, 242501 (2013).

[27] E. Epelbaum *et al.* (LENPIC Collaboration), "Few- and many-nucleon systems with semilocal coordinate-space regularized chiral two- and three-body forces," Phys. Rev. C **99**, 024313 (2019).

[28] D. Lonardoni, J. Carlson, S. Gandolfi, J. E. Lynn, K. E. Schmidt, A. Schwenk, and X. B. Wang, "Properties of Nuclei up to $A = 16$ using Local Chiral Interactions," Phys. Rev. Lett. **120**, 122502 (2018).

[29] G. Hagen, G. R. Jansen, and T. Papenbrock, "Structure of ^{78}Ni from First-Principles Computations," Phys. Rev. Lett. **117**, 172501 (2016).

[30] R. F. Garcia Ruiz *et al.*, "Unexpectedly large charge radii of neutron-rich calcium isotopes," Nat. Phys. **12**, 594 (2016).

[31] K. Hebeler, S. K. Bogner, R. J. Furnstahl, A. Nogga, and A. Schwenk, "Improved nuclear matter calculations from chiral low-momentum interactions," Phys. Rev. C **83**, 031301 (2011).

[32] C. Drischler, K. Hebeler, and A. Schwenk, "Chiral Interactions up to Next-to-Next-to-Next-to-Leading Order and Nuclear Saturation," Phys. Rev. Lett. **122**, 042501 (2019).

[33] K. Hebeler, "Three-Nucleon Forces: Implementation and Applications to Atomic Nuclei and Dense Matter," (2020), arXiv:2002.09548.

[34] E. Epelbaum *et al.* (LENPIC collaboration), "Towards high-order calculations of three-nucleon scattering in chiral effective field theory," Eur. Phys. J. A **56**, 92 (2020).

[35] E. Epelbaum, H. Krebs, and P. Reinert, "High-Precision Nuclear Forces From Chiral EFT: State-of-the-Art, Challenges, and Outlook," Front. Phys. **8**, 98 (2020).

[36] V. G. J. Stoks, R. A. M. Klomp, M. C. M. Rentmeester, and J. J. de Swart, “Partial-wave analysis of all nucleon-nucleon scattering data below 350 MeV,” Phys. Rev. C **48**, 792 (1993).

[37] R. A. Arndt, W. J. Briscoe, I. I. Strakovsky, and R. L. Workman, “Updated analysis of NN elastic scattering to 3 GeV,” Phys. Rev. C **76**, 025209 (2007).

[38] A. Maj, W. Nazarewicz, A. Ramos, and M. Lugaro, “Meeting Reports,” Nucl. Phys. News **23**, 34 (2013).

[39] D. G. Ireland and W. Nazarewicz, “Enhancing the interaction between nuclear experiment and theory through information and statistics,” J. Phys. G: Nucl. Part. Phys. **42**, 030301 (2015).

[40] R. J. Furnstahl, D. R. Phillips, and S. Wesolowski, “A recipe for EFT uncertainty quantification in nuclear physics,” J. Phys. G: Nucl. Part. Phys. **42**, 034028 (2015).

[41] R. J. Furnstahl, N. Klco, D. R. Phillips, and S. Wesolowski, “Quantifying truncation errors in effective field theory,” Phys. Rev. C **92**, 024005 (2015).

[42] J. A. Melendez, S. Wesolowski, and R. J. Furnstahl, “Bayesian truncation errors in chiral effective field theory: Nucleon-nucleon observables,” Phys. Rev. C **96**, 024003 (2017).

[43] J. A. Melendez, R. J. Furnstahl, D. R. Phillips, M. T. Pratola, and S. Wesolowski, “Quantifying correlated truncation errors in effective field theory,” Phys. Rev. C **100**, 044001 (2019).

[44] C. Drischler, R. J. Furnstahl, J. A. Melendez, and D. R. Phillips, “How well do we know the neutron-matter equation of state at the densities inside neutron stars? A Bayesian approach with correlated uncertainties,” (2020), arXiv:2004.07232.

[45] C. Drischler, J. A. Melendez, R. J. Furnstahl, and D. R. Phillips, “Quantifying uncertainties and correlations in the nuclear-matter equation of state,” (2020), arXiv:2004.07805.

[46] IOP Publishing, *Focus on further enhancing the interaction between nuclear experiment and theory through information and statistics (ISNET 2.0)*, (2019) https://iopscience.iop.org/journal/0954-3899/page/ISNET2 (visited on 08/24/2020).

[47] S. Wesolowski, *ISNET series*, (2020) https://isnet-series.github.io (visited on 08/24/2020).

[48] A. Ekström, “Analyzing the Nuclear Interaction: Challenges and New Ideas,” Front. Phys. **8**, 29 (2020).

[49] D. O. Riska and G. E. Brown, “Meson exchange effects in $\mathrm{n} + \mathrm{p} \to \mathrm{d} + \gamma$,” Phys. Lett. B **38**, 193 (1972).

[50] D. Gazit, S. Quaglioni, and P. Navrátil, “Three-Nucleon Low-Energy Constants from the Consistency of Interactions and Currents in Chiral Effective Field Theory,” Phys. Rev. Lett. **103**, 102502 (2009). [Erratum: Phys. Rev. Lett. **122**, 029901 (2019)].

[51] S. Pastore, S. C. Pieper, R. Schiavilla, and R. B. Wiringa, “Quantum Monte Carlo calculations of electromagnetic moments and transitions in $A \leq 9$ nuclei with meson-exchange currents derived from chiral effective field theory,” Phys. Rev. C **87**, 035503 (2013).

[52] E. M. Lyman, A. O. Hanson, and M. B. Scott, "Scattering of 15.7-MeV Electrons by Nuclei," Phys. Rev. **84**, 626 (1951).

[53] R. Hofstadter, "Electron Scattering and Nuclear Structure," Rev. Mod. Phys. **28**, 214 (1956).

[54] E. E. Chambers and R. Hofstadter, "Structure of the Proton," Phys. Rev. **103**, 1454 (1956).

[55] R. Hofstadter, "The electron-scattering method and its application to the structure of nuclei and nucleons," Nobel Lecture (1961).

[56] J. D. Bjorken, "Asymptotic Sum Rules at Infinite Momentum," Phys. Rev. **179**, 1547 (1969).

[57] J. I. Friedman and H. W. Kendall, "Deep Inelastic Electron Scattering," Ann. Rev. Nucl. Sci. **22**, 203 (1972).

[58] J. D. Walecka, *Electron Scattering for Nuclear and Nucleon Structure* (Cambridge University Press, 2001).

[59] I. Sick, "Elastic electron scattering from light nuclei," Prog. Part. Nucl. Phys. **47**, 245 (2001).

[60] P. J. Mohr, D. B. Newell, and B. N. Taylor, "CODATA recommended values of the fundamental physical constants: 2014," Rev. Mod. Phys. **88**, 035009 (2016).

[61] R. Pohl, R. Gilman, G. A. Miller, and K. Pachucki, "Muonic Hydrogen and the Proton Radius Puzzle," Ann. Rev. Nucl. Part. Sci. **63**, 175 (2013).

[62] W. Xiong *et al.*, "A small proton charge radius from an electron–proton scattering experiment," Nature **575**, 147 (2019).

[63] A. Beyer *et al.*, "The Rydberg constant and proton size from atomic hydrogen," Science **358**, 79 (2017).

[64] N. Bezginov, T. Valdez, M. Horbatsch, A. Marsman, A. C. Vutha, and E. A. Hessels, "A measurement of the atomic hydrogen Lamb shift and the proton charge radius," Science **365**, 1007 (2019).

[65] E. Tiesinga, P. J. Mohr, D. B. Newell, and B. N. Taylor (2020), *The 2018 CODATA Recommended Values of the Fundamental Physical Constants (Web Version 8.1)*. Database developed by J. Baker, M. Douma, S. Kotochigova. Available at http://physics.nist.gov/constants. National Institute of Standards, and Technology, Gaithersburg, MD 20899.

[66] R. Pohl *et al.*, "Laser spectroscopy of muonic deuterium," Science **353**, 669 (2016).

[67] R. Pohl *et al.*, "Deuteron charge radius and Rydberg constant from spectroscopy data in atomic deuterium," Metrologia **54**, L1 (2017).

[68] Y. Kohl, "Cross section measurements of the elastic electron - Deuteron scattering," PoS Proc. Sci. **238**, 1 (2015).

[69] B. S. Schlimme *et al.*, "Deuteron form factor measurements at low momentum transfers," EPJ. Web Conf. **113**, 4017 (2016).

[70] M. Piarulli, L. Girlanda, L. E. Marcucci, S. Pastore, R. Schiavilla, and M. Viviani, "Electromagnetic structure of A=2 and 3 nuclei in chiral effective field theory," Phys. Rev. C **87**, 014006 (2013).

[71] D. R. Phillips, "Electromagnetic Structure of Two- and Three-Nucleon Systems: An Effective Field Theory Description," Ann. Rev. Nucl. Part. Sci. **66**, 421 (2016).

[72] A. A. Filin, V. Baru, E. Epelbaum, H. Krebs, D. Möller, and P. Reinert, "Extraction of the Neutron Charge Radius from a Precision Calculation of the Deuteron Structure Radius," Phys. Rev. Lett. **124**, 082501 (2020).

[73] A. Antognini *et al.*, "Illuminating the proton radius conundrum: the μHe$^+$ Lamb shift," Can. J. Phys. **89**, 47 (2011).

[74] S. Schmidt *et al.*, "The next generation of laser spectroscopy experiments using light muonic atoms," J. Phys. Conf. Ser. **1138**, 12010 (2018).

[75] A. Amroun *et al.*, "^{3}H and ^{3}He electromagnetic form factors," Nucl. Phys. A **579**, 596 (1994).

[76] L. E. Marcucci, F. Gross, M. T. Peña, M. Piarulli, R. Schiavilla, I. Sick, A. Stadler, J. W. V. Orden, and M. Viviani, "Electromagnetic structure of few-nucleon ground states," J. Phys. G: Nucl. Part. Phys. **43**, 023002 (2016).

[77] T. de Forest Jr. and J. D. Walecka, "Electron scattering and nuclear structure," Adv. Phys. **15**, 1 (1966).

[78] T. W. Donnelly and J. D. Walecka, "Electron Scattering and Nuclear Structure," Ann. Rev. Nucl. Sci. **25**, 329 (1975).

[79] T. W. Donnelly and I. Sick, "Elastic magnetic electron scattering from nuclei," Rev. Mod. Phys. **56**, 461 (1984).

[80] J. Carlson and R. Schiavilla, "Structure and dynamics of few-nucleon systems," Rev. Mod. Phys. **70**, 743 (1998).

[81] S. Bacca and S. Pastore, "Electromagnetic reactions on light nuclei," J. Phys. G **41**, 123002 (2014).

[82] F. Villars, "On the Magnetic Exchange Moment for H^3 and He^3," Phys. Rev. **72**, 256 (1947).

[83] H. Miyazawa, "Deviations of Nuclear Magnetic Moments from the Schmidt Lines," Prog. Theor. Phys. **6**, 801 (1951).

[84] T.-S. Park, D.-P. Min, and M. Rho, "Chiral dynamics and heavy-fermion formalism in nuclei: exchange axial currents," Phys. Rep. **233**, 341 (1993).

[85] T.-S. Park, D.-P. Min, and M. Rho, "Chiral Lagrangian approach to exchange vector currents in nuclei," Nucl. Phys. A **596**, 515 (1996).

[86] C. Ordóñez, L. Ray, and U. van Kolck, "Nucleon-nucleon potential from an effective chiral Lagrangian," Phys. Rev. Lett. **72**, 1982 (1994).

[87] C. Ordóñez, L. Ray, and U. van Kolck, "Two-nucleon potential from chiral Lagrangians," Phys. Rev. C **53**, 2086 (1996).

[88] S. Pastore, R. Schiavilla, and J. L. Goity, "Electromagnetic two-body currents of one- and two-pion range," Phys. Rev. C **78**, 064002 (2008).

[89] S. Pastore, L. Girlanda, R. Schiavilla, M. Viviani, and R. B. Wiringa, "Electromagnetic currents and magnetic moments in chiral effective field theory (χEFT)," Phys. Rev. C **80**, 034004 (2009).

[90] S. Pastore, L. Girlanda, R. Schiavilla, and M. Viviani, “Two-nucleon electromagnetic charge operator in chiral effective field theory (χEFT) up to one loop,” Phys. Rev. C **84**, 024001 (2011).

[91] S. Kölling, E. Epelbaum, H. Krebs, and U.-G. Meißner, “Two-pion exchange electromagnetic current in chiral effective field theory using the method of unitary transformation,” Phys. Rev. C **80**, 045502 (2009).

[92] S. Kölling, E. Epelbaum, H. Krebs, and U.-G. Meißner, “Two-nucleon electromagnetic current in chiral effective field theory: One-pion exchange and short-range contributions,” Phys. Rev. C **84**, 054008 (2011).

[93] S. Ôkubo, “Diagonalization of Hamiltonian and Tamm-Dancoff Equation,” Prog. Theor. Phys. **12**, 603 (1954).

[94] N. Fukuda, K. Sawada, and M. Taketani, “On the Construction of Potential in Field Theory,” Prog. Theor. Phys. **12**, 156 (1954).

[95] E. Epelbaum, W. Glöckle, and U.-G. Meißner, “Nuclear forces from chiral Lagrangians using the method of unitary transformation (I): Formalism,” Nucl. Phys. A **637**, 107 (1998).

[96] E. Epelbaum, H. Krebs, and U. G. Meißner, “Improved chiral nucleon-nucleon potential up to next-to-next-to-next-to-leading order,” Eur. Phys. J. A **A51**, 53 (2015).

[97] D. B. Kaplan, “Five lectures on effective field theory,” in (2005), arXiv:nucl-th/0510023.

[98] E. Epelbaum, “Nuclear forces from chiral effective field theory: a primer,” (2010), arXiv:1001.3229.

[99] R. Aaij *et al.* (LHCb Collaboration), “Observation of $J/\psi p$ Resonances Consistent with Pentaquark States in $\Lambda_b^0 \to J/\psi K^- p$ Decays,” Phys. Rev. Lett. **115**, 072001 (2015).

[100] R. Aaij *et al.* (LHCb Collaboration), “Observation of a Narrow Pentaquark State, $P_c(4312)^+$, and of the Two-Peak Structure of the $P_c(4450)^+$,” Phys. Rev. Lett. **122**, 222001 (2019).

[101] R. Aaij *et al.* (LHCb Collaboration), “Amplitude analysis of $B^+ \to J/\psi\phi K^+$ decays,” Phys. Rev. D **95**, 012002 (2017).

[102] R. Aaij *et al.* (LHCb Collaboration), “Observation of $J/\psi\phi$ Structures Consistent with Exotic States from Amplitude Analysis of $B^+ \to J/\psi\phi K^+$ Decays,” Phys. Rev. Lett. **118**, 022003 (2017).

[103] M. Tanabashi *et al.* (Particle Data Group), “Review of Particle Physics,” Phys. Rev. D **98**, 030001 (2018).

[104] J. Goldstone, A. Salam, and S. Weinberg, “Broken Symmetries,” Phys. Rev. **127**, 965 (1962).

[105] D. J. Gross and F. Wilczek, “Ultraviolet Behavior of Non-Abelian Gauge Theories,” Phys. Rev. Lett. **30**, 1343 (1973).

[106] H. D. Politzer, “Reliable Perturbative Results for Strong Interactions?” Phys. Rev. Lett. **30**, 1346 (1973).

[107] C. Gattringer and C. B. Lang, *Quantum Chromodynamics on the Lattice - An Introductory Presentation* (Springer-Verlag Berlin Heidelberg, 2010).

[108] P. de Forcrand, "Simulating QCD at finite density," PoS Proc. Sci. **LAT2009**, 10 (2009).

[109] T. Yamazaki, K.-i. Ishikawa, Y. Kuramashi, and A. Ukawa, "Helium nuclei, deuteron, and dineutron in 2+1 flavor lattice QCD," Phys. Rev. D **86**, 074514 (2012).

[110] S. R. Beane, E. Chang, S. Cohen, W. Detmold, H. W. Lin, K. Orginos, A. Parreño, M. J. Savage, and B. C. Tiburzi (NPLQCD Collaboration), "Magnetic Moments of Light Nuclei from Lattice Quantum Chromodynamics," Phys. Rev. Lett. **113**, 252001 (2014).

[111] E. Chang, W. Detmold, K. Orginos, A. Parreño, M. J. Savage, B. C. Tiburzi, and S. R. Beane (NPLQCD Collaboration), "Magnetic structure of light nuclei from lattice QCD," Phys. Rev. D **92**, 114502 (2015).

[112] D. B. Kaplan, M. J. Savage, and M. B. Wise, "Nucleon-nucleon scattering from effective field theory," Nucl. Phys. B **478**, 629 (1996).

[113] D. B. Kaplan, M. J. Savage, and M. B. Wise, "A new expansion for nucleon-nucleon interactions," Phys. Lett. B **424**, 390 (1998).

[114] P. F. Bedaque and U. van Kolck, "Nucleon-deuteron scattering from an effective field theory," Phys. Lett. B **428**, 221 (1998).

[115] H. Krebs, E. Epelbaum, and U.-G. Meißner, "Nuclear forces with Δ excitations up to next-to-next-to-leading order, part I: Peripheral nucleon-nucleon waves," Eur. Phys. J. A **32**, 127 (2007).

[116] H. Krebs, A. M. Gasparyan, and E. Epelbaum, "Three-nucleon force in chiral effective field theory with explicit $\Delta(1232)$ degrees of freedom: Longest-range contributions at fourth order," Phys. Rev. C **98**, 014003 (2018).

[117] C. A. Bertulani, H.-W. Hammer, and U. van Kolck, "Effective field theory for halo nuclei: shallow p-wave states," Nucl. Phys. A **712**, 37 (2002).

[118] H.-W. Hammer, C. Ji, and D. R. Phillips, "Effective field theory description of halo nuclei," J. Phys. G: Nucl. Part. Phys. **44**, 103002 (2017).

[119] L. Platter, "Effective Field Theory for Halo Nuclei," Few-Body Syst. **58**, 105 (2017).

[120] H.-W. Hammer, "The hypertriton in effective field theory," Nucl. Phys. A **705**, 173 (2002).

[121] H. Polinder, J. Haidenbauer, and U.-G. Meißner, "Hyperon–nucleon interactions—a chiral effective field theory approach," Nucl. Phys. A **779**, 244 (2006).

[122] S.-I. Ando, G.-S. Yang, and Y. Oh, "${}^{4}_{\Lambda\Lambda}$H in halo effective field theory," Phys. Rev. C **89**, 014318 (2014).

[123] H.-W. Hammer, S. König, and U. van Kolck, "Nuclear effective field theory: Status and perspectives," Rev. Mod. Phys. **92**, 025004 (2020).

[124] E. Epelbaum, "Few-nucleon forces and systems in chiral effective field theory," Prog. Part. Nucl. Phys. **57**, 654 (2006).

[125] E. Epelbaum, H.-W. Hammer, and U.-G. Meißner, "Modern theory of nuclear forces," Rev. Mod. Phys. **81**, 1773 (2009).

[126] R. Machleidt and D. R. Entem, “Chiral effective field theory and nuclear forces,” Phys. Rep. **503**, 1 (2011).

[127] D. R. Entem, N. Kaiser, R. Machleidt, and Y. Nosyk, “Dominant contributions to the nucleon-nucleon interaction at sixth order of chiral perturbation theory,” Phys. Rev. C **92**, 064001 (2015).

[128] D. R. Entem, R. Machleidt, and Y. Nosyk, “Nucleon-Nucleon Scattering Up to N^{5}LO in Chiral Effective Field Theory,” Front. Phys. **8**, 57 (2020).

[129] P. Navrátil, “Local three-nucleon interaction from chiral effective field theory,” Few-Body Syst. **41**, 117 (2007).

[130] S. Ishikawa and M. R. Robilotta, “Two-pion exchange three-nucleon potential: $\mathcal{O}(q^4)$ chiral expansion,” Phys. Rev. C **76**, 014006 (2007).

[131] V. Bernard, E. Epelbaum, H. Krebs, and U.-G. Meißner, “Subleading contributions to the chiral three-nucleon force: Long-range terms,” Phys. Rev. C **77**, 064004 (2008).

[132] V. Bernard, E. Epelbaum, H. Krebs, and U.-G. Meißner, “Subleading contributions to the chiral three-nucleon force. II. Short-range terms and relativistic corrections,” Phys. Rev. C **84**, 054001 (2011).

[133] K. Hebeler, H. Krebs, E. Epelbaum, J. Golak, and R. Skibiński, “Efficient calculation of chiral three-nucleon forces up to N^{3}LO for ab initio studies,” Phys. Rev. C **91**, 044001 (2015).

[134] H. Krebs, A. Gasparyan, and E. Epelbaum, “Chiral three-nucleon force at N^{4}LO: Longest-range contributions,” Phys. Rev. C **85**, 054006 (2012).

[135] H. Krebs, A. Gasparyan, and E. Epelbaum, “Chiral three-nucleon force at N^{4}LO. II. Intermediate-range contributions,” Phys. Rev. C **87**, 054007 (2013).

[136] H. Krebs, “Nuclear Currents in Chiral Effective Field Theory,” (2020), arXiv:2008.00974.

[137] A. Baroni, L. Girlanda, S. Pastore, R. Schiavilla, and M. Viviani, “Nuclear axial currents in chiral effective field theory,” Phys. Rev. C **93**, 015501 (2016). [Errata: Phys. Rev. C **93**, 049902 (2016); Phys. Rev. C **95**, 059901 (2017)].

[138] H. Krebs, E. Epelbaum, and U.-G. Meißner, “Nuclear axial current operators to fourth order in chiral effective field theory,” Ann. Phys. **378**, 317 (2017).

[139] E. Epelbaum, A. Nogga, W. Glöckle, H. Kamada, U.-G. Meißner, and H. Witała, “Three-nucleon forces from chiral effective field theory,” Phys. Rev. C **66**, 064001 (2002).

[140] A. Gårdestig and D. R. Phillips, “Using chiral perturbation theory to extract the neutron-neutron scattering length from $\pi^- d \to nn\gamma$,” Phys. Rev. C **73**, 014002 (2006).

[141] T.-S. Park, L. E. Marcucci, R. Schiavilla, M. Viviani, A. Kievsky, S. Rosati, K. Kubodera, D.-P. Min, and M. Rho, “Parameter-free effective field theory calculation for the solar proton-fusion and hep processes,” Phys. Rev. C **67**, 055206 (2003).

[142] T. Park, K. Kubodera, D. Min, and M. Rho, “The Solar Proton Burning Process Revisited in Chiral Perturbation Theory,” Astrophys. J. **507**, 443 (1998).

[143] L. E. Marcucci, A. Kievsky, S. Rosati, R. Schiavilla, and M. Viviani, “Chiral Effective Field Theory Predictions for Muon Capture on Deuteron and ^{3}He,” Phys. Rev. Lett. **108**, 052502 (2012). [Erratum: Phys. Rev. Lett. **121**, 049901 (2018)].

[144] A. Baroni, L. Girlanda, A. Kievsky, L. E. Marcucci, R. Schiavilla, and M. Viviani, “Tritium β decay in chiral effective field theory,” Phys. Rev. C **94**, 024003 (2016). [Erratum: Phys. Rev. C **95**, 059902 (2017)].

[145] P. Klos, A. Carbone, K. Hebeler, J. Menéndez, and A. Schwenk, “Uncertainties in constraining low-energy constants from ^{3}H β decay,” Eur. Phys. J. A **53**, 168 (2017). [Erratum: Eur. Phys. J. A **54**, 76 (2018)].

[146] A. Baroni *et al.*, “Local chiral interactions, the tritium Gamow-Teller matrix element, and the three-nucleon contact term,” Phys. Rev. C **98**, 044003 (2018).

[147] G. B. King, L. Andreoli, S. Pastore, M. Piarulli, R. Schiavilla, R. B. Wiringa, J. Carlson, and S. Gandolfi, “Chiral Effective Field Theory Calculations of Weak Transitions in Light Nuclei,” (2020), arXiv:2004.05263.

[148] P. Gysbers *et al.*, “Discrepancy between experimental and theoretical β-decay rates resolved from first principles,” Nat. Phys. **15**, 428 (2019).

[149] V. Cirigliano, M. L. Graesser, and G. Ovanesyan, “WIMP-nucleus scattering in chiral effective theory,” J. High Energy Phys. **25**, 25 (2012).

[150] M. Hoferichter, P. Klos, and A. Schwenk, “Chiral power counting of one- and two-body currents in direct detection of dark matter,” Phys. Lett. B **746**, 410 (2015).

[151] M. Hoferichter, P. Klos, J. Menéndez, and A. Schwenk, “Analysis strategies for general spin-independent WIMP-nucleus scattering,” Phys. Rev. D **94**, 063505 (2016).

[152] F. Bishara, J. Brod, B. Grinstein, and J. Zupan, “Chiral effective theory of dark matter direct detection,” J. Cosmol. Astropart. Phys. **02**, 9 (2017).

[153] C. Körber, A. Nogga, and J. de Vries, “First-principle calculations of dark matter scattering off light nuclei,” Phys. Rev. C **96**, 035805 (2017).

[154] H. Krebs, E. Epelbaum, and U.-G. Meißner, “Subleading contributions to the nuclear scalar isoscalar currents,” (2020), arXiv:2005.07433.

[155] M. P. Valderrama and D. R. Phillips, “Power Counting of Contact-Range Currents in Effective Field Theory,” Phys. Rev. Lett. **114**, 82502 (2015).

[156] H. Krebs, E. Epelbaum, and U.-G. Meißner, “Nuclear Electromagnetic Currents to Fourth Order in Chiral Effective Field Theory,” Few-Body Syst. **60**, 31 (2019).

[157] R. G. Sachs, “High-Energy Behavior of Nucleon Electromagnetic Form Factors,” Phys. Rev. **126**, 2256 (1962).

[158] R. Skibiński, J. Golak, K. Topolnicki, H. Witała, E. Epelbaum, H. Krebs, H. Kamada, U.-G. Meißner, and A. Nogga, “Testing semilocal chiral two-nucleon interaction in selected electroweak processes,” Phys. Rev. C **93**, 064002 (2016).

[159] D. Siemens, V. Bernard, E. Epelbaum, A. Gasparyan, H. Krebs, and U.-G. Meißner, “Elastic pion-nucleon scattering in chiral perturbation theory: A fresh look,” Phys. Rev. C **94**, 014620 (2016).

[160] D. Siemens, V. Bernard, E. Epelbaum, A. M. Gasparyan, H. Krebs, and U.-G. Meißner, "Elastic and inelastic pion-nucleon scattering to fourth order in chiral perturbation theory," Phys. Rev. C **96**, 055205 (2017).

[161] J. Hoppe, C. Drischler, K. Hebeler, A. Schwenk, and J. Simonis, "Probing chiral interactions up to next-to-next-to-next-to-leading order in medium-mass nuclei," Phys. Rev. C **100**, 024318 (2019).

[162] N. Nevo Dinur, O. J. Hernandez, S. Bacca, N. Barnea, C. Ji, S. Pastore, M. Piarulli, and R. B. Wiringa, "Zemach moments and radii of ^{2,3}H and ^{3,4}He," Phys. Rev. C **99**, 034004 (2019).

[163] S. Binder *et al.* (LENPIC Collaboration), "Few-nucleon and many-nucleon systems with semilocal coordinate-space regularized chiral nucleon-nucleon forces," Phys. Rev. C **98**, 014002 (2018).

[164] BUQEYE Collaboration, *What is BUQEYE? Bayesian Uncertainty Quantification: Error in Your EFT*, (2020) https://buqeye.github.io (visited on 08/21/2020).

[165] J. A. Melendez, *gsum (version 0.3)*, (2020) https://buqeye.github.io/gsum/ (visited on 08/21/2020).

[166] D. A. Varshalovich, A. N. Moskalev, and K. V. Khersonskii, *Quantum Theory of Angular Momentum* (World Scientific, 1988).

[167] D. R. Phillips and T. D. Cohen, "Deuteron electromagnetic properties and the viability of effective field theory methods in the two-nucleon system," Nucl. Phys. A **668**, 45 (2000).

[168] D. M. Bishop and L. M. Cheung, "Quadrupole moment of the deuteron from a precise calculation of the electric field gradient in D_2," Phys. Rev. A **20**, 381 (1979).

[169] T. Ericson and M. Rosa-Clot, "The deuteron asymptotic D-state as a probe of the nucleon-nucleon force," Nucl. Phys. A **405**, 497 (1983).

[170] M. Garçon and J. W. Van Orden, "The Deuteron: Structure and Form Factors," in *Advances in nuclear physics*, edited by J. W. Negele and E. W. Vogt (Springer US, Boston, MA, 2001), pp. 293–378.

[171] E. Epelbaum, W. Glöckle, and U.-G. Meißner, "Nuclear forces from chiral Lagrangians using the method of unitary transformation II: The two-nucleon system," Nucl. Phys. A **671**, 295 (2000).

[172] W. Glöckle, *The Quantum Mechanical Few-Body Problem* (Springer-Verlag Berlin Heidelberg, 1983).

[173] J. Golak *et al.*, "A new way to perform partial wave decompositions of few-nucleon forces," Eur. Phys. J. A **43**, 241 (2010).

[174] A. Stadler, W. Glöckle, and P. U. Sauer, "Faddeev equations with three-nucleon force in momentum space," Phys. Rev. C **44**, 2319 (1991).

[175] W. Glöckle, H. Witała, D. Hüber, H. Kamada, and J. Golak, "The Three nucleon continuum: Achievements, challenges and applications," Phys. Rep. **274**, 107 (1996).

[176] D. Hüber, H. Kamada, H. Witała, and W. Glöckle, "How to include a three-nucleon force into Faddeev equations for the 3N continuum: A New form," Acta Phys. Polon. B **28**, 1677 (1997).

[177] G. Höhler, E. Pietarinen, I. Sabba Stefanescu, F. Borkowski, G. G. Simon, V. H. Walther, and R. D. Wendling, "Analysis of Electromagnetic Nucleon Form-Factors," Nucl. Phys. **B114**, 505 (1976).

[178] J. J. Kelly, "Simple parametrization of nucleon form factors," Phys. Rev. C **70**, 068202 (2004).

[179] Z. Ye, J. Arrington, R. J. Hill, and G. Lee, "Proton and neutron electromagnetic form factors and uncertainties," Phys. Lett. B **777**, 8 (2018).

[180] B. Kubis and U.-G. Meißner, "Low-energy analysis of the nucleon electromagnetic form factors," Nucl. Phys. A **679**, 698 (2001).

[181] E. Epelbaum, A. M. Gasparyan, J. Gegelia, and M. R. Schindler, "Deuteron electromagnetic form factors in a renormalizable formulation of chiral effective field theory," Eur. Phys. J. A **50**, 51 (2014).

[182] R. G. Arnold *et al.*, "Measurements of deuteron magnetic form factor high momentum transfer," Phys. Rev. Lett. **58**, 1723 (1987).

[183] A. Camsonne *et al.* (The Jefferson Lab Hall A Collaboration), "JLab Measurements of the ^{3}He Form Factors at Large Momentum Transfers," Phys. Rev. Lett. **119**, 162501 (2017). [Erratum: Phys. Rev. Lett. **119**, 209901 (2017)].

[184] M. Walzl and U.-G. Meißner, "Elastic electron–deuteron scattering in chiral effective field theory," Phys. Lett. B **513**, 37 (2001).

[185] D. R. Phillips, "Higher-order calculations of electron–deuteron scattering in nuclear effective theory," Phys. Lett. B **567**, 12 (2003).

[186] D. R. Phillips, "Chiral effective theory predictions for deuteron form factor ratios at low Q^2," J. Phys. G: Nucl. Part. Phys. **34**, 365 (2007).

[187] M. Pavón Valderrama, A. Nogga, E. Ruiz Arriola, and D. R. Phillips, "Deuteron form factors in chiral effective theory: Regulator-independent results and the role of two-pion exchange," Eur. Phys. J. A **36**, 315 (2008).

[188] S. Kölling, E. Epelbaum, and D. R. Phillips, "Magnetic form factor of the deuteron in chiral effective field theory," Phys. Rev. C **86**, 047001 (2012).

[189] D. R. Entem and R. Machleidt, "Accurate charge-dependent nucleon-nucleon potential at fourth order of chiral perturbation theory," Phys. Rev. C **68**, 041001 (2003).

[190] R. Schiavilla *et al.*, "Local chiral interactions and magnetic structure of few-nucleon systems," Phys. Rev. C **99**, 034005 (2019).

[191] L. de Broglie, "XXXV. A tentative theory of light quanta," Philos. Mag. **47**, 446 (1924).

[192] V. Punjabi, C. F. Perdrisat, M. K. Jones, E. J. Brash, and C. E. Carlson, "The structure of the nucleon: Elastic electromagnetic form factors," Eur. Phys. J. A **51**, 79 (2015).

[193] C. Patrignani (Particle Data Group), "Review of Particle Physics," Chin. Phys. C **40**, 100001 (2016).

[194] F. Gross, "Relativistic Calculation of the Deuteron Electromagnetic Form Factor. II," Phys. Rev. **136**, B140 (1964).

[195] R. G. Arnold, C. E. Carlson, and F. Gross, "Elastic electron-deuteron scattering at high energy," Phys. Rev. C **21**, 1426 (1980).

[196] W. Glöckle, G. Hasberg, and A. R. Neghabian, "Numerical treatment of few body equations in momentum space by the Spline method," Z. Phys. A **305**, 217 (1982).

[197] M. E. Schulze *et al.*, "Measurement of the Tensor Polarization in Electron-Deuteron Elastic Scattering," Phys. Rev. Lett. **52**, 597 (1984).

[198] M. Garçon *et al.*, "Tensor polarization in elastic electron-deuteron scattering in the momentum transfer range $3.8 \leq Q \leq 4.6$ fm^{-1}," Phys. Rev. C **49**, 2516 (1994).

[199] V. F. Dmitriev, D. M. Nikolenko, S. G. Popov, I. A. Rachek, Y. Shatunov, D. K. Toporkov, E. P. Tsentalovich, Y. Ukraintsev, B. B. Voitsekhovskii, and V. G. Zelevinsky, "First measurement of the asymmetry in electron scattering by a jet target of polarized deuterium atoms," Phys. Lett. B **157**, 143 (1985).

[200] B. B. Voitsekhovskii, D. M. Nikolenko, K. T. Ospanov, S. G. Popov, I. A. Rachek, D. K. Toporkov, E. P. Tsentalovich, and Y. M. Shatunov, "Asymmetry in the reaction d(e,e'd) at a momentum transfer of 1-1.5 fm^{-1}," JETP Lett. **43**, 733 (1986).

[201] R. Gilman *et al.*, "Measurement of tensor analyzing power in electron-deuteron elastic scattering," Phys. Rev. Lett. **65**, 1733 (1990).

[202] D. M. Nikolenko *et al.*, "Measurement of the Tensor Analyzing Powers T_{20} and T_{21} in Elastic Electron-Deuteron Scattering," Phys. Rev. Lett. **90**, 072501 (2003).

[203] B. Boden *et al.*, "Elastic electron deuteron scattering on a tensor polarized solid ND_3 target," Z. Phys. C **49**, 175 (1991).

[204] M. Ferro-Luzzi *et al.*, "Measurement of Tensor Analyzing Powers for Elastic Electron Scattering from a Polarized ^{2}H Target Internal to a Storage Ring," Phys. Rev. Lett. **77**, 2630 (1996).

[205] M. Bouwhuis *et al.*, "Measurement of T_{20} in Elastic Electron-Deuteron Scattering," Phys. Rev. Lett. **82**, 3755 (1999).

[206] D. Abbott *et al.* (The Jefferson Lab t20 Collaboration), "Measurement of Tensor Polarization in Elastic Electron-Deuteron Scattering at Large Momentum Transfer," Phys. Rev. Lett. **84**, 5053 (2000).

[207] C. Zhang *et al.* (The BLAST collaboration), "Precise Measurement of Deuteron Tensor Analyzing Powers with BLAST," Phys. Rev. Lett. **107**, 252501 (2011).

[208] E. Epelbaum, W. Glöckle, and U.-G. Meißner, "The two-nucleon system at next-to-next-to-next-to-leading order," Nucl. Phys. A **747**, 362 (2005).

[209] C. D. Buchanan and M. R. Yearian, "Elastic Electron-Deuteron Scattering and Possible Meson-Exchange Effects," Phys. Rev. Lett. **15**, 303 (1965).

[210] G. G. Simon, C. Schmitt, and V. H. Walther, "Elastic electric and magnetic e-d scattering at low momentum transfer," Nucl. Phys. A **364**, 285 (1981).

[211] R. Cramer *et al.*, "Measurement of the magnetic form factor of the deuteron for $Q^2 = 0.5$ to 1.3 (GeV/c)^2 by a coincidence experiment," Z. Phys. C **29**, 513 (1985).

[212] S. Auffret *et al.*, "Magnetic Form Factor of the Deuteron," Phys. Rev. Lett. **54**, 649 (1985).

[213] P. E. Bosted *et al.*, "Measurements of the deuteron and proton magnetic form factors at large momentum transfers," Phys. Rev. C **42**, 38 (1990).

[214] U. van Kolck, "Few-nucleon forces from chiral Lagrangians," Phys. Rev. C **49**, 2932 (1994).

[215] S. K. Bogner, R. J. Furnstahl, and A. Schwenk, "From low-momentum interactions to nuclear structure," Prog. Part. Nucl. Phys. **65**, 94 (2010).

[216] J. Simonis, S. R. Stroberg, K. Hebeler, J. D. Holt, and A. Schwenk, "Saturation with chiral interactions and consequences for finite nuclei," Phys. Rev. C **96**, 014303 (2017).

[217] T. D. Morris, J. Simonis, S. R. Stroberg, C. Stumpf, G. Hagen, J. D. Holt, G. R. Jansen, T. Papenbrock, R. Roth, and A. Schwenk, "Structure of the Lightest Tin Isotopes," Phys. Rev. Lett. **120**, 152503 (2018).

[218] I. Sick and D. Trautmann, "On the rms radius of the deuteron," Nucl. Phys. A **637**, 559 (1998).

[219] A. Antognini, "Muonic atoms and the nuclear structure," (2015), arXiv:1512.01765.

[220] O. J. Hernandez, C. Ji, S. Bacca, N. Nevo Dinur, and N. Barnea, "Improved estimates of the nuclear structure corrections in μD," Phys. Lett. B **736**, 344 (2014).

[221] C. Ji, S. Bacca, N. Barnea, O. J. Hernandez, and N. Nevo Dinur, "*Ab initio* calculation of nuclear-structure corrections in muonic atoms," J. Phys. G: Nucl. Part. Phys. **45**, 093002 (2018).

[222] U. Friman-Gayer *et al.*, "Role of chiral two-body currents in ^{6}Li magnetic properties in light of a new precision measurement with the relative self-absorption technique," (2020), arXiv:2005.07837.

[223] Y.-H. Song, R. Lazauskas, T.-S. Park, and D.-P. Min, "Effective field theory approach for the M1 properties of $A = 2$ and 3 nuclei," Phys. Lett. B **656**, 174 (2007).

[224] Y.-H. Song, R. Lazauskas, and T.-S. Park, "Up to N^{3}LO heavy-baryon chiral perturbation theory calculation for the $M1$ properties of three-nucleon systems," Phys. Rev. C **79**, 064002 (2009).

[225] J. D. Walecka, *Theoretical Nuclear and Subnuclear Physics*, Second Edition (Imperial College Press and World Scientific, 2004).

[226] M. J. Blatt and F. victor Weisskopf, *Theoretical nuclear physics*, First Edition (John Wiley & Sons, 1952).

[227] F. J. Ernst, R. G. Sachs, and K. C. Wali, "Electromagnetic Form Factors of the Nucleon," Phys. Rev. **119**, 1105 (1960).

[228] M. Gourdin, "Electromagnetic form factors," Il Nuovo Cimento **36**, 129 (1965).

[229] V. Z. Jankus, "Calculation of Electron-Deuteron Scattering Cross Sections," Phys. Rev. **102**, 1586 (1956).

[230] R. G. Sachs, "Phenomenological Theory of Exchange Currents in Nuclei," Phys. Rev. **74**, 433 (1948).

[231] I. Talmi, "Nuclear spectroscopy with harmonic oscillator wave-functions," Helv. Phys. Acta **25**, 185 (1952).

[232] M. Moshinsky, "Transformation brackets for harmonic oscillator functions," Nucl. Phys. **13**, 104 (1959).

[233] S. Binder, A. Ekström, G. Hagen, T. Papenbrock, and K. A. Wendt, "Effective field theory in the harmonic oscillator basis," Phys. Rev. C **93**, 044332 (2016).

[234] G. P. Kamuntavičius, R. K. Kalinauskas, B. R. Barrett, S. Mickevičius, and D. Germanas, "The general harmonic-oscillator brackets: compact expression, symmetries, sums and Fortran code," Nucl. Phys. A **695**, 191 (2001).

[235] O. J. Hernandez, private communication, 2019.

[236] P. Ring and P. Schuck, *The nuclear many-body problem*, First Edition (Springer-Verlag Berlin Heidelberg, 1980).

[237] P. Maris *et al.*, "No Core CI calculations for light nuclei with chiral 2-and 3-body forces," J. Phys. Conf. Ser. **454**, 012063 (2013).

[238] B. R. Barrett, P. Navrátil, and J. P. Vary, "Ab initio no core shell model," Prog. Part. Nucl. Phys. **69**, 131 (2013).

[239] A. Szabo and N. S. Ostlund, *Modern Quantum Chemistry: Introduction to Advanced Electronic Structure Theory*, Revised Edition (Dover Publications, 1996).

[240] P. Maris, J. P. Vary, and A. M. Shirokov, "*Ab initio* no-core full configuration calculations of light nuclei," Phys. Rev. C **79**, 014308 (2009).

[241] P. Navrátil, J. P. Vary, and B. R. Barrett, "Large-basis *ab initio* no-core shell model and its application to ^{12}C," Phys. Rev. C **62**, 054311 (2000).

[242] P. Navrátil, J. P. Vary, and B. R. Barrett, "Properties of ^{12}C in the *Ab Initio* Nuclear Shell Model," Phys. Rev. Lett. **84**, 5728 (2000).

[243] R. Roth and P. Navrátil, "*Ab Initio* Study of ^{40}Ca with an Importance-Truncated No-Core Shell Model," Phys. Rev. Lett. **99**, 092501 (2007).

[244] R. Roth, "Importance truncation for large-scale configuration interaction approaches," Phys. Rev. C **79**, 064324 (2009).

[245] L. E. Marcucci, M. Pervin, S. C. Pieper, R. Schiavilla, and R. B. Wiringa, "Quantum Monte Carlo calculations of magnetic moments and $M1$ transitions in $A \leqslant 7$ nuclei including meson-exchange currents," Phys. Rev. C **78**, 065501 (2008).

[246] R. Roth, J. Langhammer, A. Calci, S. Binder, and P. Navrátil, "Similarity-Transformed Chiral $NN+3N$ Interactions for the *Ab Initio* Description of ^{12}C and ^{16}O," Phys. Rev. Lett. **107**, 072501 (2011).

[247] R. Roth, A. Calci, J. Langhammer, and S. Binder, "Evolved chiral $NN+3N$ Hamiltonians for *ab initio* nuclear structure calculations," Phys. Rev. C **90**, 024325 (2014).

[248] R. B. Wiringa, V. G. J. Stoks, and R. Schiavilla, "Accurate nucleon-nucleon potential with charge-independence breaking," Phys. Rev. C **51**, 38 (1995).

[249] S. C. Pieper, V. R. Pandharipande, R. B. Wiringa, and J. Carlson, "Realistic models of pion-exchange three-nucleon interactions," Phys. Rev. C **64**, 014001 (2001).

[250] S. C. Pieper, "The Illinois Extension to the Fujita-Miyazawa Three-Nucleon Force," AIP Conf. Proc. **1011**, 143 (2008).

[251] D. R. Tilley, C. M. Cheves, J. L. Godwin, G. M. Hale, H. M. Hofmann, J. H. Kelley, C. G. Sheu, and H. R. Weller, "Energy levels of light nuclei $A = 5, 6, 7$," Nucl. Phys. A **708**, 3 (2002).

[252] A. Richter, “Operational experience at the S-DALINAC,” in Proc. epac’96 (1996), p. 110.

[253] N. Pietralla, “The Institute of Nuclear Physics at the TU Darmstadt,” Nucl. Phys. News **28**, 4 (2018).

[254] P. J. Nolan and J. F. Sharpey-Schafer, “The measurement of the lifetimes of excited nuclear states,” Rep. Prog. Phys. **42**, 1 (1979).

[255] R. G. H. Robertson, P. Dyer, R. C. Melin, T. J. Bowles, A. B. McDonald, G. C. Ball, W. G. Davies, and E. D. Earle, “Upper limit on the isovector parity-violating decay width of the 0^+ $T = 1$ state of ^{6}Li,” Phys. Rev. C **29**, 755 (1984).

[256] O. Hashimoto and H. Tamura, “Spectroscopy of Λ hypernuclei,” Prog. Part. Nucl. Phys. **57**, 564 (2006).

[257] K. Sonnabend *et al.*, “The Darmstadt High-Intensity Photon Setup (DHIPS) at the S-DALINAC,” Nucl. Instrum. Meth. A **640**, 6 (2011).

[258] C. Romig *et al.*, “Direct determination of ground-state transition widths of low-lying dipole states in ^{140}Ce with the self-absorption technique,” Phys. Lett. B **744**, 369 (2015).

[259] C. Romig, *Investigation of Nuclear Structure with Relative Self-Absorption Measurements*, PhD thesis (TU Darmstadt, 2015).

[260] A. Knecht *et al.*, “Precision Measurement of the ^{6}He Half-Life and the Weak Axial Current in Nuclei,” Phys. Rev. Lett. **108**, 122502 (2012).

[261] A. Nogga, P. Navrátil, B. R. Barrett, and J. P. Vary, “Spectra and binding energy predictions of chiral interactions for ^{7}Li,” Phys. Rev. C **73**, 064002 (2006).

[262] J. Simonis, *Ab initio calculations of nuclei using chiral interactions with realistic saturation properties*, PhD thesis (TU Darmstadt, 2017).

[263] E. Kessler, Jr, M. Dewey, R. Deslattes, A. Henins, H. Börner, M. Jentschel, C. Doll, and H. Lehmann, “The deuteron binding energy and the neutron mass,” Phys. Lett. A **255**, 221 (1999).

[264] S. Rau, F. Heiße, F. Köhler-Langes, S. Sasidharan, R. Haas, D. Renisch, C. E. Düllmann, W. Quint, S. Sturm, and K. Blaum, “Penning trap mass measurements of the deuteron and the HD$^+$ molecular ion,” Nature **585**, 43 (2020).

[265] C. G. Parthey, A. Matveev, J. Alnis, R. Pohl, T. Udem, U. D. Jentschura, N. Kolachevsky, and T. W. Hänsch, “Precision Measurement of the Hydrogen-Deuterium $1S$-$2S$ Isotope Shift,” Phys. Rev. Lett. **104**, 233001 (2010).

[266] P. Abbon *et al.* (COMPASS Collaboration), “The COMPASS experiment at CERN,” Nucl. Instrum. Methods Phys. Res. A **577**, 455 (2007).

[267] R. Gilman, “Studying the proton "radius" puzzle with μp elastic scattering,” AIP Conf. Proc. **1563**, 167 (2013).

[268] R. Pohl *et al.*, “Laser Spectroscopy of Muonic Atoms and Ions,” JPS Conf. Proc. **18**, 011021 (2017).

[269] R. G. H. Robertson, J. A. Nolen, T. Chapuran, and R. Vodhanel, “Mass of ^{6}Li and the excitation energy of its 3.56-MeV state,” Phys. Rev. C **23**, 973 (1981).

[270] P. Raghavan, “Table of nuclear moments,” At. Data Nucl. Data Tables **42**, 189 (1989).

CURRICULUM VITAE

Zur Person

Name	Rodric Seutin
Geburtsdatum	23. Januar 1992
Geburtsort	Leuven, Belgien
Nationalität	belgisch

Akademische Ausbildung

03/2017 - 11/2020	Wissenschaftlicher Mitarbeiter, im Rahmen der “International Max Planck Research School of Precision Tests of Fundamental Symmetries”, Max-Planck-Institut für Kernphysik, Heidelberg
09/2016 - 11/2020	Promotion in Physik, Institut für Kernphysik, Technische Universität Darmstadt
09/2015 - 02/2016	Auslandsstudium, International Exchange Program, ETH Zürich, Schweiz
09/2014 - 06/2016	Master of Science in Physics, KU Leuven, Belgien, Thesis: *Revision of the Ramsey curve for a more reliable neutron electric dipole moment value*, Betreuer: Prof. Dr. Nathal Severijns
09/2010 - 09/2014	Bachelor of Science in Physics, KU Leuven, Belgien, Thesis: *Scanning force microscopy of graphene based samples*, Betreuer: Dr. Alexander Volodin

ERKLÄRUNG ZUR DISSERTATION

Gemäß §9 Promotionsordnung:

Hiermit versichere ich, dass ich die vorliegende Dissertation selbständig angefertigt und keine anderen als die angegebenen Quellen und Hilfsmittel verwendet habe. Alle wörtlichen und paraphrasierten Zitate wurden angemessen kenntlich gemacht. Die Arbeit hat bisher noch nicht zu Prüfungszwecken gedient.

Darmstadt, den 9. Oktober 2020

Rodric Seutin